DESIGN AND ANALYSIS OF NUMERICAL METHODS FOR FREE- AND MOVING-BOUNDARY PROBLEMS

A DISSERTATION
SUBMITTED TO THE INSTITUTE FOR COMPUTATIONAL AND MATHEMATICAL ENGINEERING
AND THE COMMITTEE ON GRADUATE STUDIES
OF STANFORD UNIVERSITY
IN PARTIAL FULFILLMENT OF THE REQUIREMENTS
FOR THE DEGREE OF
DOCTOR OF PHILOSOPHY

Evan Scott Gawlik
August 2015

© 2015 by Evan Scott Gawlik. All Rights Reserved.

Re-distributed by Stanford University under license with the author.

This work is licensed under a Creative Commons Attribution-Noncommercial 3.0 United States License.
http://creativecommons.org/licenses/by-nc/3.0/us/

This dissertation is online at: http://purl.stanford.edu/qq535zr7369

I certify that I have read this dissertation and that, in my opinion, it is fully adequate in scope and quality as a dissertation for the degree of Doctor of Philosophy.

Adrian Lew, Primary Adviser

I certify that I have read this dissertation and that, in my opinion, it is fully adequate in scope and quality as a dissertation for the degree of Doctor of Philosophy.

Charbel Farhat

I certify that I have read this dissertation and that, in my opinion, it is fully adequate in scope and quality as a dissertation for the degree of Doctor of Philosophy.

George Papanicolaou

Approved for the Stanford University Committee on Graduate Studies.

Patricia J. Gumport, Vice Provost for Graduate Education

This signature page was generated electronically upon submission of this dissertation in electronic format. An original signed hard copy of the signature page is on file in University Archives.

Abstract

This thesis presents the design and analysis of numerical methods for free- and moving-boundary problems: partial differential equations posed on domains that change with time. Two principal developments are presented.

First, a novel framework is introduced for solving free- and moving-boundary problems with a high order of accuracy. This framework has the distinct advantage that it can handle large domain deformations easily (a common difficulty faced by conventional deforming-mesh methods) while representing the geometry of the moving domain exactly (an infeasible task for conventional fixed-mesh methods). This is accomplished using a universal mesh: a background mesh that contains the moving domain and conforms to its geometry at all times by perturbing a small number of nodes in a neighborhood of the moving boundary. The resulting framework admits, in a general fashion, the construction of methods that are of arbitrarily high order of accuracy in space and time when the boundary evolution is prescribed. Numerical examples involving phase-change problems, fluid flow around moving obstacles, and free-surface flows are presented to illustrate the technique.

Second, a unified analytical framework is developed for establishing the convergence properties of a wide class of numerical methods for moving-boundary problems. This class includes, as special cases, the technique described above as well as conventional deforming-mesh methods (commonly known as arbitrary Lagrangian-Eulerian, or ALE, schemes). An instrumental tool developed in this analysis is an abstract estimate, which applies to rather general mesh motions, for the error incurred by finite element discretizations of parabolic moving-boundary problems. Specializing the abstract estimate to particular choices of the mesh motion strategy and finite element space leads to error estimates in terms of the mesh spacing for various semidiscrete schemes. We illustrate this by deriving error estimates for ALE schemes under mild assumptions on the nature of the mesh deformation and the regularity of the exact solution and the moving domain, and we do the same for universal meshes.

Acknowledgements

During my Ph.D., I've been fortunate to have the support, friendship, and collaboration of many individuals. First and foremost, I thank my advisor, Adrian Lew. Over the years, Adrian has taught me a great deal of engineering and mathematics, and he's continually inspired me to be a better researcher – by challenging me to think critically and rigorously, by exuding excitement, and by engaging me in lively discussions. Thank you, Adrian, for all of your guidance in my research and in my career.

I'd like to next say thank you to the two people who have shared an office with me for the vast majority of my time at Stanford: Maurizio Chiaramonte and Hardik Kabaria. Thank you both for being great friends and for sharing so many good times, stories, jokes, and ideas over the years. Thanks also to those that arrived more recently – Yi Shu, Kyuwon Kim, Felipe Montefuscolo, and Ben Grossman-Ponemon – as well as those that left earlier on – Ram Rangarajan, Raymond Ryckman, Michael Hunsweck, and Sohan Dharmaraja – for your friendship. I'm especially thankful to Ram for getting me started on the right foot when I began my doctoral research.

During the spring of 2014, I had the pleasure of spending a quarter in the mathematics department at the University of Pavia. I'm very grateful to have been hosted by Matteo Negri, who made me feel at home many thousands of miles abroad. I owe him many thanks for all of the fond memories I have of my visit.

I'm very thankful to Charbel Farhat, George Papanicolaou, Sanjiva Lele, and Christian Linder for their service on my thesis committee. I thank them for the time they have sacrificed and the valuable feedback they have given me.

I'm also grateful to have had the support of the DOE Computational Science Graduate Fellowship, and later the National Science Foundation Graduate Research Fellowship, throughout my time at Stanford.

In the years leading up to graduate school, I was fortunate to be able to do research as a Caltech undergraduate under the supervision of Jerrold Marsden and Mathieu Desbrun. I'm forever grateful to them for strengthening my passion for applied mathematics and for guiding me in my academic pursuits. I'm also lucky to have a cohort of friends from my undergraduate house at Caltech who have remained tight-knit well after graduating. It was a pleasure to spend time with all of you in

the “Avery Friends of the Bay Area” crowd.

My enjoyment of life during the past five years has been vastly enriched by my girlfriend, Chao. Thank you, Chao, for being a constant source of happiness in my life and joining me on countless adventures.

Finally, thank you to my mom, dad, and brother Matt for supporting me in all that I do.

Contents

List of Tables

List of Figures

Chapter 1

Introduction

Many important and challenging problems in computational science and engineering involve partial differential equations posed on moving domains. Notable examples include fluid-structure interaction, phase-change problems, cardiovascular flow, fracture mechanics, and biolocomotion. This thesis presents novel numerical methods for the solution of such problems, as well as mathematical tools for analyzing their accuracy.

Broadly speaking, computational methods for moving-boundary problems typically adhere to one of two paradigms. *Deforming-mesh* methods employ a computational mesh that deforms in concert with the moving domain, whereas *fixed-mesh* methods employ a stationary background mesh in which the domain is immersed. Figs. 1.1-1.2 illustrate these two paradigms schematically. Chapter 2 of this thesis introduces an alternative framework for solving moving-boundary problems which has the distinct advantage that it can handle large domain deformations easily (a common difficulty faced by deforming-mesh methods) while representing the geometry of the moving domain exactly (an infeasible task for fixed-mesh methods). This is accomplished using a *universal mesh*: a background mesh that contains the moving domain and conforms to its geometry at all times by perturbing a small number of nodes in a neighborhood of the moving boundary, as depicted in Fig. 1.3. The resulting framework admits, in a general fashion, the construction of methods that are of arbitrarily high order of accuracy in space and time.

In the process of deriving our method, we present a unified analytical framework that puts our method and existing deforming-mesh methods on a common footing suitable for analysis. We then carry out such an analysis, in a unified manner, in Chapter 3. There, an abstract a priori estimate is derived for the error incurred by finite element discretizations of parabolic moving-boundary problems. This abstract estimate, which applies to rather general mesh motion strategies, bounds the semidiscrete error at a fixed positive time in terms of quantities dependent on the approximation order of the finite element spaces, the regularity of the mesh's evolution, and the projector adopted at remeshing times (instances at which the mesh changes abruptly) to transfer information between

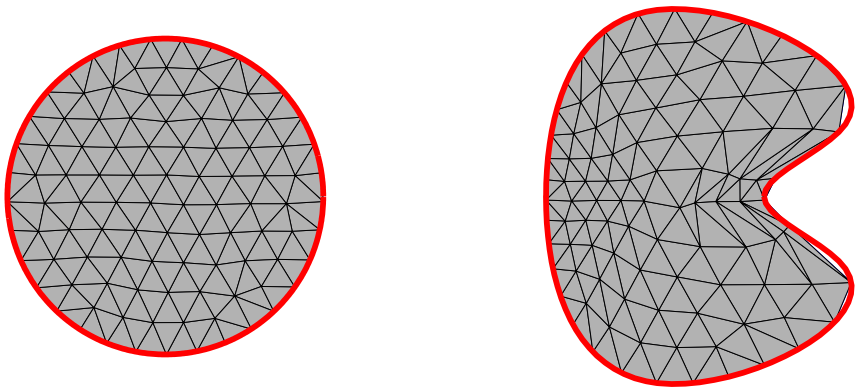

(a) $t = 0$ (b) $t > 0$

Figure 1.1: Schematic depiction of a deforming-mesh method. Without a careful choice of nodal motions, elements can suffer unwanted distortions under large deformations of the moving domain. Here, for purely illustrative purposes, we have employed a nodal mapping of the form $(r, \theta) \mapsto (f(\theta)r, \theta)$ in polar coordinates.

finite element spaces. An important feature of this estimate is that it applies to both universal meshes and conventional deforming-mesh methods, even though the ultimate convergence orders of the two approaches with respect to the mesh spacing differ markedly. We accomplish this by leaving the precise choice of the mesh motion strategy, remeshing times, finite elements, and projector unspecified throughout much of the analysis.

The error analysis in Chapter 3 highlights, among other things, the manner in which remeshing influences the accuracy of numerical methods. This aspect of the analysis motivates Chapter 4, which studies orthogonal projections of smooth functions onto "nearby" finite element spaces. The theory presented therein, loosely speaking, verifies the intuitive notion that errors committed during remeshing are mitigated when the updated mesh differs from the original mesh over only a small fraction of the domain. This observation is of crucial importance for universal meshes, since, as shall be seen, the abrupt changes in the mesh are always restricted to a band of elements whose measure tends to zero under refinement.

Leveraging the results of Chapter 4, we apply the abstract error analysis of Chapter 3 to derive concrete error estimates for methods based on universal meshes in Chapter 5. There, the delicate interplay between errors due to remeshing and errors due to semidiscretization is brought to light, and an error estimate in terms of the mesh spacing that is suboptimal by half an order in the L^2-norm is derived.

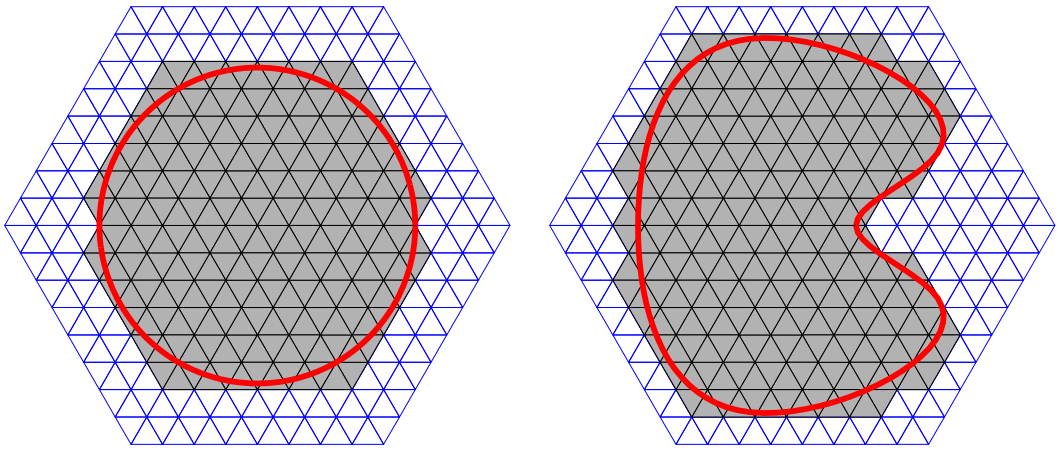

(a) $t = 0$ (b) $t > 0$

Figure 1.2: Schematic depiction of a fixed-mesh method. Such methods employ a fixed background mesh which does not conform to the immersed domain.

We conclude in Chapter 6 with several numerical examples illustrating the performance of universal meshes. These examples include flow past moving obstacles as well as free-surface flow with surface tension. We showcase the framework's ability to simultaneously deliver high-order accuracy and handle large domain deformations.

Much of this thesis is based on published and submitted articles. The framework introduced in Chapter 2 for solving moving-boundary problems with universal meshes was proposed in [59]. The abstract analysis in Chapter 3 was developed in [61], and the study of projections onto nearby finite element spaces appearing in Chapter 4 was carried out in [60]. Finally, many of the numerical examples in Chapter 6 appeared in [58] and [33].

1.1 Related Work

In what follows, we review some of the existing numerical methods for moving-boundary problems, including deforming-mesh methods and fixed-mesh methods. We conclude with a discussion of prior work on universal meshes, as well as prior work on the analysis of numerical methods for moving-boundary problems.

1.1.1 Review of Numerical Methods for Moving-Boundary Problems

Deforming-mesh methods. Deforming-mesh methods have enjoyed widespread success in the scientific and engineering communities, where they are best known as Arbitrary Lagrangian Eulerian (ALE) methods. The appellation refers to the fact that in prescribing a motion of the mesh, a

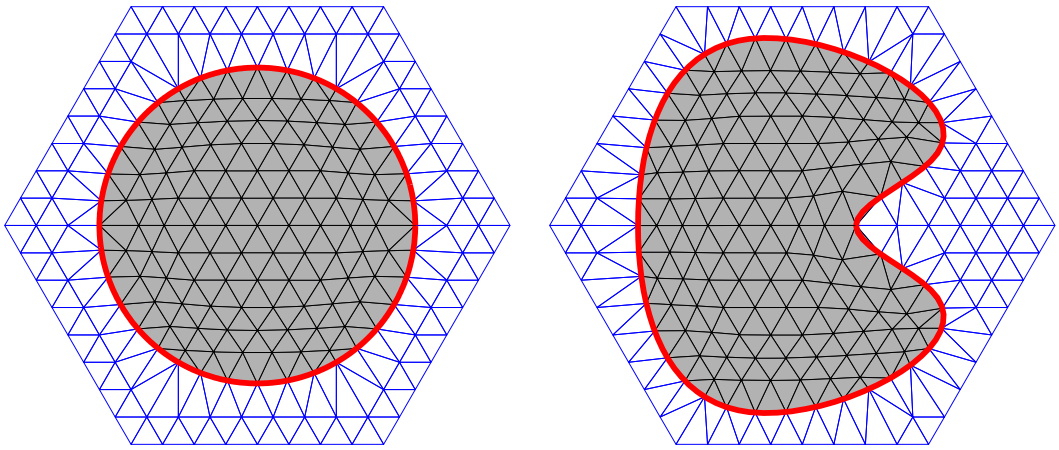

(a) $t = 0$ (b) $t > 0$

Figure 1.3: Schematic depiction of a universal mesh. By adapting the mesh to the immersed domain, one obtains a mesh that conforms to the domain exactly and is immune to large distortions of elements.

kinematic description of the physics is introduced that is neither Eulerian (in which the domain moves over a fixed mesh) nor Lagrangian (in which the domain does not move with respect to the mesh). The resulting formalism leads to governing equations that contain a term involving the velocity of the prescribed mesh motion that is otherwise absent in schemes on a fixed mesh [89, 100]. Early appearances of the ALE framework date back to the works of Hirt et. al. [74], Hughes et. al. [77], and Donea et. al. [42]. ALE methods have seen use in fluid-structure interaction [48, 50, 51, 63, 126, 128], solid mechanics [8, 82, 97, 135], thermodynamics [1, 19, 127, 142], and other applications.

Accuracy considerations render deforming-mesh methods attractive, especially if implemented using curved elements along the boundary, since errors in the discretization of the domain's geometry (and in the discretization, if any, of its temporal evolution) can dictate the order of a method. In this light, it is perhaps surprising that many examples of deforming-mesh methods in the literature, with a few noteworthy exceptions [22, 37, 54, 72, 99, 105, 107, 108, 136, 140], are often restricted to at most second-order accuracy [21, 50, 51, 55–57, 63, 81, 101].

One of the key challenges that ALE methods face is the maintenance of a good-quality mesh during large deformations of the domain [10, 16]. Fig. 1.1 illustrates a case where, using an intentionally naive choice of nodal motions, a domain deformation can lead to triangles with poor aspect ratios. In more severe cases, element inversions can occur. Such distortions are detrimental both to the accuracy of the spatial discretization and to the conditioning of the discrete governing equations [104]. For this reason, it is common to use sophisticated mesh motion strategies that

involve solving systems of equations (such as those of linear elasticity) for the positions of mesh nodes [52, 73, 78, 80]. Regardless of a deforming-mesh method's mesh motion strategy, sufficiently large domain deformations can, in some cases, mandate that the domain be remeshed from scratch at various instants during a simulation [78, 84, 98, 126].

A related class of methods are spacetime methods (e.g., [131]), where the spacetime domain swept out by the moving spatial domain is discretized with straight or curved elements. These methods resemble deforming-mesh methods in the sense that spatial slices of the spacetime mesh at fixed temporal nodes constitute a mesh of the moving domain at those times. Bonnerot and Jamet [24, 25] have used a spacetime framework to construct high-order methods for the Stefan problem in one dimension. They require the use of curved elements along the moving boundary to achieve the desired temporal accuracy. Jamet [79] provides a generalization of these high-order methods to dimensions greater than one in the case that the boundary evolution is prescribed in advance. More recently, Rhebergen and Cockburn [119, 120] created hybridizable-discontinuous-Galerkin-based spacetime methods for advection-diffusion and incompressible flow problems with moving domains.

Fixed-mesh methods. At the other extreme are fixed-mesh methods, which cover a sufficiently large domain with a mesh and evolve a numerical representation of the boundary, holding the background mesh fixed [47, 90, 114, 133]. Several techniques can be used to represent the boundary, including level sets [64, 125], marker particles [144], and splines [138]. Fixed-mesh methods require special care in order to account for the disagreement between the immersed boundary and element interfaces. A variety of strategies aim to deal with this discrepancy, including adaptive refinement near the immersed boundary [18, 40, 111], cutting elements [13, 75, 106, 123, 124], enriching finite element spaces [62, 147], cutting elements and enriching finite element spaces[9, 91, 117], Nitsche-inspired methods [41, 71], smearing the interface [4, 53], modifying finite-difference stencils near the boundary [2, 102, 111, 133], and introducing surrogate forcing terms in lieu of the boundary conditions [47, 114]. Integration in time poses an additional challenge for fixed-mesh methods, since nodes of the background mesh may occupy differing states (e.g., fluid vs. solid) over the course of a single time step. This peculiarity is known to introduce numerical artifacts such as spurious oscillations in the pressure field for some fixed-mesh methods designed for simulating flow past moving obstacles [88, 124, 139]. Furthermore, even if a given spatial discretization is known to deliver high-order spatial accuracy for time-independent PDEs with embedded boundaries, its incorporation into a numerical method for solving time-dependent PDEs in the presence of *moving* boundaries with high spatial and temporal accuracy is arguably a nontrivial task. These observations help to explain why many fixed mesh methods, again with a few notable exceptions [38, 95, 143], are often restricted to first- or second-order accuracy [47, 67, 83, 93, 133, 138].

Universal meshes. Universal meshes were first introduced in [115, 116], where a strategy for meshing smooth two-dimensional domains by adjusting the elements of a background mesh was proposed and later analyzed [118]. Since the strategy delivers a conforming discretization of the domain, its application to the solution of time-independent problems, and even quasi-steady moving-boundary problems, is immediate: one may construct a finite element space over the conforming mesh, and solve, for instance, a Galerkin discretization of the governing equations. Solving time-dependent moving-boundary problems with moving boundaries, however, poses a greater challenge. The reasons for this are analogous to those that prevent fixed-mesh methods for PDEs on static, embedded domains from being extended trivially to PDEs on embedded moving domains. Notably, the approximation space over the moving domain generally needs to evolve in time, resulting in a changing set of degrees of freedom, and the approximation of time-derivatives of the solution near the moving boundary needs to be carefully constructed, since solution values at a given spatial location may not be defined at all time instants within a time step. We address these issues in Chapter 2.

Despite its conceptual simplicity, the method presented in this thesis has not been proposed in the literature. An idea similar to ours, dubbed a "fixed-mesh ALE" method, has recently been proposed by Baiges and Codina [13, 14], though there are several important differences. In particular, their method uses element splitting to define intermediate meshes during temporal integration, whereas our method leaves the connectivity of the mesh intact. Second, they advocate imposing boundary conditions approximately to improve efficiency; our method imposes boundary conditions exactly without extra computational effort. Finally, they focus only on low-order schemes with piecewise linear approximations to the domain deformation, while we derive schemes of arbitrarily high order.

1.1.2 Review of Numerical Analyses for Moving-Boundary Problems

The analysis of deforming-mesh methods has received the attention of several prior authors, though none to our knowledge have adopted the same focus or scope as the present work. Many efforts have addressed the stability of temporal discretizations [21, 55, 56], often focusing on a well-known condition (the so-called *Geometric Conservation Law*) that ensures stability of certain low-order schemes [49, 68]. Bonito and co-authors [22, 23] study ALE schemes in the temporally discrete, spatially continuous setting and present a family of high-order time integrators that achieve optimal order of accuracy in time for a model parabolic problem on a moving domain. They derive, among other things, sufficient conditions to ensure mesh-motion-independent stability of the time integrators. Gastaldi [57] proves a priori error estimates for a second-order accurate fully discrete scheme, and the spatially discrete analysis presented therein bears some similarity to the present work. Our analysis, however, generalizes Gastaldi's in several key respects. We consider general mesh deformations, rather than those derived from solutions to the equations of linear elasticity; we account for remeshing; and we consider finite element spaces of arbitrary order, rather than piecewise linears. Another study that is much in the spirit of the present work is Elliott & Venkataraman's

analysis [44] of a finite element method for an advection-diffusion equation on an evolving surface, which considers the use of piecewise linears without remeshing. Finally, Dupont [43] analyzes finite element methods on moving meshes over fixed domains and accounts for remeshing. There, the focus is on a special choice of norm over the spacetime domain in which the error is quasi-optimal.

Chapter 2

High-Order Methods for Moving-Boundary Problems Using Universal Meshes

2.1 Introduction

One of the key challenges in numerical simulations of moving-boundary problems is the discretization of an evolving domain. Commonly, this challenge is addressed using one of two tools: a deforming mesh, which deforms in concert with the moving fluid domain, or a fixed mesh, which triangulates or quadrangulates a larger domain in which the moving boundary is immersed for all times. In contrast, this chapter presents a family of methods for solving problems with moving boundaries using a *universal mesh*: a background triangulation that contains the moving domain for all times *and conforms to its geometry* at all times by perturbing a small number of nodes in a neighborhood of the moving boundary.

The framework presented in this chapter distinguishes itself from traditional approaches by exhibiting the following features simultaneously. First, a universal mesh delivers a conforming representation of the evolving domain at all times. This conforming mesh is obtained by perturbing the nodes of a background mesh using a mapping which supplies not only an adaptation of the background mesh, but also a mesh motion over short time intervals suitable for constructing high-order discretizations of the governing equations. Second, the mesh motion strategy is robust, in the sense that large domain deformations pose no threat to the quality of the conforming mesh, being at all times derived from a small perturbation of the background mesh. Third, our approach provides a systematic framework for constructing methods of a desired order of accuracy in space and in time, simply by discretizing in space with a finite element space of the appropriate order and choosing

a time integrator of the appropriate order. We demonstrate this by combining polynomial finite elements with high-order implicit Runge Kutta schemes. Finally, the framework is algorithmically simple. In its basic form, the alteration of the background mesh requires adjustments to nodal coordinates only, not the mesh's connectivity, and the nodal motions are independent and explicitly defined.

Organization. This chapter is organized as follows. We begin in Section 2.2 by giving an informal overview of our method, and illustrating the ideas by formulating the method for a moving-boundary problem in one spatial dimension. We formulate a two-dimensional model moving boundary problem on a predefined, curved spacetime domain in Section 2.3, and proceed to derive its equivalent reformulation on cylindrical spacetime slabs. In Section 2.4 we present, in an abstract manner, the general form of a finite-element discretization of the same moving boundary problem, as well as its reformulation on cylindrical spacetime slabs. This formalism will lead to a statement of the general form of a numerical method for moving-boundary problems with prescribed boundary evolution that includes our method and conventional deforming-mesh methods as special cases. In Section 2.5, we present the key ingredient that distinguishes our proposed method from standard approaches: the use of a universal mesh. In Section 2.6, we demonstrate numerically our method's convergence on a prescribed-boundary variant of a classic moving-boundary problem called the Stefan problem, which asks for the evolution of a solid-liquid interface during a melting process. Some concluding remarks are given in Section 2.7.

2.2 Overview of the Method

There are three main difficulties to overcome in constructing high-order methods for problems with moving domains: (a) Since the domain is changing in time, approximations of the domain of the appropriate order need to be constructed at all times at which the time-integration scheme is evaluated, (b) the approximation space over the evolving domain generally needs to evolve in time as well, resulting in a changing set of degrees of freedom, and (c) the approximation of time-derivatives of the solution near the evolving boundary needs to be carefully constructed, since solution values at a given spatial location may not be defined at all time instants within a time step.

Pulling back to a reference domain. A natural approach to sidestep these issues is to reformulate the problem as an evolution in a reference, fixed domain Ω^0 through a diffeomorphism $\varphi^t \colon \Omega^0 \to \Omega^t$ that maps it to the evolving domain Ω^t at each time t. If the solution sought is $u(x,t)$, defined over the domain Ω^t at each time t, then this approach involves obtaining the partial differential equation that the function $U(X,t) = u(\varphi^t(X),t)$, defined over Ω^0 at all times, would satisfy. The obvious advantage of this perspective is that any of the standard numerical methods constructed

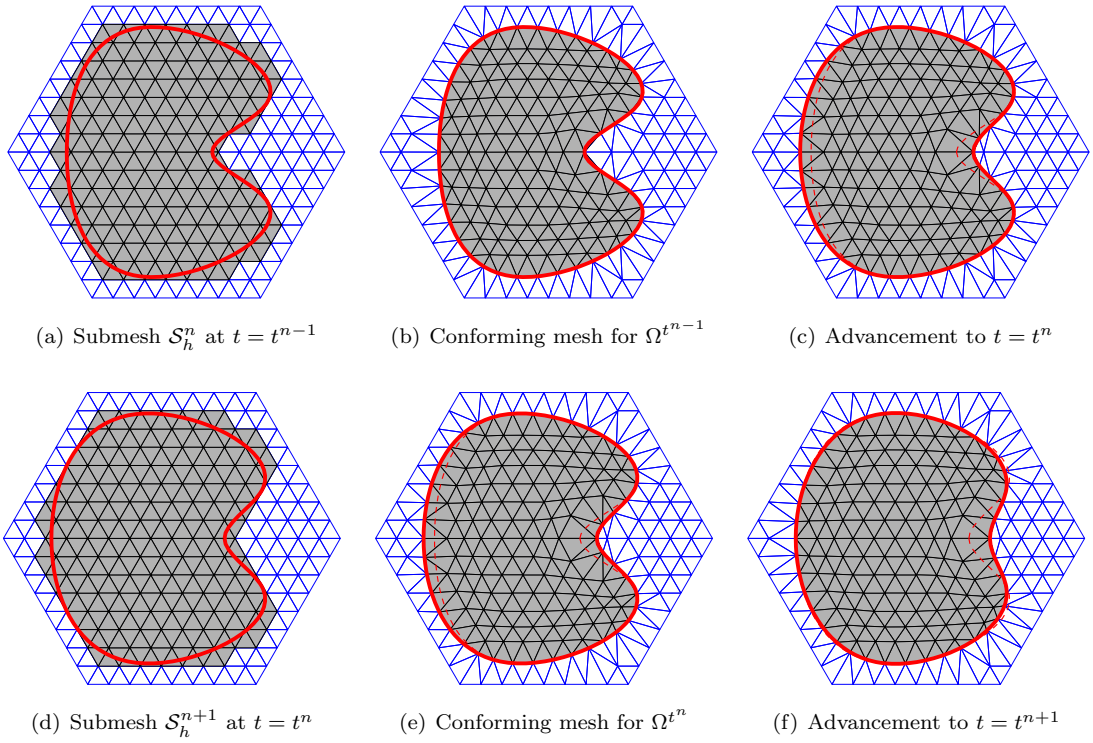

(a) Submesh $\mathcal{S}_h^n$ at $t = t^{n-1}$ (b) Conforming mesh for $\Omega^{t^{n-1}}$ (c) Advancement to $t = t^n$

(d) Submesh $\mathcal{S}_h^{n+1}$ at $t = t^n$ (e) Conforming mesh for Ω^{t^n} (f) Advancement to $t = t^{n+1}$

Figure 2.1: Sketch of how the reference domain is periodically redefined, and the mesh over it obtained. The triangles intersected by the domain in (a) are deformed through the universal mesh map to obtain a domain-matching discretization in (b). The evolution of the domain during $(t^{n-1}, t^n]$ is then described through a map φ^t defined over $\Omega^{t^{n-1}}$. The deformed mesh due to φ^{t^n} is then shown in (c), where the boundary of the reference domain $\Omega^{t^{n-1}}$ is still depicted in dashed red lines. These steps are then repeated in (d), (e), and (f), for the interval $(t^n, t^{n+1}]$. The meshes in (c) and (e) both mesh Ω^{t^n}, but since the two differ near the domain boundary, a projection of the solution is needed to continue the integration in time.

for evolution problems on fixed domains can now be applied, and hence high-order methods can be easily formulated.

With this idea, the issues associated with discretizing an evolving domain are transformed into algorithmically constructing and computing the map φ^t. This is not too difficult when the changes in the domain are small, i.e., when φ^t is close to a rigid body motion for all times. However, it becomes challenging when φ^t induces large deformations of the domain. This is the typical problem faced by Arbitrary Lagrangian-Eulerian methods: how to deform the mesh, or alternatively, how to construct the ALE map (see Fig. 1.1). In terms of the map φ^t, these same problems materialize as a loss of local or global injectivity.

A restatement of this same idea from a different perspective is to consider approximation spaces, such as a finite element spaces, that evolve with the domain. This is precisely what is obtained if

each function in the approximation space over the reference configuration is pushed forward by the map φ^t at each time t. For example, for finite element spaces, each shape function over Ω^t has the form $n_a(\varphi^t(X)) = N_a(X)$, where N_a is a shape function in the finite element space over Ω^0. We take advantage of this equivalence throughout this chapter.

Construction of maps. One of the central ideas we introduce here is one way to construct maps φ^t. To circumvent the problems that appear under large deformations, we periodically redefine the reference domain to be Ω^{t^n}, $n = 0, 1, \ldots, N$, $t^n = n\tau$ for some $\tau > 0$, and accordingly $\varphi^t \colon \Omega^{t^n} \to \Omega^t$ for $t \in (t^n, t^{n+1}]$.

The combination of periodically redefining the reference configuration and constructing a mesh over it with the map proposed here is illustrated in Fig. 2.1, for a two-dimensional moving domain $\Omega^t \subset \mathbb{R}^2$. Upon choosing a fixed background triangulation $\mathcal{T}_h$ of a domain $\mathcal{D} \subset \mathbb{R}^2$ that contains the domains Ω^t for all $t \in [0, T]$, $T = N\tau$, the method proceeds as follows: (a) At each temporal node t^{n-1}, a submesh $\mathcal{S}_h^n$ of $\mathcal{T}_h$ that approximates $\Omega^{t^{n-1}}$ (Fig. 2.1(a)) is identified; (b) The polygonal domain meshed by $\mathcal{S}_h^n$ is deformed through the universal mesh map onto $\Omega^{t^{n-1}}$ (Fig. 2.1(b)); (c) The map φ^t for $t \in (t^{n-1}, t^n]$ is constructed as the identity everywhere except over the elements with one edge over the moving boundary. Over these elements φ^t is defined as an extension of the closest point projection of $\partial\Omega^{t^{n-1}}$ to $\partial\Omega^t$. Fig. 2.1(c) shows the mesh over Ω^{t^n} obtained as $\varphi^{t^n}(\Omega^{t^{n-1}})$. These three steps are repeated over $(t^n, t^{n+1}]$, as shown in Figs. 2.1(d), 2.1(e), and 2.1(f).

Discretization and time integration. As highlighted earlier, the introduction of the map φ^t enables the construction of approximations of any order within each interval $(t^{n-1}, t^n]$, and we elaborate on this next.

We denote the solution over $(t^{n-1}, t^n]$ with $U^{n-1}(X, t)$, which takes values over $\Omega^{t^{n-1}}$ at each time instant in this interval. To obtain appropriate spatial accuracy, notice that a finite element space of any order over $\Omega^{t^{n-1}}$ (Fig. 2.1(b)) can be defined in a standard way, by composing finite element functions over $\mathcal{S}_h^n$ with the universal mesh map. The spatially discretized equations for U^{n-1} over this space form an ordinary system of differential equations whose unknowns are the degrees of freedom for U^{n-1}, and hence any standard, off-the-self integrator of any order can be adopted to approximate its solution.

The crucial role played by the universal mesh map is in full display here, since for smooth domains it provides an exact triangulation of $\Omega^{t^{n-1}}$. By ensuring that the mesh conforms exactly to the moving domain at all times, the method is free of geometric errors – errors that result from discrepancies between the exact domain and the computational approximation to the domain.

Projection. To continue the time integration from the interval $(t^{n-1}, t^n]$ to the interval $(t^n, t^{n+1}]$, an initial condition at t^n is needed, based on the solution computed in $(t^{n-1}, t^n]$. This initial condition is $U^n(x, t^n_+) = \lim_{t \searrow t^n} U^n(x, t) = U^{n-1}(\left[\varphi^{t^n}\right]^{-1}(x), t)$, which is defined over Ω^{t^n}. In

general, however, $U^n(x, t^n_+)$ does not belong to the discrete approximation space over Ω^{t^n}, so we project $U^n(x, t^n_+)$ onto it through a suitably defined projection operator; ideally an L^2-projection, but numerical experiments with interpolation have rendered very good results as well.

The introduction of this projection N times would generally have the detrimental effect of reducing the order of convergence by one if the spacing τ between temporal nodes t^n is proportional to mesh size h. Nevertheless, one of the highlights of the map φ^t we construct is that it differs from the identity in a region of thickness $O(h)$ from the domain boundary. This feature makes the net reduction of the convergence rate due to the projection to be only of half an order (in the L^2 norm), as we show in Chapter 5.

The implementation of this idea with finite element spaces is facilitated by regarding this method as a way to construct approximation spaces that evolve with the domain. This reduces the effect of the map φ^t to defining a "curved" mesh over Ω^t. By further interpolating the map φ^t with the finite element space, an isoparametric approximation of the domain is obtained. In this way, standard finite element procedures can be adopted to compute all needed quantities over either the exact or the isoparametric approximation of Ω^t. This curved mesh is constructed at each stage of the time-integration scheme.

Comparison with conventional ALE schemes. In light of the preceding paragraph, the reader may recognize that our method resembles a conventional ALE scheme with a peculiar mesh motion strategy and regular, systematic "remeshing." In particular, the mesh motion defined by φ^t leaves all elements stationary except those with an edge on the moving boundary, and the "remeshing" entails the selection of a subtriangulation of a fixed background mesh and perturbing a few of its elements.

The peculiarity of the approach endows it with several unique features. Since the mesh motion is restricted to boundary elements, the lengths of the time intervals $(t^{n-1}, t^n]$ between "remeshing" (and hence the time step Δt adopted during time integration over those intervals) are restricted by the mesh spacing. An advantage of this strategy is that it easily handles large domain deformations, and the nodal motions are independent and explicitly defined. However, for the reasons described earlier, the theoretical convergence rate of the method is suboptimal by half an order in the L^2 norm; see Chapter 5.

Remarks. Getting back to the difficulties highlighted at the beginning of this section, it should be evident by now that the basic idea we just outlined provides approximations of the domain of the proper order at all times, and that at no point does the difficulty of dealing with nodes that belong to Ω^t for only a fraction of the interval $(t^{n-1}, t^n]$ arise. The set of degrees of freedom in the approximation space does generally change because of the periodic redefinition of the reference configuration, a seemingly inevitable step for large enough deformations of the domain, but the introduction of the projection enables the continuation of the high-order integration in time with a

minimal accuracy loss. We should also mention that a common difficulty for fixed-mesh methods, which is the imposition of Dirichlet or Neumann boundary conditions, is handled in a standard way with the approach in this chapter.

In the following, we construct the method in one spatial dimension, to present some of the main ideas in a rigorous way, yet sidestepping the notational and algorithmic difficulties introduced by domain boundaries that are defined by curves instead of isolated points.

2.2.1 Construction of the Method in One Spatial Dimension

Consider the following moving-boundary problem: Given a spacetime domain $\Omega = \{(x,t) \in \mathbb{R}^2 \mid 0 < x < s(t),\ 0 < t < T\}$, find $u\colon \Omega \to \mathbb{R}$ such that

$$\frac{\partial u}{\partial t} - \frac{\partial^2 u}{\partial x^2} = 0, \qquad (x,t) \in \Omega \tag{2.1a}$$

$$u(0,t) = u(s(t),t) = 0, \qquad 0 < t < T \tag{2.1b}$$

$$u(x,0) = u^0(x), \qquad 0 < x < s(0) \tag{2.1c}$$

where $s\colon [0,T] \to (0,1)$ is a smooth, prescribed function of time, and $u^0\colon (0,s(0)) \to \mathbb{R}$ is the initial condition.

For such a problem, it suffices to adopt a grid $0 = X_0 < X_1 < \cdots < X_M = 1$ of the unit interval as the universal mesh – a stationary background mesh that covers the domains $(0,s(t))$ for all times $0 \le t \le T$. We shall also employ a partition $0 = t^0 < t^1 < \ldots < t^N = T$ of the time axis that is fine enough so that the change in $s(t)$ over a given interval $(t^{n-1}, t^n]$ never exceeds the minimum mesh spacing. That is,

$$\max_{t \in (t^{n-1}, t^n]} |s(t) - s(t^{n-1})| < \min_{0<i\le M} (X_i - X_{i-1}).$$

The universal mesh can be adapted to conform exactly to the domain $(0,s(t))$ at any time t by perturbing nodes in a small neighborhood of $s(t)$. A simple prescription for $t \in (t^{n-1}, t^n]$ is, for each i,

$$x_i(t) = \begin{cases} X_i - \delta h \left(1 - \frac{s(t^{n-1}) - X_i}{Rh}\right) & \text{if } s(t^{n-1}) - Rh \le X_i < s(t^{n-1}) \\ s(t) & \text{if } X_{i-1} < s(t^{n-1}) \le X_i \\ X_i & \text{otherwise} \end{cases} \tag{2.2}$$

where R is a small positive integer, δ is a small positive number, and $h = \max_{0<i\le M}(X_i - X_{i-1})$. See Fig. 2.2 for an illustration. In this case, $\varphi^t(X) = \sum_{i=0}^{M} x_i(t) M_i(X)$, where M_i is the standard P_1 finite element shape function for node i: it is affine over each element and satisfies $M_i(X_j) = \delta_{ij}$.

On this adapted mesh we may construct shape functions $n_a(x,t) = N_a((\varphi^t)^{-1}(x))$, where $N_a(X)$ are the shape functions over the universal mesh. The shape functions n_a are (for instance) piecewise polynomial in x on each interval $[x_{i-1}(t), x_i(t)]$ for any fixed t, and are continuous in $t \in (t^{n-1}, t^n)$

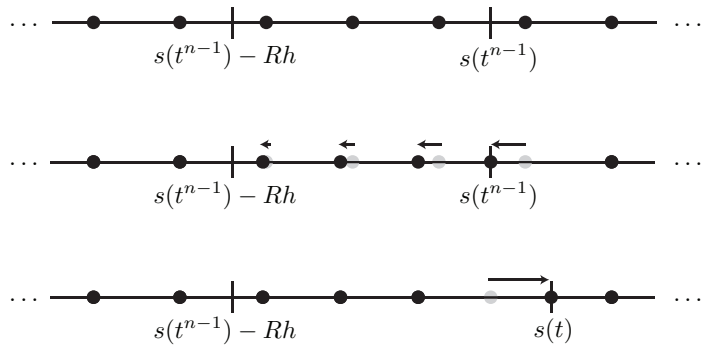

Figure 2.2: Illustration of the manner in which a one-dimensional universal mesh adapts to the immersed domain $(0, s(t))$ for $t \in (t^{n-1}, t^n]$. At $t = t_+^{n-1}$, the background mesh (top) is deformed by snapping the node that is closest to $s(t^{n-1})$ (among nodes outside the immersed domain) onto $s(t^{n-1})$ (middle). In the process, the nodes between $s(t^{n-1}) - Rh$ and $s(t^{n-1})$ are relaxed away from the boundary. At later times $t \in (t^{n-1}, t^n]$ (bottom), the snapped node tracks the position of the boundary, while all other nodes remain in the positions they adopted at $t = t_+^{n-1}$. Here, we used the map (2.2) with $R = 3$ and $\delta = 0.3$.

for each fixed x. For each $t \in (t^{n-1}, t^n)$, the shape functions n_a satisfy that

$$\frac{\partial n_a}{\partial t}(x,t) = -\frac{\partial n_a}{\partial x}(x,t) v_h(x,t), \tag{2.3}$$

where $v_h(\varphi^t(X), t) = \frac{\partial}{\partial t}\varphi^t(X)$ is the (spatial/Eulerian) velocity of the adapted mesh. For $x_{i-1}(t) < x < x_i(t)$,

$$v_h(x,t) = \dot{x}_i(t)\left(\frac{x - x_{i-1}(t)}{x_i(t) - x_{i-1}(t)}\right) + \dot{x}_{i-1}(t)\left(\frac{x_i(t) - x}{x_i(t) - x_{i-1}(t)}\right).$$

We then seek an approximate solution

$$u_h(x,t) = \sum_{a=1}^{A} \mathbf{u}_a(t) n_a(x,t)$$

lying in the space of functions

$$\mathcal{V}_h(t) = \operatorname{span}\{n_a(\cdot,t) : n_a(x,t) = 0 \,\forall x > s(t)\}.$$

Here, $\mathbf{u}(t) = (\mathbf{u}_1(t), \mathbf{u}_2(t), \ldots, \mathbf{u}_A(t))^T \in \mathbb{R}^A$ is a vector of time-dependent coefficients, which we allow to be discontinuous across the temporal nodes t^n. We denote

$$\mathbf{u}(t_+^n) = \lim_{t \searrow t^n} \mathbf{u}(t)$$

and similarly for other scalar- or vector-valued functions. To obtain an equation for u_h, we perform a

standard Galerkin projection of (2.1a) onto the space of functions $\mathcal{V}_h(t)$, which leads to the following ordinary differential equation for $\mathbf{u}$ at each $t \in (t^{n-1}, t^n]$,

$$\mathbf{M}(t)\dot{\mathbf{u}}(t) - \mathbf{B}(t)\mathbf{u}(t) + \mathbf{K}(t)\mathbf{u}(t) = 0. \tag{2.4}$$

Here $\mathbf{M}(t) \in \mathbb{R}^{A\times A}$ is a mass matrix, $\mathbf{K}(t) \in \mathbb{R}^{A\times A}$ is a stiffness matrix, and $\mathbf{B}(t) \in \mathbb{R}^{A\times A}$ is an advection matrix, constructed according to the following prescription. For a such that $n_a(\cdot, t) \in \mathcal{V}_h(t)$,

$$\begin{aligned}
\mathbf{M}_{ab}(t) &= \int_0^1 n_b(x,t)n_a(x,t)\,dx \\
\mathbf{B}_{ab}(t) &= \int_0^1 v_h(x,t)\frac{\partial n_b}{\partial x}(x,t)n_a(x,t)\,dx \\
\mathbf{K}_{ab}(t) &= \int_0^1 \frac{\partial n_b}{\partial x}(x,t)\frac{\partial n_a}{\partial x}(x,t)\,dx,
\end{aligned}$$

while for a such that $n_a(\cdot, t) \notin \mathcal{V}_h(t)$,

$$\begin{aligned}
\mathbf{M}_{ab}(t) &= 0 \\
\mathbf{B}_{ab}(t) &= 0 \\
\mathbf{K}_{ab}(t) &= \delta_{ab}.
\end{aligned}$$

These last values are set so that $u_h(x,t) = 0$ for $x > s(t)$, which follows from imposing (2.1b). The algorithm is then given in Algorithm 2.2.1.

Several salient features of the method should be evident at this point:

- *The connectivity of the universal mesh never changes* during deformation – only the nodal positions change. As a consequence, the sizes and sparsity structures of various discrete quantities (the solution vector $\mathbf{u}$, the mass matrix $\mathbf{M}$, the stiffness matrix $\mathbf{K}$, and the advection matrix $\mathbf{B}$) can be held fixed, even though differing subsets of degrees of freedom may participate in the discrete equations at any interval $(t^{n-1}, t^n]$. One merely needs to impose "homogeneous Dirichlet boundary conditions" on the solution at nonparticipating degrees of freedom.

- Large deformations of the domain pose no threat to the quality of the deformed mesh, provided $\max_{1\le n\le N}(t^n - t^{n-1})$ is sufficiently small and the domain evolution is sufficiently regular.

- In two dimensions, the nodal motions are independent and explicitly defined, rendering the mesh motion strategy low-cost and easily parallelizable. See Section 2.5 for details.

Algorithm 2.2.1 Time integration for a universal mesh in one dimension.

Require: Initial condition $u(x,0) = u^0(x)$.

1: **for** $n = 1, 2, \ldots, N$ **do**

2: Project the current numerical solution

$$u_h(x, t^{n-1}) = \sum_{a=1}^{A} \mathbf{u}_a(t^{n-1}) n_a(x, t^{n-1})$$

(or the initial condition $u(x,0)$ if $n = 1$) onto $\mathcal{V}_h(t_+^{n-1})$ to obtain the vector of coefficients $\mathbf{u}(t_+^{n-1})$ in the expansion

$$u_h(x, t_+^{n-1}) = \sum_{a=1}^{A} \mathbf{u}_a(t_+^{n-1}) n_a(x, t_+^{n-1}).$$

3: Numerically integrate

$$\mathbf{M}(t)\dot{\mathbf{u}}(t) - \mathbf{B}(t)\mathbf{u}(t) + \mathbf{K}(t)\mathbf{u}(t) = 0$$

for $t \in (t^{n-1}, t^n]$ with the initial condition $\mathbf{u}(t_+^{n-1})$ and the constraints induced by (2.1b) to obtain $\mathbf{u}(t^n)$.

4: **end for**

5: **return** $u_h(x, t^N)$

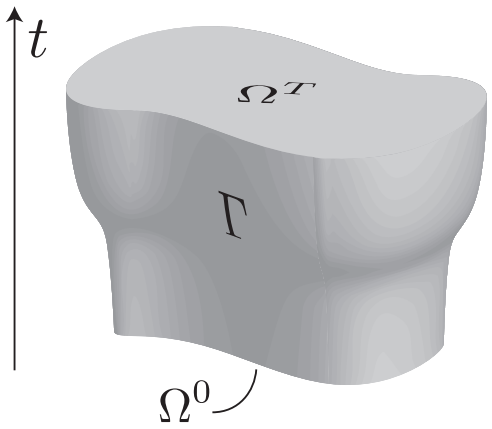

Figure 2.3: Spacetime domain Ω.

2.3 A Model Moving-Boundary Problem

2.3.1 The Continuous Problem

Consider a moving-boundary problem on a bounded spacetime domain $\Omega \subset \mathbb{R}^2 \times [0,T]$, as in Fig. 2.3. For each $t \in [0,T]$, denote by $\Omega^t \subset \mathbb{R}^2$ the spatial component of the spacetime slice $\Omega \cap (\mathbb{R}^2 \times \{t\})$, and denote by Γ^t the boundary of Ω^t. Finally, let $\Gamma = \bigcup_{0<t<T} (\Gamma^t \times \{t\})$ denote the lateral boundary

of the spacetime domain Ω. We assume that Ω^t is open in $\mathbb{R}^2$ for each t. As a regularity requirement, we assume that for every $t \in [0,T]$, the set Γ^t can be expressed as the image of an embedding $c(\cdot,t)$ of the unit circle S^1 into $\mathbb{R}^2$, where $c \in C^2(S^1 \times (0,T), \mathbb{R}^2)$.

Now consider the following abstract moving-boundary problem: Given $f\colon \Omega \to \mathbb{R}$ and $u^0\colon \Omega^0 \to \mathbb{R}$, find $u\colon \Omega \to \mathbb{R}$ satisfying

$$\frac{\partial u}{\partial t} + \mathcal{a}(u) = f \text{ in } \Omega \tag{2.5a}$$

$$u = 0 \qquad \text{on } \Gamma \tag{2.5b}$$

$$u = u^0 \qquad \text{on } \Omega^0, \tag{2.5c}$$

where $\mathcal{a}$ is a partial differential operator of the form

$$\mathcal{a}(u) = -\nabla_x \cdot (k_1 \nabla_x u) + k_2 \cdot \nabla_x u + k_3 u$$

with coefficients $k_1(x,t) \in \mathbb{R}^{2\times 2}$, $k_2(x,t) \in \mathbb{R}^2$, and $k_3(x,t) \in \mathbb{R}$ for every $(x,t) \in \Omega$. We assume that k_1 is uniformly positive definite. That is, there exists $C > 0$ such that $v \cdot k_1(x,t)v \geq Cv \cdot v$ for every $v \in \mathbb{R}^2$ and every $(x,t) \in \Omega$.

It is known [94, Theorem 7.17] that if $k_1 \in L^\infty(\Omega)^{2\times 2}$, $k_2 \in L^\infty(\Omega)^2$, $k_3 \in L^\infty(\Omega)$, the components of k_1 are Lipschitz in spacetime, $f \in L^p(\Omega)$, and $u^0 \in W^{2,p}(\Omega^0)$ with $1 < p < \infty$, then the problem (2.5) has a unique solution u with $u(\cdot,t) \in W^{2,p}(\Omega^t)$ and $\frac{\partial u}{\partial t}(\cdot,t) \in L^p(\Omega^t)$ for every $0 \leq t \leq T$. Here, $W^{s,p}$ denotes the Sobolev space of differentiability $s \geq 0$ and integrability $1 \leq p \leq \infty$, and $L^p = W^{0,p}$ denotes the Lebesgue space of integrability $1 \leq p \leq \infty$. Later, we shall also denote $H^s = W^{s,2}$, and we write $H^1_0(\Omega^t)$ for the space of functions in $H^1(\Omega^t)$ with vanishing trace. We denote the norm on $W^{s,p}(\Omega^t)$ by $\|\cdot\|_{s,p,\Omega^t}$ and the associated semi-norm by $|\cdot|_{s,p,\Omega^t}$.

2.3.2 Equivalent Formulation of the Continuous Problem

In the following, we derive an equivalent formulation of the moving-boundary problem (2.5) that is well-suited for numerical discretization. For reasons that will soon be made clearer, we restrict our attention to a temporal subinterval $(t^{n-1}, t^n] \subset [0,T]$ for the remainder of this section.

Weak formulation. A weak formulation of (2.5) reads: Find $u(\cdot,t) \in \mathcal{V}(\Omega^t) := H^1_0(\Omega^t)$ such that

$$m^t(\dot{u}, w) + a^t(u, w) = m^t(f, w) \quad \forall w \in \mathcal{V}(\Omega^t) \tag{2.6}$$

for every $t \in (t^{n-1}, t^n]$, where the time-dependent bilinear forms m^t and a^t are given by

$$\begin{aligned} m^t(u,w) &= \int_{\Omega^t} uw\,dx \\ a^t(u,w) &= \int_{\Omega^t} \nabla_x w \cdot k_1 \nabla_x u + (k_2 \cdot \nabla_x u)w + k_3 uw\,dx. \end{aligned}$$

Here and throughout this thesis, the dot notation denotes differentiation with respect to time while holding the remaining arguments to the function fixed.

Pulling back to a cylindrical domain. Given any sufficiently smooth family of bijections $\{\varphi^{n,t} : \Omega^{t^{n-1}} \to \Omega^t \mid t \in (t^{n-1}, t^n]\}$, equation (2.6) may be recast on the cylindrical spacetime domain $\Omega^{t^{n-1}} \times (t^{n-1}, t^n]$, since, by a change of variables, (2.6) is equivalent to the statement

$$M^t(\dot{U}, W) - B^t(U, W) + A^t(U, W) = M^t(F, W) \quad \forall W \in (\varphi^{n,t})^* \mathcal{V}(\Omega^t) \tag{2.7}$$

for every $t \in (t^{n-1}, t^n]$, where

$$(\varphi^{n,t})^* \mathcal{V}(\Omega^t) = \left\{ W : \Omega^{t^{n-1}} \to \mathbb{R} \mid W = w \circ \varphi^{n,t} \text{ for some } w \in \mathcal{V}(\Omega^t) \right\}$$

is the space of functions in $\mathcal{V}(\Omega^t)$ pulled back to $\Omega^{t^{n-1}}$ by $\varphi^{n,t}$,

$$\dot{U}(X,t) = \left.\frac{\partial}{\partial t}\right|_X U(X,t),$$

and

$$\begin{aligned} M^t(U,W) &= \int_{\Omega^{t^{n-1}}} UW\,|\nabla_X \varphi^{n,t}|\,dX \\ B^t(U,W) &= \int_{\Omega^{t^{n-1}}} \left((\nabla_X \varphi^{n,t})^{-\dagger} \nabla_X U \cdot V^{n,t}\right) W |\nabla_X \varphi^{n,t}| dX \\ A^t(U,W) &= \int_{\Omega^{t^{n-1}}} \Big[\left((\nabla_X \varphi^{n,t})^{-\dagger} \nabla_X W\right) \cdot K_1 \left((\nabla_X \varphi^{n,t})^{-\dagger} \nabla_X U\right) \\ &\qquad + \left((\nabla_X \varphi^{n,t})^{-\dagger} \nabla_X U \cdot K_2\right) W + K_3 UW \Big] |\nabla_X \varphi^{n,t}|\,dX, \end{aligned}$$

with $|\nabla_X \varphi^{n,t}|$ denoting the absolute value of the Jacobian determinant of $\varphi^{n,t}$ and $(\nabla_X \varphi^{n,t})^{-\dagger}$ denoting the inverse adjoint of $\nabla_X \varphi^{n,t}$. Here, $K_i = k_i \circ \varphi^{n,t}$, $i = 1, 2, 3$ and $F = f \circ \varphi^{n,t}$ are the Lagrangian counterparts of k_1, k_2, k_3, and f, and

$$V^{n,t}(X) := \dot{\varphi}^{n,t}(X) = \left.\frac{\partial}{\partial t}\right|_X \varphi^{n,t}(X)$$

is the *material* or *Lagrangian velocity*.

The validity of the preceding change of variables will hold if, for instance,

$$t \mapsto \varphi^{n,t} \in C^1\left((t^{n-1}, t^n], W^{1,\infty}(\Omega^{t^{n-1}})^2\right), \tag{2.8}$$

and $(\varphi^{n,t})^{-1} \in W^{1,\infty}(\Omega^t)^2$ for $t \in (t^{n-1}, t^n]$. Note that under these assumptions, $(\varphi^{n,t})^* \mathcal{V}(\Omega^t) = \mathcal{V}(\Omega^{t^{n-1}}) = H_0^1(\Omega^{t^{n-1}})$.

The presence of the term $B^t(U, W)$ in (2.7) arises from the identity

$$\frac{\partial U}{\partial t}(X,t) = \frac{\partial u}{\partial t}(\varphi^{n,t}(X), t) + \nabla_x u(\varphi^{n,t}(X), t) \cdot v^{n,t}(\varphi^{n,t}(X)), \tag{2.9}$$

which relates the partial time derivative of u to the *material time derivative*

$$\frac{Du}{Dt}(\varphi^{n,t}(X), t) := \frac{\partial U}{\partial t}(X,t)$$

of u via a term involving the *spatial* or *Eulerian velocity*

$$v^{n,t}\left(\varphi^{n,t}(X)\right) = V^{n,t}(X).$$

Upon discretization, the term $B^t(U, W)$ corresponds precisely to the term $\mathbf{B}(t)\mathbf{u}(t)$ that the reader encountered earlier in (2.4).

"Hybrid" Eulerian formulation. A third equivalent statement of (2.6) and (2.7) is obtained by acknowledging that, by (2.9),

$$\frac{\partial u}{\partial t}(x,t) = \frac{Du}{Dt}(x,t) - \nabla_x u(x,t) \cdot v^{n,t}(x). \tag{2.10}$$

It then follows that (2.6) is equivalent to

$$m^t\left(\frac{Du}{Dt}, w\right) - b^t(u,w) + a^t(u,w) = m^t(f,w) \quad \forall w \in \mathcal{V}(\Omega^t) \tag{2.11}$$

for every $t \in (t^{n-1}, t^n]$, where the time-dependent bilinear form b^t is given by

$$b^t(u,w) = \int_{\Omega^t} \nabla_x u \cdot v^{n,t}\, w\, dx. \tag{2.12}$$

So, u satisfies (2.6) if and only if it satisfies (2.11) and if and only if U satisfies (2.7). The advantage of this formulation is that it involves simpler expressions for the bilinear forms than those in (2.7), and these simpler expressions will be convenient for the numerical implementation later. Notice as well that the material time derivative on $\partial\Omega^t$ is now a directional derivative in a direction tangential to the spacetime boundary $\partial\Omega$, in contrast to $\dot{u}$, which can only be defined as a one-side derivative

therein.

2.4 Discretization

2.4.1 Spatial Discretization on Short Time Intervals

At this point it is instructive to derive, in a systematic manner, the general form of a finite element spatial discretization of (2.5) obtained via Galerkin projection. We begin by spatially discretizing the weak formulation (2.6) and proceed by pulling the semidiscrete equations back to a cylindrical spacetime domain, and by obtaining the "hybrid" Eulerian formulation of the same semidiscrete equations. The utility of these three formulations will be evident towards the end of this section.

Galerkin formulation. A Galerkin projection of (2.6) requires choosing a finite-dimensional subspace $\mathcal{V}_h(\Omega^t) \subset \mathcal{V}(\Omega^t)$ at each time t and finding $u_h(t) \in \mathcal{V}_h(\Omega^t)$ such that

$$m^t(\dot{u}_h, w_h) + a^t(u_h, w_h) = m^t(f, w_h) \quad \forall w_h \in \mathcal{V}_h(\Omega^t) \tag{2.13}$$

for every $t \in (t^{n-1}, t^n]$. For concreteness, let us construct such a family of finite element spaces by fixing a reference triangulation $\mathcal{S}_h^n$ of a polygonal domain $\mathcal{D}(\mathcal{S}_h^n) \subset \mathbb{R}^2$ and constructing a family of continuous, bijective maps

$$\Phi_h^{n,t} : \mathcal{D}(\mathcal{S}_h^n) \to \Omega^t$$

that are differentiable in time and are affine on each triangle $K \in \mathcal{S}_h^n$, except perhaps near the boundary, see Fig. 2.4. In informal language, the image of $\Phi_h^{n,t}$ provides a moving mesh that triangulates Ω^t for each $t \in (t^{n-1}, t^n]$. Then, with $\{\tilde{N}_a\}_a$ denoting shape functions on the reference triangulation, we may set

$$\mathcal{V}_h(\Omega^t) = \operatorname{span}\{n_a^t\}_a \tag{2.14}$$

with

$$n_a^t = \tilde{N}_a \circ (\Phi_h^{n,t})^{-1}$$

for each $t \in (t^{n-1}, t^n]$.

Pulling back to a cylindrical domain. We may pull back the semidiscrete equations (2.13) to the cylindrical spacetime domain $\Omega^{t^{n-1}} \times (t^{n-1}, t^n]$ with the aid of the bijections

$$\varphi^{n,t} := \Phi_h^{n,t} \circ (\Phi_h^{n,t_+^{n-1}})^{-1}. \tag{2.15}$$

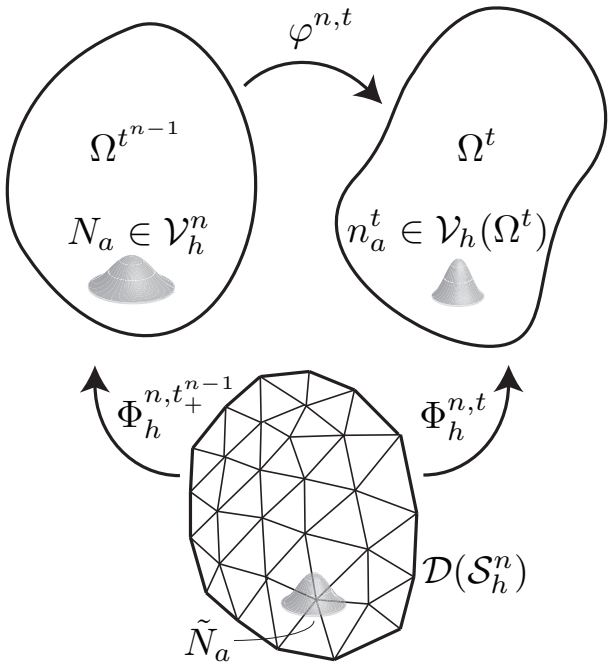

Figure 2.4: For each $t \in (t^{n-1}, t^n]$, the map $\Phi_h^{n,t}$ provides a bijection from a fixed reference triangulation $\mathcal{S}_h^n$ of a polygonal domain $\mathcal{D}(\mathcal{S}_h^n)$ to the moving domain Ω^t. Depicted pictorially is a shape function $\tilde{N}_a$ on the reference triangulation and its pushforward to $\Omega^{t^{n-1}}$ and Ω^t, denoted N_a and n_a^t, respectively.

The resulting equivalent semidiscrete equation reads

$$M^t(\dot{U}_h, W_h) - B^t(U_h, W_h) + A^t(U_h, W_h) = M^t(F, W_h) \quad \forall W_h \in (\varphi^{n,t})^* \mathcal{V}_h(\Omega^t) \tag{2.16}$$

for every $t \in (t^{n-1}, t^n]$.

"Hybrid" Eulerian formulation. Similarly, the discrete "hybrid" Eulerian formulation follows by taking advantage of (2.9) to replace $\dot{u}_h$ in (2.13), to get

$$m^t\left(\frac{Du_h}{Dt}, w_h\right) - b^t(u_h, w_h) + a^t(u_h, w_h) = m^t(f, w_h) \quad \forall w_h \in \mathcal{V}_h(\Omega^t) \tag{2.17}$$

for every $t \in (t^{n-1}, t^n]$.

Remark. We note that (2.13), (2.16), and (2.17) do not define three different methods; they are three ways of writing precisely the same one. That is, u_h satisfies (2.13) if and only if it satisfies (2.17) and if and only if $U_h(t) = (\varphi^{n,t})^* u_h(t)$ satisfies (2.16).

Finite element spaces. Notice that (2.16) is a discretization of (2.7) with a particular choice of a finite element subspace of $\mathcal{V}(\Omega^{t^{n-1}})$, namely $(\varphi^{n,t})^*\mathcal{V}_h(\Omega^t)$. The shape functions for this space are given by

$$\begin{aligned} N_a &= n_a^t \circ \varphi^{n,t} \\ &= \tilde{N}_a \circ (\Phi_h^{n,t_+^{n-1}})^{-1}, \end{aligned}$$

which are time-independent.

As a consequence, the material time derivative of functions in $\mathcal{V}_h(\Omega^t)$ takes a particularly simple form. Let

$$u_h(\varphi^{n,t}(X),t) = \sum_a u_a(t) n_a^t(\varphi^{n,t}(X)) = \sum_a u_a(t) N_a^t(X) = U_h(X,t).$$

Then

$$\frac{Du_h}{Dt}(\varphi^{n,t}(X),t) = \frac{\partial U_h}{\partial t}(X,t) = \sum_a \dot{u}_a(t) N_a^t(X) = \sum_a \dot{u}_a(t) n_a^t(\varphi^{n,t}(X)), \tag{2.18}$$

since the shape functions $\{N_a\}_a$ do not depend on time.

Since the map (2.15) depends upon h, we make that dependence explicit by appending a subscript h to $\varphi^{n,t}$ and all derived quantities ($v^{n,t}$, $V^{n,t}$, M^t, A^t, and B^t) in the remainder of this text.

Summary. In summary, we have shown that if the semidiscrete equation (2.13) is pulled back to the reference domain $\Omega^{t^{n-1}}$ through the use of a map

$$\varphi_h^{n,t} = \Phi_h^{n,t} \circ (\Phi_h^{n,t_+^{n-1}})^{-1},$$

then the resulting semidiscrete equation (2.16) involves a finite element space that does not change with time. We may label that space $\mathcal{V}_h^n$ and write

$$M_h^t(\dot{U}_h, W_h) - B_h^t(U_h, W_h) + A_h^t(U_h, W_h) = M_h^t(F, W_h) \quad \forall W_h \in \mathcal{V}_h^n \tag{2.19}$$

for every $t \in (t^{n-1}, t^n]$. The shape functions for $\mathcal{V}_h^n$ are simply shape functions on the reference triangulation $\mathcal{S}_h^n$ pushed forward to $\Omega^{t^{n-1}}$:

$$N_a = \tilde{N}_a \circ (\Phi_h^{n,t_+^{n-1}})^{-1}.$$

The utility of the above formulation is transparent. Upon expanding U_h as a linear combination of shape functions, the system (2.19) is a system of ordinary differential equations for the coefficients of the expansion. This is also evident from the "hybrid" Eulerian formulation (2.17) upon replacing the material time derivative by (2.18). To this system of ODEs we may apply a time integrator of choice to advance from time t^{n-1} to time t^n.

2.4.2 Integration over Long Time Intervals

In the preceding sections, we elected to restrict our attention to a temporal subinterval $(t^{n-1}, t^n] \subset [0, T]$ and construct finite element subspaces of $\mathcal{V}(\Omega^t)$, $t \in (t^{n-1}, t^n]$, using a smoothly varying triangulation of Ω^t given by the image of $\Phi_h^{n,t}$, $t \in (t^{n-1}, t^n]$. This decision allows for the use of different reference triangulations $\mathcal{S}_h^n$ on different temporal subintervals, simplifying the task of maintaining a nondegenerate triangulation of a domain undergoing large deformations.

To complete the picture and construct an algorithm for integration over the interval $[0, T]$ of interest, we choose a partition $0 = t^0 < t^1 < \cdots < t^N = T$ and make use of one last ingredient: a linear projector p_h^n onto $\mathcal{V}_h^n$ for each n. For the definition of the algorithm, we require that the domain of definition of p_h^n contains at least the space $\mathcal{U}_h^n$ given by

$$\mathcal{U}_h^n = \begin{cases} \mathcal{V}(\Omega^0) & \text{if } n = 1 \\ (\varphi_h^{n-1,t^{n-1}})_* \mathcal{V}_h^{n-1} + \mathcal{V}_h^n & \text{if } 1 < n \leq N, \end{cases}$$

where

$$(\varphi_h^{n-1,t^{n-1}})_* \mathcal{V}_h^{n-1} = \left\{ w : \Omega^{t^{n-1}} \to \mathbb{R} \mid w \circ \varphi_h^{n-1,t^{n-1}} \in \mathcal{V}_h^{n-1} \right\}$$

is the space of functions in $\mathcal{V}_h^{n-1}$ pushed forward to $\Omega^{t^{n-1}}$ by $\varphi_h^{n-1,t^{n-1}}$. We assume the projector is surjective for each n; equivalently, $p_h^n|_{\mathcal{V}_h^n} = \text{identity}$ for each n.

Some examples of projectors are the orthogonal projector p_{h,L^2}^n onto $\mathcal{V}_h^n$ with respect to the L^2-inner product, the orthogonal projector p_{h,H^1}^n onto $\mathcal{V}_h^n$ with respect to the H^1-inner product, and the nodal interpolant i_h^n onto $\mathcal{V}_h^n$; see [45, Chapter 1] for details. The appropriate projector depends on the problem being approximated and the choice of temporal nodes t^n, triangulations $\mathcal{S}_h^n$, and maps $\Phi_h^{n,t}$. As we shall mention, p_{h,L^2}^n is the projector best suited for use with the choices detailed in Section 2.5.

With such a family of projectors at hand, a method for integration over the full time interval $[0, T]$ is then summarized in Algorithm 2.4.1.

Relationship to ALE. Let us emphasize that Algorithm 2.4.1 has been formulated with enough generality that it encompasses not only the method specific to this chapter involving universal meshes (which is detailed in Section 2.5) but also conventional ALE schemes. In the case of an ALE scheme, the reference triangulation $\mathcal{S}_h^n$ is a triangulation of $\Omega^{t^{n-1}}$, the map $\varphi_h^{n,t}$ corresponds to a mesh motion derived from, e.g., solutions to the equations of linear elasticity, and the temporal nodes t^n correspond to times at which remeshing is performed. In the case of the method specific to this chapter, we shall see in Section 2.5 that the reference triangulation $\mathcal{S}_h^n$ is a subtriangulation of a fixed background mesh, the map $\varphi_h^{n,t}$ induces deformations of triangles on the boundary of $\mathcal{S}_h^n$ while leaving the remaining triangles fixed, and the temporal nodes t^n are spaced closely enough so that these deformations of boundary triangles remain well-behaved.

Algorithm 2.4.1 General form of a time integrator for moving-boundary problems with a finite element discretization in space.

Require: Initial condition $u^0 \in \mathcal{V}(\Omega^0)$.

1: **for** $n = 1, 2, \ldots, N$ **do**

2: Choose a reference triangulation $\mathcal{S}_h^n$ and a family of maps $\Phi_h^{n,t} : \mathcal{D}(\mathcal{S}_h^n) \to \Omega^t$, $t \in (t^{n-1}, t^n]$.

3: Generate a finite-dimensional subspace $\mathcal{V}_h^n$ of the continuous solution space $\mathcal{V}(\Omega^{t^{n-1}})$ using shape functions on $\mathcal{S}_h^n$ composed with $(\Phi_h^{n,t_+^{n-1}})^{-1}$.

4: Project the current numerical solution (or the initial condition if $n = 1$) onto $\mathcal{V}_h^n$ by setting

$$U_h(\cdot, t_+^{n-1}) = p_h^n u_h(\cdot, t^{n-1}),$$

where $u_h(\cdot, t^0) = u^0$ or, for $n > 1$,

$$u_h(x, t^{n-1}) = U_h((\varphi_h^{n-1,t^{n-1}})^{-1}(x), t^{n-1})$$

is the pushforward of $U_h(\cdot, t^{n-1}) \in \mathcal{V}_h^{n-1} \subset \mathcal{V}(\Omega^{t^{n-2}})$ to $\Omega^{t^{n-1}}$.

5: Numerically integrate (2.19) over $(t^{n-1}, t^n]$ with the projected initial condition $U_h(\cdot, t_+^{n-1})$.

6: **end for**

7: **return** $u_h(\cdot, t^N)$

2.4.3 Example: a Runge-Kutta Time-Integrator

We next exemplify how a time integrator of any given order can be incorporated into step 5 of the algorithm. In this case we consider an s-stage Singly Diagonally Implicit Runge-Kutta (SDIRK) method of order $\leq s$ as the time integrator [32, 70]. Such an integrator requires solving a sequence of s systems of equations

$$M_h^{t_i}(U_i, W) = M_h^{t_i}\left(\sum_{j=0}^{i-1} \beta_{ij} U_j, W\right) + \gamma \Delta t G_h^{t_i}(U_i, F(t_i); W) \quad \forall W \in \mathcal{V}_h^n \tag{2.20}$$

for $U_i \in \mathcal{V}_h^n$, $i = 1, 2, \ldots, s$, where $U_0 = U_h(\cdot, t_0)$, $t_0 \in (t^{n-1}, t^n]$, $t_i = \sum_{j=0}^{i-1} \beta_{ij} t_j + \gamma \Delta t$ for $0 < i \leq s$, and

$$G_h^t(U, F; W) = M_h^t(F, W) - A_h^t(U, W) + B_h^t(U, W).$$

The time-Δt advancement of U_0 is then given by U_s. The coefficients $\gamma > 0$ and $\beta_{ij} \in \mathbb{R}$, $i = 1, 2, \ldots, s$, $j = 0, 1, \ldots, i-1$, for various SDIRK methods are tabulated in 2.A, Tables 2.3-2.6. Pragmatically, implementing an SDIRK method amounts to computing s "backward-Euler" steps, with the initial condition at the i^{th} stage given by a linear combination of the solutions at the previous stages.

2.5 Universal Meshes

The algorithm presented in the preceding section requires at each temporal node t^{n-1} the selection of a family of maps $\Phi_h^{n,t} : \mathcal{D}(\mathcal{S}_h^n) \to \Omega^t$, $t \in (t^{n-1}, t^n]$, from a fixed polygonal domain $\mathcal{D}(\mathcal{S}_h^n)$ to the moving domain Ω^t. Here we present a means of constructing such maps using a single, *universal mesh* that triangulates an ambient domain $\mathcal{D} \subset \mathbb{R}^2$ containing the domains $\{\Omega^t\}_{t=0}^T$ for all times $t \in [0, T]$. Full details of the method are described in [116].

The essence of the method is to triangulate $\mathcal{D}$ with a fixed mesh $\mathcal{T}_h$ and to identify, for each time interval $(t^{n-1}, t^n]$, a submesh $\mathcal{S}_h^n$ of $\mathcal{T}_h$ that approximates $\Omega^{t^{n-1}}$. Triangles on the boundary of $\mathcal{S}_h^n$ are then deformed in such a way that the submesh conforms exactly to the moving domain Ω^t for all $t \in (t^{n-1}, t^n]$.

The conditions under which a given triangulation $\mathcal{T}_h$ can be so adapted to conform to a family of domains Ω^t, $t \in [0, T]$, are laid forth in [116, 118]. Briefly, the procedure is guaranteed to succeed if:

1. Ω^t is C^2-regular for every t.
2. $\mathcal{T}_h$ is sufficiently refined in a neighborhood of $\partial\Omega^t$ for every t.
3. All triangles in $\mathcal{T}_h$ have angles bounded above by a constant $\vartheta < \pi/2$.

The level of refinement requested by condition (2) is dictated primarily by the minimum radius of curvature of $\partial\Omega^t$ among all times $t \in [0, T]$, which, roughly speaking, must be no less than a small multiple of the maximum element diameter. This notion is made precise in [118]. Note that condition (1) precludes an application of the method in its present form to domains with corners.

2.5.1 Construction of an Exactly Conforming Mesh

In detail, consider a triangulation $\mathcal{T}_h$ of $\mathcal{D}$ satisfying conditions (1-3), with the parameter h denoting the length of the longest edge in the triangulation. For a given domain $\Omega^t \subset \mathcal{D}$, $t \in [0, T]$, let $\phi^t : \mathcal{D} \to \mathbb{R}$ denote the signed distance function to $\partial\Omega^t$, taken to be positive outside Ω^t and negative inside Ω^t. Let $\pi^t : \mathcal{D} \to \partial\Omega^t$ denote the closest point projection onto $\partial\Omega^t$. For $i = 0, 1, 2, 3$, let $\mathcal{T}_{h,i}^t$ denote the collection of triangles $K \in \mathcal{T}_h$ for which exactly i vertices of K do not lie in the interior of Ω^t.

For a given subtriangulation $\mathcal{S}_h$ of $\mathcal{T}_h$, we make the distinction between $\mathcal{S}_h$, the list of vertices in the subtriangulation and their connectivities, and $\mathcal{D}(\mathcal{S}_h)$, the polygonal domain occupied by triangles in $\mathcal{S}_h$. We write $K \in \mathcal{S}_h$ to refer to triangles $K \subseteq \mathcal{D}(\mathcal{S}_h)$ who have vertices in $\mathcal{S}_h$.

To construct a conforming mesh for Ω^t from the mesh $\mathcal{T}_h$, we choose

$$\mathcal{S}_h^n = \mathcal{T}_{h,0}^{t^{n-1}} \cup \mathcal{T}_{h,1}^{t^{n-1}} \cup \mathcal{T}_{h,2}^{t^{n-1}}$$

as the reference subtriangulation for the domains Ω^t, $t \in (t^{n-1}, t^n]$. This subtriangulation is simply the set of triangles in $\mathcal{T}_h$ with at least one vertex in $\Omega^{t^{n-1}}$. The map $\Phi_h^{n,t} : \mathcal{D}(\mathcal{S}_h^n) \to \Omega^t$ will then make use of three important mappings, described in the following paragraphs, and illustrated in Fig. 2.5. The *universal mesh map*, as described in [116], is $\Phi_h^{n,t^{n-1}}$.

Boundary evolution map. The first is a *boundary evolution map* $\gamma_h^{n,t} : \partial\mathcal{D}(\mathcal{S}_h^n) \to \partial\Omega^t$, which provides a correspondence between the piecewise linear boundary of $\mathcal{D}(\mathcal{S}_h^n)$ and the boundary of Ω^t for $t \in (t^{n-1}, t^n]$, as in Fig. 2.5. The choice of $\gamma_h^{n,t}$ is not unique, although a simple choice is the closest point projection onto Ω^t composed with the closest point projection onto $\Omega^{t^{n-1}}$:

$$\gamma_h^{n,t} = \pi^t \circ \pi^{t^{n-1}}\big|_{\partial\mathcal{D}(\mathcal{S}_h^n)}. \tag{2.21}$$

By the regularity of the spacetime domain Ω, this map is well-defined for h sufficiently small and t sufficiently close to t^{n-1}; see [118].

Relaxation map. The second is a *relaxation map* $\mathfrak{p}_h^{n,t}$ that perturbs vertices lying both inside Ω^t and near $\partial\Omega^t$ in a direction away from $\partial\Omega^t$. A simple choice of relaxation is the map

$$\mathfrak{p}_h^{n,t}(x) = \begin{cases} x - \delta h \left(1 + \frac{\phi^{t^{n-1}}(x)}{Rh}\right) \nabla\phi^{t^{n-1}}(x) & \text{if } -Rh < \phi^{t^{n-1}}(x) < 0 \\ x & \text{otherwise,} \end{cases} \tag{2.22}$$

which moves vertices within a distance Rh of $\partial\Omega^{t^{n-1}}$ by an amount $\leq \delta h$ in a direction normal to the boundary, with $R > 1$ a small positive integer and $(1 + 1/R)^{-1} \leq \delta \leq 1$. It is proven in [116] that for a straight boundary (or one of small enough radius of curvature compared with the mesh size) such a map results in elements of bounded quality at $t = t^{n-1}$ when conditions (1-3) hold.

Note that this choice of relaxation leaves relaxed vertices fixed over the duration of the interval $(t^{n-1}, t^n]$. We denote by $\mathfrak{p}_h^{n,t}(\mathcal{T}_h)$ the triangulation obtained by applying the relaxation $\mathfrak{p}_h^{n,t}$ to the vertices of $\mathcal{T}_h$ while preserving the mesh's connectivity.

Blend map. Finally, we will make use of a *blend map* $\psi_h^{n,t}$ which takes a straight triangle $K \in \mathfrak{p}_h^{n,t}\left(\mathcal{T}_{h,2}^{t^{n-1}}\right)$ to a curved triangle that conforms exactly to the boundary. The map we employ is proposed in [116]. Letting u, v, w denote the vertices of K, the blend map reads

$$\begin{aligned} \psi_h^{n,t}(x) = &\frac{1}{2(1-\lambda_u)}[\lambda_v \gamma_h^{n,t}(\lambda_u u + (1-\lambda_u)v) + \lambda_u\lambda_w\gamma_h^{n,t}(u)] \\ &+ \frac{1}{2(1-\lambda_v)}[\lambda_u\gamma_h^{n,t}((1-\lambda_v)u + \lambda_v v) + \lambda_v\lambda_w\gamma_h^{n,t}(v)] + \lambda_w w, \end{aligned} \tag{2.23}$$

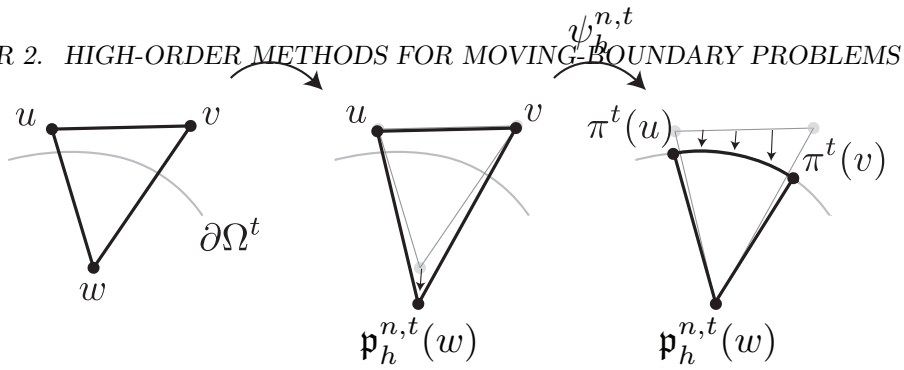

Figure 2.5: The action of $\Phi_h^{n,t}$ on a triangle $K \in \mathcal{T}_{h,2}^{t^{n-1}}$ comprises two steps: A relaxation step that moves w away from the boundary, and a nonlinear blend map $\psi_h^{n,t}$ that maps the straight triangle to a curved one.

where $\lambda_u, \lambda_v, \lambda_w$ are the barycentric coordinates of $x \in K$. Here, we have employed the convention the vertex w is the unique vertex of K lying inside $\Omega^{t^{n-1}}$. It is not difficult to check that for fixed t, the blend map $\psi_h^{n,t}$ maps points x lying on the edge uv to their images under the boundary evolution map $\gamma_h^{n,t}$, preserves the location of the vertex w, and is affine on the edges wu and wv.

Culmination. We now define $\Phi_h^{n,t}$ over each triangle $K \in \mathcal{S}_h^n$ with vertices u, v, w according to

$$\Phi_h^{n,t}(x) = \begin{cases} \lambda_u \mathfrak{p}_h^{n,t}(u) + \lambda_v \mathfrak{p}_h^{n,t}(v) + \lambda_w \mathfrak{p}_h^{n,t}(w) & \text{if } K \in \mathcal{T}_{h,0}^{t^{n-1}} \\ \lambda_u \gamma_h^{n,t}(u) + \lambda_v \mathfrak{p}_h^{n,t}(v) + \lambda_w \mathfrak{p}_h^{n,t}(w) & \text{if } K \in \mathcal{T}_{h,1}^{t^{n-1}} \\ \psi_h^{n,t}(\lambda_u u + \lambda_v v + \lambda_w \mathfrak{p}_h^{n,t}(w)) & \text{if } K \in \mathcal{T}_{h,2}^{t^{n-1}}, \end{cases} \tag{2.24}$$

where $\lambda_u, \lambda_v, \lambda_w$ are the barycentric coordinates of $x \in K$. Once again, we have employed the convention that for triangles $K \in \mathcal{T}_{h,2}^{t^{n-1}}$, the vertex w is the unique vertex of K lying inside $\Omega^{t^{n-1}}$, and for triangles $K \in \mathcal{T}_{h,1}^{t^{n-1}}$, the vertex u is the unique vertex of K lying outside $\Omega^{t^{n-1}}$.

The domain evolution and its velocity. It is now straightforward to record explicit expressions for the domain mapping $\varphi_h^{n,t}$ and its material velocity $V_h^{n,t}$. By definition,

$$\varphi_h^{n,t} = \Phi_h^{n,t} \circ \left(\Phi_h^{n,t_+^{n-1}} \right)^{-1}. \tag{2.25}$$

The velocity field $V_h^{n,t}$ is then given by differentation with respect to time:

$$V_h^{n,t} = \dot{\Phi}_h^{n,t} \circ \left(\Phi_h^{n,t_+^{n-1}} \right)^{-1}.$$

If the relaxation map $\mathfrak{p}_h^{n,t}$ is independent of time over $(t^{n-1}, t^n]$ (as is the case for the choice (2.22)), this expression for $V_h^{n,t}$ is given explicitly by

$$V_h^{n,t}(X) = \begin{cases} 0 & \text{if } K \in \mathcal{T}_{h,0}^{t^{n-1}} \\ \lambda_u \dot{\gamma}_h^{n,t}(u) & \text{if } K \in \mathcal{T}_{h,1}^{t^{n-1}} \\ \dfrac{\lambda_v}{2(1-\lambda_u)} \dot{\gamma}_h^{n,t}(\lambda_u u + (1-\lambda_u)v) + \dfrac{\lambda_u \lambda_w}{2(1-\lambda_u)} \dot{\gamma}_h^{n,t}(u) & \\ \quad + \dfrac{\lambda_u}{2(1-\lambda_v)} \dot{\gamma}_h^{n,t}((1-\lambda_v)u + \lambda_v v) + \dfrac{\lambda_v \lambda_w}{2(1-\lambda_v)} \dot{\gamma}_h^{n,t}(v) & \text{if } K \in \mathcal{T}_{h,2}^{t^{n-1}}, \end{cases} \tag{2.26}$$

where $\lambda_u, \lambda_v, \lambda_w$ are the barycentric coordinates of $(\Phi_h^{n,t_+^{n-1}})^{-1}(X) \in K$, with the conventional ordering of the vertices described earlier. Formulas for the time derivative of π^t (which are needed for the choice $\gamma_h^{n,t} = \pi^t \circ \pi^{t^{n-1}}$) in terms of local measures of the boundary's shape and velocity are given in 2.B.

2.5.2 Alternative: Isoparametric Approximation of the Domain

A convenient alternative to exact representations of the domain is to adopt superparametric or isoparametric representations of the domain. This entails approximating the map $\Phi_h^{n,t}$ (and hence the domain Ω^t) with a polynomial interpolant

$$\Phi_{h,\text{approx}}^{n,t}(\tilde{X}) = \sum_a \tilde{M}_a(\tilde{X}) \Phi_h^{n,t}(\tilde{Y}_a) \tag{2.27}$$

constructed from shape functions $\tilde{M}_a$ of a triangular Lagrange element (henceforth termed Lagrange shape functions) with corresponding degrees of freedom $\tilde{Y}_a$ on the reference triangulation $\mathcal{S}_h^n$. In this way, expressions for the spatial derivatives of the corresponding shape functions

$$N_{a,\text{approx}} = \tilde{N}_a \circ \left(\Phi_{h,\text{approx}}^{n,t_+^{n-1}} \right)^{-1} \tag{2.28}$$

and

$$n_{a,\text{approx}}^t = \tilde{N}_a \circ \left(\Phi_{h,\text{approx}}^{n,t} \right)^{-1}$$

involve only derivatives of the reference triangulation's shape functions $\tilde{N}_a$ and the Lagrange shape functions $\tilde{M}_a$, and not the gradients of the exact map $\Phi_h^{n,t}$:

$$\nabla_X N_{a,\text{approx}}(X) = \nabla_{\tilde{X}} \tilde{N}_a(\tilde{X}) \cdot \left(\nabla_{\tilde{X}} \Phi_{h,\text{approx}}^{n,t_+^{n-1}} \right)^{-1} = \nabla_{\tilde{X}} \tilde{N}_a(\tilde{X}) \cdot \left(\sum_a \nabla_{\tilde{X}} \tilde{M}_a(\tilde{X}) \Phi_h^{n,t_+^{n-1}}(\tilde{Y}_a) \right)^{-1}$$

$$\nabla_x n_{a,\text{approx}}^t(x) = \nabla_{\tilde{X}} \tilde{N}_a(\tilde{X}) \cdot \left(\nabla_{\tilde{X}} \Phi_{h,\text{approx}}^{n,t} \right)^{-1} = \nabla_{\tilde{X}} \tilde{N}_a(\tilde{X}) \cdot \left(\sum_a \nabla_{\tilde{X}} \tilde{M}_a(\tilde{X}) \Phi_h^{n,t}(\tilde{Y}_a) \right)^{-1}.$$

This, in turn, eliminates the need to compute gradients of the closest point projection π^t. This, and other reasons detailed later, make approximating the domain in this way more computationally convenient in practice.

For completeness, we next detail the corresponding approximate domain map

$$\varphi_{\text{approx}}^{n,t} = \Phi_{h,\text{approx}}^{n,t} \circ \left(\Phi_{h,\text{approx}}^{n,t_+^{n-1}} \right)^{-1}$$

and velocity fields, which take particularly simple forms. In fact, with

$$y_a(t) = \Phi_h^{n,t}(\tilde{Y}_a)$$

denoting the trajectory of a degree of freedom $\tilde{Y}_a$ and

$$M_a = \tilde{M}_a \circ \left(\Phi_{h,\text{approx}}^{n,t_+^{n-1}} \right)^{-1}$$

denoting the pushforward of the Lagrange shape functions $\tilde{M}_a$ to $\Omega^{t^{n-1}}$, we have

$$\begin{aligned} \varphi_{h,\text{approx}}^{n,t}(X) &= \Phi_{h,\text{approx}}^{n,t} \left(\left(\Phi_{h,\text{approx}}^{n,t_+^{n-1}} \right)^{-1}(X) \right) \\ &= \sum_a \tilde{M}_a \left(\left(\Phi_{h,\text{approx}}^{n,t_+^{n-1}} \right)^{-1}(X) \right) \Phi_h^{n,t}(\tilde{Y}_a) \\ &= \sum_a M_a(X) y_a(t). \end{aligned}$$

The corresponding material and spatial velocity fields are thus

$$V_{h,\text{approx}}^{n,t}(X) = \sum_a M_a(X) \dot{y}_a(t)$$

and

$$v_{h,\text{approx}}^{n,t}(x) = \sum_a m_a^t(x) \dot{y}_a(t),$$

respectively, with $m_a^t = \tilde{M}_a \circ \left(\Phi_{h,\text{approx}}^{n,t}\right)^{-1}$.

Introducing approximations of the domain requires some extra care in the imposition of boundary conditions. In the example problem here, homogeneous Dirichlet boundary conditions are imposed on the boundary of the approximate domain. Therefore, the order of the Lagrange shape functions $\tilde{M}_a$ should be high enough to ensure that the errors introduced by approximating Ω^t with $\Phi_{h,\text{approx}}^{n,t}(\mathcal{S}_h^n)$ converge to zero at least as quickly as the error in the original spatial discretization as $h \to 0$. It is well-known [28] that if the shape functions $\tilde{N}_a$ are themselves Lagrange shape functions, then it suffices to use Lagrange shape functions $\tilde{M}_a$ of equal or higher degree for the approximation of the domain geometry. Elements of this type are referred to as *isoparametric* or *superparametric* elements, depending upon whether the functions $\tilde{M}_a$ have equal or higher degree, respectively, than the functions $\tilde{N}_a$.

2.5.3 Example: A Complete Algorithm

We now present an algorithm that takes advantage of the SDIRK method of §2.4.3 for time integration and of the isoparametric representation of the domain of §2.5.2. For concreteness, we consider the case in which the partial differential operator $\mathcal{a}(u) = -\Delta_x u$, so that

$$a^t(u, w) = \int_{\Omega^t} \nabla_x u \cdot \nabla_x w \, dx,$$

In what follows, we denote matrices and vectors with uppercase and lowercase boldface letters, respectively. As shorthand notation, we denote by

$$(u, w)_{K^t} = \int_{K^t} u(x) w(x) \, dx$$

the inner product of two functions u and w over an element $K^t = \Phi_h^{n,t}(K)$, $K \in \mathcal{S}_h^n$. The algorithm is labeled Algorithm 2.5.1.

Implementation. We discuss some key steps of the algorithm next, to show how the motion of the domain is accounted for in the implementation of the algorithm, and how it affects the computation of elemental quantities such as the mass matrix. For concreteness, in the following it is useful to keep in mind a very simple example, such as when the moving domain Ω^t is the circle centered at the origin of radius $1+t$, for each small $t \geq 0$ (this is the geometry used to draw Fig. 2.6 later). Without loss of generality, we discuss the case in which $n = 1$, so that $t^{n-1} = 0$. Finally, we will also use the standard triangle $\hat{K}$, such as that with vertices $(0, 0)$, $(0, 1)$, and $(1, 0)$, which has traditionally been used in finite element codes to perform quadrature.

In step 2 we identify triangles in $\mathcal{T}_{h,i}^0$, for $i = 0, 1, 2$, by labeling vertices of triangles in the universal mesh according to whether they are inside or outside Ω^0. For example, Fig. 2.6 shows

Algorithm 2.5.1 Time integration using a universal mesh with an s-stage SDIRK method

Require: Initial condition $u^0 \in H_0^1(\Omega^0)$.

1: **for** $n = 1, 2, \ldots, N$ **do**

2: Identify triangles in $\mathcal{T}_{h,i}^{t^{n-1}}$, $i = 0, 1, 2$. Set $\mathcal{S}_h^n = \mathcal{T}_{h,0}^{t^{n-1}} \cup \mathcal{T}_{h,1}^{t^{n-1}} \cup \mathcal{T}_{h,2}^{t^{n-1}}$.

3: Compute $\Phi_h^{n,t_+^{n-1}}(\tilde{Y}_a)$ for every degree of freedom $\tilde{Y}_a \in \mathcal{D}(\mathcal{S}_h^n)$ using (2.24).

4: Set $\mathcal{V}_h^n = \text{span}\{N_{a,\text{approx}}\}_a$, where $\{N_{a,\text{approx}}\}_a$ are the shape functions (2.28).

5: Project $u_h^{\Delta t,n-1} \in (\varphi_h^{n-1,t^{n-1}})_* \mathcal{V}_h^{n-1}$ (or u^0 if $n = 1$) onto $\mathcal{V}_h^n$ using a projector p_h^n. Denote by $\mathbf{u}_0$ the vector of coefficients in the expansion

$$p_h^n u_h^{\Delta t,n-1} = \sum_a (\mathbf{u}_0)_a N_{a,\text{approx}}.$$

6: **for** $i = 1, 2, \ldots, s$ **do**

7: Compute $\Phi_h^{n,t_i}(\tilde{Y}_a)$ for every degree of freedom $\tilde{Y}_a \in \mathcal{D}(\mathcal{S}_h^n)$ using (2.24).

8: With $K^{t_i} = \Phi_{h,\text{approx}}^{t_i}(K)$ for every $K \in \mathcal{S}_h^n$, assemble

$$\begin{aligned}
\mathbf{M}_{ab} &= \sum_K \left(n_{b,\text{approx}}^{t_i},\, n_{a,\text{approx}}^{t_i} \right)_{K^{t_i}} \\
\mathbf{B}_{ab} &= \sum_K \left(v_{h,\text{approx}}^{n,t_i} \cdot \nabla_x n_{b,\text{approx}}^{t_i},\, n_{a,\text{approx}}^{t_i} \right)_{K^{t_i}} \\
\mathbf{K}_{ab} &= \sum_K \left(\nabla_x n_{b,\text{approx}}^{t_i},\, \nabla_x n_{a,\text{approx}}^{t_i} \right)_{K^{t_i}} \\
\mathbf{f}_a &= \sum_K \left(f(t_i),\, n_{a,\text{approx}}^{t_i} \right)_{K^{t_i}}
\end{aligned}$$

9: With $\mathbf{u}_* = \sum_{j=0}^{i-1} \beta_{ij} \mathbf{u}_j$ and $\Delta t^n = t^n - t^{n-1}$, define

$$\begin{aligned}
\mathbf{A} &= \mathbf{M} + \gamma \Delta t^n (\mathbf{K} - \mathbf{B}) \\
\mathbf{b} &= \mathbf{M}\mathbf{u}_* + \mathbf{f}
\end{aligned}$$

10: For every degree of freedom $\tilde{Y}_a \notin \text{int}(\mathcal{D}(\mathcal{S}_h^n))$, set

$$\begin{aligned}
\mathbf{A}_{ab} &= \delta_{ab} \\
\mathbf{b}_a &= 0.
\end{aligned}$$

11: Solve $\mathbf{A}\mathbf{u}_i = \mathbf{b}$ for $\mathbf{u}_i$.

12: **end for**

13: Set $u_h^{\Delta t,n}(x) = \sum_a (\mathbf{u}_s)_a n_{a,\text{approx}}^{t^n}(x)$.

14: **end for**

15: **return** $u_h^{\Delta t,N}$

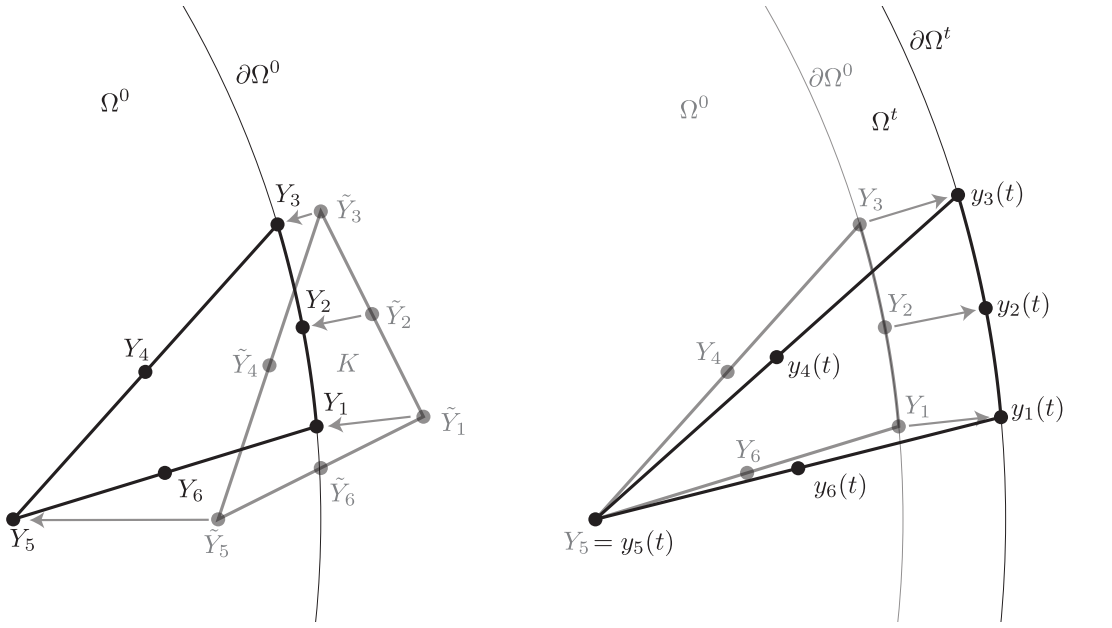

(a) Construction of $\Phi^{1,0+}_{h,\text{approx}}(\tilde{K})$ for $\tilde{K} \in \mathcal{T}^0_{h,2}$

(b) Construction of $\Phi^{1,t}_{h,\text{approx}}(\tilde{K})$ for $\tilde{K} \in \mathcal{T}^0_{h,2}$, $0 < t \leq \Delta t$

Figure 2.6: Example of how the approximate evolving domain is accounted for in practice. See text in §2.5.3 for the explanation.

one triangle $\tilde{K} \in \mathcal{T}^0_{h,2}$. For this example $\tilde{K}$ will be assumed to be quadratic and hence consists of 6 nodes, with its nodes labeled by $\tilde{Y}_a$, $a = 1, \ldots, 6$.

In step 3, the positions $\{Y_a\}_a$ of these six nodes in the mesh conforming to Ω_0 are computed, and in general, of all nodes in triangles intersecting $\partial\Omega_0$. This computation involves computing the closest point projection for nodes $\tilde{Y}_1, \tilde{Y}_2, \tilde{Y}_3$, and $\tilde{Y}_5$, moving the first 3 nodes to their closest point projections, and moving $\tilde{Y}_5$ along the normal to the boundary emanating from its closest point projection, according to (2.22). Nodes $\tilde{Y}_4$ and $\tilde{Y}_6$ are then mapped to the midpoints of segments Y_3Y_5 and Y_1Y_5, respectively. These six nodes define the isoparametric quadratic triangle $K = \Phi^{1,0+}_{h,\text{approx}}(\tilde{K})$. Henceforth, *the construction of shape functions and quadrature rules follow standard finite element procedures over isoparametric elements.* For example, in this case, $K = \hat{\Psi}(\hat{K})$, where the isoparametric map is $\hat{\Psi}(\hat{X}) = \sum_{a=1}^{6} Y_a \hat{N}_a(\hat{X})$ and $\{\hat{N}_a\}_a$ denote the shape functions over $\hat{K}$. This is equivalent to (2.27).

In step 4, the shape functions over K are constructed. Because the map between $\hat{K}$ and $\tilde{K}$ is affine, the shape function $\{N_{a,\text{approx}}\}_a$ can be constructed over $\hat{K}$, namely, $N_{a,\text{approx}}(X) = \hat{N}_a(\hat{\Psi}^{-1}(X))$, for $X \in K$. This is, again, standard procedure for isoparametric elements.

As the boundary of the domain moves at each stage i of the time integration, the nodes $\{Y_a\}_a$ of triangle K are deformed as follows (step 7): Nodes Y_1, Y_2, Y_3 are mapped to their closest point

projections onto $\partial\Omega^{t_i}$, labeled y_1, y_2, and y_3, respectively, node Y_5 remains where it is, so $y_5 = Y_5$, and nodes Y_4 and Y_6 are mapped to y_4 and y_6, the midpoints of edges y_3y_5 and y_1y_5, respectively, see Fig. 2.6b. Shape functions over triangle K^{t_i} are formed in precisely the same way as those for triangle K, in this case with nodal positions $\{y_a\}_a$.

To assemble the system needed to solve (2.20) at each stage of the time integration (step 8) it is useful to notice that the elemental mass matrix for each element is computed as

$$\begin{aligned}
\mathbf{M}_{ab}^{K} &= \int_{K^{t_i}} n_{a,\text{approx}}^{t_i} n_{b,\text{approx}}^{t_i}\, dx \\
&= \int_{K} N_{a,\text{approx}} N_{b,\text{approx}} |\nabla_X \varphi_{h,\text{approx}}^{1,t_i}|\, dX \\
&= \int_{\tilde{K}} \tilde{N}_a \tilde{N}_b |\nabla_{\tilde{X}} \Phi_{h,\text{approx}}^{1,t_i}|\, d\tilde{X} \\
&= \int_{\hat{K}} \hat{N}_a \hat{N}_b |\nabla_{\hat{X}} \hat{\Psi}|\, d\hat{X},
\end{aligned} \tag{2.29}$$

and similarly for the elemental contributions to the other terms of (2.20). Consequently, quadrature could be performed on any of the triangles K, $\tilde{K}$, $\hat{K}$, or K^{t_i}, but for convenience and following standard practice, we do it over the standard element $\hat{K}$.

Notice then that, in order to perform the quadrature over $\hat{K}$, it is convenient to build the deformed mesh at time t_i, since it makes the construction of $\hat{\Psi}$ straightforward. So, in this time-integration scheme the deformed mesh is built s times in a time step.

An important practical matter we wish to highlight is the simplicity of the data structures needed to implement our method. In particular, *the connectivity of the universal mesh never changes* during deformation – only the nodal positions change. As a consequence, the sizes and sparsity structures of various discrete quantities (the solution vector $\mathbf{u}$, the mass matrix $\mathbf{M}$, the stiffness matrix $\mathbf{K}$, the convection matrix $\mathbf{B}$, and the forcing vector $\mathbf{f}$) can be held fixed, even though differing subsets of degrees of freedom may participate in the discrete equations at different intervals $(t^{n-1}, t^n]$. This can be accomplished by simply imposing "homogeneous Dirichlet boundary conditions" on the solution at degrees of freedom not belonging to the subtriangulation $\mathcal{S}_h^n$. In practice, this amounts to replacing the corresponding rows of a particular matrix $\mathbf{A}$ with rows whose only nonzero entries are 1 on the diagonal, and setting to zero the corresponding entries of a vector (see step 10 of Algorithm 2.5.1). Note that $\mathbf{A}$ is automatically asymmetric at the outset, so any concerns of breaking symmetry via row replacement are irrelevant.

2.5.4 Exact vs. Approximate Map: Cost Considerations

The computational cost of evaluating the map $\Phi_h^{n,t}$ or its approximant $\Phi_{h,\text{approx}}^{n,t}$ is dominated by the cost of evaluating closest-point projections onto $\partial\Omega^t$. In our numerical experiments (which used $\Phi_{h,\text{approx}}^{n,t}$), these calculations accounted for little more than $5-10\%$ of the total run time of a typical

simulation.

Note that implementations that employ the exact map $\Phi_h^{n,t}$ require evaluations of the closest point projection and its gradient at *quadrature points* in triangles $K \in \mathcal{T}_{h,1}^{t^{n-1}} \cup \mathcal{T}_{h,2}^{t^{n-1}}$, whereas implementations that employ the approximate map $\Phi_{h,\text{approx}}^{n,t}$ require evaluations only of the closest point projection (not its gradient) on those triangles' *degrees of freedom*. A counting argument reveals that the computational savings that accompany the use of $\Phi_{h,\text{approx}}^{n,t}$ over $\Phi_h^{n,t}$ are significant: For a polynomial interpolant $\Phi_{h,\text{approx}}^{n,t}$ constructed from Lagrange elements of a fixed polynomial degree, it is not difficult to show that the use of $\Phi_{h,\text{approx}}^{n,t}$ over $\Phi_h^{n,t}$ reduces the computational cost (measured by number of closest point projection evaluations) by factors of 9, 9, and 5.2, respectively, for affine, quadratic, and cubic Lagrange elements, assuming the use of a quadrature rule that exactly computes entries of the elemental mass matrix on straight triangles.

2.6 Numerical Examples

In this section, we apply the proposed method to a modification of a classical moving-boundary problem: Stefan's problem. In our modification, the evolution of the boundary is imposed through the exact solution, instead of being computed. Our aim in this example is is to illustrate the convergence rate of the method with respect to the mesh spacing h and time step Δt.

We begin by demonstrating, using a one-dimensional numerical test, that the order of accuracy of the method is suboptimal by half an order in the L^2 norm when Δt and h scale proportionately. We observe, however, that the suboptimal rate is difficult to detect from an inspection of the total error $\|u_h^{N,\Delta t} - u^N\|_{0,2,\Omega^T}$, since the terms of suboptimal order contributing to the total error are dominated by terms of optimal order (for practical values of the mesh spacing h). We follow with a convergence test in two-dimensions, where, for the reason just described, optimal rates are observed for the total error.

2.6.1 The (Modified) One-Dimensional Stefan Problem with Prescribed Boundary Evolution

Consider the following instance of the one-dimensional Stefan problem: Find $u(x,t)$ and $s(t)$ such that

$$\frac{\partial u}{\partial t} = \frac{\partial^2 u}{\partial x^2}, \qquad 0 < x < s(t),\ t \geq 1 \tag{2.30a}$$

$$\frac{ds}{dt} = -\frac{\partial u}{\partial x}, \qquad x = s(t) \tag{2.30b}$$

$$u(0,t) = e^t - 1, \qquad t \geq 1 \tag{2.30c}$$

$$u(s(t),t) = 0, \qquad t \geq 1 \tag{2.30d}$$

$$u(x,1) = e^{1-x} - 1, \qquad 0 \leq x \leq 1 \tag{2.30e}$$

$$s(1) = 1. \tag{2.30f}$$

The exact solution is

$$u(x,t) = e^{t-x} - 1$$
$$s(t) = t.$$

In this case, we treat the boundary evolution as prescribed by supplying the exact evolution $s(t)$, instead of solving for it by integrating (2.30b).

We computed the numerical solution $u_h^{\Delta t,N}$ using a finite element space made of continuous elementwise-affine functions on a sequence of uniform meshes with spacing $h = 2^{-k}h_0$, $k = 0,1,2,3$ over the time interval $[1,T]$ with $h_0 = 1/4$ and $T = 1 + 10^{-6}$ (the short time interval was chosen, on the basis of numerical experiments, in order to detect the suboptimal rate predicted by the theory). The restriction of the algorithm to a single spatial dimension is that specified in Algorithm 2.2.1, and is complemented with the choice $p_h^n = p_{h,L^2}^n$ for the projection, relaxation parameters $\delta = 0.3$ and $R = 3$, and the singly diagonally implicit Runge-Kutta (SDIRK) scheme of order 2 given in Table 2.4 with a time step $\Delta t = 10^{-6}h/h_0$ for time-integration.

Table 2.1 presents the convergence of the method measured at time $t = T$ in $L^2(\Omega^T)$. The third column of the table suggests that the total error $\|u_h^{\Delta t,N} - u^N\|_{0,2,\Omega^T}$ converges at an optimal rate $O(h^2)$. However, columns 1 and 2 reveal that a piece of the error, namely the discrepancy between the numerical solution $u_h^{\Delta t,N}$ and the nodal interpolant $i_h^{t^N}u^N$ of the exact solution, decays at a suboptimal rate $O(h^{3/2})$. Since standard estimates from the theory of interpolation give $\|u^N - i_h^{t^N}u^N\|_{0,2,\Omega^T} = O(h^2)$, it follows from the inequality

$$\|u_h^{\Delta t,N} - i_h^{t^N}u^N\|_{0,2,\Omega^T} \leq \|u_h^{\Delta t,N} - u^N\|_{0,2,\Omega^T} + \|u^N - i_h^{t^N}u^N\|_{0,2,\Omega^T}$$

Table 2.1: Convergence rates in the L^2-norm on Ω^T for the solution to the (modified) one-dimensional Stefan problem using a finite element space made of continuous elementwise-affine functions with a second-order implicit Runge-Kutta time integrator, see §2.6.1. Differences between the exact solution u^N, the numerical approximation $u_h^{\Delta t,N}$, and the nodal interpolant of the exact solution $i_h^{t^N} u^N$ are shown in each column. These values are used in §2.6.1 to illustrate that the expected theoretical convergence rate of $h^{3/2}$ is observed. Nevertheless, the slowly converging part is so small, that the apparent convergence rate is h^2, as the third column shows.

h_0/h	$\|u_h^{\Delta t,N} - i_h^{t^N} u^N\|_{0,2,\Omega^T}$	Order	$\|i_h^{t^N} u^N - u^N\|_{0,2,\Omega^T}$	Order	$\|u_h^{\Delta t,N} - u^N\|_{0,2,\Omega^T}$	Order
1	1.2e-11	-	4.4e-05	-	4.4e-05	-
2	4.6e-12	1.42	1.1e-05	2.04	1.1e-05	2.04
4	1.6e-12	1.49	2.6e-06	2.02	2.6e-06	2.02
8	5.5e-13	1.56	6.5e-07	2.01	6.5e-07	2.01

Table 2.2: Convergence rates in the L^2-norm on Ω^T for the solution to the (modified) two-dimensional Stefan problem (2.31) using linear, quadratic, and cubic elements together with nodal interpolation as the projection operator, and second-, third-, and fourth-order implicit Runge-Kutta schemes, respectively, as time integrators. See Fig. 2.7 for a graphical depiction of the same results.

	Linear		Quadratic		Cubic	
h_0/h	Error	Order	Error	Order	Error	Order
1	3.0e-02	-	1.3e-03	-	2.9e-05	-
2	9.8e-03	1.59	1.4e-04	3.21	3.1e-06	3.24
4	2.6e-03	1.94	2.1e-05	2.66	2.2e-07	3.84
8	6.4e-04	2.00	2.6e-06	3.03	1.4e-08	3.97
16	1.6e-04	2.00	3.3e-07	2.97	-	-

that $\|u_h^{\Delta t,N} - u^N\|_{0,2,\Omega^T}$ must be decaying no faster than $O(h^{3/2})$. However, the contribution to the error supplied by $u_h^{\Delta t,N} - i_h^{t^N} u^N$ is several orders of magnitude smaller than the remaining contribution, $i_h^{t^N} u^N - u^N$, explaining the apparent optimal rate observed for the total error.

2.6.2 The (Modified) Two-Dimensional Stefan Problem with Prescribed Boundary Evolution

We consider now the following instance of the two-dimensional, cylindrically symmetric Stefan problem with a circular boundary of radius $\rho(t)$ centered at the origin. Find the scalar functions $u(x,t)$

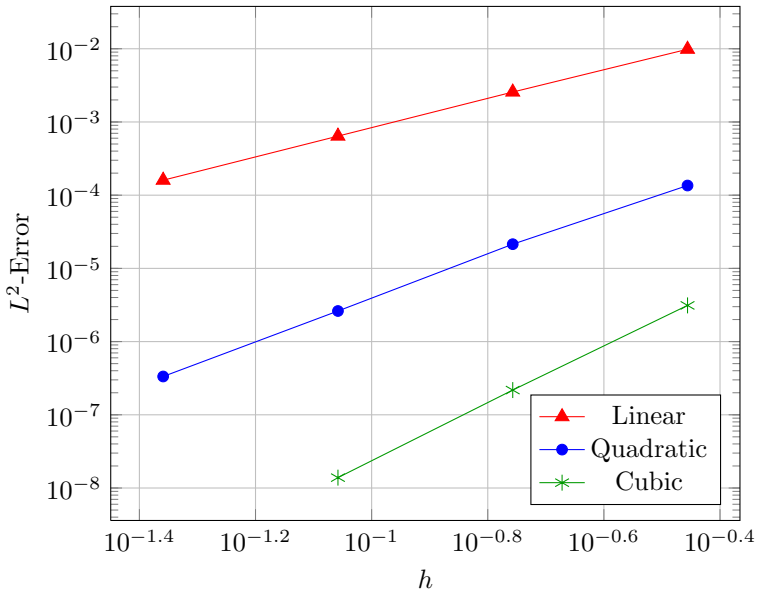

Figure 2.7: L^2-error $\|u_h^{\Delta t,N} - u^N\|_{0,2,\Omega^T}$ at a fixed final time as a function of the mesh spacing h for the (modified) two-dimensional Stefan problem (2.31) with prescribed boundary evolution. The problem was solved using linear, quadratic, and cubic elements together with nodal interpolation as the projection operator, and second-, third-, and fourth-order implicit Runge-Kutta schemes, respectively, as time integrators, with $h \propto \Delta t$.

and $\rho(t)$ such that for all times $t \in [0, T]$,

$$\frac{\partial u}{\partial t} - \Delta_x u = f, \qquad 0 \leq |x| < \rho(t) \tag{2.31a}$$

$$\frac{d\rho}{dt} = -\frac{\partial u}{\partial n}, \qquad |x| = \rho(t) \tag{2.31b}$$

$$u(x,t) = 0, \qquad |x| = \rho(t) \tag{2.31c}$$

$$u(x,0) = J_0(r_0|x|), \tag{2.31d}$$

$$\rho(0) = 1, \tag{2.31e}$$

where J_0 is the zeroth-order Bessel function of the first kind, r_0 is the smallest positive root of J_0, and

$$\begin{aligned} f(x,t) &= \frac{\alpha r_0^3 \beta(t)^2 |x|}{2\sigma(t)^3} J_0'\left(\frac{r_0|x|}{\sigma(t)}\right) \\ \sigma(t) &= \exp\left(\frac{\alpha(\beta(t)-1)}{2}\right) \\ \beta(t) &= \frac{1}{\alpha}\mathrm{Ei}^{-1}\left(\mathrm{Ei}(\alpha) - r_0^2 t e^{\alpha}\right) \\ \alpha &= \frac{2J_0'(r_0)}{r_0}. \end{aligned}$$

Here, $\mathrm{Ei}(z) = -\int_{-z}^{\infty} \frac{e^{-\zeta}}{\zeta} d\zeta$, the exponential integral. The exact solution is

$$\begin{aligned} u(x,t) &= \beta(t) J_0\left(\frac{r_0|x|}{\sigma(t)}\right) \\ \rho(t) &= \sigma(t). \end{aligned}$$

In our implementation, we treat the boundary evolution as prescribed by supplying the exact evolution of the moving domain's radius $\rho(t)$, instead of solving for it. To study the convergence of the method, the problem was solved using finite element spaces of continuous functions that are affine, quadratic, and cubic over each element (linear, quadratic, and cubic Lagrange elements) together with nodal interpolation as the projection operator, relaxation parameters $\delta = 0.8$ and $R = 3$, and singly diagonally implicit Runge-Kutta (SDIRK) schemes of orders 2, 3, and 4, respectively, as the time integrators (see the coefficients in Tables 2.3-2.6). The solution was computed on a uniform mesh of equilateral triangles with a lowest resolution mesh spacing of $h_0 = 0.35$ and a time step $\Delta t = Th/h_0$, up to a final time $T = 0.005$.

Fig. 2.7 displays the L^2-error of the numerical solution as a function of the mesh spacing h at $t = T$. Optimal convergence orders of 2, 3, and 4 are observed for the three schemes, in agreement with the observations made in the one-dimensional test case. Table 2.2 shows the same results.

To illustrate the method on a second, more interesting example, we solved the partial differential equation (2.31a) with homogeneous Dirichlet boundary conditions and initial condition

$$u(x) = J_0\left(\frac{10 r_0 |x|}{10 + \cos 10\theta}\right)$$

on a prescribed domain Ω^t whose boundary is given by a sinusoidal perturbation of the unit circle. Namely,

$$\Omega^t = \left\{ x \;\middle|\; |x| < 1 + \frac{1}{10}\cos 10\theta \cos 250t \right\}$$

with $\theta = \tan^{-1}(x_2/x_1)$. Fig. 2.8 shows snapshots of the solution, which was computed using

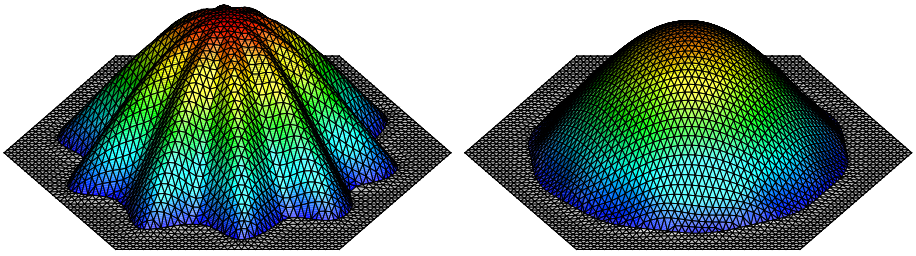

(a) $t = 0$ (b) $t = 0.02$

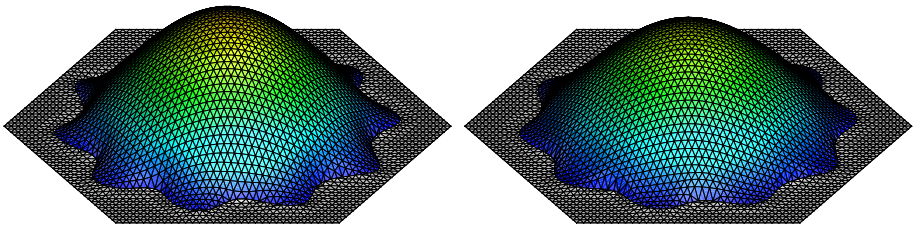

(c) $t = 0.04$ (d) $t = 0.06$

Figure 2.8: Solution to a prescribed-boundary variant of the Stefan problem in which the moving boundary is a sinusoidal perturbation of the unit circle.

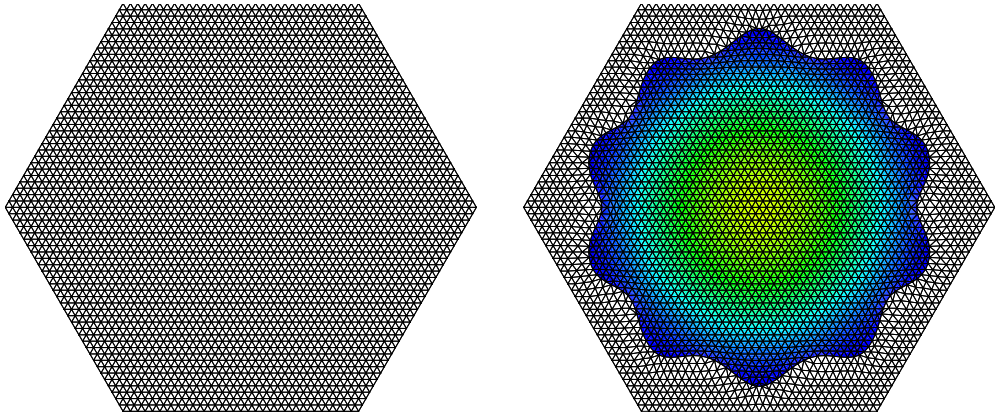

(a) Universal mesh (b) $t = 0.06$

Figure 2.9: (a) Universal mesh adopted during the simulation depicted in Fig. 2.8, and (b) its image under the universal mesh map at $t = 0.06$, superposed with the contours of the solution.

Table 2.3: SDIRK(1): Coefficients β_{ij} for a $s = 1$-stage SDIRK scheme of order 1. ($\gamma = 1$)

$i \setminus j$	0
1	1

Table 2.4: Coefficients β_{ij} for a $s = 2$-stage SDIRK scheme of order 2. ($\gamma = 1 - \sqrt{2}/2$)

$i \setminus j$	0	1
1	1	
2	$-\sqrt{2}$	$1 + \sqrt{2}$

Table 2.5: Coefficients β_{ij} for a $s = 3$-stage SDIRK scheme of order 3.
($\gamma = 0.43586652150845899942$)

$i \setminus j$	0	1	2
1	1.00000000000000000		
2	0.352859819860479140	0.647140180139520860	
3	−1.25097989505606042	3.72932966244456977	−1.47834976738850935

quadratic Lagrange elements on a uniform mesh of equilateral triangles ($h = 0.04375$) together with nodal interpolation as the projection operator, relaxation parameters $\delta = 0.8$ and $R = 3$, and the third-order SDIRK scheme (2.5) with time step $\Delta t = 0.000625$. The universal mesh and its image under the universal mesh map at an instant in time are shown in Fig. 2.9.

2.7 Conclusion

We have presented a general framework for the design of high-order finite element methods for moving-boundary problems with prescribed boundary evolution. A key role in our approach was played by universal meshes, which combine the immunity to large mesh distortions enjoyed by conventional fixed-mesh methods with the geometric fidelity of deforming-mesh methods. A given accuracy in space and time may be achieved by choosing an appropriate finite element space on the universal mesh and an appropriate time integrator for ordinary differential equations. The order of accuracy of the resulting scheme is suboptimal by one half an order according to theory (see Chapter 5), although we observed in our numerical examples that terms of optimal order tend to dominate in practice.

Table 2.6: Coefficients β_{ij} for a $s = 5$-stage SDIRK scheme of order 4. ($\gamma = 1/4$)

$i \setminus j$	0	1	2	3	4
1	1				
2	-1	2			
3	$-\frac{13}{25}$	$\frac{42}{25}$	$-\frac{4}{25}$		
4	$-\frac{4}{17}$	$\frac{89}{68}$	$-\frac{25}{136}$	$\frac{15}{136}$	
5	$\frac{7}{3}$	$-\frac{37}{12}$	$-\frac{103}{24}$	$\frac{275}{8}$	$-\frac{85}{3}$

2.A Singly Diagonally Implicit Runge Kutta Time Integrators

Tables 2.3-2.6 record the coefficients $\gamma > 0$ and $\beta_{ij} \in \mathbb{R}$, $i = 1, 2, \ldots, s$, $j = 0, 1, \ldots, i-1$ for a collection of SDIRK methods (2.20) of orders 1 through 4.

Note that the structure of the Runge-Kutta stages in (2.20) differs from the structure that is most familiar to Runge-Kutta practitioners [70]. The former structure, which is algorithmically better-suited for problems with time-dependent mass matrices, is obtainable from any L-stable SDIRK scheme as follows. Let a_{ij}, b_j, and c_j, $i, j = 1, 2, \ldots, s$, be the coefficients of an SDIRK scheme with Butcher tableaux

$$\begin{array}{c|cccc} c_1 & a_{11} & a_{12} & \cdots & a_{1s} \\ c_2 & a_{21} & a_{22} & \cdots & a_{2s} \\ \vdots & \vdots & \vdots & \ddots & \vdots \\ c_s & a_{s1} & a_{s2} & \cdots & a_{ss} \\ \hline & b_1 & b_2 & \cdots & b_s \end{array} \tag{2.32}$$

By definition, $a_{11} = a_{22} = \cdots = a_{ss}$ and $a_{ij} = 0$ for $j > i$. Assume that the scheme is L-stable, i.e. $b_j = a_{sj}$, $j = 1, 2, \ldots, s$. Then the coefficients γ and β_{ij} in the formulation (2.20) are related to a_{ij}, b_j, and c_j via

$$\gamma = a_{11}$$
$$\beta_{ij} = \begin{cases} \delta_{ij} - a^*_{ij} & \text{if } j > 0 \\ \sum_{k=1}^{i} a^*_{ik} & \text{if } j = 0. \end{cases}$$

Here, δ_{ij} denotes the Kronecker delta and a^*_{ij} is the i, j entry of the matrix γA^{-1}, where $A = (a_{ij})$. The equivalence between (2.20) and the scheme defined by (2.32) is proven in [141].

2.B The Closest Point Projection onto a Moving Curve and its Time Derivative

The following paragraphs derive explicit expressions for the time derivative of the closest point projection of a fixed point in space onto a moving curve. Such expressions are needed in numerical implementations for the evaluation of (2.26) when the boundary evolution operator $\gamma_h^{n,t}$ is given by (2.21).

Consider a moving curve $c^t \in \mathcal{C} := \{s \in C^2([0,1], \mathbb{R}^2) \mid s'(\theta) \neq 0 \ \forall \theta \in [0,1]\}$ whose velocity at any point $y = c^t(\theta) \in \text{image}(c^t)$ is given by $v^t(y) = \dot{c}^t(\theta)$. Let $\hat{n}^t(y)$, $\hat{t}^{\,t}(y)$, and $\kappa^t(y)$ denote the unit normal vector, unit tangent vector, and signed curvature at y, respectively, and let π^t and ϕ^t denote the closest point projection onto $\text{image}(c^t)$ and the signed distance function on $\mathbb{R}^2$, respectively, as in Section 2.5. Let τ denote the arclength parameter on $\text{image}(c^t)$. Henceforth, we employ the arclength parametrization and write $c^t(\tau)$ to denote the point on $\text{image}(c^t)$ with arclength parameter τ.

With respect to the arclength parametrization, the unit normal, unit tangent, and signed curvature satisfy the following relations at any point $y = c^t(\tau)$:

$$\hat{t}^{\,t}(y) = \frac{\partial c^t}{\partial \tau}(\tau), \quad \frac{\partial \hat{t}^{\,t}}{\partial \tau}(y) = \kappa^t(y)\hat{n}^t(y), \quad \frac{\partial \hat{n}^t}{\partial \tau}(y) = -\kappa^t(y)\hat{t}^{\,t}(y).$$

Here, for a given function $f^t : \text{image}(c^t) \to \mathbb{R}^k$, $k \in \{1,2\}$, we are abusing notation by writing

$$\frac{\partial f^t}{\partial \tau}(y) := \left.\frac{\partial}{\partial \tau}\right|_t f^t(c^t(\tau))$$

for any $y = c^t(\tau) \in \text{image}(c^t)$. Likewise, we write

$$\frac{\partial g^t}{\partial t}(x) = \left.\frac{\partial}{\partial t}\right|_x g^t(x)$$

for a function $g^t : \mathbb{R}^2 \to \mathbb{R}^k$, $k \in \{1,2\}$.

The closest point projection satisfies

$$x - \pi^t(x) = \phi^t(x)\hat{n}^t(\pi^t(x)) \tag{2.33}$$

for any $x \in \mathbb{R}^2$ for which $\pi^t(x)$ is uniquely defined. Another identity that will be of use momentarily concerns the normal velocity $v_n^t(y) := v^t(y) \cdot \hat{n}^t(y)$. Namely,

$$\frac{\partial v_n^t}{\partial \tau}(y) = \hat{n}^t(y) \cdot \frac{\partial v^t}{\partial \tau}(y) - \kappa^t(y)\hat{t}^{\,t}(y) \cdot v^t(y) \tag{2.34}$$

for any $y \in \text{image}(c^t)$ by the product rule.

Proposition 2.B.1. *Suppose $\{c^t\}_{t\in[0,T]} \subset \mathcal{C}$ is a family of curves such that the map*

$$\begin{aligned} c : \{(\tau, t) : 0 \le \tau \le \text{length}(\text{image}(c^t)), 0 \le t \le T\} &\to \mathbb{R}^2 \\ (\tau, t) &\mapsto c^t(\tau) \end{aligned}$$

is of class C^2. Let $x \in \mathbb{R}^2$ be a point for which $\pi^t(x)$ is uniquely defined and $\phi^t(x)\kappa^t(\pi^t(x)) < 1$ for every $0 \le t \le T$. Then

$$\frac{\partial \pi^t}{\partial t}(x) = v_n^t(\pi^t(x))\hat{n}^t(\pi^t(x)) + \sigma^t(x)\hat{t}^t(\pi^t(x)) \tag{2.35}$$

for every $0 \le t \le T$, where

$$\sigma^t(x) = \frac{\phi^t(x)\frac{\partial v_n^t}{\partial \tau}(\pi^t(x))}{1 - \phi^t(x)\kappa^t(\pi^t(x))}. \tag{2.36}$$

Proof. Let $\bar{\tau}^t(x)$ denote the arclength parameter along image(c^t) assumed by $\pi^t(x)$; that is,

$$c^t(\bar{\tau}^t(x)) = \pi^t(x). \tag{2.37}$$

Differentiating this relation with respect to time gives

$$v^t(\pi^t(x)) + \hat{t}^t(\pi^t(x))\frac{\partial \bar{\tau}^t}{\partial t}(x) = \frac{\partial \pi^t}{\partial t}(x). \tag{2.38}$$

On the other hand, relation (2.33) implies that

$$\big(x - c^t(\bar{\tau}^t(x))\big) \cdot \hat{t}^t(c^t(\bar{\tau}^t(x)) = 0 \tag{2.39}$$

for every t. Using the fact that $\hat{t}^t(c^t(\bar{\tau}^t(x)) = \frac{\partial c^t}{\partial \tau}(\bar{\tau}^t(x))$ has unit length, the time derivative of (2.39) reads

$$-v^t(\pi^t(x)) \cdot \hat{t}^t(\pi^t(x)) - \frac{\partial \bar{\tau}^t}{\partial t} + \phi^t(x)\hat{n}^t(\pi^t(x)) \cdot \left(\frac{\partial v^t}{\partial \tau}(\pi^t(x)) + \kappa^t(\pi^t(x))\hat{n}^t(\pi^t(x))\frac{\partial \bar{\tau}^t}{\partial t}\right) = 0. \tag{2.40}$$

Together, relations (2.38) and (2.40) provide enough information to solve for the normal and tangential components of $\frac{\partial \pi^t}{\partial t}(x)$.

The normal component of $\frac{\partial \pi^t}{\partial t}(x)$ is obtained easily by dotting (2.38) with $\hat{n}^t(\pi^t(x))$, resulting in

$$\frac{\partial \pi^t}{\partial t}(x) \cdot \hat{n}^t(\pi^t(x)) = v_n^t(\pi^t(x)).$$

To compute the tangential component $\sigma^t(x) := \frac{\partial \pi^t}{\partial t} s(x) \cdot \hat{t}^t(\pi^t(x))$, take the dot product of (2.38) with $\hat{t}^t(\pi^t(x))$ and simplify (2.40) to obtain the following system of equations in two unknowns $\sigma^t(x)$

and $\frac{\partial \bar{\tau}^t}{\partial t}$:

$$v^t(\pi^t(x)) \cdot \hat{t}(\pi^t(x)) + \frac{\partial \bar{\tau}^t}{\partial t}(x) = \sigma^t(x)$$
$$-v^t(\pi^t(x)) \cdot \hat{t}(\pi^t(x)) - \frac{\partial \bar{\tau}^t}{\partial t}(x) + \phi^t(x)\hat{n}^t(\pi^t(x)) \cdot \frac{\partial v^t}{\partial \tau}(\pi^t(x)) + \kappa^t(\pi^t(x))\phi^t(x)\frac{\partial \bar{\tau}^t}{\partial t}(x) = 0.$$

Solving this system and invoking (2.34) leads to (2.36). □

Remark. The restriction $\phi^t(x)\kappa^t(\pi^t(x)) < 1$ in the preceding proposition is mild. In general, $\phi^t(x)\kappa^t(\pi^t(x)) \leq 1$ whenever $\pi^t(x)$ is uniquely defined. Indeed, since $|x - c^t(\tau)|^2$ is minimal at $\tau = \bar{\tau}^t(x)$, it follows that

$$0 \leq \frac{\partial^2}{\partial \tau^2}\bigg|_{\tau=\bar{\tau}^t(x)} |x - c^t(\tau)|^2 = 2(1 - \phi^t(x)\kappa^t(\pi^t(x))).$$

The assumption of strict inequality rules out degenerate cases in which $\frac{\partial^2}{\partial \tau^2}\Big|_{\tau=\bar{\tau}^t(x)} |x - c^t(\tau)|^2 = 0$.

Chapter 3

Unified Analysis of Finite Element Methods for Problems with Moving Boundaries

3.1 Introduction

This chapter develops a unified analytical framework for establishing the convergence properties of a wide class of numerical methods for moving-boundary problems. This class includes, as special cases, schemes based on universal meshes as well as conventional ALE schemes. We do so by studying an abstract parabolic problem posed on a moving domain with prescribed evolution, discretized in space with a finite element space defined over a moving mesh that conforms to the domain at all times. The moving mesh is assumed to evolve smoothly in time, except perhaps at a finite number of remeshing times where the solution is transferred between finite element spaces via a projection.

It is easy to see that conventional ALE schemes fit into the class of methods so described. In these schemes, the deformation of the mesh is commonly constructed by solving a system of equations, such as those of linear elasticity, for the nodal positions [52, 78, 80]. In addition, the number of instants at which remeshing is performed during the course of a given simulation does not change (or, at the very least, remains bounded) as the spatial discretization is refined. What is perhaps less obvious is that schemes based on universal meshes fit into this framework. This observation was made in Chapter 2, Section 2.1, where it was remarked that schemes based on universal meshes resemble ALE schemes with a peculiar mesh motion strategy and regular, systematic remeshing. Namely, the mesh motion is derived from small deformations of a periodically updated reference subtriangulation of the universal mesh, and the mesh deformations deviate from the identity only in a band of elements near the moving boundary. Furthermore, the number of number of instants

at which "remeshing" (updating the reference subtriangulation) is performed during the course of a given simulation grows unboundedly under mesh refinement.

An important feature of our analysis is that it applies to both of the settings described above, even though the ultimate convergence orders of the two approaches with respect to the mesh spacing differ markedly. We accomplish this in a unified manner by leaving the precise choice of the mesh motion strategy, remeshing times, finite elements, and projector unspecified throughout much of the analysis.

In light of the relationship between conventional ALE schemes and schemes based on universal meshes, we abuse terminology in this chapter by referring to both as *deforming-mesh methods*. This marks a slight departure from the language adopted earlier in this thesis, where the term was reserved for conventional ALE schemes only. We hope that this change in terminology, which reflects a maturer perspective developed in Chapter 2, does not cause confusion.

The primary contributions of this chapter are presented in two theorems and one corollary. The first is Theorem 3.4.1, which provides an abstract upper bound on the L^2-norm of the error between the exact and semidiscrete solutions at a fixed positive time, expressed in terms of the total variation in time of a quantity ρ that measures difference between the exact solution at time t and its elliptic projection onto the finite element space at time t. The second is Theorem 3.4.2, which bounds the material time derivative of ρ. Finally, Corollary 3.4.3 illustrates an application of Theorems 3.4.1 and 3.4.2 by exhibiting an error estimate of optimal order in the mesh spacing for ALE schemes under mild assumptions on the nature of the mesh deformation and the regularity of the exact solution and the moving domain. An analogous application of the abstract theory to universal meshes is performed later in this thesis in Chapter 5.

The use of the elliptic projection in the a priori error analysis of finite element methods for parabolic problems on fixed domains is a well-established technique used heavily in the text of Thomee [132]. Our analysis is, to some extent, a generalization of this strategy to the setting in which the domain is time-dependent and the finite element spaces are permitted to change abruptly finitely many times.

This chapter is organized as follows. We begin in Section 3.2 by giving a preview of our results, postponing the technical details to allow for a simple presentation of the main ideas. The analysis begins in Section 3.3, where we state an abstract parabolic problem on a moving domain and delineate a class of numerical methods to be analyzed. In Section 3.4, we present the statements of Theorem 3.4.1, Theorem 3.4.2, and Corollary 3.4.3. We prove Theorem 3.4.1 in Sections 3.5, and we prove Theorem 3.4.2 and Corollary 3.4.3 in Section 3.6. In Section 3.7, we check the hypotheses of Corollary 3.4.3 when the PDE under consideration is the diffusion equation and the mesh motion under consideration satisfies certain uniform bounds on its velocity. Some concluding remarks are given in Section 3.8.

3.2 Preview of Results

In this section, we present an overview of our main results in an unrigorous manner that highlights the key ideas of the theorems without dwelling on their technicalities and the precise hypotheses under which they hold.

For simplicity of exposition, we consider (in this section only) the problem of finding $u(x,t)$ such that

$$\begin{aligned} \frac{\partial u}{\partial t}(x,t) - \Delta_x u(x,t) = f(x,t) \quad & x \in \Omega^t, \qquad 0 < t < T \\ u(x,0) = u^0(x) \quad & x \in \Omega^0 \\ u(x,t) = 0 \quad & x \in \partial\Omega^t, \quad 0 < t < T, \end{aligned}$$

where $\Omega^t \subset \mathbb{R}^d$, $d \geq 1$, is a moving domain, and f and u^0 are given.

A deforming-mesh method seeks a numerical approximation

$$u_h(x,t) = \sum_a \mathbf{u}_a(t) n_a^t(x)$$

to $u(x,t)$ belonging to a finite element space $\mathcal{V}_h^t = \text{span}\{n_a^t\}_a$ for each t, where the shape functions $\{n_a^t\}_a$ spanning $\mathcal{V}_h^t$ are associated with a moving mesh $\mathcal{T}_h^t$ that conforms to Ω^t and has maximum element diameter $\leq h$ for all times t. We assume that this mesh evolves smoothly over a finite number N of intervals $(t^{n-1}, t^n]$, $n = 1, 2, \ldots, N$, which form a partition of $(0, T]$, but we allow for abrupt changes in the mesh at each t^n, $n = 1, 2, \ldots, N$. We refer to these instants as *remeshing times*. We allow the number N of remeshing times, as well as their values, to depend on h.

Over each interval $t^{n-1} < t \leq t^n$, the mesh $\mathcal{T}_h^t$ can be viewed as the image of a mesh of $\Omega^{t^{n-1}}$ under a bijective map

$$\varphi_h^t : \Omega^{t^{n-1}} \to \Omega^t, \quad t^{n-1} < t \leq t^n.$$

Often this map is referred to as an ALE map in the literature [23], although we avoid this terminology since we allow for more general mesh deformations that need not derive from traditional approaches that are characteristic of ALE schemes. We denote by

$$v_h(\varphi_h^t(X), t) = \left.\frac{\partial}{\partial t}\right|_X \varphi_h^t(X,t), \quad X \in \Omega^{t^{n-1}},\ t^{n-1} < t \leq t^n$$

the velocity of the moving mesh $\mathcal{T}_h^t$.

The derivative of a function in the direction of the mesh motion is given by its *material time derivative*

$$D_t u(\varphi_h^t(X), t) = \left.\frac{\partial}{\partial t}\right|_X U(X,t), \quad X \in \Omega^{t^{n-1}},\ t^{n-1} < t \leq t^n,$$

where $U(\cdot,t) = u(\varphi_h^t(\cdot),t)$.

A deforming-mesh method generates u_h by solving a finite element semidiscretization of an ALE formulation of the governing equations over each interval $(t^{n-1},t^n]$ and transferring the solution between differing meshes at the remeshing times t^n via a projection. That is, u_h is generated by solving a sequence of initial-value problems

$$m^t(D_t u_h, w_h) - b_h^t(u_h,w_h) + a^t(u_h,w_h) = m^t(f,w_h) \quad \forall w_h \in \mathcal{V}_h^t,\ t^{n-1} < t \le t^n,$$

where

$$\begin{aligned} m^t(u,w) &= \int_{\Omega^t} uw\,dx, \\ b_h^t(u,w) &= \int_{\Omega^t} (v_h \cdot \nabla_x u) w\,dx, \\ a^t(u,w) &= \int_{\Omega^t} \nabla_x u \cdot \nabla_x w\,dx, \end{aligned}$$

and the initial condition $u_h(\cdot,t_+^{n-1}) := \lim_{t\searrow t^{n-1}} u_h(\cdot,t)$ comes from a projection of $u_h(\cdot,t^{n-1})$ (or u^0 if $n=0$) onto $\mathcal{V}_h^{t_+^{n-1}}$. Namely,

$$u_h(\cdot,t_+^{n-1}) = p_h^{t_+^{n-1}} u_h(\cdot,t^{n-1})$$

when $n>0$ and

$$u_h(\cdot,t_+^{n-1}) = p_h^{t_+^{n-1}} u^0$$

when $n=0$, where p_h^t is a projector onto $\mathcal{V}_h^t$. We assume that this projector is linear, surjective, and stable in the sense that there exists a constant C_p such that

$$\|p_h^{t_+^n} w\| \le C_p \|w\|$$

for every $w \in \mathcal{V}_h^{t^n} + \mathcal{V}_h^{t_+^n}$, where $\|\cdot\|$ denotes the L^2-norm on the appropriate domain (here Ω^{t^n}).

The first theorem that we prove in this chapter (Theorem 3.4.1) is an abstract estimate for the error $\|u(\cdot,T) - u_h(\cdot,T)\|$, expressed in terms of an *elliptic projection* of $u(\cdot,t)$ onto $\mathcal{V}_h^t$. This elliptic projection $r_h^t u \in \mathcal{V}_h^t$ is defined by the relation

$$a_h^t(r_h^t u, w_h) = a_h^t(u,w_h) \quad \forall w_h \in \mathcal{V}_h^t,$$

where

$$a_h^t(u,w) = a^t(u,w) - b_h^t(u,w) + \kappa m^t(u,w)$$

and $\kappa \ge 0$ is a constant chosen such that a_h^t is coercive, uniformly in h and t.

Theorem 3.4.1 states that, under suitable hypotheses,

$$\|u(\cdot,T) - u_h(\cdot,T)\| \leq C_p^N \|\rho(0_+)\| + \sum_{n=1}^{N} C_p^{N-n} \left(\int_{t^{n-1}}^{t^n} e^{\kappa t} \|D_t \rho(t)\| \, dt + e^{\kappa t^n} \|\rho(t_+^n) - \rho(t^n)\| \right),$$

where

$$\rho(t) = e^{-\kappa t}(r_h^t u(\cdot,t) - u(\cdot,t))$$

and $\rho(T_+) := 0$. In other words, a study of the error at time T reduces to an analysis of the (scaled) difference between the exact solution $u(\cdot,t)$ at times $t \in (0,T]$ and its elliptic projection onto the current finite element space. The error bound resembles the total variation of ρ: a (weighted) time integral of the norm of $D_t\rho$, plus a (weighted) summation of the jumps in ρ across the times of remeshing, where the weights are related to the constant κ and the stability constant C_p of the projector. The time integral of $\|D_t\rho\|$ encapsulates the error introduced by Galerkin projection, while the jumps in ρ encapsulate the errors introduced by projecting onto a new finite element space at each remeshing time t^n.

Our second theorem (Theorem 3.4.2) provides an upper bound for $\|D_t\rho\|$ that can be computed for a given mesh motion and finite element space using knowledge of two properties: the approximation power of the finite element space and the regularity of the mesh's evolution. The regularity of the mesh's evolution will be measured in terms of a bilinear form Λ_h^t which resembles, in loose language, the Lie derivative of a_h^t along the direction of the mesh motion. Namely, it satisfies

$$\frac{d}{dt} a_h^t(u,w) = a_h^t(D_t u, w) + a_h^t(u, D_t w) + \Lambda_h^t(u,w)$$

for all sufficiently smooth u and w. Theorem 3.4.2 states that

$$\|D_t\rho(t)\| \leq C\Big[h \inf_{w_h \in \mathcal{V}_h^t} \|D_t(e^{-\kappa t}u) - w_h\|_{1,2,\Omega^t} + c_\eta(\Lambda_h^t)\left(\|\rho\|_{0,\eta,\Omega^t} + h|\rho|_{1,\eta,\Omega^t}\right)\Big],$$

for every $\eta \in [2,\infty]$, where $c_\eta(\Lambda_h^t)$ is a quantity whose explicit dependence on Λ_h^t and η is provided in the statement of Theorem 3.4.2. Here, $\|\cdot\|_{0,\eta,\Omega^t}$, $\|\cdot\|_{1,\eta,\Omega^t}$, and $|\cdot|_{1,\eta,\Omega^t}$ denote the $L^\eta(\Omega^t)$-norm, $W^{1,\eta}(\Omega^t)$-norm, and $W^{1,\eta}(\Omega^t)$-seminorm, respectively. The appearance of $c_\eta(\Lambda_h^t)$ in the estimate above reveals the influence of the mesh's evolution on the method's accuracy, and the estimation of the scaling of $c_\eta(\Lambda_h^t)$ with respect to h plays a fundamental role in the determination of the order of accuracy of a given scheme.

Theorems 3.4.1 and 3.4.2 provide the key ingredients needed to estimate the order of accuracy of a wide range of numerical methods belonging to the class of schemes we have detailed above. A simple illustration of this fact is provided in Corollary 3.4.3, which presents a concrete bound for the error when using piecewise polynomial finite elements over a shape-regular mesh whose motion is representative of a typical ALE scheme. Namely, if the finite element spaces consist of continuous

functions that are elementwise polynomials of degree $\leq r-1$ for an integer $r \geq 2$, and if the mesh velocity satisfies certain uniform bounds under refinement that are characteristic of ALE schemes, then Corollary 3.4.3 states that, under suitable hypotheses on the exact solution and the moving domain,

$$\|u(\cdot,T) - u_h(\cdot,T)\| \leq Ch^r$$

for a constant C independent of h.

Another situation to which Theorems 3.4.1 and 3.4.2 may be applied is to a mesh motion obtained from a universal mesh. As described in Chapter 2, this strategy utilizes a background triangulation of an ambient domain $\mathcal{D} \supset \Omega^t$, $0 \leq t \leq T$, to construct a conforming mesh for the immersed domain at all times using small deformations of a periodically updated reference subtriangulation of the background mesh. In that setting, the number N of "remeshing" times (the periodic updates of the reference subtriangulation) scales like h^{-1}, the mesh velocity is nonzero only in a region of measure $O(h)$, and its spatial gradient scales like h^{-1}. When such a strategy is used with piecewise polynomial finite elements of degree $\leq r-1$, it is possible to show that (under suitable regularity assumptions) the quantity $\|D_t\rho\|_{0,2,\Omega^t}$ associated with the mesh motion under consideration scales like $h^{r-1/2}$, whereas the jumps $\|\rho(t_+^n) - \rho(t^n)\|_{0,2,\Omega^{t^n}}$ scale like $h^{r+1/2}$, up to a logarithmic factor if $r = 2$. This leads to an error estimate for universal meshes that is suboptimal by half an order in the L^2-norm. Namely, under suitable hypotheses on the exact solution and the moving domain,

$$\|u(\cdot,T) - u_h(\cdot,T)\| \leq C\ell_r(h)h^{r-1/2}$$

for a constant C independent of h. Here, $\ell_r(h) := \log(h^{-1})$ if $r = 2$ and $\ell_r(h) := 1$ otherwise. We postpone the details of the latter estimate to Chapter 5, since its proof is less immediate than that for ALE schemes.

3.3 Continuous Problem and its Discretization

This section and those that follow are devoted to the rigorous statements and proofs of the results that were sketched out in Section 3.2.

The present section details the moving-boundary problem under consideration and the class of numerical methods to be analyzed. We begin by stating the continuous problem and its weak formulation in Section 3.3.1. We discuss its spatial discretization via finite elements in Section 3.3.2. Finally, in Section 3.3.3, we present the class of numerical methods under scrutiny.

3.3.1 Continuous Problem

As indicated in Section 3.2, this chapter considers a moving-boundary problem posed on an evolving domain $\Omega^t \subset \mathbb{R}^d$, $t \in [0,T]$, $d \geq 1$, where Ω^t is open, bounded, and Lipchitz for every $t \in [0,T]$ and

T is a fixed positive number. We denote by $\Omega \subset \mathbb{R}^{d+1}$ the spacetime domain

$$\Omega = \{(x,t) \in \mathbb{R}^{d+1} \mid x \in \Omega^t, 0 < t < T\}.$$

To state precisely the moving-boundary problem under consideration, we require the following notation and definitions.

Notation. For $s \geq 0$, $1 \leq p \leq \infty$, and $D = \Omega^t$ or $D = \Omega$, we denote by $W^{s,p}(D)$ the Sobolev space of differentiability s and integrability p, equipped with the norm $\|\cdot\|_{s,p,D}$ and semi-norm $|\cdot|_{s,p,D}$. We denote $H^s(D) = W^{s,2}(D)$ for every $s \geq 0$ and $L^p(D) = W^{0,p}(D)$ for every $1 \leq p \leq \infty$. We use $H_0^1(D)$ to denote the space of functions in $H^1(D)$ with vanishing trace on ∂D, and we denote by $H^{-1}(D)$ its dual. We use $W^{s,p}(D)^d$, $L^p(D)^d$, $H^s(D)^d$, and $H^{-1}(D)^d$ to denote the analogous spaces of vector valued functions $u : D \to \mathbb{R}^d$.

For a given Banach space B and integer $s \geq 0$, we denote the Bochner spaces

$$W^{s,p}(0,T;B) = \left\{ U : (0,T) \to B \mid \int_0^T \sum_{i=0}^{s} \|U^{(i)}(t)\|_B^p \, dt < \infty \right\}, \quad 1 \leq p < \infty,$$
$$W^{s,\infty}(0,T;B) = \left\{ U : (0,T) \to B \mid \sup_{0<t<T} \sum_{i=0}^{s} \|U^{(i)}(t)\|_B < \infty \right\},$$

where $U^{(i)}$ denotes the i^{th} weak time derivative of a Banach space-valued function U. We denote $H^s(0,T;B) = W^{s,2}(0,T;B)$ for every $s \geq 0$ and $L^p(0,T;B) = W^{0,p}(0,T;B)$ for every $1 \leq p \leq \infty$.

For notational convenience, we denote $\mathcal{V}^t = H_0^1(\Omega^t)$, and we define the space

$$\mathcal{U} = \{U \in L^2(0,T;H_0^1(\Omega^0)) \mid U^{(1)} \in L^2(0,T;H^{-1}(\Omega^0))\}.$$

Note that $\mathcal{U} \subset C([0,T], L^2(\Omega^0))$ [46, Chapter 5.9, Theorem 3], the space of continuous functions in $[0,T]$ taking values in $L^2(\Omega^0)$.

Finally, we introduce the notion of a regular domain deformation (see also [23, Definition 2.1]).

Definition 3.3.1. *For $0 \leq \tau_0 < \tau_1 \leq T$, let $\{\varphi^t : \Omega^{\tau_0} \to \Omega^t \mid \tau_0 < t \leq \tau_1\}$ be a family of continuous maps. We say that $\{\varphi^t \mid \tau_0 < t \leq \tau_1\}$ is a* regular domain deformation *over $(\tau_0, \tau_1]$ if the following conditions are satisfied:*

(3.3.1.i) The map $t \mapsto \varphi^t$ belongs to $W^{1,\infty}\left(\tau_0, \tau_1; W^{1,\infty}(\Omega^{\tau_0})^d\right)$.

(3.3.1.ii) For every $t \in (\tau_0, \tau_1]$, φ^t is surjective.

(3.3.1.iii) There exists $C > 0$ independent of t, X, and Y such that for every $t \in (\tau_0, \tau_1]$ and every $X, Y \in \Omega^{\tau_0}$,

$$\|\varphi^t(X) - \varphi^t(Y)\|_{\mathbb{R}^d} \geq C\|X - Y\|_{\mathbb{R}^d},$$

where $\|\cdot\|_{\mathbb{R}^d}$ *denotes the Euclidean distance in* $\mathbb{R}^d$.

(3.3.1.iv) $\varphi^{\tau_0+} := \lim_{t \searrow \tau_0} \varphi^t = i$, *where* i *denotes the identity.*

Later in this chapter, we reuse the letter C to denote a generic constant, not necessarily the same at each occurrence, whose dependence (or lack thereof) on other parameters of interest will be specified as needed.

Note that if $\{\varphi^t \mid \tau_0 < t \leq \tau_1\}$ is a regular domain deformation, then conditions (3.3.1.ii-3.3.1.iii) ensure that for each $t \in (\tau_0, \tau_1]$, φ^t is bijective with Lipschitz inverse. Furthermore, a function $u : \Omega^t \to \mathbb{R}$ belongs to $\mathcal{V}^t = H_0^1(\Omega^t)$ if and only if $u \circ \varphi^t \in \mathcal{V}^{\tau_0} = H_0^1(\Omega^{\tau_0})$; see [23, Section 2.1].

As a regularity requirement on the domain's evolution, we shall assume the existence of a regular domain deformation $\{\psi^t : \Omega^0 \to \Omega^t \mid 0 < t \leq T\}$ for which the map $(X, t) \mapsto \psi^t(X)$ belongs to $C^2(\Omega^0 \times [0, T], \mathbb{R}^d)$. We denote

$$\mathcal{W} = \{u : \Omega \to \mathbb{R} \mid t \mapsto u(\psi^t(\cdot), t) \in \mathcal{U}\},$$
$$\mathcal{F} = \{f : \Omega \to \mathbb{R} \mid t \mapsto f(\psi^t(\cdot), t) \in C([0, T], L^2(\Omega^0))\}.$$

Moving-boundary problem. Our interest is in problems of the following form: Given $f \in \mathcal{F}$ and $u^0 \in \mathcal{V}^0$, find $u \in \mathcal{W}$ such that $u(\cdot, 0) = u^0$ and

$$m^t(\dot{u}, w) + a^t(u, w) = m^t(f, w) \quad \forall w \in \mathcal{V}^t \tag{3.1}$$

for a.e. $t \in (0, T)$, where $\dot{u} := \frac{\partial u}{\partial t}$,

$$m^t(u, w) := \int_{\Omega^t} uw \, dx,$$

and $a^t : \mathcal{V}^t \times \mathcal{V}^t \to \mathbb{R}$ is a time-dependent bilinear form satisfying the following hypotheses:

(3.3.iv) There exist positive constants M_0 and α_0 independent of t such that for every $t \in [0, T]$ and every $u, w \in \mathcal{V}^t$,

$$a^t(u, u) \geq \alpha_0 \|u\|^2_{1,2,\Omega^t},$$
$$|a^t(u, w)| \leq M_0 \|u\|_{1,2,\Omega^t} \|w\|_{1,2,\Omega^t}.$$

(3.3.v) For any regular domain deformation $\{\varphi^t : \Omega^0 \to \Omega^t \mid 0 < t \leq T\}$, there exists $C > 0$ such that for every $U, W \in \mathcal{V}^0$, the map

$$t \mapsto y(t) := a^t(U \circ (\varphi^t)^{-1}, W \circ (\varphi^t)^{-1})$$

is Lipschitz with

$$|y(\tau_1) - y(\tau_0)| \leq C\|U\|_{1,2,\Omega^0}\|W\|_{1,2,\Omega^0}|\tau_1 - \tau_0| \tag{3.2}$$

for every $\tau_0, \tau_1 \in (0, T]$.

We shall assume the existence of a unique solution $u \in \mathcal{W}$ to (3.1) satisfying the additional regularity

$$\int_0^T \|u\|_{2,2,\Omega^t} + \|\dot{u}\|_{1,2,\Omega^t}\, dt < \infty. \tag{3.3}$$

Note that this assumption guarantees that for any regular domain deformation $\{\varphi^t : \Omega^0 \to \Omega^t \mid 0 < t \leq T\}$, the map $t \mapsto u(\varphi^t(\cdot), t)$ belongs to $W^{1,1}(0, T; H^1_0(\Omega^0))$. Furthermore, the embedding $W^{1,1}(0, T; H^1_0(\Omega^0)) \subset C([0, T], H^1_0(\Omega^0))$ [46, Chapter 5.9, Theorem 2] ensures that the trace of u on any constant-time slice Ω^t is a well-defined member of $\mathcal{V}^t$; that is, $u(\cdot, t) \in \mathcal{V}^t$ for every $t \in [0, T]$.

For $0 \leq \tau_0 \leq \tau_1 \leq T$, let $\Phi^{\tau_1}_{\tau_0} : \mathcal{V}^{\tau_0} \to \mathcal{V}^{\tau_1}$ denote the flow of the differential equation (3.1). That is, if $y \in \mathcal{V}^{\tau_0}$ and u solves (3.1) with the initial condition $u(\cdot, \tau_0) = y$, then $\Phi^{\tau_1}_{\tau_0} y = u(\cdot, \tau_1)$.

3.3.2 Spatial Discretization

In what follows, we present the general form of a finite element spatial discretization of (3.1) obtained via Galerkin projection onto an evolving finite element space. It is assumed that the finite element space is associated with a deforming mesh that conforms to the domain at all times and evolves smoothly in time, except at a finite number of remeshing times where the solution is transferred between finite element spaces via a projection. We use the term *mesh of* Ω^t to refer to a finite collection of compact, connected, Lipschitz sets (*elements*) with non-empty interior that provide a partition of Ω^t. For an element K of a mesh of Ω^t, we denote its diameter by h_K.

We begin by introducing the notion of a deforming mesh, which we allow to evolve in a discontinuous fashion.

Definition 3.3.2. *We say that* $\{\mathcal{T}^t_h \mid 0 < t \leq T\}$ *is a* deforming mesh with remeshing times $0 = t^0 < t^1 < \cdots < t^N = T$ and mesh spacing h *if:*

(3.3.2.i) *For each* $t \in (0, T]$, $\mathcal{T}^t_h$ *is a mesh of* Ω^t.

(3.3.2.ii) $h = \sup_{0<t\leq T} \max_{K\in\mathcal{T}^t_h} h_K$.

(3.3.2.iii) *For every* $n = 1, 2, \ldots, N$, *there exists a mesh* $\mathcal{T}^{t^{n-1}_+}_h$ *of* $\Omega^{t^{n-1}}$ *and a regular domain deformation* $\{\varphi^t_h : \Omega^{t^{n-1}} \to \Omega^t \mid t^{n-1} < t \leq t^n\}$ *such that for every* $t \in (t^{n-1}, t^n]$,

$$K \in \mathcal{T}^{t^{n-1}_+}_h \iff \varphi^t_h(K) \in \mathcal{T}^t_h.$$

For a given deforming mesh $\{\mathcal{T}_h^t\}_t$, we denote by $v_h : \Omega \to \mathbb{R}^d$ the vector field

$$v_h(\varphi_h^t(X), t) = \left.\frac{\partial}{\partial t}\right|_X \varphi_h^t(X), \quad X \in \Omega^{t^{n-1}},\ t \in (t^{n-1}, t^n].$$

We refer to v_h as the *mesh velocity* in the sequel. For a function $w : \Omega \to \mathbb{R}$, we denote by $D_t w : \Omega \to \mathbb{R}$ the function

$$D_t w(\varphi_h^t(X), t) = \left.\frac{\partial}{\partial t}\right|_X W(X, t), \quad X \in \Omega^{t^{n-1}},\ t \in (t^{n-1}, t^n]$$

whenever the right-hand side is defined, where $W(\cdot, t) = w(\varphi_h^t(\cdot), t)$. We refer to $D_t w$ as the *material time derivative* of w. The chain rule for weakly differentiable functions [145, Theorem 2.2.2] shows that if $w \in W^{1,1}(\Omega)$, then $D_t w$ exists and the well-known relation

$$D_t w = \dot{w} + v_h \cdot \nabla_x w$$

holds.

Finally, we introduce finite element spaces that evolve in concert with $\{\mathcal{T}_h^t\}_t$.

Definition 3.3.3. *Let $\{\mathcal{T}_h^t \mid 0 < t \le T\}$ be a deforming mesh with remeshing times $0 = t^0 < t^1 < \cdots < t^N = T$. We say that $\{\mathcal{V}_h^t \mid 0 < t \le T\}$ is an* evolving finite element space *over $\{\mathcal{T}_h^t\}_t$ if:*

(3.3.3.i) For every $0 < t \le T$, $\mathcal{V}_h^t$ is a finite-dimensional subspace of $\mathcal{V}^t$.

(3.3.3.ii) For every $n = 1, 2, \ldots, N$ there exist functions $\{N_a\}_a$ such that the functions

$$n_a^t = N_a \circ (\varphi_h^t)^{-1} \tag{3.4}$$

form a basis for $\mathcal{V}_h^t$ for each $t \in (t^{n-1}, t^n]$, where φ_h^t is the map described in (3.3.2.iii).

We denote $\mathcal{V}_h^{t_+^{n-1}} = \operatorname{span}\{N_a\}_a$ and remark that in general, $\mathcal{V}_h^{t_+^{n-1}} \neq \mathcal{V}_h^{t^{n-1}}$.

Galerkin projection. On each interval $(t^{n-1}, t^n]$, a Galerkin projection of (3.1) onto an evolving finite element space $\{\mathcal{V}_h^t\}_t$ reads: Find $u_h \in \mathcal{V}_h^{(t^{n-1}, t^n]}$ such that

$$m^t(\dot{u}_h, w_h) + a^t(u_h, w_h) = m^t(f, w_h) \quad \forall w_h \in \mathcal{V}_h^t \tag{3.5}$$

for every $t \in (t^{n-1}, t^n]$, where

$$\mathcal{V}_h^{(t^{n-1}, t^n]} = \left\{ (x, t) \mapsto \sum_a \mathbf{u}_a(t) n_a^t(x) \;\middle|\; \mathbf{u}_a = \bar{\mathbf{u}}_a|_{(t^{n-1}, t^n]} \text{ for some } \bar{\mathbf{u}}_a \in C^1([t^{n-1}, t^n]) \right\}.$$

Expanding u_h as a linear combination of the basis functions (3.4) shows that (3.5) is equivalent to a linear system of ordinary differential equations which, via an application of the Cauchy-Lipschitz theorem [3], admits a unique solution $u_h \in \mathcal{V}_h^{(t^{n-1},t^n]}$ for any initial condition $u_h(\cdot, t_+^{n-1}) \in \mathcal{V}_h^{t_+^{n-1}}$.

For $t^{n-1} < \tau_0 \leq \tau_1 \leq t^n$, $1 \leq n \leq N$, let $\Phi_{h,\tau_0}^{\tau_1} : \mathcal{V}_h^{\tau_0} \to \mathcal{V}_h^{\tau_1}$ denote the flow of the differential equation (3.5). That is, if $y_h \in \mathcal{V}_h^{\tau_0}$ and u_h solves (3.5) with the initial condition $u_h(\cdot, \tau_0) = y_h$, then $\Phi_{h,\tau_0}^{\tau_1} y_h = u_h(\cdot, \tau_1)$.

Remark. Trivially, (3.5) is equivalent to the problem: Find $u_h \in \mathcal{V}_h^{(t^{n-1},t^n]}$ such that

$$m^t(D_t u_h, w_h) - b_h^t(u_h, w_h) + a^t(u_h, w_h) = m^t(f, w_h) \quad \forall w_h \in \mathcal{V}_h^t \tag{3.6}$$

for every $t \in (t^{n-1}, t^n]$, where

$$b_h^t(u, w) = \int_{\Omega^t} (v_h \cdot \nabla_x u) w \, dx. \tag{3.7}$$

Of course, it also holds that the solution u to the continuous problem (3.1) satisfies

$$m^t(D_t u, w) - b_h^t(u, w) + a^t(u, w) = m^t(f, w) \quad \forall w \in \mathcal{V}^t \tag{3.8}$$

for a.e. $t \in (t^{n-1}, t^n]$. These formulations are the well-known ALE formulations familiar to ALE practitioners.

3.3.3 Numerical Method

We now fix an evolving finite element space $\{\mathcal{V}_h^t \subset \mathcal{V}^t \mid 0 < t \leq T\}$ with remeshing times $0 = t^0 < t^1 < \ldots t^N = T$ and study numerical methods obtained by solving (3.6), (or, equivalently, (3.5)) over each interval $(t^{n-1}, t^n]$ and transferring the solution across remeshing times via a projection. We view $\{\mathcal{V}_h^t\}_t$ as a member of a family of evolving finite element spaces parametrized by $h \in (0, h_0]$, where h_0 is a fixed positive constant. Note that we allow the number N of remeshing times t^n, as well as the values of t^n, to depend on h. When we wish to emphasize this dependence, we write $N(h)$ and $t^n(h)$, respectively; otherwise, we simply write N and t^n (with the dependence on h implied).

Projector onto finite element spaces. To transfer the solution $u_h(\cdot, t^n) \in \mathcal{V}_h^{t^n}$ to $\mathcal{V}_h^{t_+^n}$ at each remeshing time t^n, we assume that a linear projector

$$p_h^{t_+^n} : \mathcal{V}_h^{t^n} + \mathcal{V}_h^{t_+^n} \to \mathcal{V}_h^{t_+^n},$$

is adopted for each $n = 1, 2, \ldots, N-1$ and a linear projector $p_h^{0_+} : \mathcal{V}^0 \to \mathcal{V}_h^{0_+}$ is adopted when $n = 0$.

We make the following hypotheses on the projectors:

(3.4.1.i) The projectors are surjective; equivalently, $p_h^{t_+^n}\Big|_{\mathcal{V}_h^{t_+^n}} = i$ for every $h \le h_0$ and every $n = 0, 1, \dots, N-1$, where i denotes the identity.

(3.4.1.ii) There exists a constant C_p independent of h such that for every $h \le h_0$ and every $n = 0, 1, \dots, N-1$, the inequality

$$\|p_h^{t_+^n} w\|_{0,2,\Omega^{t^n}} \le C_p \|w\|_{0,2,\Omega^{t^n}}$$

holds for every $w \in \mathcal{V}_h^{t^n} + \mathcal{V}_h^{t_+^n}$ (if $n > 0$) and every $w \in \mathcal{V}^0$ (if $n = 0$).

Recursions. For $n = 1, 2, \dots, N$, we denote by

$$\mathfrak{f}^n : \mathcal{V}^{t^{n-1}} \to \mathcal{V}^{t^n}$$

the advancement of the solution to (3.8) (or, equivalently, (3.1)) from $t = t^{n-1}$ to $t = t^n$, i.e. $\mathfrak{f}^n = \Phi_{t^{n-1}}^{t^n}$, and by

$$\mathfrak{f}_h^n : \mathcal{V}_h^{t_+^{n-1}} \to \mathcal{V}_h^{t^n}$$

the advancement of the semidiscrete solution to (3.6), (or, equivalently, (3.5)) from $t = t_+^{n-1}$ to $t = t^n$, i.e. $\mathfrak{f}_h^n = \Phi_{h,t_+^{n-1}}^{t^n}$.

In terms of the operators defined above, the values of the exact solution $u^n := u(\cdot, t^n)$ at the temporal nodes satisfy the recursion

$$u^n = \mathfrak{f}^n u^{n-1} \tag{3.9}$$

with the initial condition

$$u^0 = u(\cdot, 0). \tag{3.10}$$

In this chapter, we study numerical approximations $u_h^n \approx u^n$ generated by recursions of the form

$$u_h^n = \mathfrak{f}_h^n p_h^{t_+^{n-1}} u_h^{n-1} \tag{3.11}$$

with the initial condition

$$u_h^0 = u(\cdot, 0). \tag{3.12}$$

Note that $u_h^n \in \mathcal{V}_h^{t^n}$ for every $n \ge 1$. In contrast, $u_h^0 \in \mathcal{V}^0$ (though the numerical algorithm immediately projects u_h^0 onto $\mathcal{V}_h^{0+}$).

3.4 Statement of Results

3.4.1 Abstract Error Estimate

We now present an abstract estimate for the global error

$$\varepsilon^n = u^n - u_h^n$$

at $n = N$.

A statement of the estimate makes use of an *elliptic projector*

$$r_h^t : \mathcal{V}^t \to \mathcal{V}_h^t$$

associated with the bilinear form $a^t(u,w) - b_h^t(u,w)$, where b_h^t is given by (3.7). Since this bilinear form is not necessarily coercive, it is useful to consider a modified bilinear form

$$a_h^t(u,w) = a^t(u,w) - b_h^t(u,w) + \kappa m^t(u,w), \tag{3.13}$$

with $\kappa \geq 0$ chosen such that a_h^t is coercive uniformly in t and h. This is accomplished in Section 3.5.3, under the following assumption on the mesh velocity:

(3.4.1.iii) There exists v_{max} independent of h such that

$$\|v_h\|_{0,\infty,\Omega} \leq v_{max}$$

for every $h \leq h_0$.

Now define r_h^t for $t \in (0,T]$ via

$$a_h^t(r_h^t u - u, w_h) = 0 \quad \forall w_h \in \mathcal{V}_h^t. \tag{3.14}$$

Let

$$\rho(t) = e^{-\kappa t}(r_h^t u(\cdot,t) - u(\cdot,t)) \tag{3.15}$$

for $t \in (0,T]$. To simplify the forthcoming analysis, it is convenient to also define $\rho(0) = 0$ and $\rho(T_+) = 0$.

The following theorem will be proved in Section 3.5.

Theorem 3.4.1. *Let $\{u_h^n\}_{n=0}^N$ be generated by the recursion (3.11) with the initial condition (3.12), using an evolving finite element space $\{\mathcal{V}_h^t \mid 0 < t \leq T\}$ satisfying (3.4.1.iii) and projectors $\{p_h^{t_+^n}\}_{n=0}^{N-1}$*

satisfying (3.4.1.i-3.4.1.ii). Then for every $h \le h_0$, the error $\varepsilon^N = u(\cdot,T) - u_h^N$ satisfies

$$\|\varepsilon^N\|_{0,2,\Omega^T} \le \sum_{n=1}^{N} C_p^{N-n}\Big(\int_{t^{n-1}}^{t^n} e^{\kappa t}\|D_t\rho\|_{0,2,\Omega^t}\,dt + e^{\kappa t^n}\|\rho(t_+^n) - \rho(t^n)\|_{0,2,\Omega^{t^n}}\Big) + C_p^N\|\rho(0_+)\|_{0,2,\Omega^0}$$

with ρ given by (3.15) and κ given by (3.25).

3.4.2 Bound on $D_t\rho$

Our second theorem provides an upper bound for the L^2-norm of the material time derivative of $\rho(t) = e^{-\kappa t}(r_h^t u(\cdot,t) - u(\cdot,t))$. It will require the following additional hypotheses concerning elliptic regularity, the approximation properties of $\mathcal{V}_h^t$, and the mesh velocity v_h.

(3.4.2.i) There exists $C > 0$ independent of h and t such that for every $0 < t \le T$, every $h \le h_0$, and every $f \in L^2(\Omega^t)$, the solution $y \in \mathcal{V}^t$ to the problem

$$a_h^t(w,y) = m^t(f,w) \quad \forall w \in \mathcal{V}^t$$

satisfies

$$\|y\|_{2,2,\Omega^t} \le C\|f\|_{0,2,\Omega^t}. \tag{3.16}$$

(3.4.2.ii) There exists $C > 0$ independent of h and t such that for every $0 < t \le T$, every $h \le h_0$, and every $w \in H^2(\Omega^t) \cap \mathcal{V}^t$,

$$\inf_{w_h \in \mathcal{V}_h^t} \|w - w_h\|_{1,2,\Omega^t} \le Ch|w|_{2,2,\Omega^t}.$$

(3.4.2.iii) There exists $C > 0$ independent of h and t such that for every $h \le h_0$, every $n = 1,2,\dots,N$, and every $t \in (t^{n-1},t^n)$,

$$\|\dot{v}_h\|_{0,\infty,\Omega^t} \le C.$$

A statement of the theorem also requires the definition of a bilinear form $\Lambda_h^t : \mathcal{V}^t \times \mathcal{V}^t \to \mathbb{R}$ which embodies the time rate of change of a_h^t, constructed as follows. For a given $t \in (t^{n-1},t^n]$, let $u,w \in \mathcal{V}^t$. For each $h \le h_0$, associate with u and w a pair of functions $U \in \mathcal{V}^{t^{n-1}}$ and $W \in \mathcal{V}^{t^{n-1}}$ satisfying

$$U(X) = u(\varphi_h^t(X)), \quad W(X) = w(\varphi_h^t(X))$$

for every $X \in \Omega^{t^{n-1}}$. Now define

$$\Lambda_h^t(u,w) = \frac{d}{d\tau}\Big|_{\tau=t} A_h^\tau(U,W), \tag{3.17}$$

where $A_h^\tau : \mathcal{V}^{t^{n-1}} \times \mathcal{V}^{t^{n-1}} \to \mathbb{R}$ denotes the pullback of a_h^τ to $\mathcal{V}^{t^{n-1}} \times \mathcal{V}^{t^{n-1}}$ under the map φ_h^t. That is,

$$A_h^\tau(u \circ \varphi_h^\tau, w \circ \varphi_h^\tau) = a_h^\tau(u, w) \tag{3.18}$$

for every $\tau \in (t^{n-1}, t^n]$ and every $u, w \in \mathcal{V}^\tau$. The (weak) differentiability of A_h^τ in (3.17) is proven in Section 3.6 under assumptions (3.3.v) and (3.4.2.iii). Note that Λ_h^t is a bilinear form resembling, in loose language, the Lie derivative of a_h^t along the direction of the mesh motion.

To measure the size of the bilinear form Λ_h^t, we make use of the following family of h-dependent norms on the space of continuous bilinear forms $\Lambda : \mathcal{V}^t \times \mathcal{V}^t \to \mathbb{R}$. For $s \geq 0$ and $2 \leq \theta, \eta \leq \infty$ with $\frac{1}{\theta} + \frac{1}{\eta} = \frac{1}{2}$, denote

$$\|\Lambda\|_{-s,\theta,\Omega^t} = \sup_{\substack{u \in W^{1,\eta}(\Omega^t) \cap \mathcal{V}^t \\ w \in H^s(\Omega^t) \cap \mathcal{V}^t \\ u,w \neq 0}} \frac{|\Lambda(u,w)|}{(\|u\|_{0,\eta,\Omega^t} + h|u|_{1,\eta,\Omega^t})\|w\|_{s,2,\Omega^t}}. \tag{3.19}$$

Note that this definition allows one to write

$$|\Lambda(u,w)| \leq \|\Lambda\|_{-s,\theta,\Omega^t} \left(\|u\|_{0,\eta,\Omega^t} + h|u|_{1,\eta,\Omega^t}\right) \|w\|_{s,2,\Omega^t}$$

for any continuous bilinear form $\Lambda : \mathcal{V}^t \times \mathcal{V}^t \to \mathbb{R}$, any $s \geq 0$, any $2 \leq \theta, \eta \leq \infty$ with $\frac{1}{\theta} + \frac{1}{\eta} = \frac{1}{2}$, any $u \in W^{1,\eta}(\Omega^t) \cap \mathcal{V}^t$, and any $w \in H^s(\Omega^t) \cap \mathcal{V}^t$.

We note in passing that a sample calculation of Λ_h^t and its norms for a particular bilinear form a^t and mesh motion strategy is illustrated in Section 3.7.

The following theorem will be proved in Section 3.6.

Theorem 3.4.2. *Let $\{\mathcal{V}_h^t \mid 0 < t \leq T,\ h \leq h_0\}$ be a family of evolving finite element spaces with mesh velocity v_h satisfying (3.4.1.iii) and (3.4.2.i-3.4.2.iii). Let ρ, κ, and Λ_h^t be given by (3.15), (3.25), and (3.17), respectively. Then there exists $C > 0$ independent of h and t such that*

$$\|D_t\rho\|_{0,2,\Omega^t} \leq C\Big[h \inf_{w_h \in \mathcal{V}_h^t} \|D_t(e^{-\kappa t}u) - w_h\|_{1,2,\Omega^t} + c_\eta(\Lambda_h^t)\left(\|\rho\|_{0,\eta,\Omega^t} + h|\rho|_{1,\eta,\Omega^t}\right)\Big]$$

for every $h \leq h_0$, a.e. $t \in (t^{n-1}, t^n)$, every $n = 1, 2, \ldots, N$, and every $2 \leq \theta, \eta \leq \infty$ satisfying $\frac{1}{\theta} + \frac{1}{\eta} = \frac{1}{2}$, where

$$c_\eta(\Lambda_h^t) = \|\Lambda_h^t\|_{-2,\theta,\Omega^t} + h\|\Lambda_h^t\|_{-1,\theta,\Omega^t}.$$

Remark. A slightly sharper variant of the estimate above, which will be useful in Chapter 5, reads

$$\|D_t\rho\|_{0,2,\Omega^t} \le C\left(h \inf_{w_h\in\mathcal{V}_h^t} \|D_t(e^{-\kappa t}u) - w_h\|_{1,2,\Omega^t} + \sup_{w\in H^2(\Omega^t)\cap H_0^1(\Omega^t)} \frac{|\Lambda_h^t(\rho,w)|}{\|w\|_{2,2}} + h \sup_{w\in H_0^1(\Omega^t)} \frac{|\Lambda_h^t(\rho,w)|}{\|w\|_{1,2}}\right).$$

Its proof is an easy modification of the one presented here.

3.4.3 Concrete Error Estimate

As we mentioned earlier, Theorems 3.4.1 and 3.4.2 provide the key ingredients needed to estimate the order of accuracy of numerical methods belonging to the broad class of schemes having the form (3.11). As an illustration, let us consider the case in which the finite element space $\mathcal{V}_h^t$ contains functions which approximate $u(\cdot,t)$ and $D_tu(\cdot,t)$ to order h^r in the L^2-norm, with $r \ge 2$ an integer. To make this precise, and to account for the fact that practical choices of the mesh velocity typically endow $D_tu = \dot{u} + v_h\cdot\nabla_x u$ with lower global regularity than elementwise regularity, let

$$\|u\|_{s,p,\Omega^t,h} = \left(\sum_{K\in\mathcal{T}_h^t} \|u\|_{s,p,K}^p\right)^{1/p}, \quad |u|_{s,p,\Omega^t,h} = \left(\sum_{K\in\mathcal{T}_h^t} |u|_{s,p,K}^p\right)^{1/p}$$

denote the "broken" $W^{s,p}(\Omega^t)$-norm and semi-norm, respectively, for each $s \ge 0$, $1 \le p \le \infty$. Define the broken Sobolev spaces

$$W_h^{s,p}(\Omega^t) = \{u \in L^p(\Omega^t) \mid \|u\|_{s,p,\Omega^t,h} < \infty\}$$

and $H_h^s(\Omega^t) = W_h^{s,2}(\Omega^t)$. We shall assume that the finite element spaces $\mathcal{V}_h^t$ satisfy the following approximation hypothesis with an integer $r \ge 2$ and a real number $q \in [1,\infty]$ satisfying $q < \infty$ if $d = 2r-2$ and $q \le 2d/(d-2r+2)$ if $d > 2r-2$:

(3.4.3.i) There exists $C > 0$ independent of h and t such that for every $h \le h_0$, every $t \in (0,T]$, every $2 \le s \le r$, and every $w \in H_h^s(\Omega^t) \cap W^{1,q}(\Omega^t) \cap \mathcal{V}^t$,

$$\inf_{w_h\in\mathcal{V}_h^t} \|w - w_h\|_{m,2,\Omega^t} \le Ch^{s-m}|w|_{s,2,\Omega^t,h}, \quad m = 0,1. \tag{3.20}$$

Note that this hypothesis can be satisfied, for instance, by a finite element space $\mathcal{V}_h^t$ consisting of continuous functions that are elementwise polynomials of degree $\le r-1$ over a shape-regular mesh $\mathcal{T}_h^t$ in dimension $d \le 3$. In this case, we may take w_h equal to the nodal interpolant of w in (3.20), which is well-defined as long as q is chosen larger than d (so that $W^{1,q}(\Omega^t) \subset C^0(\overline{\Omega^t})$); see [35, Remark 3.2.2].

Finally, let us suppose that the mesh motion strategy is such that the following bounds hold for the number of remeshing times $N(h)$, the bilinear form Λ_h^t, and the mesh velocity v_h:

(3.4.3.ii) There exists $C > 0$ independent of h such that for every $h \leq h_0$,

$$N(h) \leq C, \tag{3.21}$$

$$\sup_{0<t\leq T} \|\Lambda_h^t\|_{-2,\infty,\Omega^t} + h\|\Lambda_h^t\|_{-1,\infty,\Omega^t} \leq C, \tag{3.22}$$

$$\sup_{0<t\leq T} \|v_h\|_{r,\infty,\Omega^t,h} \leq C. \tag{3.23}$$

We remark that hypothesis (3.4.3.ii) is representative of conventional ALE schemes under mild assumptions on the mesh motion; see Section 3.7.

The next corollary is then a straightforward consequence of Theorems 3.4.1 and 3.4.2 together with classical estimates for $\|\rho(t)\|_{0,2,\Omega^t}$ and $|\rho(t)|_{1,2,\Omega^t}$, which we summarize in Section 3.6.3.

Corollary 3.4.3. *Let $\{u_h^n\}_{n=0}^N$ be generated by the recursion (3.11) with the initial condition (3.12), using an evolving finite element space $\{\mathcal{V}_h^t \mid 0 < t \leq T\}$ satisfying (3.4.1.iii) and projectors $\{p_+^{t^n}\}_{n=0}^{N-1}$ satisfying (3.4.1.i-3.4.1.ii). Suppose that (3.4.2.i-3.4.2.iii), (3.4.3.i), and (3.4.3.ii) hold with an integer $r \geq 2$. Then there exists C independent of h and u such that for every $h \leq h_0$, the error $\varepsilon^N = u(\cdot,T) - u_h^N$ satisfies*

$$\|\varepsilon^N\|_{0,2,\Omega^T} \leq Ch^r \left(\sup_{0\leq t\leq T} |u|_{r,2,\Omega^t} + \int_0^T \left(|\dot{u}|_{r,2,\Omega^t} + \|u\|_{r+1,2,\Omega^t}\right) dt \right),$$

provided that for each $t \in [0,T]$, $u(\cdot,t) \in H^{r+1}(\Omega^t)$, and $\dot{u}(\cdot,t) \in H^r(\Omega^t)$.

Remark. It is worthwhile to note that there are examples of less conventional mesh motion strategies for which the bounds in hypothesis (3.4.3.ii) are satisfied not uniformly, but with right-hand sides that depend on the mesh spacing h. For such a scheme, Theorems 3.4.1 and 3.4.2 can still be applied to derive an error estimate, potentially with a differing order in h, as described in Section 3.2.

3.5 Proof of the Abstract Error Estimate

This section is devoted to the proof of Theorem 3.4.1.

3.5.1 Outline of the Proof

After establishing a stability estimate for the semidiscrete flow in Section 3.5.2 and fixing an appropriate value for the constant κ in Section 3.5.3, the proof of Theorem 3.4.1 will proceed in three steps.

First, in Section 3.5.4, the semidiscrete solution u_h^n is compared with a discrete representative of the exact solution, namely $r_h^{t^n} u^n$. Using standard arguments from the analysis of numerical integrators, the difference $r_h^{t^n} u^n - u_h^n$ is decomposed into a summation of local errors (errors that can be studied over a single interval $(t^{n-1}, t^n]$), each amplified by a power of the projector's stability constant C_p. The decomposition of the error into a summation of local errors is illuminated by Fig. 3.1, where the evolution of the exact and semidiscrete solutions is illustrated schematically. Next, in Section 3.5.5, the local error at each n is decomposed into two parts that can be understood as an error related to the spatial discretization and an error related to the projection of the semidiscrete solution onto a new finite element space at the start of each interval. These errors can be estimated in terms of the material time derivative of ρ and the jumps in ρ across each remeshing time, respectively. Finally, the aforementioned estimates are combined to yield Theorem 3.4.1.

3.5.2 Stability of the Semidiscrete Flow

We start by stating a stability estimate for the semidiscrete advancement operator. In what follows, we denote by

$$\Omega^I = \{(x,t) \mid x \in \Omega^t, t \in I\}$$

the spacetime slab swept out by Ω^t over an interval $I \subset [0,T]$.

Lemma 3.5.1. *For every $h \leq h_0$, every $1 \leq n \leq N$, and every $\bar{u}_h \in \mathcal{V}_h^{t_+^{n-1}}$,*

$$\|\mathfrak{f}_h^n \bar{u}_h\|_{0,2,\Omega^{t^n}} \leq \|\bar{u}_h\|_{0,2,\Omega^{t^{n-1}}} + \int_{t^{n-1}}^{t^n} \|f\|_{0,2,\Omega^t}\, dt.$$

Proof. Let u_h solve (3.5) with initial condition $u_h(\cdot, t_+^{n-1}) = \bar{u}_h$. Choose $w_h = u_h$ in (3.5) and integrate with respect to time. Noting that $a^t(u_h, u_h) \geq 0$, we obtain

$$\int_{t^{n-1}}^{\tau} \int_{\Omega^t} \frac{\partial}{\partial t}\left(\frac{1}{2} u_h^2\right) dx\, dt \leq \int_{t^{n-1}}^{\tau} \|f\|_{0,2,\Omega^t} \|u_h\|_{0,2,\Omega^t}\, dt$$

for every $\tau \in (t^{n-1}, t^n]$. The regularity $u_h \in \mathcal{V}_h^{(t^{n-1}, t^n]}$ implies via Sobolev embeddings that $u_h^2 \in W^{1,p}(\Omega^{(t^{n-1}, t^n)})$ with a scalar $p > 1$. Hence, the Gauss-Green theorem [121, Chapter 3, Theorem 6.1] on the spacetime slab $\Omega^{(t^{n-1}, \tau)}$ may be applied to give

$$\frac{1}{2}\|u_h\|_{0,2,\Omega^\tau}^2 \leq \frac{1}{2}\|\bar{u}_h\|_{0,2,\Omega^{t^{n-1}}}^2 + \int_{t^{n-1}}^{\tau} \|f\|_{0,2,\Omega^t} \|u_h\|_{0,2,\Omega^t}\, dt$$

for every $\tau \in (t^{n-1}, t^n]$, where we have used the fact that $u_h = 0$ on $\partial\Omega^t$ for every $t \in (t^{n-1}, t^n]$. The result is then an immediate consequence of the following lemma, whose proof is given in, for instance, [30, Lemma A.5]. □

Lemma 3.5.2. *Let $y \in C^0([a,b])$ and $g \in L^1(a,b)$ be nonnegative functions on a bounded interval $[a,b] \subset \mathbb{R}$. Suppose that*

$$\frac{1}{2}y(t)^2 \leq \frac{1}{2}y(a)^2 + \int_a^t g(\tau)y(\tau)\,d\tau$$

for every $t \in [a,b]$. Then

$$y(t) \leq y(a) + \int_a^t g(\tau)\,d\tau$$

for every $t \in [a,b]$.

A consequence of Lemma 3.5.1 and the linearity of (3.5) is that for any $\bar{u}_h, \bar{w}_h \in \mathcal{V}_h^{t_+^{n-1}}$,

$$\|\mathfrak{f}_h^n \bar{u}_h - \mathfrak{f}_h^n \bar{w}_h\|_{0,2,\Omega^{t^n}} \leq \|\bar{u}_h - \bar{w}_h\|_{0,2,\Omega^{t^{n-1}}}. \tag{3.24}$$

Later, we often abuse notation by writing $\mathfrak{f}_h^n \bar{u}_h - \mathfrak{f}_h^n \bar{w}_h = \mathfrak{f}_h^n(\bar{u}_h - \bar{w}_h)$, bearing in mind that the right-hand side tacitly denotes the advancement $(\bar{u}_h - \bar{w}_h)$ with a vanishing source term f. We also make frequent use of the fact that in the absence of a source term f, the operator $\mathfrak{f}_h^n$ is linear.

3.5.3 Elliptic Projection

As mentioned earlier, our analysis will rely on the use of an elliptic projector associated with a modified bilinear form

$$a_h^t(u,w) = a^t(u,w) - b_h^t(u,w) + \kappa m^t(u,w),$$

with $\kappa \geq 0$ chosen in such a way such that a_h^t is coercive, uniformly in t and h. The following lemma, which is a statement of *Garding's inequality* (see, for example, [28, Theorem 5.6.8]), shows that such a κ exists when (3.4.1.iii) holds.

Lemma 3.5.3. *Let*

$$\kappa = \frac{v_{max}^2}{2\alpha_0}. \tag{3.25}$$

Then the inequality

$$a_h^t(u,u) \geq \alpha \|u\|_{1,2,\Omega^t}^2 \quad \forall u \in \mathcal{V}^t \tag{3.26}$$

holds for every $t \in (0,T]$ and every $h \leq h_0$ with $\alpha = \alpha_0/2$.

Proof. The proof is a trivial modification of the proof in [28, Theorem 5.6.8], where it is assumed that $a^t(u,u) \geq \alpha_0 |u|_{1,2,\Omega^t}^2$ rather than $a^t(u,u) \geq \alpha_0 \|u\|_{1,2,\Omega^t}^2$. □

For the remainder of this chapter, let κ be given by (3.25). It is clear that with κ so defined, a_h^t is continuous, uniformly in t and h. That is, there exists $M > 0$ independent of h and t such that for every $t \in (0,T]$, every $h \leq h_0$, and every $u, w \in \mathcal{V}^t$,

$$|a_h^t(u,w)| \leq M \|u\|_{1,2,\Omega^t} \|w\|_{1,2,\Omega^t}.$$

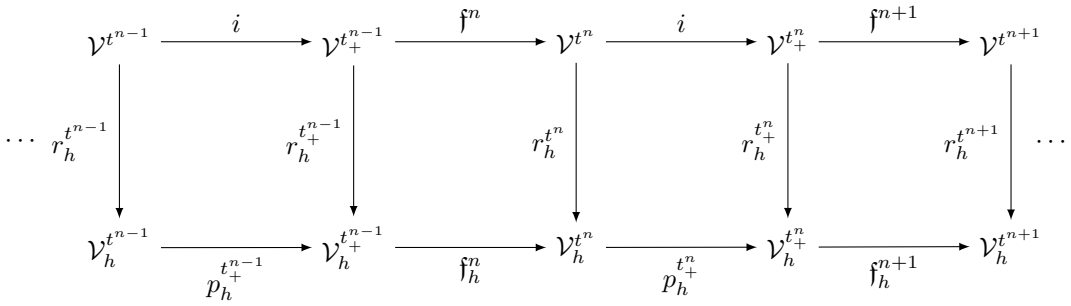

Figure 3.1: Schematic diagram depicting the evolution of the continuous and semidiscrete solutions u^n and u_h^n, respectively. The semidiscrete solution u_h^n advances to the right along the bottom row of the diagram (after an initial projection onto $\mathcal{V}_h^{0_+}$ at $t = 0$) via an alternating sequence of projections $p_h^{t_+^{n-1}} : \mathcal{V}_h^{t^{n-1}} \to \mathcal{V}_h^{t_+^{n-1}}$ and semidiscrete advancements $\mathfrak{f}_h^n : \mathcal{V}_h^{t_+^{n-1}} \to \mathcal{V}_h^{t^n}$. The exact solution advances to the right along the top row of the diagram via an alternating sequence of identity maps $i : \mathcal{V}^{t^{n-1}} \to \mathcal{V}^{t_+^{n-1}}$ and continuous advancements $\mathfrak{f}^n : \mathcal{V}^{t_+^{n-1}} \to \mathcal{V}^{t^n}$, where we have introduced the identity maps and defined the spaces $\mathcal{V}^{t_+^n} := \mathcal{V}^{t^n}$ to facilitate an analogy with the evolution of the semidiscrete solution. If the continuous solution is mapped onto the current finite element space via the elliptic projection $r_h^t : \mathcal{V}^t \to \mathcal{V}_h^t$ (vertical arrows), then the difference $r_h^{t^n} u^n - u_h^n$ measures the extent to which this diagram fails to commute.

Define for each $t \in (0, T]$ the *elliptic projector* $r_h^t : \mathcal{V}^t \to \mathcal{V}_h^t$ according to (3.14). It is a consequence of the Lax-Milgram theorem that r_h^t is a well-defined linear projector for each t.

3.5.4 Error Decomposition

To derive an estimate for the global error $\varepsilon^n = u^n - u_h^n$, let us compare u_h^n with a discrete representative of the exact solution, namely $r_h^{t^n} u^n$, by writing

$$\varepsilon^n = -e^{\kappa t^n} \rho(t^n) + \ell^n,$$

with ρ given by (3.15) and

$$\ell^n = r_h^{t^n} u^n - u_h^n.$$

Next, decompose ℓ^n as $\ell^n = \ell_1^n + \ell_2^n$ with

$$\ell_1^n = r_h^{t^n} u^n - \mathfrak{f}_h^n p_h^{t_+^{n-1}} r_h^{t^{n-1}} u^{n-1},$$
$$\ell_2^n = \mathfrak{f}_h^n p_h^{t_+^{n-1}} r_h^{t^{n-1}} u^{n-1} - u_h^n.$$

Note that r_h^0 is undefined; in the relations above, it is to be understood that $r_h^0 u^0 = u^0$, so that

when $n = 1$,

$$\begin{aligned}\ell_1^1 &= r_h^{t^1} u^1 - \mathfrak{f}_h^1 p_h^{0+} u^0 = r_h^{t^1} u^1 - u_h^1,\\ \ell_2^1 &= \mathfrak{f}_h^1 p_h^{0+} u^0 - u_h^1 = 0.\end{aligned}$$

The linearity of $\mathfrak{f}_h^n$ (in the absence of a source term) and the linearity of $p_h^{t_+^{n-1}}$ imply that

$$\begin{aligned}\ell_2^n &= \mathfrak{f}_h^n p_h^{t_+^{n-1}} \left(r_h^{t^{n-1}} u^{n-1} - u_h^{n-1} \right)\\ &= \mathfrak{f}_h^n p_h^{t_+^{n-1}} \left(\ell_1^{n-1} + \ell_2^{n-1} \right).\end{aligned}$$

The stability assumption (3.4.1.ii) and the stability estimate (3.24) then imply

$$\|\ell_2^n\|_{0,2,\Omega^{t^n}} \le C_p \left(\|\ell_1^{n-1}\|_{0,2,\Omega^{t^{n-1}}} + \|\ell_2^{n-1}\|_{0,2,\Omega^{t^{n-1}}} \right).$$

Combining this recursion with the initial condition $\ell_2^1 = 0$ leads to the bound

$$\|\ell^n\|_{0,2,\Omega^T} \le \sum_{n=1}^{N} C_p^{N-n} \|\ell_1^n\|_{0,2,\Omega^{t^n}}. \tag{3.27}$$

3.5.5 Estimates for Local Errors

To estimate the local errors ℓ_1^n, $n = 1, 2, \ldots, N$, write

$$\ell_1^n = \gamma^n + \delta^n$$

with

$$\begin{aligned}\gamma^n &= r_h^{t^n} u^n - \mathfrak{f}_h^n r_h^{t_+^{n-1}} u^{n-1},\\ \delta^n &= \mathfrak{f}_h^n r_h^{t_+^{n-1}} u^{n-1} - \mathfrak{f}_h^n p_h^{t_+^{n-1}} r_h^{t^{n-1}} u^{n-1}.\end{aligned}$$

Again, it is to be understood that $r_h^0 u^0 = u^0$, so that

$$\delta^1 = \mathfrak{f}_h^1 \left(r_h^{0+} u^0 - p_h^{0+} u^0 \right).$$

To bound δ^n, use the linearity of $\mathfrak{f}_h^n$ (in the absence of a source term) together with the linearity

and surjectivity of $p_h^{t_+^{n-1}}$ to write

$$\begin{aligned}\delta^n &= \mathfrak{f}_h^n p_h^{t_+^{n-1}} \left(r_h^{t_+^{n-1}} - r_h^{t^{n-1}} \right) u^{n-1} \\ &= e^{\kappa t^{n-1}} \mathfrak{f}_h^n p_h^{t_+^{n-1}} \left(\rho(t_+^{n-1}) - \rho(t^{n-1}) \right).\end{aligned}$$

Now by the stability assumption (3.4.1.ii) and the stability estimate (3.24),

$$\|\delta^n\|_{0,2,\Omega^{t^n}} \leq C_p e^{\kappa t^{n-1}} \|\rho(t_+^{n-1}) - \rho(t^{n-1})\|_{0,2,\Omega^{t^{n-1}}}. \tag{3.28}$$

Finally, a bound on γ^n is given in the following lemma.

Lemma 3.5.4. *For every* $1 \leq n \leq N$,

$$\|\gamma^n\|_{0,2,\Omega^{t^n}} \leq \int_{t^{n-1}}^{t^n} e^{\kappa t} \|D_t \rho\|_{0,2,\Omega^t} \, dt. \tag{3.29}$$

Proof. Let y_h denote the solution to (3.6) over $(t^{n-1}, t^n]$ with the initial condition

$$y_h(\cdot, t_+^{n-1}) = r_h^{t_+^{n-1}} u^{n-1},$$

so that

$$y_h(\cdot, t^n) = \mathfrak{f}_h^n r_h^{t_+^{n-1}} u^{n-1}.$$

Then, denoting $\theta_h(t) = y_h(\cdot, t) - r_h^t u(\cdot, t)$, we have

$$\begin{aligned}\theta_h(t_+^{n-1}) &= 0, \\ \theta_h(t^n) &= -\gamma^n,\end{aligned}$$

and

$$y_h(\cdot, t) - u(\cdot, t) = \theta_h(t) + e^{\kappa t} \rho(t).$$

A bound on $\theta_h(t^n)$, and hence γ^n, follows from subtracting (3.8) from (3.6) with $w = w_h \in \mathcal{V}_h^t$ and simplifying, using (3.13) together with the equalities

$$a_h^t(\rho, w_h) = 0$$

and

$$D_t(e^{\kappa t} \rho) = \kappa e^{\kappa t} \rho + e^{\kappa t} D_t \rho.$$

The resulting differential equation for θ_h reads

$$m^t(\dot{\theta}_h, w_h) + a^t(\theta_h, w_h) = -m^t(e^{\kappa t} D_t\rho, w_h)$$

for every $w_h \in \mathcal{V}_h^t$, $t \in (t^{n-1}, t^n]$. Lemma 3.5.1 then gives

$$\|\gamma^n\|_{0,2,\Omega^{t^n}} = \|\mathfrak{f}_h^n \theta_h(t_+^{n-1})\|_{0,2,\Omega^{t^n}} \leq \int_{t^{n-1}}^{t^n} e^{\kappa t} \|D_t\rho\|_{0,2,\Omega^t}\, dt.$$

□

Combining the bounds (3.27), (3.28), and (3.29) leads to the general error estimate in Theorem 3.4.1.

3.6 Proof of the Bound on $D_t\rho$

This section presents a proof of Theorem 3.4.2, which concerns the material time derivative of $\rho = e^{-\kappa t}(r_h^t u - u)$, the (scaled) difference between u and its elliptic projection $r_h^t u$ onto an evolving finite element space $\{\mathcal{V}_h^t\}_t$ with respect to the bilinear form (3.13).

To prove Theorem 3.4.2, we derive in Lemma 3.6.4 an equation that relates the material time derivative of ρ to the function ρ itself. Deriving this relation involves some preliminary calculations that lead to a formula in Lemma 3.6.2 for the time derivative of a time-dependent bilinear form. The relation between $D_t\rho$ and ρ that we derive in Lemma 3.6.4 then leads to an estimate for the H^1-norm of $D_t\rho$ in Lemma 3.6.5. Finally, we use a duality argument to estimate the L^2-norm of $D_t\rho$, thereby proving Theorem 3.4.2. Corollary 3.4.3 will then follow readily using classical estimates for $\|\rho\|_{0,2,\Omega^t}$ and $|\rho|_{1,2,\Omega^t}$, as we explain in Section 3.6.3.

3.6.1 Differentiating the Bilinear Form

We begin by presenting a statement of the Reynolds transport theorem for weakly differentiable functions.

Lemma 3.6.1. *Let $\{\varphi^t : \Omega^{\tau_0} \to \Omega^t \mid \tau_0 < t \leq \tau_1\}$ be a regular domain deformation with velocity $v(\cdot, t) = \dot{\varphi}^t \circ (\varphi^t)^{-1}$ over an interval $(\tau_0, \tau_1] \subset [0, T]$. Let $g : \Omega^{(\tau_0,\tau_1]} \to \mathbb{R}$ be such that the map $t \mapsto g(\varphi^t(\cdot), t)$ belongs to $W^{1,p}(\tau_0, \tau_1; L^1(\Omega^{\tau_0}))$ for some $1 \leq p \leq \infty$. Then the map*

$$t \mapsto \int_{\Omega^t} g\, dx$$

belongs to $W^{1,p}(\tau_0,\tau_1)$ *and satisfies*

$$\frac{d}{dt}\int_{\Omega^t} g\,dx = \int_{\Omega^t} D_t g + g\nabla_x\cdot v\,dx$$

for a.e. $t\in(\tau_0,\tau_1)$.

Proof. A proof of this identity when $g\in W^{1,1}(\Omega^{(\tau_0,\tau_1)})$ is outlined in [23, Lemma 2.2]. A similar proof applies to the case in which $t\mapsto g(\varphi^t(\cdot),t)\in W^{1,p}(\tau_0,\tau_1;L^1(\Omega^{\tau_0}))$. □

Let us now fix a family of evolving finite element spaces $\{\mathcal{V}_h^t \mid 0<t\le T\}$, $h\le h_0$, over a family of moving meshes $\{\mathcal{T}_h^t \mid 0<t\le T\}$, $h\le h_0$, associated with regular domain deformations $\varphi_h^t : \Omega^{t^{n-1}}\to\Omega^t$, $t\in(t^{n-1},t^n]$, $n=1,2,\dots,N$. We assume throughout the remainder of this section that (3.4.2.iii) holds. Our aim at the moment is to derive a formula for the time-derivative of $a_h^t(u,w)$ for a pair of functions $u,w:\Omega^{(t^{n-1},t^n]}\to\mathbb{R}$ whose regularity will be specified shortly.

The hypothesis (3.3.v) ensures that if $u=U\circ(\varphi_h^t)^{-1}$ and $w=W\circ(\varphi_h^t)^{-1}$ for some functions $U,W\in\mathcal{V}^{t^{n-1}}$, then the map $t\mapsto a^t(u,w)$ is Lipschitz, and hence weakly differentiable. Lemma 3.6.1 reveals that for such functions u and w, the maps $t\mapsto b_h^t(u,w)$ and $t\mapsto m^t(u,w)$ (and hence $t\mapsto a_h^t(u,w)$) are likewise Lipschitz, satisfying a bound of the form (3.2). This can be checked by choosing $g=(v_h\cdot\nabla_x u)w$ and $g=uw$, respectively, in Lemma 3.6.1, bearing in mind that (3.4.2.iii) is assumed to hold. It follows, in particular, that the bilinear form Λ_h^t given by (3.17) exists and is continuous for a.e. t, with a modulus of continuity bounded uniformly in time. The next lemma examines the time-differentiability of $a_h^t(u,w)$ for more general u and w.

Lemma 3.6.2. *Let* $u,w:\Omega^{(t^{n-1},t^n]}\to\mathbb{R}$ *be such that the maps* $t\mapsto u(\varphi_h^t(\cdot),t)$ *and* $t\mapsto w(\varphi_h^t(\cdot),t)$, $t\in(t^{n-1},t^n]$, *belong to* $W^{1,1}(t^{n-1},t^n;\mathcal{V}^{t^{n-1}})$. *Then for every* $h\le h_0$, *the map*

$$t\mapsto a_h^t(u,w)$$

belongs to $W^{1,1}(t^{n-1},t^n)$ *and satisfies*

$$\frac{d}{dt}a_h^t(u,w) = a_h^t(D_t u,w)+a_h^t(u,D_t w)+\Lambda_h^t(u,w) \tag{3.30}$$

for a.e. $t\in(t^{n-1},t^n)$, *where* Λ_h^t *is given by (3.17).*

Proof. Let $U(t):=u(\varphi_h^t(\cdot),t)$ and $W(t):=w(\varphi_h^t(\cdot),t)$. Note that $U,W\in C([t^{n-1},t^n],\mathcal{V}^{t^{n-1}})$ by the embedding $W^{1,1}(t^{n-1},t^n;\mathcal{V}^{t^{n-1}})\subset C([t^{n-1},t^n],\mathcal{V}^{t^{n-1}})$ [46, Chapter 5.9, Theorem 2]. Using mollification in time, there exist sequences of infinitely differentiable $\mathcal{V}^{t^{n-1}}$-valued functions $U_\epsilon,W_\epsilon:(-\infty,\infty)\to\mathcal{V}^{t^{n-1}}$ with compact support whose restrictions to $[t^{n-1},t^n]$ converge to U and W uniformly on $[t^{n-1},t^n]$ as $\epsilon\to0$, and whose derivatives converge to $\frac{\partial U}{\partial t}$ and $\frac{\partial W}{\partial t}$ in $L^1(t^{n-1},t^n;\mathcal{V}^{t^{n-1}})$

as $\epsilon \to 0$. Define

$$p_\epsilon(\sigma,\tau) = A_h^\tau(U_\epsilon(\sigma), W_\epsilon(\sigma)), \quad \sigma,\tau \in (t^{n-1}, t^n),$$

where $A_h^t : \mathcal{V}^{t^{n-1}} \times \mathcal{V}^{t^{n-1}} \to \mathbb{R}$ denotes the pullback of a_h^t under φ_h^t, as defined in (3.18). The remarks preceding this lemma imply that for a.e. $\tau \in (t^{n-1}, t^n)$, $\frac{\partial p_\epsilon}{\partial \tau}(\sigma,\tau)$ exists and is given by

$$\frac{\partial p_\epsilon}{\partial \tau}(\sigma,\tau) = \Lambda_h^\tau \left(U_\epsilon(\sigma)\circ(\varphi_h^\tau)^{-1}, W_\epsilon(\sigma)\circ(\varphi_h^\tau)^{-1}\right)$$

for every $\sigma \in (t^{n-1}, t^n)$. Furthermore, since A_h^τ is a continuous bilinear form for each τ, the equality

$$\frac{\partial p_\epsilon}{\partial \sigma}(\sigma,\tau) = A_h^\tau\left(\frac{\partial U_\epsilon}{\partial \sigma}(\sigma), W_\epsilon(\sigma)\right) + A_h^\tau\left(U_\epsilon(\sigma), \frac{\partial W_\epsilon}{\partial \sigma}(\sigma)\right).$$

holds for every $(\sigma,\tau) \in (t^{n-1}, t^n)\times(t^{n-1}, t^n)$ [103, Theorem 2.4.4]. Notice that $\frac{\partial p_\epsilon}{\partial \sigma}$ is continuous in $(t^{n-1}, t^n)\times(t^{n-1}, t^n)$ by virtue of the (temporally uniform) continuity of A_h^t and Λ_h^t, and the regularity of φ_h^t, U_ϵ, and W_ϵ. It follows [6, Theorem 12.11] that $p_\epsilon(\sigma,\tau)$ is differentiable at $(\sigma,\tau) = (t,t)$ for a.e. $t \in (t^{n-1}, t^n)$ and satisfies

$$\frac{d}{dt}p_\epsilon(t,t) = \left.\frac{\partial}{\partial \sigma}\right|_{\sigma=t} p_\epsilon(\sigma,t) + \left.\frac{\partial}{\partial \tau}\right|_{\tau=t} p_\epsilon(t,\tau).$$

Now multiply by a smooth real-valued function with compact support in (t^{n-1}, t^n) and integrate in time. Integrating by parts and taking the limit as $\epsilon \to 0$ shows that the equality

$$\begin{aligned}\frac{d}{dt}A_h^t(U(\cdot,t), W(\cdot,t)) = A_h^t\left(\frac{\partial U}{\partial t}(\cdot,t), W(\cdot,t)\right) + A_h^t\left(U(\cdot,t), \frac{\partial W}{\partial t}(\cdot,t)\right)\\ + \Lambda_h^t\left(u(\cdot,t), w(\cdot,t)\right)\end{aligned}$$

holds in the sense of distributions. Conclude using the definition of A_h^t together with the relations

$$\begin{aligned}\frac{\partial U}{\partial t}(\cdot,t) &= D_t u(\varphi_h^t(\cdot),t),\\ \frac{\partial W}{\partial t}(\cdot,t) &= D_t w(\varphi_h^t(\cdot),t).\end{aligned}$$

□

3.6.2 Estimating $D_t\rho$

We now use Lemma 3.6.2 to derive a relation between $\rho = e^{-\kappa t}(r_h^t u - u)$ and its material time derivative. In order to justify the forthcoming calculations, we first make the following observation concerning the regularity of ρ. A proof is given in Appendix 3.A.

Lemma 3.6.3. *For each $n = 1, 2, \dots, N$ the map $t \mapsto \rho(t) \circ \varphi_h^t$, $t \in (t^{n-1}, t^n]$, belongs to $W^{1,1}(t^{n-1}, t^n, \mathcal{V}^{t^{n-1}})$.*

One consequence of the preceding lemma is that $D_t\rho \in \mathcal{V}^t$ for a.e. $t \in (t^{n-1}, t^n)$. We tacitly make use of the regularity of ρ in the following lemma.

Lemma 3.6.4. *For every $h \le h_0$, every $n = 1, 2, \dots, N$, and a.e. $t \in (t^{n-1}, t^n)$, it holds that*

$$a_h^t(D_t\rho, w_h) = -\Lambda_h^t(\rho, w_h) \quad \forall w_h \in \mathcal{V}_h^t. \tag{3.31}$$

Proof. For a given $w_h \in \mathcal{V}_h^t$, take $w(\cdot, \tau) = w_h \circ \varphi_h^t \circ (\varphi_h^\tau)^{-1}$ and $u(\cdot, \tau) = \rho(\tau)$ for each $\tau \in (t^{n-1}, t^n]$ in (3.30). Then use the relation

$$a_h^t(\rho, w) = 0 \quad \forall t$$

together with the fact that the material time derivative of w is zero. □

The relation (3.31) leads to the following estimate for the H^1-norm of the material time derivative of ρ.

Lemma 3.6.5. *There exists $C > 0$ independent of h and t such that*

$$\|D_t\rho\|_{1,2,\Omega^t} \le C \left(\inf_{w_h \in \mathcal{V}_h^t} \|D_t(e^{-\kappa t}u) - w_h\|_{1,2,\Omega^t} + \|\Lambda_h^t\|_{-1,\theta,\Omega^t} \left(\|\rho\|_{0,\eta,\Omega^t} + h|\rho|_{1,\eta,\Omega^t} \right) \right)$$

for every $h \le h_0$, a.e. $t \in (t^{n-1}, t^n)$, every $n = 1, 2, \dots, N$, and every $2 \le \theta, \eta \le \infty$ such that $\frac{1}{\theta} + \frac{1}{\eta} = \frac{1}{2}$.

Proof. The coercivity of a_h^t and the relation (3.31) imply that

$$\begin{aligned} \alpha \|D_t\rho\|_{1,2,\Omega^t}^2 &\le a_h^t(D_t\rho, D_t\rho) \\ &= a_h^t(D_t\rho, D_t\rho - w_h) + \Lambda_h^t(\rho, D_t\rho - w_h) - \Lambda_h^t(\rho, D_t\rho) \end{aligned}$$

for any $w_h \in \mathcal{V}_h^t$. Now by the continuity of a_h^t and the definition (3.19),

$$\begin{aligned} \alpha \|D_t\rho\|_{1,2,\Omega^t}^2 \le\ & M \|D_t\rho\|_{1,2,\Omega^t} \|D_t\rho - w_h\|_{1,2,\Omega^t} \\ & + \|\Lambda_h^t\|_{-1,\theta,\Omega^t} \left(\|\rho\|_{0,\eta,\Omega^t} + h|\rho|_{1,\eta,\Omega^t} \right) \left(\|D_t\rho - w_h\|_{1,2,\Omega^t} + \|D_t\rho\|_{1,2,\Omega^t} \right) \end{aligned}$$

for any $2 \le \theta, \eta \le \infty$ with $\frac{1}{\theta} + \frac{1}{\eta} = \frac{1}{2}$. Using the fact that for real numbers $x, a, b \ge 0$,

$$x^2 \le ax + bx + ab \implies x \le \frac{1 + \sqrt{2}}{2}(a + b),$$

it follows that

$$\|D_t\rho\|_{1,2,\Omega^t} \leq C\left(\inf_{w_h\in\mathcal{V}_h^t}\|D_t\rho - w_h\|_{1,2,\Omega^t} + \|\Lambda_h^t\|_{-1,\theta,\Omega^t}\left(\|\rho\|_{0,\eta,\Omega^t} + h|\rho|_{1,\eta,\Omega^t}\right)\right),$$

with C depending only on M and α. Finally, observe that $D_t(e^{-\kappa t}r_h^t u) = D_t(r_h^t(e^{-\kappa t}u)) \in \mathcal{V}_h^t$. □

We shall now use a duality argument to derive an estimate for the L^2-norm of the material time derivative of ρ, thereby proving Theorem 3.4.2. To this end, suppose that (3.4.2.i-3.4.2.ii) hold and let $y \in \mathcal{V}^t$ solve the adjoint problem

$$a_h^t(w, y) = m^t(w, D_t\rho) \quad \forall w \in \mathcal{V}^t.$$

Observe that

$$\begin{aligned} m^t(D_t\rho, D_t\rho) &= a_h^t(D_t\rho, y) \\ &= a_h^t(D_t\rho, y - w_h) + \Lambda_h^t(\rho, y - w_h) - \Lambda_h^t(\rho, y) \end{aligned}$$

for any $w_h \in \mathcal{V}_h^t$. Hence,

$$\begin{aligned} \|D_t\rho\|_{0,2,\Omega^t}^2 \leq\ & M\|D_t\rho\|_{1,2,\Omega^t}\inf_{w_h\in\mathcal{V}_h^t}\|y - w_h\|_{1,2,\Omega^t} \\ &+ \|\Lambda_h^t\|_{-1,\theta,\Omega^t}\left(\|\rho\|_{0,\eta,\Omega^t} + h|\rho|_{1,\eta,\Omega^t}\right)\inf_{w_h\in\mathcal{V}_h^t}\|y - w_h\|_{1,2,\Omega^t} \\ &+ \|\Lambda_h^t\|_{-2,\theta,\Omega^t}\left(\|\rho\|_{0,\eta,\Omega^t} + h|\rho|_{1,\eta,\Omega^t}\right)\|y\|_{2,2,\Omega^t} \end{aligned}$$

The theorem then follows from Lemma 3.6.5, hypothesis (3.4.2.ii), and the elliptic regularity estimate (3.16).

3.6.3 Deducing the Concrete Error Estimate

Deducing Corollary 3.4.3 is now a matter of using (3.4.3.i) and (3.4.3.ii) to simplify the bound in Theorem 3.4.2, inserting the resulting bound for $\|D_t\rho\|_{0,2,\Omega^t}$ into the inequality in Theorem 3.4.1, and invoking estimates for $\|\rho\|_{0,2,\Omega^t}$, $|\rho|_{1,2,\Omega^t}$, and $\|\rho(t_+^n) - \rho(t^n)\|_{0,2,\Omega^{t^n}}$ which we summarize below. We assume in what follows that u and v_h satisfy the regularity assumptions made in the statement of Corollary 3.4.3.

Estimates for ρ. By the (temporally uniform) coercivity and continuity of a_h^t, it follows from classical arguments (namely, via Céa's Lemma [45, Lemma 2.28], the Aubin-Nitsche Lemma [45, Lemma 2.31], (3.4.3.i), and (3.4.2.i)) that there exists $C > 0$ independent of h and t such that

$$e^{\kappa t}\|\rho(t)\|_{m,2,\Omega^t} \leq Ch^{s-m}|u|_{s,2,\Omega^t}, \quad m = 0, 1, \tag{3.32}$$

for every $2 \le s \le r$, every $0 < t \le T$, and every $h \le h_0$.

Estimates for $\rho(t_+^n) - \rho(t^n)$. The triangle inequality and (3.32) (with $m = 0$) provide the following upper bound for the jumps in ρ across the times of remeshing: For every $2 \le s \le r$, every $n = 1, 2, \ldots, N$, and every $h \le h_0$,

$$e^{\kappa t^n} \|\rho(t_+^n) - \rho(t^n)\|_{0,2,\Omega^{t^n}} \le Ch^s |u|_{s,2,\Omega^{t^n}}. \tag{3.33}$$

We remark that sharper estimates for $\rho(t_+^n) - \rho(t^n)$ may hold when the meshes $\mathcal{T}_h^{t_+^n}$ and $\mathcal{T}_h^{t^n}$ coincide over a large fraction of the domain, though we do not address this situation here. This phenomenon is the subject of Chapter 4 and plays a role in error estimates for universal meshes.

To simplify the bound in Theorem 3.4.2 and thereby obtain Corollary 3.4.3, expand

$$\begin{aligned} D_t(e^{-\kappa t} u) &= \partial_t(e^{-\kappa t} u) + v_h \cdot \nabla_x (e^{-\kappa t} u) \\ &= e^{-\kappa t} \dot{u} - \kappa e^{-\kappa t} u + e^{-\kappa t} v_h \cdot \nabla_x u. \end{aligned}$$

Now use the facts that $\dot{u}(\cdot, t) \in H^r(\Omega^t)$, $u(\cdot, t) \in H^{r+1}(\Omega^t)$, $\nabla_x u(\cdot, t) \in H^r(\Omega^t)^d \subset W^{1,q}(\Omega^t)^d$, and $v_h(\cdot, t) \in W^{1,\infty}(\Omega^t) \cap W_h^{r,\infty}(\Omega^t)$ to deduce that $D_t(e^{-\kappa t} u) \in H_h^r(\Omega^t) \cap W^{1,q}(\Omega^t) \cap \mathcal{V}^t$ for any $q \in [1, \infty]$ satisfying $q < \infty$ if $d = 2r - 2$ and $q \le 2d/(d - 2r + 2)$ if $d > 2r - 2$. Thus, by (3.4.3.i),

$$\begin{aligned} e^{\kappa t} \inf_{w_h \in \mathcal{V}_h^t} \|D_t(e^{-\kappa t} u) - w_h\|_{1,2,\Omega^t} &\le Ch^{r-1} |\dot{u} - \kappa u + v_h \cdot \nabla_x u|_{r,2,\Omega^t,h} \\ &\le Ch^{r-1} \left(|\dot{u}|_{r,2,\Omega^t,h} + \kappa |u|_{r,2,\Omega^t,h} + |v_h \cdot \nabla_x u|_{r,2,\Omega^t,h} \right) \\ &= Ch^{r-1} \left(|\dot{u}|_{r,2,\Omega^t} + \kappa |u|_{r,2,\Omega^t} + |v_h \cdot \nabla_x u|_{r,2,\Omega^t,h} \right). \end{aligned} \tag{3.34}$$

Next, use the fact that, with a constant C depending only on r and d, it holds that

$$\begin{aligned} |v_h \cdot \nabla_x u|_{r,2,\Omega^t,h} &\le C \|v_h\|_{r,\infty,\Omega^t,h} \|u\|_{r+1,2,\Omega^t,h} \\ &= C \|v_h\|_{r,\infty,\Omega^t,h} \|u\|_{r+1,2,\Omega^t}. \end{aligned} \tag{3.35}$$

The proof of Corollary 3.4.3 is completed by combining Thoerems 3.4.1 and 3.4.2 with (3.32), (3.33), (3.34), and (3.35).

3.7 Application to ALE Schemes

In this section, we verify the hypotheses of Corollary 3.4.3 for a more concrete mesh motion strategy and bilinear form a^t. The situation we have in mind is that in which the mesh motion is associated with an arbitrary Lagrangian-Eulerian (ALE) scheme, which prescribes a motion of the mesh by choosing a mesh for Ω^0 and solving a global system of equations (such as those of linear elasticity)

for the nodal positions at times $t > 0$, remeshing as often as needed to maintain a mesh of adequate quality. Rather than considering an explicit instance of such a method, we leave the precise choice of the mesh deformation unspecified and simply provide an example of an assumption on the mesh deformation that ensures optimal order of convergence.

The assumption we make is that the mesh velocity v_h approximates a smooth velocity v in the following sense.

(3.7.i) There exists $v : \Omega \to \mathbb{R}^d$ and constants $C_i(v)$, $i = 0, 1, 2, 3$, independent of h and t such that for every $t \in (t^{n-1}, t^n)$ and every $n = 1, 2, \ldots, N$,

$$\|v_h - v\|_{0,\infty,\Omega^t} \leq C_0(v)h, \quad |v_h - v|_{1,\infty,\Omega^t} \leq C_1(v)h, \quad \|\dot{v}_h - \dot{v}\|_{0,\infty,\Omega^t} \leq C_2(v)h,$$

and

$$C_3(v) := \max_{1\leq n\leq N} \sup_{t\in(t^{n-1},t^n)} \|v\|_{2,\infty,\Omega^t} + \|\dot{v}\|_{1,\infty,\Omega^t} < \infty.$$

We consider the case in which the bilinear form a^t is given by

$$a^t(u, w) = \int_{\Omega^t} \nabla_x u \cdot \nabla_x w \, dx. \tag{3.36}$$

By virtue of the Poincaré inequality and the boundedness of the spacetime domain Ω, this bilinear form is coercive and continuous, uniformly in time. Furthermore, its satisfaction of condition (3.3.v) can be inferred from Lemma 3.7.2 below.

Our aim in this section is to show that the bilinear form Λ_h^t (defined in (3.17)) in this setting satisfies a bound of the form (3.22), thereby validating the conditions of Corollary 3.4.3 for such a mesh motion strategy whenever (3.21) and (3.23) hold as well.

We begin by presenting an explicit formula for Λ_h^t when a^t is given by (3.36). A proof of this result is given in Appendix 3.A.

Lemma 3.7.1. *Let a^t and Λ_h^t be given by (3.36) and (3.17), respectively. Then Λ_h^t satisfies*

$$\begin{aligned}\Lambda_h^t(u, w) = &- \int_{\Omega^t} \nabla_x u \cdot \left(\nabla_x v_h + (\nabla_x v_h)^\dagger\right) \nabla_x w \, dx - \int_{\Omega^t} (\dot{v}_h \cdot \nabla_x u) w \, dx \\ &+ \int_{\Omega^t} (\nabla_x u \cdot \nabla_x w) \nabla_x \cdot v_h \, dx - \int_{\Omega^t} (v_h \cdot \nabla_x u) w \nabla_x \cdot v_h \, dx + \kappa \int_{\Omega^t} uw \nabla_x \cdot v_h \, dx\end{aligned} \tag{3.37}$$

for every $h \leq h_0$, a.e. $t \in (t^{n-1}, t^n)$, every $n = 1, 2, \ldots, N$, and every $u, w \in \mathcal{V}^t$, where $(\nabla_x v_h)^\dagger$ denotes the adjoint of $\nabla_x v_h$.

We conclude with estimates for $\|\Lambda_h^t\|_{-1,\infty,\Omega^t}$ and $\|\Lambda_h^t\|_{-2,\infty,\Omega^t}$, which imply (3.22) when combined.

Lemma 3.7.2. *Suppose that (3.7.i) holds. Then there exists C independent of h and t such that the bilinear form (3.37) satisfies*

$$\|\Lambda_h^t\|_{-1,\infty,\Omega^t} \leq Ch^{-1}$$

for every $h \leq h_0$, a.e. $t \in (t^{n-1}, t^n)$, and every $n = 1, 2, \ldots, N$.

Proof. Let $u, w \in \mathcal{V}^t$. Apply the Cauchy-Schwarz inequality to each term in (3.37) to obtain

$$|\Lambda_h^t(u,w)| \leq C\left((1+\kappa+v_{max})|v_h|_{1,\infty,\Omega^t} + \|\dot{v}_h\|_{0,\infty,\Omega^t}\right)\|u\|_{1,2,\Omega^t}\|w\|_{1,2,\Omega^t}.$$

Then use hypothesis (3.7.i) to bound $|v_h|_{1,\infty,\Omega^t}$ and $\|\dot{v}_h\|_{0,\infty,\Omega^t}$ uniformly in h and t. Finally, use the fact that

$$\|u\|_{1,2,\Omega^t} \leq h^{-1}\max\{1, h_0\}(\|u\|_{0,2,\Omega^t} + h|u|_{1,2,\Omega^t})$$

to deduce that

$$|\Lambda_h^t(u,w)| \leq Ch^{-1}(\|u\|_{0,2,\Omega^t} + h|u|_{1,2,\Omega^t})\|w\|_{1,2,\Omega^t}$$

with a constant C independent of h and t. □

Lemma 3.7.3. *Suppose that (3.7.i) holds. Then there exists C independent of h and t such that bilinear form (3.37) satisfies*

$$\|\Lambda_h^t\|_{-2,\infty,\Omega^t} \leq C$$

for every $h \leq h_0$, a.e. $t \in (t^{n-1}, t^n)$, and every $n = 1, 2, \ldots, N$.

Proof. Let $u \in \mathcal{V}^t$ and $w \in H^2(\Omega^t) \cap \mathcal{V}^t$. Define

$$\begin{aligned}\Lambda^t(u,w) = &-\int_{\Omega^t} \nabla_x u \cdot \left(\nabla_x v + (\nabla_x v)^\dagger\right)\nabla_x w\,dx - \int_{\Omega^t}(\dot{v}\cdot\nabla_x u)w\,dx \\ &+ \int_{\Omega^t}(\nabla_x u\cdot\nabla_x w)\nabla_x\cdot v\,dx - \int_{\Omega^t}(v\cdot\nabla_x u)w\nabla_x\cdot v\,dx + \kappa\int_{\Omega^t} uw\nabla_x\cdot v\,dx,\end{aligned} \tag{3.38}$$

where v denotes the smooth vector field described in (3.7.i). A straightforward calculation gives

$$|\Lambda_h^t(u,w) - \Lambda^t(u,w)| \leq Ch\|u\|_{1,2,\Omega^t}\|w\|_{1,2,\Omega^t}$$

with C depending only on κ, v_{max}, and the constants $C_i(v)$, $i = 0, 1, 2, 3$, appearing in (3.7.i). On the other hand, integrating each term of (3.38) except the last by parts leads to the bound

$$|\Lambda^t(u,w)| \leq C\|u\|_{0,2,\Omega^t}\|w\|_{2,2,\Omega^t}.$$

with C depending only on κ and $C_3(v)$. The conclusion then follows from

$$\begin{aligned}|\Lambda_h^t(u,w)| &\le |\Lambda^t(u,w)| + |\Lambda_h^t(u,w) - \Lambda^t(u,w)| \\ &\le C\left(\|u\|_{0,2,\Omega^t} + h|u|_{1,2,\Omega^t}\right)\|w\|_{2,2,\Omega^t}.\end{aligned}$$

□

3.8 Conclusion

We have presented an a priori error analysis of finite element methods for problems with moving boundaries. We proved a general error estimate that applies to methods which employ a conforming mesh of the moving domain whose deformation is smooth in time except at a finite number of instants where remeshing is performed. Examples include ALE schemes with remeshing, as well as methods that employ a universal mesh. Specializing the general error estimate to a given mesh motion strategy requires the estimation of certain quantities that depend on the mesh velocity v_h associated with the prescribed mesh motion. We illustrated such a calculation for an ALE scheme in Section 3.7, and we do the same for universal meshes in Chapter 5.

3.A Auxiliary Lemmas

Below, we prove Lemmas 3.6.3 and 3.7.1.

Lemma 3.6.3. By the remark following (3.3), it suffices to check that the map $t \mapsto r_h^t u(\varphi_h^t(\cdot), t)$ belongs to $W^{1,1}(t^{n-1}, t^n, \mathcal{V}^{t^{n-1}})$. For this purpose, expand

$$r_h^t u = \sum_a \mathbf{r}_a(t) n_a^t$$

as a linear combination of the shape functions $n_a^t \in \mathcal{V}_h^t$ of Definition 3.3.3. According to (3.14), the coefficients $\mathbf{r}_a(t)$ satisfy the (nonsingular) linear system

$$\mathbf{A}(t)\mathbf{r}(t) = \mathbf{c}(t)$$

with

$$\mathbf{A}_{ab}(t) = a_h^t(n_b^t, n_a^t), \quad \mathbf{c}_a(t) = a_h^t(u, n_a^t).$$

The entries of $\mathbf{c}(t)$ are weakly differentiable by virtue of Lemma 3.6.2 and the regularity of u and n_a^t. On the other hand, the entries of $\mathbf{A}(t)$ are Lipschitz by the (temporally uniform) continuity of Λ_h^t. Furthermore, $\mathbf{A}(t)$ is uniformly positive definite by the (temporally uniform) coercivity of a_h^t. These facts can be used to show that the entries of $\mathbf{A}^{-1}(t)$ are Lipschitz. It then follows from the

product rule for weak derivatives of univariate functions [29, Corollary 8.10] that the entries of $\mathbf{r}(t)$ are weakly differentiable, which proves the result. □

Lemma 3.7.1. With $U = u \circ \varphi_h^t$ and $W = w \circ \varphi_h^t$, define extensions of u and w to all of $\Omega^{(t^{n-1},t^n]}$ via $u(\cdot,\tau) = U \circ (\varphi_h^\tau)^{-1}$, $w(\cdot,\tau) = W \circ (\varphi_h^\tau)^{-1}$, $\tau \in (t^{n-1}, t^n]$. Then, by definition,

$$\Lambda_h^t(u,w) = \frac{d}{dt}\int_{\Omega^t} g\,dx$$

with

$$g = \nabla_x u \cdot \nabla_x w - (v_h \cdot \nabla_x u)w + \kappa uw.$$

Noting that the last three terms on the right-hand side of (3.37) coincide with $\int_{\Omega^t} g\nabla_x \cdot v_h\,dx$, the relation (3.37) will follow from Lemma 3.6.1 if we show that

$$D_t g = -\nabla_x u \cdot \left(\nabla_x v_h + (\nabla_x v_h)^\dagger\right)\nabla_x w - (\dot{v}_h \cdot \nabla_x u)w. \tag{3.39}$$

To this end, observe that the pullback $G(\cdot,t) := g(\varphi_h^t(\cdot),t)$ of g to $\Omega^{t^{n-1}}$ satisfies

$$G(\cdot,t) = \nabla_X U \cdot \left[(\nabla_X \varphi_h^t)^{-1}(\nabla_X \varphi_h^t)^{-\dagger}\right]\nabla_X W - \left((\nabla_X \varphi_h^t)^{-1}V_h \cdot \nabla_X U\right)W + \kappa UW,$$

where $V_h(\cdot,t) := v_h(\varphi_h^t(\cdot),t)$. Now differentiate with respect to time, using the fact that $\frac{\partial U}{\partial t} = \frac{\partial W}{\partial t} = 0$ together with the relations

$$\frac{\partial}{\partial t}\left[(\nabla_X \varphi_h^t)^{-1}(\nabla_X \varphi_h^t)^{-\dagger}\right] = -(\nabla_X \varphi_h^t)^{-1}\left(K_h + (K_h)^\dagger\right)(\nabla_X \varphi_h^t)^{-\dagger},$$
$$\frac{\partial}{\partial t}\left[(\nabla_X \varphi_h^t)^{-1}V_h\right] = (\nabla_X \varphi_h^t)^{-1}\frac{\partial V_h}{\partial t} - (\nabla_X \varphi_h^t)^{-1}K_h V_h,$$

where $K_h := \nabla_X V_h (\nabla_X \varphi_h^t)^{-1}$. Finally, recast the result on Ω^t to obtain (3.39). □

Chapter 4

Supercloseness of Orthogonal Projections onto Nearby Finite Element Spaces

4.1 Introduction

One of the hallmarks of the finite element method is its geometric flexibility: it permits the construction of numerical approximations to solutions of partial differential equations using meshes that are designed according to the practitioner's discretion. When two meshes are used to solve the same problem, the norm of the difference between the corresponding numerical solutions is, of course, no larger than the sum of the norms of the differences between each numerical solution and the exact solution. This chapter addresses the question of whether or not a sharper estimate holds in the event that the two meshes coincide over a large fraction of the domain.

Beyond its inherent mathematical appeal, the reader of Chapter 3 will have observed that the question raised above has important consequences in the study of numerical solutions to time-dependent PDEs on meshes that change abruptly in time. Notable examples are remeshing during finite element simulations of problems with moving boundaries, and adaptive refinement during finite element simulations of problems on fixed (or moving) domains. The relevance of the aforementioned question in this setting was elucidated in Chapter 3, where it was shown that if a parabolic PDE is discretized in space with finite elements and the solution is transferred finitely many times between meshes using a suitable projector, then it is possible to derive an upper bound on the error in the numerical solution at a fixed time $T > 0$ that involves the norms of the jumps in $r_h u(t)$ across the remeshing times, where $r_h u(t)$ denotes an elliptic projection of the exact solution $u(t)$ onto the current finite element space. These jumps are precisely the differences between the finite element

solutions of an elliptic PDE on two different meshes.

Intuition. It is perhaps not surprising that two finite element solutions associated with nearly identical meshes should differ by an amount that is small relative to their individual differences with the exact solution, under suitable conditions on the finite element spaces and the PDE under consideration. To develop some intuition, it is instructive to first consider the similarity between the *interpolants* of a smooth function u onto two finite element spaces associated with nearby meshes.

To this end, consider two families of shape-regular, quasi-uniform meshes $\{\mathcal{T}_h\}_{h\leq h_0}$ and $\{\mathcal{T}_h^+\}_{h\leq h_0}$ of an open, bounded, Lipschitz domain $\Omega \subset \mathbb{R}^d$, $d \geq 1$. Assume that the two families are parametrized by a scalar h that equals the maximum diameter of an element among all elements of $\mathcal{T}_h$ and $\mathcal{T}_h^+$ for every $h \leq h_0$, where h_0 is a positive scalar. Let $\mathcal{V}_h$ and $\mathcal{V}_h^+$ be finite element spaces consisting of, for definiteness, continuous functions that are elementwise polynomials of degree at most $r-1$ over $\mathcal{T}_h$ and $\mathcal{T}_h^+$, respectively, where $r > 1$ is an integer.

For $s \geq 0$ and $p \in [1, \infty]$, we denote by $W^{s,p}(\Omega)$ the Sobolev space of differentiability s and integrability p, equipped with the norm $\|\cdot\|_{s,p}$ and semi-norm $|\cdot|_{s,p}$. We sometimes write $\|\cdot\|_{s,p,\Omega}$ and $|\cdot|_{s,p,\Omega}$ to emphasize the domain under consideration. We denote $H^s(\Omega) = W^{s,2}(\Omega)$ for every $s \geq 1$ and $L^p(\Omega) = W^{0,p}(\Omega)$ for every $p \in [1, \infty]$.

For finite element spaces of the aforementioned type, the nodal interpolants $i_h u \in \mathcal{V}_h$ and $i_h^+ u \in \mathcal{V}_h^+$ of a function $u \in W^{r,\eta}(\Omega) \cap C^0(\overline{\Omega})$ onto $\mathcal{V}_h$ and $\mathcal{V}_h^+$, respectively, satisfy the standard interpolation estimate

$$\|i_h^+ u - u\|_{s,\eta} + \|i_h u - u\|_{s,\eta} \leq C h^{r-s} |u|_{r,\eta} \tag{4.1}$$

for any $s \in \{0, 1\}$, any $\eta \in [2, \infty]$, and every $h \leq h_0$ [45]. Here and throughout this chapter, the letter C denotes a constant that is not necessarily the same at each occurrence and is independent of h.

Using the triangle inequality and (4.1) with $\eta = 2$ gives an immediate upper bound on the L^2- and H^1-norms of the difference between $i_h^+ u$ and $i_h u$. Namely,

$$\|i_h^+ u - i_h u\|_{s,2} \leq C h^{r-s} |u|_{r,2} \tag{4.2}$$

for any $s \in \{0, 1\}$ and every $h \leq h_0$.

Suppose, however, that $\mathcal{T}_h$ and $\mathcal{T}_h^+$ are nearby in the following sense: the two meshes coincide except on a region of measure $O(h^\gamma)$ for some scalar $\gamma \geq 0$. In this scenario, $i_h u$ and $i_h^+ u$ agree everywhere except in the region over which the meshes differ. Hence, by an application of Holder's

inequality (cf. Lemma 4.3.1), the triangle inequality, and (4.1),

$$\begin{aligned}\|i_h^+ u - i_h u\|_{s,2} &\leq Ch^{\gamma(1/2-1/\eta)}\|i_h^+ u - i_h u\|_{s,\eta} \\ &\leq Ch^{\gamma(1/2-1/\eta)}\left(\|i_h^+ u - u\|_{s,\eta} + \|u - i_h u\|_{s,\eta}\right) \\ &\leq Ch^{r-s+\gamma(1/2-1/\eta)}|u|_{r,\eta} \end{aligned} \tag{4.3}$$

for any $s \in \{0,1\}$, any $\eta \in [2,\infty]$, and every $h \leq h_0$.

A comparison of (4.3) with the naive estimate (4.2) reveals that $i_h u$ and $i_h^+ u$ are *superclose* in the L^2- and H^1-norms when the corresponding meshes are nearby. The primary goal of this chapter is to prove an analogous superconvergent estimate when $i_h u$ and $i_h^+ u$ are replaced by the orthogonal projections $r_h u$ and $r_h^+ u$ of u onto $\mathcal{V}_h$ and $\mathcal{V}_h^+$, respectively, with respect to a coercive, continuous bilinear form $a : \mathcal{V} \times \mathcal{V} \to \mathbb{R}$, where $\mathcal{V} \subseteq H^s(\Omega)$ and s is a nonnegative integer. As special cases, our results apply to L^2-projections (the case $s = 0$) and elliptic projections (the case $s = 1$) onto piecewise polynomial finite element spaces. Another applicable case of interest is that in which the bilinear form a is of the form

$$a(u,w) = \int_\Omega \nabla u \cdot \nabla w \, dx - \int_\Omega (v \cdot \nabla u) w \, dx + \kappa \int_\Omega uw \, dx$$

with a constant $\kappa > 0$ and a vector field $v : \Omega \to \mathbb{R}^d$. This bilinear form appeared in the analysis of finite element methods for the diffusion equation on a moving domain presented in Chapter 3, with v playing the role of the velocity of a moving mesh and κ an auxiliary constant introduced to ensure coercivity.

It is not obvious that superconvergent estimates of the form (4.3) should hold in these settings, since the projections of u onto $\mathcal{V}_h$ and $\mathcal{V}_h^+$ need not agree on the region over which the meshes coincide. Nevertheless, Corollaries 4.2.3 and 4.2.5 provide such estimates under suitable assumptions on the finite element spaces $\mathcal{V}_h$ and $\mathcal{V}_h^+$ and the bilinear form a. The proof uses the observation that, loosely speaking, $a(r_h^+ u - r_h u, r_h^+ u - r_h u)$ is small if $r_h^+ u - r_h u$ is well-approximated by an element of $\mathcal{V}_h^+ \cap \mathcal{V}_h$, since

$$a(r_h^+ u - r_h u, w_h) = a(r_h^+ u - u, w_h) + a(u - r_h u, w_h) = 0$$

for any $w_h \in \mathcal{V}_h^+ \cap \mathcal{V}_h$. In particular, if $\|r_h^+ u - r_h u - w_h\|_{s,2}$ decays to zero more rapidly as $h \to 0$ than do $\|r_h^+ u - u\|_{s,2}$ and $\|r_h u - u\|_{s,2}$, then a superconvergent estimate for $\|r_h^+ u - r_h u\|_{s,2}$ follows from the relation

$$a(r_h^+ u - r_h u, r_h^+ u - r_h u) = a(r_h^+ u - r_h u, r_h^+ u - r_h u - w_h)$$

together with the coercivity and continuity of a. We in fact prove a more general result that applies

to the case in which the projectors r_h and r_h^+ are associated not only with different subspaces $\mathcal{V}_h$ and $\mathcal{V}_h^+$, but also with different bilinear forms a_h and a_h^+ that may depend on h.

Organization. This chapter is organized as follows. In Section 4.2, we summarize our main results. We begin with an abstract estimate (Theorem 4.2.1) for the H^s-norm of $r_h^+ u - r_h u$. We then apply Theorem 4.2.1 to the setting of finite element spaces with nontrivial intersection in Theorem 4.2.2. Under some additional assumptions on the finite element spaces, the bilinear forms, and the regularity of u, we deduce in Corollary 4.2.3 a superconvergent estimate for $\|r_h^+ u - r_h u\|_{s,2}$ that parallels (4.3). Next, we specialize to the case in which $s = 1$ and a_h and a_h^+ are bilinear forms associated with elliptic operators that possess smoothing properties. We use a duality argument to prove a superconvergent estimate (Theorem 4.2.4 and Corollary 4.2.5) for the L^2-norm of $r_h^+ u - r_h u$ that is up to one order higher than the corresponding estimate in the H^1-norm given by Corollary 4.2.3.

In Section 4.3, we present proofs of the preceding results and provide a few remarks along the way.

In Section 4.4, we demonstrate the necessity of the regularity assumptions on u that are imposed in the theorems by exhibiting an example of a pair of projectors r_h and r_h^+ and a function u whose insufficient regularity leads to a reduction in the rates of convergence of $\|r_h^+ u - r_h u\|_{1,2}$ and $\|r_h^+ u - r_h u\|_{0,2}$.

Finally, we give numerical examples to illustrate our positive theoretical results in Section 4.5.

Related work. The results presented in this chapter bear resemblance to the well-studied phenomenon of superconvergence in finite element theory, where the functions under comparison are typically the solution to a PDE and the numerical solution to a finite element discretization of the same problem. The phenomenon often manifests itself as an exceptional rate of convergence of the finite element solution to the exact solution at isolated points in the domain, as in [12, 17, 65, 85, 122, 134]. Related results involve exceptional rates of convergence of the finite element solution to a discrete representative of the exact solution, such as its interpolant [5, 15, 26, 76, 92, 96, 109]. Finally, post-processing techniques can lead to modifications of a finite element solution that converge more rapidly to the exact solution than the unprocessed finite element solution [11, 15, 36, 66, 85, 86, 146]. To our knowledge, however, little attention has been paid to the supercloseness of finite element solutions associated with differing meshes.

4.2 Statement of Results

Notation. Fixing a nonnegative integer s and an open, bounded, Lipschitz domain $\Omega \subset \mathbb{R}^d$, let $\mathcal{V}$ be a closed subspace of $H^s(\Omega)$. Let $a_h : \mathcal{V} \times \mathcal{V} \to \mathbb{R}$ and $a_h^+ : \mathcal{V} \times \mathcal{V} \to \mathbb{R}$ be bilinear forms that may depend on a parameter $h \leq h_0$, where h_0 is a positive scalar. We assume that a_h and a_h^+ are

continuous and coercive uniformly in h. In other words, for every $h \le h_0$ and every $u, w \in \mathcal{V}$, the inequalities

$$a_h(u,u) \ge \alpha \|u\|_{s,2}^2,$$
$$a_h(u,w) \le M \|u\|_{s,2} \|w\|_{s,2}$$

hold with constants α and M independent of h, and similarly for a_h^+ (with the same constants α and M).

Let $\{\mathcal{V}_h\}_{0<h\le h_0}$ and $\{\mathcal{V}_h^+\}_{0<h\le h_0}$ be two families of finite element subspaces of $\mathcal{V}$. It is a consequence of the Lax-Milgram theorem that the maps $r_h : \mathcal{V} \to \mathcal{V}_h$ and $r_h^+ : \mathcal{V} \to \mathcal{V}_h^+$ defined by the relations

$$a_h(r_h u - u, w_h) = 0 \quad \forall w_h \in \mathcal{V}_h$$

and

$$a_h^+(r_h^+ u - u, w_h^+) = 0 \quad \forall w_h^+ \in \mathcal{V}_h^+,$$

respectively, are well-defined linear projectors.

For intuition, it is useful to think of $\mathcal{V}_h$ and $\mathcal{V}_h^+$ as finite element spaces associated with a pair of meshes $\mathcal{T}_h$ and $\mathcal{T}_h^+$ of Ω, with the parameter h denoting the maximum diameter of an element among all elements of $\mathcal{T}_h$ and $\mathcal{T}_h^+$. This level of concreteness, however, is not needed for a presentation of the results that follow.

Abstract estimate. Our first result is an abstract estimate for the H^s-norm of $r_h^+ u - r_h u$. It provides an alternative to the obvious upper bound

$$\|r_h^+ u - r_h u\|_{s,2} \le \|r_h^+ u - u\|_{s,2} + \|u - r_h u\|_{s,2}$$

that one obtains from the triangle inequality. Its utility will be made apparent shortly.

Theorem 4.2.1. *Let a_h^+ and a_h be uniformly coercive and continuous bilinear forms on $\mathcal{V} \times \mathcal{V}$. Then for every $u \in \mathcal{V}$ and every $h \le h_0$,*

$$\begin{aligned} \|r_h^+ u - r_h u\|_{s,2} \le \inf_{\substack{e_h \in \mathcal{V}_h \\ e_h^+ \in \mathcal{V}_h^+}} \Big[& \frac{M}{\alpha} \big\| r_h^+ u - r_h u - (e_h + e_h^+) \big\|_{s,2} \\ & + \frac{1}{\sqrt{\alpha}} \Big(\big| a_h^+(r_h^+ u - u, e_h) \big|^{1/2} + \big| a_h(r_h u - u, e_h^+) \big|^{1/2} \\ & + \big| a_h^+(r_h u - u, e_h + e_h^+) - a_h(r_h u - u, e_h + e_h^+) \big|^{1/2} \Big) \Big]. \end{aligned} \tag{4.4}$$

The preceding theorem provides a heuristic for estimating the H^s-norm of $r_h^+ u - r_h u$. Namely, one seeks functions $e_h \in \mathcal{V}_h$ and $e_h^+ \in \mathcal{V}_h^+$ that are nearly (right-) orthogonal to $r_h^+ u - u$ and $r_h u - u$

with respect to $a_h^+(\cdot,\cdot)$ and $a_h(\cdot,\cdot)$, respectively, but whose sum is close to $r_h^+u - r_hu$. In general, near orthogonality and closeness to $r_h^+u - r_hu$ are competing interests. Exact orthogonality holds for $e_h, e_h^+ \in \mathcal{V}_h^+ \cap \mathcal{V}_h$, whereas $e_h + e_h^+$ can be made equal to $r_h^+u - r_hu$ by choosing, for instance, $e_h^+ = r_h^+u$ and $e_h = -r_hu$. If a suitable choice of e_h and e_h^+ leads to adequate satisfaction of both interests simultaneously, and if a_h^+ is close to a_h (in the sense that the last term in (4.4) is small), then the prospects of producing a superconvergent bound on $\|r_h^+u - r_hu\|_{s,2}$ are favorable.

Finite element spaces with nontrivial intersection. We now apply Theorem 4.2.1 to the case in which the finite element spaces $\mathcal{V}_h^+$ and $\mathcal{V}_h$ intersect nontrivially. The setting that we have in mind is that in which $\mathcal{V}_h$ and $\mathcal{V}_h^+$ consist of continuous functions that are elementwise polynomials over shape-regular, quasi-uniform meshes of Ω that coincide except on a region of measure $O(h^\gamma)$ for some constant $\gamma \geq 0$. To allow for more generality, we state the assumptions on $\mathcal{V}_h^+$ and $\mathcal{V}_h$ abstractly, and we refer the reader to Appendix 4.A for a proof of their satisfaction in the aforementioned setting.

In particular, we assume the existence of a constant $\eta \in [2,\infty]$ such that the following properties hold:

(4.2.2.i) For every $h \leq h_0$, $\mathcal{V}_h, \mathcal{V}_h^+ \subset W^{s,\eta}(\Omega) \cap \mathcal{V}$.

(4.2.2.ii) There exists $C > 0$ independent of h such that the inverse estimate

$$\|w_h\|_{m,\eta} \leq Ch^{-m}\|w_h\|_{0,\eta}$$

holds for every $m = 0, 1, \ldots, s$, every $w_h \in \mathcal{V}_h^+ \cap \mathcal{V}_h$, and every $h \leq h_0$.

(4.2.2.iii) There exist constants $\gamma \geq 0$ and $C > 0$ independent of h and a map $\pi_h : \mathcal{V}_h^+ + \mathcal{V}_h \to \mathcal{V}_h^+ \cap \mathcal{V}_h$ such that

$$\|\pi_h w_h\|_{0,\eta} \leq C\|w_h\|_{0,\eta}$$

and

$$|\mathrm{supp}(\pi_h w_h - w_h)| \leq Ch^\gamma$$

for every $w_h \in \mathcal{V}_h^+ + \mathcal{V}_h$ and every $h \leq h_0$.

In the context of finite element spaces consisting of continuous functions that are elementwise polynomials over shape-regular, quasi-uniform meshes of Ω, a befitting choice for π_h in (4.2.2.iii) is the nodal interpolant onto $\mathcal{V}_h^+ \cap \mathcal{V}_h$; see Appendix 4.A. In that setting, the constant γ appearing in (4.2.2.iii) may take on any real value between 0 and d, unless the two meshes coincide entirely (in which case γ may be chosen arbitrarily large). To realize a pair of meshes $\mathcal{T}_h$ and $\mathcal{T}_h^+$ fulfilling (4.2.2.iii) with $\gamma \in [0,d]$, one may, for instance, consider a shape-regular, quasi-uniform mesh $\mathcal{T}_h$ of Ω and perturb the positions of $O(h^{-d+\gamma})$ of its nodes by a sufficiently small amount to define $\mathcal{T}_h^+$.

The following theorem results from applying Theorem 4.2.1 to the setting delineated in conditions (4.2.2.i-4.2.2.iii), with the choice $e_h = \pi_h(r_h^+ u - r_h u)$ and $e_h^+ = 0$ in (4.4).

Theorem 4.2.2. *Suppose the conditions of Theorem 4.2.1 hold and the finite element spaces $\mathcal{V}_h^+$ and $\mathcal{V}_h$ satisfy conditions (4.2.2.i-4.2.2.iii). Suppose further that there exist constants $C_1 > 0$, $\delta \geq 0$, $1 \leq q \leq \eta$, and $\mu, \nu \in \{0, 1, \ldots, s\}$ independent of h such that*

$$|a_h^+(v, w) - a_h(v, w)| \leq C_1 h^\delta \|v\|_{\mu,\eta} \|w\|_{\nu,q} \tag{4.5}$$

for every $v, w \in W^{s,\eta}(\Omega) \cap \mathcal{V}$ and every $h \leq h_0$. Then there exists $C > 0$ independent of h such that for any $h \leq h_0$ and any $u \in W^{s,\eta}(\Omega) \cap \mathcal{V}$,

$$\begin{aligned}\|r_h^+ u - r_h u\|_{s,2} \leq C h^{\sigma - s} \Big[& h^s \|r_h^+ u - u\|_{s,\eta} + h^s \|r_h u - u\|_{s,\eta} + \|r_h^+ u - u\|_{0,\eta} + \|r_h u - u\|_{0,\eta} \\ & + \left(h^\mu \|r_h u - u\|_{\mu,\eta}\right)^{1/2} \left(\|r_h^+ u - u\|_{0,\eta} + \|r_h u - u\|_{0,\eta}\right)^{1/2} \Big]\end{aligned}$$

with

$$\sigma = \min\left\{ \gamma \left(\frac{1}{2} - \frac{1}{\eta} \right), \frac{\delta + 2s - \mu - \nu}{2} \right\}. \tag{4.6}$$

The meaning of Theorem 4.2.2 is clearest when the quantities $h^m \|r_h u - u\|_{m,p}$ and $h^m \|r_h^+ u - u\|_{m,p}$, $m = 0, 1, \ldots, s$, $p = 2, \eta$, all decay at the same rate with respect to h as $h \to 0$. In such a setting, the theorem states that $\|r_h^+ u - r_h u\|_{s,2}$ tends to zero faster than $\|r_h u - u\|_{s,2} + \|r_h^+ u - u\|_{s,2}$ by a factor $O(h^\sigma)$, where the order of superconvergence σ depends primarily upon two features: (1) the extent to which the finite element spaces $\mathcal{V}_h$ and $\mathcal{V}_h^+$ coincide, as measured by the constant γ in (4.2.2.iii), and (2) the difference between the bilinear forms a_h and a_h^+, as measured by the constants δ, μ, and ν in (4.5). The regularity of u also plays a role in the estimate via the constant η, which is in the best case equal to ∞.

To be more concrete, let us point out that in many contexts (which we detail in Appendix 4.B), the quantities $r_h u - u$ and $r_h^+ u - u$ satisfy estimates of the form

$$\|r_h u - u\|_{0,\eta} + \|r_h^+ u - u\|_{0,\eta} \leq C \ell(h) h^r |u|_{r,\eta}, \tag{4.7}$$

$$\|r_h u - u\|_{m,\eta} + \|r_h^+ u - u\|_{m,\eta} \leq C h^{r-m} |u|_{r,\eta}, \quad m = 1, 2, \ldots, s, \tag{4.8}$$

for every $u \in W^{r,\eta}(\Omega) \cap \mathcal{V}$ and every $h \leq h_0$, where $r > s$ is an integer and $\ell(h)$ is either identically unity or equal to $\log(h^{-1})$. Note that (4.8) is vacuous when $s = 0$. When such estimates hold, the following corollary to Theorem 4.2.2 is immediate.

Corollary 4.2.3. *Suppose that the conditions of Theorem 4.2.2 are satisfied and that both r_h and r_h^+ satisfy estimates of the form (4.7-4.8) for an integer $r > s$. Then there exists $C > 0$ independent*

of h such that

$$\|r_h^+ u - r_h u\|_{s,2} \leq C\ell(h)h^{r-s+\sigma}|u|_{r,\eta}$$

for every $u \in W^{r,\eta}(\Omega) \cap \mathcal{V}$ and every $h \leq h_0$, with σ given by (4.6).

In particular, if $a_h = a_h^+$, then

$$\|r_h^+ u - r_h u\|_{s,2} \leq C\ell(h)h^{r-s+\gamma(1/2-1/\eta)}|u|_{r,\eta}$$

for every $u \in W^{r,\eta}(\Omega) \cap \mathcal{V}$ and every $h \leq h_0$.

Note that to deduce the preceding corollary, the case $a_h = a_h^+$ is handled by taking $\delta = \infty$ and choosing any admissible μ, ν and q in (4.5).

L^2 estimates for elliptic projections. Finally, we restrict our attention to the case $s = 1$ with $\mathcal{V} = H_0^1(\Omega)$, so that a_h and a_h^+ are coercive, continuous bilinear forms on $H_0^1(\Omega) \times H_0^1(\Omega)$, uniformly in h. Here, $H_0^1(\Omega)$ denotes the space of functions in $H^1(\Omega)$ with vanishing trace on $\partial\Omega$. Our aim is to provide an estimate for the L^2-norm of $r_h^+ u - r_h u$ that parallels the estimate in the H^1-norm provided by Corollary 4.2.3 but is of a higher order by up to one power of h.

In addition to the assumptions stated in Theorem 4.2.2, we make the following assumptions on the bilinear forms a_h and a_h^+.

(4.2.4.i) The bilinear forms a_h and a_h^+ are associated with elliptic operators whose adjoints possess *smoothing properties* (cf. [45, Definition 3.14]), uniformly in h. Precisely, let $f \in L^2(\Omega)$ and consider the following problem: Find $w \in \mathcal{V}$ such that

$$a_h(y, w) = (f, y) \quad \forall y \in \mathcal{V}, \tag{4.9}$$

where $(f, y) := \int_\Omega fy$. Then a_h is said to have smoothing properties (uniformly in h) if there exists a constant $C > 0$ independent of h such that for every $f \in L^2(\Omega)$ and every $h \leq h_0$, there exists a unique solution w to (4.9) satisfying the elliptic regularity estimate

$$\|w\|_{2,2} \leq C\|f\|_{0,2}.$$

(4.2.4.ii) There exists $C > 0$ such that for any $h \leq h_0$, any subdomain $R \subseteq \Omega$, and any $v, w \in \mathcal{V}$ with $\operatorname{supp}(w) \subseteq R$,

$$|a_h(v, w)| \leq C\|v\|_{1,2,R}\|w\|_{1,2,R},$$

where the constant C is independent of h and R, and similarly for a_h^+.

(4.2.4.iii) The constant q appearing in the bound (4.5) satisfies the additional restriction

$$\begin{cases} q < \infty & \text{if } d = 4 - 2\nu, \\ q \leq \frac{2d}{d-4+2\nu} & \text{if } d > 4 - 2\nu. \end{cases}$$

Condition (4.2.4.iii) guarantees the validity of the Sobolev emdedding $H^2(\Omega) \subset W^{\nu,q}(\Omega)$. Note that it places no additional restriction on q if $d < 4 - 2\nu$.

Furthermore, we assume the existence of interpolation operators $i_h : \bar{\mathcal{V}} \to \mathcal{V}_h$ and $i_h^+ : \bar{\mathcal{V}} \to \mathcal{V}_h^+$ defined on a space $H^2(\Omega) \cap \mathcal{V} \subseteq \bar{\mathcal{V}} \subseteq \mathcal{V}$ that satisfy the following properties.

(4.2.4.iv) There exists $C > 0$ independent of h such that

$$\|i_h w\|_{\nu,q} + \|i_h^+ w\|_{\nu,q} \leq C\|w\|_{\nu,q}$$

for every $w \in H^2(\Omega) \cap \mathcal{V}$ and every $h \leq h_0$.

(4.2.4.v) There exists $C > 0$ independent of h such that

$$\|i_h w - w\|_{1,2} + \|i_h^+ w - w\|_{1,2} \leq Ch|w|_{2,2}$$

for every $w \in H^2(\Omega) \cap \mathcal{V}$ and every $h \leq h_0$.

(4.2.4.vi) For every $w \in H^2(\Omega) \cap \mathcal{V}$ and every $h \leq h_0$,

$$\operatorname{supp}(i_h^+ w - i_h w) \subseteq \mathcal{R}_h,$$

where

$$\mathcal{R}_h := \bigcup_{w_h \in \mathcal{V}_h + \mathcal{V}_h^+} \operatorname{supp}(w_h - \pi_h w_h)$$

and π_h is the map introduced in (4.2.2.iii).

Our estimate for the L^2-norm of $r_h^+ u - r_h u$, whose proof employs a duality argument, is as follows.

Theorem 4.2.4. *Suppose the conditions of Theorem 4.2.2 hold with $s = 1$. Assume further that conditions (4.2.4.i-4.2.4.vi) hold. Then there exists $C > 0$ independent of h such that for every $u \in W^{1,\eta}(\Omega) \cap \mathcal{V}$ and every $h \leq h_0$,*

$$\begin{aligned} \|r_h^+ u - r_h u\|_{0,2} \leq Ch^{\sigma'} \Big[& h\|r_h^+ u - u\|_{1,\eta} + h\|r_h u - u\|_{1,\eta} + \|r_h^+ u - u\|_{0,\eta} + \|r_h u - u\|_{0,\eta} \\ & + \left(h^\mu \|r_h u - u\|_{\mu,\eta}\right)^{1/2} \left(\|r_h^+ u - u\|_{0,\eta} + \|r_h u - u\|_{0,\eta}\right)^{1/2} \\ & + h^\mu \|r_h u - u\|_{\mu,\eta} \Big], \end{aligned}$$

with

$$\sigma' = \min\left\{\gamma\left(\frac{1}{2}-\frac{1}{\eta}\right), \frac{\delta+2-\mu-\nu}{2}, \delta-\mu\right\}. \tag{4.10}$$

Just as in Theorem 4.2.2, the meaning of Theorem 4.2.4 is clearest when the quantities $h^m\|r_h u - u\|_{m,p}$ and $h^m\|r_h^+ u - u\|_{m,p}$, $m = 0, 1, \ldots, s$, $p = 2, \eta$, all decay at the same rate with respect to h as $h \to 0$. In such a setting, Theorem 4.2.4 states that $\|r_h^+ u - r_h u\|_{0,2}$ tends to zero faster than $\|r_h u - u\|_{0,2} + \|r_h^+ u - u\|_{0,2}$ by a factor $O(h^{\sigma'})$, where the order of superconvergence σ' is given by (4.10). Note that $\sigma' \leq \sigma$, where σ is the order of superconvergence of the H^1-norm of $r_h^+ u - r_h u$ that was provided in Theorem 4.2.2.

Concretely, when estimates of the form (4.7-4.8) hold for $u \in W^{r,\eta}(\Omega) \cap \mathcal{V}$ with an integer $r > 1$, we arrive immediately at the following corollary to Theorem 4.2.4.

Corollary 4.2.5. *Suppose that the conditions of Theorem 4.2.2 are satisfied and that both r_h and r_h^+ satisfy estimates of the form (4.7-4.8) for an integer $r > 1$. Then there exists $C > 0$ independent of h such that*

$$\|r_h^+ u - r_h u\|_{0,2} \leq C\ell(h)h^{r+\sigma'}|u|_{r,\eta}$$

for every $u \in W^{r,\eta}(\Omega) \cap \mathcal{V}$ and every $h \leq h_0$, with σ' given by (4.10).

In particular, if $a_h = a_h^+$, then

$$\|r_h^+ u - r_h u\|_{0,2} \leq C\ell(h)h^{r+\gamma(1/2-1/\eta)}|u|_{r,\eta}$$

for every $u \in W^{r,\eta}(\Omega) \cap \mathcal{V}$ and every $h \leq h_0$.

Note that to deduce the preceding corollary, the case $a_h = a_h^+$ is again handled by taking $\delta = \infty$ and choosing any admissible μ, ν and q in (4.5).

4.3 Proofs

This section presents proofs of Theorems 4.2.1, 4.2.2, and 4.2.4.

Proof of Theorem 4.2.1. Let $e_h \in \mathcal{V}_h$ and $e_h^+ \in \mathcal{V}_h^+$, and write

$$\begin{aligned} a_h^+(r_h^+ u - r_h u, r_h^+ u - r_h u) = a_h^+\left(r_h^+ u - r_h u, r_h^+ u - r_h u - (e_h + e_h^+)\right) \\ + a_h^+(r_h^+ u - r_h u, e_h + e_h^+). \end{aligned}$$

The uniform coercivity and continuity of a_h^+ imply

$$\|r_h^+ u - r_h u\|_{s,2}^2 \leq \frac{1}{\alpha}\left(M\|r_h^+ u - r_h u\|_{s,2}\|r_h^+ u - r_h u - (e_h + e_h^+)\|_{s,2} + |a_h^+(r_h^+ u - r_h u, e_h + e_h^+)|\right).$$

Using the fact that for real numbers $x, a, b \geq 0$,

$$x^2 \leq ax + b \implies x \leq a + \sqrt{b},$$

we deduce that

$$\|r_h^+ u - r_h u\|_{s,2} \leq \frac{M}{\alpha}\|r_h^+ u - r_h u - (e_h + e_h^+)\|_{s,2} + \frac{1}{\sqrt{\alpha}}|a_h^+(r_h^+ u - r_h u, e_h + e_h^+)|^{1/2}$$

The result will then follow from the identity

$$\begin{aligned} a_h^+(r_h^+ u - r_h u, e_h + e_h^+) = a_h^+(r_h^+ u - u, e_h) + a_h(u - r_h u, e_h^+) \\ + a_h^+(u - r_h u, e_h + e_h^+) - a_h(u - r_h u, e_h + e_h^+) \end{aligned} \tag{4.11}$$

together with the subadditivity of the square root operator.

To prove (4.11), use the decomposition $r_h^+ u - r_h u = (r_h^+ u - u) + (u - r_h u)$ to write

$$a_h^+(r_h^+ u - r_h u, e_h + e_h^+) = a_h^+(r_h^+ u - u, e_h + e_h^+) + a_h^+(u - r_h u, e_h + e_h^+).$$

Now add and subtract $a_h(u - r_h u, e_h + e_h^+)$ to obtain

$$\begin{aligned} a_h^+(r_h^+ u - r_h u, e_h + e_h^+) = a_h^+(r_h^+ u - u, e_h + e_h^+) + a_h(u - r_h u, e_h + e_h^+) \\ + a_h^+(u - r_h u, e_h + e_h^+) - a_h(u - r_h u, e_h + e_h^+). \end{aligned}$$

Finally, use the definitions of r_h^+ and r_h to simplify the first two terms, giving (4.11). □

We remark that while the estimate (4.4) is not symmetric in the "+" variables and their unadorned counterparts, it can easily be made symmetric by exchanging the roles of r_h^+ and a_h^+ with r_h and a_h, respectively, and averaging the resulting estimates. The same holds true for the estimates in Theorems 4.2.2 and 4.2.4.

We now turn to the proof of Theorem 4.2.2. We begin with a lemma concerning the relationship between a function's support and its Sobolev norms.

Lemma 4.3.1. *Let $f \in W^{k,p}(\Omega)$, $k \geq 0$, $p \in [1, \infty]$. Then for any $1 \leq t \leq p$,*

$$\|f\|_{k,t} \leq |\mathrm{supp}(f)|^{1/t - 1/p}\|f\|_{k,p}.$$

Proof. Let $\chi : \Omega \to \{0, 1\}$ denote the indicator function for $\mathrm{supp}(f)$. We have

$$\begin{aligned}\|f\|_{k,t} &= \sum_{|\alpha|\le k} \|\partial^\alpha f\|_{0,t} \\ &= \sum_{|\alpha|\le k} \|\chi\partial^\alpha f\|_{0,t}.\end{aligned}$$

Now let $\tilde{p} \in [1, \infty]$ be such that $\frac{1}{\tilde{p}} + \frac{1}{p} = \frac{1}{t}$. By Holder's inequality,

$$\begin{aligned}\|f\|_{k,t} &\le \sum_{|\alpha|\le k} \|\chi\|_{0,\tilde{p}} \|\partial^\alpha f\|_{0,p} \\ &= |\mathrm{supp}(f)|^{1/\tilde{p}} \sum_{|\alpha|\le k} \|\partial^\alpha f\|_{0,p} \\ &= |\mathrm{supp}(f)|^{1/t-1/p} \|f\|_{k,p}.\end{aligned}$$

□

The proof of Theorem 4.2.2 is as follows.

Proof of Theorem 4.2.2. Choose $e_h^+ = 0$ and $e_h = \pi_h(r_h^+ u - r_h u)$ in (4.4). By the stability assumption in (4.2.2.iii),

$$\begin{aligned}\|e_h\|_{0,\eta} &\le C\|r_h^+ u - r_h u\|_{0,\eta} \\ &\le C\left(\|r_h^+ u - u\|_{0,\eta} + \|u - r_h u\|_{0,\eta}\right).\end{aligned}$$

Thus, for any $m = 0, 1, \ldots, s$,

$$\|e_h\|_{m,\eta} \le Ch^{-m}\left(\|r_h^+ u - u\|_{0,\eta} + \|u - r_h u\|_{0,\eta}\right) \tag{4.12}$$

by (4.2.2.ii). It follows that

$$\begin{aligned}\|r_h^+ u - r_h u - (e_h + e_h^+)\|_{s,\eta} &\le \|r_h^+ u - u\|_{s,\eta} + \|u - r_h u\|_{s,\eta} + \|e_h\|_{s,\eta} + \|e_h^+\|_{s,\eta} \\ &\le C\big(\|r_h^+ u - u\|_{s,\eta} + \|u - r_h u\|_{s,\eta} \\ &\qquad + h^{-s}\|r_h^+ u - u\|_{0,\eta} + h^{-s}\|u - r_h u\|_{0,\eta}\big).\end{aligned}$$

Now note that $r_h^+ u - r_h u - (e_h + e_h^+)$ has support of measure $O(h^\gamma)$ by (4.2.2.iii). Consequently, by

Lemma 4.3.1,

$$\begin{aligned}\|r_h^+u - r_hu - (e_h + e_h^+)\|_{s,2} &\le Ch^{\gamma(1/2-1/\eta)}\|r_h^+u - r_hu - (e_h + e_h^+)\|_{s,\eta} \\ &\le Ch^{\gamma(1/2-1/\eta)}\big(\|r_h^+u - u\|_{s,\eta} + \|r_hu - u\|_{s,\eta} \\ &\qquad + h^{-s}\|r_h^+u - u\|_{0,\eta} + h^{-s}\|r_hu - u\|_{0,\eta}\big). \end{aligned} \tag{4.13}$$

To estimate the remaining terms that appear in (4.4), note that

$$a_h^+(r_h^+u - u, e_h) = 0$$

since $e_h \in \mathcal{V}_h^+ \cap \mathcal{V}_h \subseteq \mathcal{V}_h^+$, and

$$a_h(r_hu - u, e_h^+) = 0$$

since $e_h^+ = 0$. Finally, using (4.12) with $m = \nu$ together with (4.5) shows that

$$\begin{aligned}\left|a_h^+(r_hu - u, e_h + e_h^+) - a_h(r_hu - u, e_h + e_h^+)\right| &\le Ch^{\delta}\|r_hu - u\|_{\mu,\eta}\|e_h\|_{\nu,q} \\ &\le Ch^{\delta}\|r_hu - u\|_{\mu,\eta}\|e_h\|_{\nu,\eta} \\ &\le Ch^{\delta-\nu}\|r_hu - u\|_{\mu,\eta}\left(\|r_h^+u - u\|_{0,\eta} + \|u - r_hu\|_{0,\eta}\right).\end{aligned}$$

Taking the square root and adding (4.13) proves the claim. □

Note that the preceding proof treats the estimate (4.5) wastefully when $q < \eta$, in the sense that the ultimate bound on $\|r_h^+u - r_hu\|_{s,2}$ is unchanged if q is replaced by η. The importance of considering scenarios in which q may be chosen less than η is made apparent in Theorem 4.2.4, where the restriction (4.2.4.iii) is enforced.

With this in mind, we now prove Theorem 4.2.4.

Proof of Theorem 4.2.4. Define $w \in \mathcal{V}$ as the solution to the dual problem

$$a_h^+(y, w) = (r_h^+u - r_hu, y) \quad \forall y \in \mathcal{V}. \tag{4.14}$$

Note that $w \in H^2(\Omega) \cap \mathcal{V}$ by (4.2.4.i).

For any $w_h^+ \in \mathcal{V}_h^+$, $w_h \in \mathcal{V}_h$, we have

$$\begin{aligned}
\|r_h^+ u - r_h u\|_{0,2}^2 &= a_h^+(r_h^+ u - r_h u, w) \\
&= a_h^+(r_h^+ u - r_h u, w - w_h^+) + a_h^+(r_h^+ u - r_h u, w_h^+) \\
&= a_h^+(r_h^+ u - r_h u, w - w_h^+) + a_h^+(u - r_h u, w_h^+) \\
&= a_h^+(r_h^+ u - r_h u, w - w_h^+) + a_h^+(u - r_h u, w_h^+ - w_h) \\
&\quad + a_h^+(u - r_h u, w_h) - a_h(u - r_h u, w_h) \\
&=: T_1 + T_2 + T_3,
\end{aligned}$$

where

$$\begin{aligned}
T_1 &= a_h^+(r_h^+ u - r_h u, w - w_h^+), \\
T_2 &= a_h^+(u - r_h u, w_h^+ - w_h), \\
T_3 &= a_h^+(u - r_h u, w_h) - a_h(u - r_h u, w_h).
\end{aligned}$$

Now choose $w_h^+ = i_h^+ w$ and $w_h = i_h w$ and bound each term separately. By the continuity of a_h^+ and (4.2.4.v),

$$\begin{aligned}
|T_1| &\le C\|r_h^+ u - r_h u\|_{1,2}\|w - w_h^+\|_{1,2} \\
&\le Ch\|r_h^+ u - r_h u\|_{1,2}|w|_{2,2}.
\end{aligned}$$

To bound T_2, note that $\operatorname{supp}(w_h^+ - w_h) \subseteq \mathcal{R}_h$ has measure $O(h^\gamma)$ by (4.2.4.vi) and (4.2.2.iii). Thus,

$$\begin{aligned}
|T_2| &\le C\|u - r_h u\|_{1,2,\mathcal{R}_h}\|w_h^+ - w_h\|_{1,2,\mathcal{R}_h} \\
&\le Ch^{\gamma(1/2-1/\eta)}\|u - r_h u\|_{1,\eta}\left(\|w_h^+ - w\|_{1,2,\mathcal{R}_h} + \|w - w_h\|_{1,2,\mathcal{R}_h}\right) \\
&\le Ch^{\gamma(1/2-1/\eta)+1}\|u - r_h u\|_{1,\eta}|w|_{2,2}
\end{aligned}$$

by (4.2.4.ii), Lemma 4.3.1, and (4.2.4.v). For T_3, we have by (4.5) that

$$|T_3| \le Ch^\delta\|u - r_h u\|_{\mu,\eta}\|w_h\|_{\nu,q}.$$

Using (4.2.4.iv) together with the Sobolev embedding $H^2(\Omega) \subset W^{\nu,q}(\Omega)$ ensured by (4.2.4.iii) gives

$$|T_3| \le Ch^\delta\|u - r_h u\|_{\mu,\eta}\|w\|_{2,2}.$$

Combining results and invoking the regularity estimate (4.2.4.i) leads to

$$\|r_h^+ u - r_h u\|_{0,2} \le C\Big[h\|r_h^+ u - r_h u\|_{1,2} + h^{\min\{\gamma(1/2-1/\eta),\delta-\mu\}}\left(h\|u - r_h u\|_{1,\eta} + h^{\mu}\|u - r_h u\|_{\mu,\eta}\right)\Big].$$

Conclude using Theorem 4.2.2. □

4.4 The Need for Regularity

When $a_h^+ = a_h$ and γ is fixed, the estimates of Corollaries 4.2.3 and 4.2.5 are of the highest order in h when $\eta = \infty$, but in this case they demand that $u \in W^{r,\infty}(\Omega) \cap \mathcal{V}$. If the regularity requirement $u \in W^{r,\infty}(\Omega) \cap \mathcal{V}$ is relaxed, the rates of convergence of $\|r_h^+ u - r_h u\|_{0,2}$ and $\|r_h^+ u - r_h u\|_{1,2}$ as $h \to 0$ may deteriorate.

Indeed, consider the case in which $\mathcal{V}_h$ is the space of piecewise affine functions on a grid $(0, h, 2h, 3h, \ldots, 1)$ of the unit interval in one dimension that vanish at 0 and 1. Let $\mathcal{V}_h^+$ be the space of piecewise affine functions on the nearby grid $(0, 3h/2, 2h, 3h, \ldots, 1)$ that vanish at 0 and 1. Let

$$a_h^+(u, w) = a_h(u, w) = \int_0^1 \frac{\partial u}{\partial x}\frac{\partial w}{\partial x}\, dx,$$

so that the projectors r_h and r_h^+ coincide with the nodal interpolants onto $\mathcal{V}_h$ and $\mathcal{V}_h^+$, respectively [45, Remark 3.25(i)]. In this setting, the conditions of Corollaries 4.2.3 and 4.2.5 hold with $\eta = \infty$, $\gamma = 1$, $r = 2$, and $\ell(h) \equiv 1$, leading to the estimates

$$\|r_h^+ u - r_h u\|_{0,2} \le Ch^{5/2}|u|_{r,\infty},$$
$$\|r_h^+ u - r_h u\|_{1,2} \le Ch^{3/2}|u|_{r,\infty}$$

for $u \in W^{2,\infty}(0,1) \cap H_0^1(0,1)$.

However, consider the function

$$u(x) = x^{2-1/p} - x$$

with $2 < p < \infty$, so that $u \in W^{2,p-\varepsilon}(0,1) \cap H_0^1(0,1)$ for any $\varepsilon > 0$. Then a direct calculation renders that

$$\|r_h^+ u - r_h u\|_{0,2} \ge Ch^{5/2-1/p},$$
$$\|r_h^+ u - r_h u\|_{1,2} \ge Ch^{3/2-1/p},$$

which are of a lower order than the rates $h^{5/2}$ and $h^{3/2}$, respectively, obtainable for a function in $W^{2,\infty}(0,1) \cap H_0^1(0,1)$. In fact, by letting $p \to 2$, these rates can be made arbitrarily close to the

Table 4.1: L^2-supercloseness of L^2-projections onto piecewise affine ($r = 2$) and piecewise quadratic ($r = 3$) finite element spaces over nearby meshes ($\gamma = 1$) in one dimension.

	Affine ($r = 2$)		Quadratic ($r = 3$)	
h_0/h	$\|r_h^+ u - r_h u\|_{0,2}$	Order	$\|r_h^+ u - r_h u\|_{0,2}$	Order
1	3.2150e-03	-	1.2843e-04	-
2	5.6505e-04	2.5084	1.0676e-05	3.5886
4	9.9837e-05	2.5007	9.1277e-07	3.5480
8	1.7645e-05	2.5003	7.9301e-08	3.5248
16	3.1189e-06	2.5002	6.9484e-09	3.5126
32	5.5132e-07	2.5001	6.1146e-10	3.5063

Table 4.2: H^1-supercloseness of elliptic projections onto piecewise affine ($r = 2$) and piecewise quadratic ($r = 3$) finite element spaces over nearby meshes ($\gamma = 1$) in one dimension.

	Affine ($r = 2$)		Quadratic ($r = 3$)	
h_0/h	$\|r_h^+ u - r_h u\|_{1,2}$	Order	$\|r_h^+ u - r_h u\|_{1,2}$	Order
1	1.4451e-01	-	7.4390e-03	-
2	5.1203e-02	1.4968	1.2835e-03	2.5351
4	1.8081e-02	1.5017	2.2408e-04	2.5180
8	6.3851e-03	1.5017	3.9364e-05	2.5090
16	2.2558e-03	1.5011	6.9369e-06	2.5045
32	7.9723e-04	1.5006	1.2243e-06	2.5023

Table 4.3: L^2-supercloseness of elliptic projections onto piecewise affine ($r = 2$) and piecewise quadratic ($r = 3$) finite element spaces over nearby meshes ($\gamma = 1$) in one dimension.

	Affine ($r = 2$)		Quadratic ($r = 3$)	
h_0/h	$\|r_h^+ u - r_h u\|_{0,2}$	Order	$\|r_h^+ u - r_h u\|_{0,2}$	Order
1	3.4546e-03	-	1.7770e-04	-
2	6.1937e-04	2.4796	1.5493e-05	3.5198
4	1.1019e-04	2.4908	1.3576e-06	3.5124
8	1.9537e-05	2.4957	1.1943e-07	3.5069
16	3.4587e-06	2.4979	1.0530e-08	3.5036
32	6.1186e-07	2.4990	9.2955e-10	3.5018

quadratic and linear rates that hold in the L^2- and H^1-norms, respectively, on a pair of unrelated meshes.

4.5 Numerical Examples

In this section, we numerically illustrate the superconvergent estimates of Corollaries 4.2.3 and 4.2.5 on test cases in one and two dimensions.

One dimension. Consider the case in which $\mathcal{V}_h$ is the space of piecewise polynomial functions of degree at most $r-1$ on a grid $(0, h, 2h, 3h, \ldots, 1)$ of the unit interval in one dimension that vanish at 0 and 1. Let $\mathcal{V}_h^+$ be the space of piecewise polynomial functions of the same degree that vanish at 0 and 1, on the same grid but with the node nearest to $x = 1/4$ perturbed by $h/4$ in the positive direction. In this scenario, assumption (4.2.2.iii) is satisfied with $\gamma = 1$. Let $u(x) = \sin(\pi x)$ and let

$$a_h^+(u, w) = a_h(u, w) = \int_0^1 uw \, dx,$$

so that r_h and r_h^+ are the L^2-projectors onto $\mathcal{V}_h$ and $\mathcal{V}_h^+$, respectively.

Table 4.1 shows the L^2-norm of the difference $r_h^+ u - r_h u$ for several values of h, beginning with $h = 1/8 =: h_0$. The table illustrates the predictions of Corollary 4.2.3, namely

$$\|r_h^+ u - r_h u\|_{0,2} \leq \begin{cases} Ch^{5/2}|u|_{2,\infty} & \text{if } r = 2, \\ Ch^{7/2}|u|_{3,\infty} & \text{if } r = 3. \end{cases}$$

Next, consider the same setup as above, but with

$$a_h^+(u, w) = a_h(u, w) = \int_0^1 \frac{\partial u}{\partial x} \frac{\partial w}{\partial x} \, dx,$$

so that r_h and r_h^+ are the standard elliptic projectors onto $\mathcal{V}_h$ and $\mathcal{V}_h^+$, respectively. Table 4.2 shows the H^1 norm of the difference $r_h^+ u - r_h u$ for the sequence of grids described above. The table illustrates the predictions of Corollary 4.2.3, namely

$$\|r_h^+ u - r_h u\|_{1,2} \leq \begin{cases} Ch^{3/2} \log(h^{-1})|u|_{2,\infty} & \text{if } r = 2, \\ Ch^{5/2}|u|_{3,\infty} & \text{if } r = 3. \end{cases}$$

Table 4.3 shows the L^2-norm of the difference $r_h^+ u - r_h u$ for the same sequence of grids. The table illustrates the predictions of Corollary 4.2.5, namely

$$\|r_h^+ u - r_h u\|_{0,2} \leq \begin{cases} Ch^{5/2} \log(h^{-1})|u|_{2,\infty} & \text{if } r = 2, \\ Ch^{7/2}|u|_{3,\infty} & \text{if } r = 3. \end{cases}$$

Note that we have not attempted to detect the presence of the factor $\log(h^{-1})$ in these numerical experiments.

Two dimensions. Consider now the case in which $\mathcal{V}_h \subset H_0^1((0,1)\times(0,1))$ is the space of piecewise affine functions on a mesh of the unit square in two dimensions consisting of equally sized isosceles right triangles, as in Fig. 4.1(a). Let $\mathcal{V}_h^+ \subset H_0^1((0,1) \times (0,1))$ be the space of piecewise affine

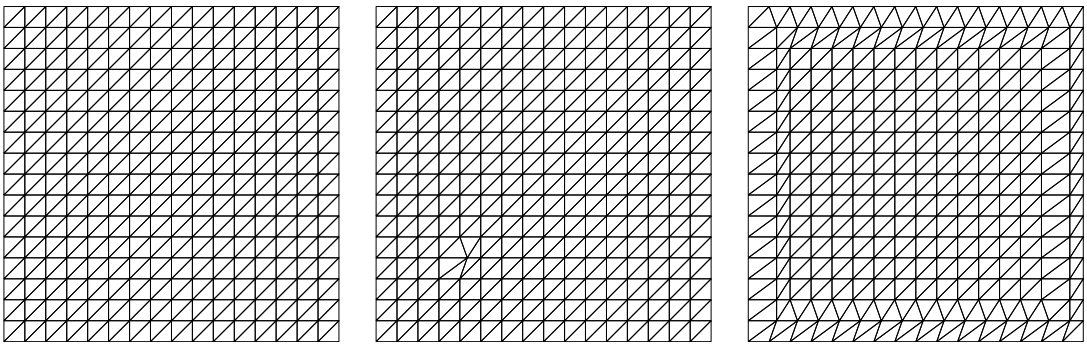

(a) (b) (c)

Figure 4.1: (a) Mesh of the unit square consisting of equally sized isosceles right triangles. (b) Identical mesh, but with the node at $(x, y) = (1/4, 1/4)$ perturbed by $h/4$ in the positive x direction. (c) Identical mesh, but with all nodes having distance $h/\sqrt{2}$ from the boundary perturbed by $h/4$ in the positive x direction.

Table 4.4: L^2-supercloseness of L^2-projections onto piecewise affine ($r = 2$) finite element spaces over nearby meshes ($\gamma = 2$; see Figs. 4.1(a) and 4.1(b)) in two dimensions.

	Affine ($r = 2$)	
h_0/h	$\|r_h^+ u - r_h u\|_{0,2}$	Order
1	6.3533e-03	-
2	7.5614e-04	3.0708
4	8.8718e-05	3.0914
8	1.1020e-05	3.0091
16	1.3781e-06	2.9993

functions on the same mesh, but with the node nearest to $(x, y) = (1/4, 1/4)$ perturbed by $h/4$ in the positive x direction, as in Fig. 4.1(b). In this scenario, assumption (4.2.2.iii) is satisfied with $\gamma = 2$. Let $u(x) = \sin(\pi x)\sin(\pi y)$ and let

$$a_h^+(u, w) = a_h(u, w) = \int_0^1 \int_0^1 uw \, dxdy,$$

so that r_h and r_h^+ are the L^2-projectors onto $\mathcal{V}_h$ and $\mathcal{V}_h^+$, respectively.

Table 4.4 shows the L^2-norm of the difference $r_h^+ u - r_h u$ for several values of h, beginning with $h = \sqrt{2}/4 =: h_0$. The table illustrates the predictions of Corollary 4.2.3, namely

$$\|r_h^+ u - r_h u\|_{0,2} \leq Ch^3 |u|_{2,\infty}. \tag{4.15}$$

Table 4.5: H^1- and L^2-supercloseness of elliptic projections onto piecewise affine ($r = 2$) finite element spaces over nearby meshes ($\gamma = 2$; see Figs. 4.1(a) and 4.1(b)) in two dimensions.

	Affine ($r = 2$)			
h_0/h	$\|r_h^+ u - r_h u\|_{1,2}$	Order	$\|r_h^+ u - r_h u\|_{0,2}$	Order
1	2.1441e-01	-	6.6386e-03	-
2	4.7374e-02	2.1782	7.8678e-04	3.0768
4	1.1359e-02	2.0603	9.6370e-05	3.0293
8	2.8114e-03	2.0144	1.2033e-05	3.0016
16	7.0176e-04	2.0023	1.5106e-06	2.9937

Table 4.6: L^2-supercloseness of L^2-projections onto piecewise affine ($r = 2$) finite element spaces over nearby meshes ($\gamma = 1$; see Figs. 4.1(a) and 4.1(c)) in two dimensions. Relative to Table 4.4, a lower order of superconvergence is observed due to the larger fraction of perturbed elements present in the perturbed mesh.

	Affine ($r = 2$)	
h_0/h	$\|r_h^+ u - r_h u\|_{0,2}$	Order
1	2.2504e-02	-
2	4.8445e-03	2.2158
4	1.0019e-03	2.2736
8	1.9159e-04	2.3866
16	3.5132e-05	2.4472
32	6.3195e-06	2.4749

Next, consider the same setup as above, but with

$$a_h^+(u,w) = a_h(u,w) = \int_0^1 \int_0^1 \left(\frac{\partial u}{\partial x}\frac{\partial w}{\partial x} + \frac{\partial u}{\partial y}\frac{\partial w}{\partial y} \right) dxdy,$$

so that r_h and r_h^+ are the elliptic projectors onto $\mathcal{V}_h$ and $\mathcal{V}_h^+$, respectively. Table 4.5 shows the H^1- and L^2-norms of the difference $r_h^+ u - r_h u$ for the sequence of meshes described above. The table illustrates the predictions of Corollaries 4.2.3 and 4.2.5, namely

$$\|r_h^+ u - r_h u\|_{m,2} \leq \begin{cases} Ch^2 \log(h^{-1})|u|_{2,\infty} & \text{if } m = 0, \\ Ch^3 \log(h^{-1})|u|_{2,\infty} & \text{if } m = 1. \end{cases} \tag{4.16}$$

Again, we have not attempted to detect the presence of the factor $\log(h^{-1})$.

More substantial mesh perturbation in two dimensions. Finally, consider the same two-dimensional tests as above, but with the mesh of Fig. 4.1(b) replaced by a different perturbation of the uniform mesh. Namely, consider perturbing all nodes whose distance from the boundary of the

Table 4.7: H^1- and L^2-supercloseness of elliptic projections onto piecewise affine ($r = 2$) finite element spaces over nearby meshes ($\gamma = 1$; see Figs. 4.1(a) and 4.1(c)) in two dimensions. Relative to Table 4.5, lower orders of superconvergence are observed due to the larger fraction of perturbed elements present in the perturbed mesh.

	Affine ($r = 2$)			
h_0/h	$\|r_h^+ u - r_h u\|_{1,2}$	Order	$\|r_h^+ u - r_h u\|_{0,2}$	Order
1	5.4318e-01	-	1.9864e-02	-
2	2.8504e-01	0.9303	4.8794e-03	2.0254
4	1.2522e-01	1.1867	1.0528e-03	2.2125
8	4.8674e-02	1.3632	1.9842e-04	2.4075
16	1.7931e-02	1.4407	3.5671e-05	2.4758
32	6.4595e-03	1.4730	6.3290e-06	2.4947

unit square is equal to $h/\sqrt{2}$ (the length of the shortest edge of each triangle) via a translation by $h/4$ in the positive x direction, as in Fig. 4.1(c).

In this scenario, assumption (4.2.2.iii) is satisfied with $\gamma = 1$, so that the estimates (4.15) and (4.16) no longer apply. Their analogues in this case read

$$\|r_h^+ u - r_h u\|_{0,2} \leq Ch^{5/2}|u|_{2,\infty}.$$

and

$$\|r_h^+ u - r_h u\|_{m,2} \leq \begin{cases} Ch^{3/2}\log(h^{-1})|u|_{2,\infty} & \text{if } m = 0, \\ Ch^{5/2}\log(h^{-1})|u|_{2,\infty} & \text{if } m = 1, \end{cases}$$

respectively. Tables 4.6-4.7 illustrate these predictions. Again, we have not attempted to detect the presence of the factor $\log(h^{-1})$.

4.6 Summary

We have derived estimates for the difference between the orthogonal projections $r_h u$ and $r_h^+ u$ of a smooth function u onto nearby finite element spaces $\mathcal{V}_h$ and $\mathcal{V}_h^+$, respectively, with respect to bilinear forms $a_h, a_h^+ : \mathcal{V} \times \mathcal{V} \to \mathbb{R}$, respectively, where $\mathcal{V}$ is a closed subspace of $H^s(\Omega)$. When $s \in \{0, 1\}$ and $\mathcal{V}_h$ and $\mathcal{V}_h^+$ consist of continuous functions that are elementwise polynomials over shape-regular, quasi-uniform meshes that coincide except on a region of measure $O(h^\gamma)$ for a constant $\gamma \geq 0$, the estimates for $\|r_h^+ u - r_h u\|_{s,2}$ are superconvergent by $O(h^{\gamma/2})$, provided that $u \in W^{s,\infty}(\Omega)$ and a_h and a_h^+ are sufficiently close. In addition, when $s = 1$ and a few more mild assumptions (namely (4.2.4.i-4.2.4.vi)) are satisfied, an $O(h^{\gamma/2})$-superconvergent estimate for $\|r_h^+ u - r_h u\|_{0,2}$ holds. Numerical experiments illustrated these estimates and verified the necessity of the regularity assumptions on u.

4.A Properties of Piecewise Polynomial Finite Element Spaces

In this section, we verify conditions (4.2.2.i-4.2.2.iii) for piecewise polynomial finite element spaces on nearby meshes for the cases $s = 0$ and $s = 1$.

As in Section 4.1, consider two families of shape-regular, quasi-uniform meshes $\{\mathcal{T}_h\}_{h\le h_0}$ and $\{\mathcal{T}_h^+\}_{h\le h_0}$ of an open, bounded, Lipschitz domain $\Omega \subset \mathbb{R}^d$, $d \ge 1$. Assume that the two families are parametrized by a scalar h that equals the maximum diameter of an element among all elements of $\mathcal{T}_h$ and $\mathcal{T}_h^+$ for every $h \le h_0$. Let $\mathcal{V}_h$ and $\mathcal{V}_h^+$ be finite element spaces consisting of continuous functions that are elementwise polynomials of degree at most $r-1$ over $\mathcal{T}_h$ and $\mathcal{T}_h^+$, respectively, where $r > 1$ is an integer.

In this setting, condition (4.2.2.i) is automatic for any $\eta \in [2,\infty]$, $s \in \{0,1\}$. Condition (4.2.2.ii) is trivial for $s = 0$ and is satisfied for $s = 1$ and any $\eta \in [2,\infty]$ [45].

Condition (4.2.2.iii) holds for any $\eta \in [2,\infty]$ when $\mathcal{T}_h$ and $\mathcal{T}_h^+$ coincide except on a region of measure $O(h^\gamma)$. To prove this, let $\{N_a\}_{a=1}^A \subset \mathcal{V}_h$ and $\{N_a^+\}_{a=1}^{A^+} \subset \mathcal{V}_h^+$ be the standard Lagrange shape functions that form bases for $\mathcal{V}_h$ and $\mathcal{V}_h^+$, respectively. Our assumptions on $\mathcal{T}_h$ and $\mathcal{T}_h^+$ imply the existence of an integer I such that $N_a = N_a^+$ for every $1 \le a \le I$ and such that

$$\left| \left(\bigcup_{a=I+1}^{A} \operatorname{supp}(N_a) \right) \cup \left(\bigcup_{a=I+1}^{A^+} \operatorname{supp}(N_a^+) \right) \right| \le Ch^\gamma \tag{4.17}$$

for every $h \le h_0$.

Define $\pi_h : \mathcal{V}_h^+ + \mathcal{V}_h \to \mathcal{V}_h^+ \cap \mathcal{V}_h$ as follows: For any

$$w_h = \sum_{a=1}^{I} c_a N_a + \sum_{a=I+1}^{A} c_a N_a + \sum_{a=I+1}^{A^+} c_a^+ N_a^+ \tag{4.18}$$

belonging to $\mathcal{V}_h^+ + \mathcal{V}_h$, set

$$\pi_h w_h := \sum_{a=1}^{I} c_a N_a. \tag{4.19}$$

Clearly,

$$|\operatorname{supp}(\pi_h w_h - w_h)| \le Ch^\gamma$$

for every $w_h \in \mathcal{V}_h^+ + \mathcal{V}_h$ and every $h \le h_0$. To prove that

$$\|\pi_h w_h\|_{0,\eta} \le C\|w_h\|_{0,\eta} \tag{4.20}$$

for every $w_h \in \mathcal{V}_h^+ + \mathcal{V}_h$ and every $h \le h_0$, there are two cases to consider: $\eta = \infty$ and $2 \le \eta < \infty$.

For $\eta = \infty$, it is enough to note that for each of the two finite element spaces, every shape function is bounded uniformly in h in the maximum norm, the number of shape functions whose

support intersects any given element is bounded uniformly in h, and the coefficients c_a, $1 \le a \le I$, in the expansion (4.18) of w_h are bounded by $\|w_h\|_{0,\infty}$. Indeed, the standard degrees of freedom σ_a, $1 \le a \le I$, for the Lagrange shape functions $N_a (= N_a^+)$, $1 \le a \le I$, satisfy

$$\sigma_a(N_b) = \delta_{ab}, \quad 1 \le b \le A$$

and

$$\sigma_a(N_b^+) = \delta_{ab}, \quad 1 \le b \le A^+,$$

where δ_{ab} denotes the Kronecker delta. Hence, for any $1 \le a \le I$,

$$|c_a| = |\sigma_a(w_h)| \le \|w_h\|_{0,\infty}.$$

For $2 \le \eta < \infty$, the proof of (4.20) relies on the following lemma.

Lemma 4.A.1. *Let $\{\mathcal{T}_h\}_{h \le h_0}$ be a shape-regular, quasi-uniform family of meshes of an open, bounded, Lipschitz domain $\Omega \subset \mathbb{R}^d$, $d \ge 1$, with h denoting the maximum diameter of an element $K \in \mathcal{T}_h$. Let $r > 1$ be an integer. For any $K \in \mathcal{T}_h$, let $\theta_1, \theta_2, \ldots, \theta_{n_{sh}}$ denote the local shape functions for the Lagrange finite element of degree at most $r-1$ on K. Then for any $2 \le \eta < \infty$, there exist $C_1, C_2 > 0$ independent of h such that for every $h \le h_0$, every $K \in \mathcal{T}_h$, and every $v = \sum_{i=1}^{n_{sh}} d_i \theta_i$,*

$$C_1 h^d \sum_{i=1}^{n_{sh}} |d_i|^\eta \le \|v\|_{0,\eta,K}^\eta \le C_2 h^d \sum_{i=1}^{n_{sh}} |d_i|^\eta.$$

Proof. A proof of this fact when $\eta = 2$ is given in [45, Lemma 9.7]. The case $2 < \eta < \infty$ is a trivial modification thereof. □

Now let w_h and $\pi_h w_h$ be as in (4.18) and (4.19), respectively. Note that the support of $\pi_h w_h$ is contained within the region $Q_h \subseteq \Omega$ over which $\mathcal{T}_h$ and $\mathcal{T}_h^+$ coincide. On any $K \in \mathcal{T}_h$ with $K \subseteq Q_h$, we can write

$$w_h|_K = \sum_{i=1}^{n_{sh}} d_i \theta_i$$

and

$$\pi_h w_h|_K = \sum_{i=1}^{n_{sh}} \bar{d}_i \theta_i,$$

with scalars $d_i \in \mathbb{R}$ and $\bar{d}_i \in \{0, d_i\}$ for every i. By Lemma 4.A.1,

$$\begin{aligned}\|\pi_h w_h\|_{0,\eta,K}^\eta &\le C_2 h^d \sum_{i=1}^{n_{sh}} |\bar{d}_i|^\eta \\ &\le C_2 h^d \sum_{i=1}^{n_{sh}} |d_i|^\eta \\ &\le C_2 C_1^{-1} \|w_h\|_{0,\eta,K}^\eta\end{aligned}$$

on every such K. Summing over all $K \in \mathcal{T}_h$ with $K \subseteq Q_h$ proves (4.20) for $2 \le \eta < \infty$.

4.B Estimates for the L^2-Projection and Elliptic Projections

Two exemplary cases in which estimates of the form (4.7-4.8) are known to hold are the following. Suppose that $\mathcal{V} = H^s(\Omega) \cap H_0^1(\Omega)$ and $\mathcal{V}_h$ is the space of continuous functions in $\mathcal{V}$ that are elementwise polynomials of degree at most $r-1$ on a shape-regular, quasi-uniform family of meshes $\{\mathcal{T}_h\}_{h \le h_0}$ whose maximum element diameter is h. Then:

(i) If $s = 0$, $d \in \{1, 2\}$, and

$$a_h(u, w) = \int_\Omega uw \, dx$$

so that r_h is the L^2-projector onto $\mathcal{V}_h$, then (4.7) holds with $\ell(h) \equiv 1$ for any $\eta \in [2, \infty]$ [39]. Note that the estimate (4.8) is vacuous in this case, since $s = 0$.

(ii) If $s = 1$, $d \in \{2, 3\}$, and

$$a_h(u, w) = \int_\Omega \left(\sum_{i,j=1}^d a_{ij}(x) \frac{\partial u}{\partial x_i} \frac{\partial w}{\partial x_j} + \sum_{j=1}^d b_j(x) \frac{\partial u}{\partial x_j} w + b_0(x) uw \right) dx$$

with h-independent coefficients a_{ij}, $i, j = 1, 2, \ldots, d$ and b_j, $j = 0, 1, \ldots, d$, then (4.7-4.8) hold [45] with $\ell(h) \equiv 1$ for any $2 \le \eta < \infty$ (if $r = 2$) and any $\eta \in [2, \infty]$ (if $r > 2$), provided that

- The coefficients satisfy $b_j \in L^\infty(\Omega)$, $j = 0, 1, \ldots, d$, and $a_{ij} \in L^\infty(\Omega) \cap W^{1,p}(\Omega)$, $i, j = 1, 2, \ldots, d$, with $p > 2$ if $d = 2$ and $p \ge 12/15$ if $d = 3$.
- The coefficients a_{ij} are coercive pointwise, i.e. there exists $c > 0$ independent of x such that

$$\sum_{i,j=1}^d a_{ij}(x) \xi_i \xi_j \ge c|\xi|^2 \tag{4.21}$$

for every $0 \ne \xi \in \mathbb{R}^d$ and a.e. $x \in \Omega$.

- There exists $C > 0$, $q_0 > d$ such that the continuous Dirichlet problem

$$a_h(u, w) = \int_\Omega f w \, dx \quad \forall w \in \mathcal{V}$$

has a unique solution satisfying

$$\|u\|_{2,q} \leq C \|f\|_{0,q} \tag{4.22}$$

for every $f \in L^p(\Omega)$ and every $1 < q < q_0$.

Under the same conditions as above but with $r = 2$ and $\eta = \infty$, the estimates (4.7-4.8) hold with $\ell(h) = \log(h^{-1})$ in dimension $d = 2$ [45].

Chapter 5

Error Estimate for Universal Meshes

5.1 Introduction

In Chapter 3, an abstract framework was introduced for analyzing the accuracy of finite element methods for moving-boundary problems under general assumptions on the mesh motion strategy. The goal of the present chapter is to apply that framework to derive a priori error estimates for schemes that use a universal mesh to discretize the moving domain. We leverage the results of Chapter 4 along the way, since in this setting they provide sharper estimates for the errors committed each time the mesh changes abruptly.

Recall that schemes based on universal meshes bear some resemblance to conventional ALE schemes, in the sense that they deliver a conforming discretization of the moving domain at all times and use projections to transfer information between finite element spaces each time the mesh changes abruptly. However, there are several peculiarities that render schemes based on universal meshes markedly different from ALE schemes and challenging to analyze. Notably, the number of instants at which remeshing (updating the subtriangulation of the background mesh) is performed during the course of a given simulation grows unboundedly under mesh refinement when using a universal mesh. In addition, the deformations of the mesh deviate from the identity only in a band of elements near the moving boundary, rendering the gradient of the mesh velocity unbounded under refinement. It will be shown in this chapter that these peculiarities endow the method with an order of accuracy that is suboptimal by half an order in the L^2-norm.

For simplicity, we focus in this chapter on the analysis of the method in the context of a one-dimensional model problem, namely the diffusion equation on an interval $(0, s(t)) \subset \mathbb{R}$ with s a prescribed function of time. This simplified setting allows us to highlight the key steps in the analysis

of the method's convergence order, while greatly simplifying the verification of various properties of the mesh motion strategy that would be more tedious in two dimensions, such as the scaling of the derivatives of the mesh deformation and mesh velocity with respect to the mesh resolution.

Organization. This chapter is organized as follows. In Section 5.2, we state a model moving-boundary problem in one dimension and record its weak formulation. In Section 5.3, we recall the manner in which the problem can be discretized with a universal mesh. This is done in the same way described in Section 2.2.1 of Chapter 2, though we formulate the method more rigorously here. In Section 5.4, we state the main result of this chapter: an a priori error estimate for the method. We prove the estimate in Section 5.5, leveraging the results of Chapters 3 and 4. We give some concluding remarks in Section 5.6, including a discussion of how the proof can be adapted to the two-dimensional setting.

5.2 Model Problem and its Weak Formulation

We consider a moving-boundary problem posed on a domain $\Omega^t = (0, s(t)) \subset \mathbb{R}$ with $s \in C^2([0,T])$ given. We assume that

$$s_{min} := \min_{0 \le t \le T} s(t) > 0,$$

and we denote

$$s_{max} := \max_{0 \le t \le T} s(t),$$
$$c_s := \max_{0 \le t \le T} |\dot{s}(t)|,$$

where the dot denotes differentiation in time. We denote by

$$\Omega = \{(x,t) \mid x \in \Omega^t,\, t \in (0,T)\}$$

the spacetime domain swept out by Ω^t between $t = 0$ and $t = T$.

The strong formulation of the moving-boundary problem that we consider reads: Find $u : \Omega \to \mathbb{R}$ such that

$$\begin{aligned} \dot{u}(x,t) - u''(x,t) &= f(x,t) \quad && 0 < x < s(t), \quad 0 < t < T, \\ u(x,0) &= u^0(x) && 0 < x < s(0), \\ u(0,t) &= 0 && 0 < t < T, \\ u(s(t),t) &= 0 && 0 < t < T, \end{aligned} \tag{5.1}$$

where the prime denotes differentiation with respect to x, and $u^0 \in H_0^1(\Omega^0)$ and $f \in C([0,T], L^2(\mathbb{R}))$ are given.

To state a corresponding weak formulation, we adopt the notation introduced in Chapter 3. With $\psi^t(X) := s(t)X/s(0)$, we denote

$$\begin{aligned}\mathcal{V}^t &= H_0^1(\Omega^t),\\ \mathcal{U} &= \{U \in L^2(0,T;H_0^1(\Omega^0)) \mid U^{(1)} \in L^2(0,T;H^{-1}(\Omega^0))\},\\ \mathcal{W} &= \{u : \Omega \to \mathbb{R} \mid t \mapsto u(\psi^t(\cdot),t) \in \mathcal{U}\}.\end{aligned}$$

The weak formulation of (5.1) then reads: Find $u \in \mathcal{W}$ such that $u(\cdot,0) = u^0$ and for a.e. $t \in (0,T)$,

$$m^t(\dot{u},w) + a^t(u,w) = m^t(f,w) \quad \forall w \in \mathcal{V}^t, \tag{5.2}$$

where

$$\begin{aligned}m^t(u,w) &= \int_0^{s(t)} uw\,dx,\\ a^t(u,w) &= \int_0^{s(t)} u'w'\,dx.\end{aligned}$$

5.3 Discretization with a Universal Mesh

We now recall the procedure introduced in Chapter 2, Section 2.1 for discretizing (5.2) with a universal mesh in one dimension.

Let $0 = \tilde{X}_0 < \tilde{X}_1 < \cdots < \tilde{X}_M = L$ be a partition of an interval $(0,L)$ with $L \geq s_{max}$. Denote

$$\tilde{h} = \max_{1\leq m\leq M}(\tilde{X}_m - \tilde{X}_{m-1})$$

and

$$\tilde{h}_{min} = \min_{1\leq m\leq M}(\tilde{X}_m - \tilde{X}_{m-1}).$$

We view $\{\tilde{X}_m\}_{m=0}^M$ as a member of a family of partitions of $(0,L)$ parametrized by $\tilde{h} > 0$. We assume this family is quasi-uniform; that is, there exists $\mu \in (0,1]$ independent of $\tilde{h}$ such that

$$\tilde{h}_{min} \geq \mu\tilde{h} \tag{5.3}$$

for every $\tilde{h} > 0$.

Using small perturbations of $\{\tilde{X}_m\}_{m=0}^M$, we shall now construct a conforming mesh of the domain $\Omega^t = (0,s(t))$ which deforms smoothly over time intervals that are short in comparison to the mesh spacing. In particular, for each $\tilde{h} > 0$, let $0 = t^0 < t^1 < \cdots < t^N = T$ be a partition of the time

interval $(0,T)$ satisfying

$$c_s \max_{1\le n\le N}(t^n - t^{n-1}) \le \lambda_1 \tilde{h}_{min}, \tag{5.4}$$

$$c_s \min_{1\le n\le N}(t^n - t^{n-1}) \ge \lambda_0 \tilde{h}_{min} \tag{5.5}$$

with constants $0 < \lambda_0 < \lambda_1 < \mu$ independent of $\tilde{h}$.

For a given $n \ge 1$, let $I = I(n)$ denote the smallest integer for which $s(t^{n-1}) \le \tilde{X}_I$. Now define for each $t \in (t^{n-1}, t^n]$ a mesh $0 = x_0(t) < x_1(t) < \cdots < x_I(t) = s(t)$ according to the following prescription: With parameters $R \ge 1$ and $\delta \in (\lambda_1, \mu)$, set

$$x_m(t) = \begin{cases} \tilde{X}_m - \delta\tilde{h}\left(1 - \frac{s(t^{n-1}) - \tilde{X}_m}{R\tilde{h}}\right) & \text{if } s(t^{n-1}) - R\tilde{h} \le \tilde{X}_m < s(t^{n-1}), \\ s(t) & \text{if } m = I, \\ \tilde{X}_m & \text{otherwise} \end{cases} \tag{5.6}$$

for each $m = 0, 1, 2, \ldots, I$. See Fig. 2.2 in Chapter 2 for an illustration. The validity of this meshing strategy is made rigorous in the following proposition, whose proof is a straightforward calculation.

Proposition 5.3.1. *Suppose that (5.3) and (5.4) are satisfied with constants $0 < \lambda_1 < \mu \le 1$. Then for any $R \ge 1$ and $\delta \in (\lambda_1, \mu)$, the prescription (5.6) supplies a mesh $0 = x_0(t) < x_1(t) < \cdots < x_I(t) = s(t)$ satisfying*

$$h_{min} := \min_{0<t\le T} \min_{1\le m\le I}(x_m(t) - x_{m-1}(t)) \ge \min\{1 - \frac{\delta}{\mu}, \delta - \lambda_1\}\tilde{h}_{min},$$
$$h := \max_{0<t\le T} \max_{1\le m\le I}(x_m(t) - x_{m-1}(t)) \le (1 + \lambda_1)\tilde{h}$$

for every $\tilde{h} > 0$.

It follows, in particular, that the ratios $\tilde{h}/h$ and $\tilde{h}_{min}/h_{min}$ are bounded above and below by positive constants independent of $\tilde{h}$. We henceforth view the discretization as being parameterized by h, and we present estimates in terms of h rather than $\tilde{h}$.

Now fix an integer $r \ge 2$ and define for each $t \in (0,T]$ and each $h > 0$ the space

$$\mathcal{V}_h^t = \Big\{ w \in C^0([0, s(t)]) \,\Big|\, w(0) = w(s(t)) = 0, \\ w|_{(x_{m-1}(t), x_m(t))} \in \mathcal{P}^{r-1}(x_{m-1}(t), x_m(t)),\ m = 1, 2, \ldots, I \Big\},$$

where $\mathcal{P}^{r-1}(x_{m-1}(t), x_m(t))$ denotes the space of polynomials of degree $\le r-1$ on $(x_{m-1}(t), x_m(t))$. To account for the fact that the nodal positions are, in general, only left-continuous at each time t^n, $n = 1, 2, \ldots, N$, we denote by $\mathcal{V}_h^{t_+^n}$ the space of elementwise polynomials of degree $\le r-1$ over the mesh $0 = x_0(t_+^n) < x_1(t_+^n) < \cdots < x_I(t_+^n) = s(t^n)$, where $x(t_+^n) = \lim_{t \searrow t^n} x(t)$.

The Galerkin projection of (5.1) onto $\mathcal{V}_h^t$ reads

$$m^t(\dot{u}_h, w_h) + a^t(u_h, w_h) = m^t(f, w_h) \quad \forall w_h \in \mathcal{V}_h^t,\ t \in (t^{n-1}, t^n]. \tag{5.7}$$

For the initial condition in (5.7), we take $u_h(\cdot, t_+^{n-1})$ equal to the L^2-projection of $u_h(\cdot, t^{n-1})$ (or u^0 if $n = 1$) onto $\mathcal{V}_h^{t_+^{n-1}}$. That is,

$$u_h(\cdot, t_+^{n-1}) = \begin{cases} p_h^{t_+^{n-1}} u_h(\cdot, t^{n-1}) & \text{if } n > 1, \\ p_h^{0+} u^0 & \text{if } n = 1, \end{cases} \tag{5.8}$$

where $p_h^t : L^2(\Omega^t) \to \mathcal{V}_h^t$ is defined according to the relation

$$m^t(p_h^t u, w_h) = m^t(u, w_h) \quad \forall w_h \in \mathcal{V}_h^t.$$

The sequence of differential equations (5.7), $n = 1, 2, \ldots, N$, together with the initial conditions (5.8), determine $u_h(\cdot, t)$ uniquely for $t \in (0, T]$. Our aim in this chapter is to apply the theory introduced in Chapter 3 (and summarized in Section 5.5.1) in order to study the convergence of $u_h(\cdot, T)$ to $u(\cdot, T)$ in the L^2-norm for this method.

Remark. For future reference, it is convenient to rewrite (5.7) in terms of the material time derivative

$$D_t u_h = \dot{u}_h + v_h u_h'$$

of u_h along the direction of the mesh motion, where $v_h : \Omega \to \mathbb{R}$ denotes the *mesh velocity*: the function which is elementwise affine and satisfies $v_h(x_m(t), t) = \dot{x}_m(t)$ for each $t \in (t^{n-1}, t^n]$, each $n = 1, 2, \ldots, N$, and each $m = 1, 2, \ldots, I$. In terms of $D_t u_h$, (5.7) reads

$$m^t(D_t u_h, w_h) - b_h^t(u_h, w_h) + a^t(u_h, w_h) = m^t(f, w_h) \quad \forall w_h \in \mathcal{V}_h^t,\ t \in (t^{n-1}, t^n], \tag{5.9}$$

where

$$b_h^t(u, w) = \int_0^{s(t)} v_h u' w \, dx.$$

5.4 Statement of Results

The following result will be proved in this chapter.

Theorem 5.4.1. *Let u_h solve the sequence of differential equations (5.7), $n = 1, 2, \ldots, N$, with the*

initial conditions (5.8). Then there exists $C > 0$ independent of h and u such that

$$\|u_h(\cdot,T) - u(\cdot,T)\|_{0,2,\Omega^T} \leq Ch^{r-1/2}\Bigg[\int_0^T \left(\|u\|_{r+1,\infty,\Omega^t} + h^{1/2}|\dot{u}|_{r,2,\Omega^t} + h^{1/2}|u|_{r,2,\Omega^t}\right) dt + \sup_{0\leq t\leq T} |u|_{r,\infty,\Omega^t} + h^{1/2}|u^0|_{r,2,\Omega^0}\Bigg]$$

for every $h > 0$, provided that for each $t \in [0,T]$, $u(\cdot,t) \in W^{r+1,\infty}(\Omega^t)$ and $\dot{u}(\cdot,t) \in H^r(\Omega^t)$.

5.5 Proofs

In this section, we present a proof of Theorem 5.4.1. The proof uses the results of Chapter 3, which provide an abstract estimate for the error incurred by finite element spatial discretizations of parabolic moving-boundary problems, under general assumptions on the mesh motion strategy. We summarize the abstract estimate in Section 5.5.1, and we apply it in Section 5.5.3 to the specific mesh motion strategy under consideration.

5.5.1 Summary of the Abstract Error Estimate

To recapitulate the abstract estimate, we require the following notation. Let

$$\kappa = c_s^2 \max\left\{1, \frac{s_{max}^2}{\pi^2}\right\}$$

and define the bilinear form

$$a_h^t(u,w) = a^t(u,w) - b_h^t(u,w) + \kappa m^t(u,w).$$

It can easily be checked, using a one-dimensional Poincaré inequality, that this bilinear form is coercive, uniformly in h and t. Namely,

$$a_h^t(u,u) \geq \alpha \|u\|_{1,2,\Omega^t}^2 \quad \forall h > 0,\, \forall t \in (0,T],$$

with

$$\alpha = \frac{1}{4}\min\left\{1, \frac{\pi^2}{s_{max}^2}\right\}.$$

Now define the *elliptic projector* $r_h^t : \mathcal{V}^t \to \mathcal{V}_h^t$ with respect to the bilinear form a_h^t according to

$$a_h^t(r_h^t u, w_h) = a_h^t(u, w_h) \quad \forall w_h \in \mathcal{V}_h^t. \tag{5.10}$$

Finally, define

$$\rho(t) = e^{-\kappa t}(r_h^t u(\cdot,t) - u(\cdot,t))$$

for $t \in (0,T]$, and set $\rho(0) := 0$ and $\rho(T_+) := 0$.

Theorem 3.4.1 from Chapter 3 tells us (noting that the stability constant for the L^2-projector is $C_p = 1$) that

$$\begin{aligned}\|u_h(\cdot,T) - u(\cdot,T)\|_{0,2,\Omega^T} \leq \sum_{n=1}^{N} \left(\int_{t^{n-1}}^{t^n} e^{\kappa t} \|D_t\rho\|_{0,2,\Omega^t}\, dt + e^{\kappa t^n} \|\rho(t_+^n) - \rho(t^n)\|_{0,2,\Omega^{t^n}} \right) \\ + \|\rho(0_+)\|_{0,2,\Omega^0}.\end{aligned} \tag{5.11}$$

In other words, an analysis of the error reduces to a study of ρ and its temporal variation.

Theorem 3.4.2 from Chapter 3 shows further that the term $\|D_t\rho\|_{0,2,\Omega^t}$ appearing in the estimate above can be bounded in terms of quantities which measure the regularity of the mesh motion. In particular, with

$$\Lambda_h^t(u,w) = -\int_0^{s(t)} v_h' u' w'\, dx - \int_0^{s(t)} (\dot{v}_h + v_h v_h') u' w\, dx + \kappa \int_0^{s(t)} v_h' u w\, dx,$$

we have

$$\begin{aligned}\|D_t\rho\|_{0,2,\Omega^t} \leq C \Bigg(h \inf_{w_h \in \mathcal{V}_h^t} \|D_t(e^{-\kappa t}u) - w_h\|_{1,2,\Omega^t} \\ + \sup_{w \in H^2(\Omega^t) \cap H_0^1(\Omega^t)} \frac{|\Lambda_h^t(\rho,w)|}{\|w\|_{2,2}} + h \sup_{w \in H_0^1(\Omega^t)} \frac{|\Lambda_h^t(\rho,w)|}{\|w\|_{1,2}} \Bigg).\end{aligned} \tag{5.12}$$

To prove Theorem 5.4.1, it remains to bound the three terms appearing on the right-hand side of the preceding inequality, and to bound $\|\rho(t_+^n) - \rho(t^n)\|_{0,2,\Omega^{t^n}}$, and $\|\rho(0_+)\|_{0,2,\Omega^0}$. We do so in the next subsections.

5.5.2 Useful Inequalities

We begin by collecting an assortment of inequalities that will be needed at several points throughout the proofs that follow.

The mesh velocity. Our first observations concern the mesh velocity velocity v_h, which satisfies the following easily verified properties:

(5.5.3.i) For every $n = 1, 2, \ldots, N$, every $t \in (t^{n-1}, t^n]$, and every $x < x_{I-1}(t)$, $v_h(x,t) = 0$. In particular, the support of $v_h(x,t)$ has measure $\leq h$ for each fixed t.

(5.5.3.ii) There exists C independent of h and t such that

$$\|v_h\|_{0,\infty,\Omega^t} + h|v_h|_{1,\infty,\Omega^t} + h|\dot{v}_h|_{1,\infty,\Omega^t} \leq C$$

for every $h > 0$ and every $t \in (0, T]$.

One consequence of (5.5.3.i) is the following. Let

$$R_h^t := \operatorname{supp}(v_h(\cdot, t)) = [x_{I-1}(t), s(t)]$$

denote the support of $v_h(\cdot, t)$. Then

$$\|w\|_{m,p,R_h^t} \leq h^{1/p-1/q}\|w\|_{m,q,R_h^t} \tag{5.13}$$

for every $m \geq 0$, every $1 \leq p \leq q \leq \infty$, and every $w \in W^{m,q}(\Omega^t)$ (see Lemma 4.3.1 in Chapter 4). Furthermore, fhe fundamental theorem of calculus gives the following Hardy-type inequality:

$$\|w\|_{0,p,R_h^t} \leq h|w|_{1,p,\Omega^t} \tag{5.14}$$

for every $1 \leq p \leq \infty$ and every $w \in W^{1,p}(\Omega^t) \cap \mathcal{V}^t$.

Interpolation and inverse estimates. We shall also make use of the following estimates concerning the finite element spaces $\mathcal{V}_h^t$. As a consequence of Proposition 5.3.1 and standard interpolation estimates [45, Corollary 1.109], there exists C independent of h and t such that

$$\inf_{w_h \in \mathcal{V}_h^t} \|w - w_h\|_{m,p,\Omega^t} \leq Ch^{s-m}|w|_{s,p,\Omega^t} \tag{5.15}$$

for every $s = 2, 3, \ldots, r$, every $p \in [1, \infty]$, every $m = 0, 1$, every $w \in H^s(\Omega^t) \cap \mathcal{V}^t$, every $h > 0$, and every $t \in (0, T]$. In addition, the inverse estimate [45, Corollary 1.141]

$$\|w_h\|_{m,p,\Omega^t} \leq Ch^{l-m+\min(0,1/p-1/q)}\|w_h\|_{l,q,\Omega^t} \tag{5.16}$$

holds for every $0 \leq l \leq m \leq 1$, every $p, q \in [1, \infty]$, every $w_h \in \mathcal{V}_h^t$, every $h > 0$, and every $t \in (0, T]$.

The elliptic projection. Finally, we gather and prove some results concerning the elliptic projector $r_h^t : \mathcal{V}^t \to \mathcal{V}_h^t$ with respect to the bilinear form (5.10) for the specific mesh velocity v_h considered in this chapter.

We will require estimates for the L^∞- and $W^{1,\infty}$-norms of $r_h^t u - u$. Since the bilinear form under consideration depends on h, such estimates are not standard results in the finite element literature. We establish the needed estimates below. Our strategy is to compare $r_h^t u$ with an elliptic projection

$\tilde{r}_h^t u$ with respect to a simpler bilinear form

$$\tilde{a}_h^t(u,w) = a^t(u,w) + \kappa m^t(u,w).$$

This elliptic projection $\tilde{r}_h^t u$, which is defined by the relation

$$\tilde{a}_h^t(\tilde{r}_h^t u, w_h) = \tilde{a}_h^t(u, w_h) \quad \forall w_h \in \mathcal{V}_h^t,$$

satisfies the estimate

$$\|\tilde{r}_h^t u - u\|_{0,\infty,\Omega^t} + h|\tilde{r}_h^t u - u|_{1,\infty,\Omega^t} \leq Ch^r \|u\|_{r,\infty,\Omega^t} \tag{5.17}$$

for every $h > 0$, every $t \in (0,T]$, and every $u \in W^{r,\infty}(\Omega^t) \cap \mathcal{V}^t$, with a constant C independent of h and t. This estimate (and the fact that it holds uniformly in t) can be verified by recasting the problem on the unit interval via a linear change of variables, invoking known L^∞-estimates [137], and using the inverse estimate (5.16) to deduce the $W^{1,\infty}$-estimate.

The next lemma shows that $r_h^t u$ is superclose to $\tilde{r}_h^t u$ in the H^1-norm.

Lemma 5.5.1. *There exists C independent of h and t such that*

$$\|r_h^t u - \tilde{r}_h^t u\|_{1,2,\Omega^t} \leq Ch^{r+1/2}|u|_{r,\infty,\Omega^t}.$$

Proof. For any $w_h \in \mathcal{V}_h^t$, we have

$$\begin{aligned} a_h^t(r_h^t u - \tilde{r}_h^t u, w_h) &= a_h^t(u - \tilde{r}_h^t u, w_h) \\ &= \tilde{a}_h^t(u - \tilde{r}_h^t u, w_h) - b_h^t(u - \tilde{r}_h^t u, w_h) \\ &= -b_h^t(u - \tilde{r}_h^t u, w_h). \end{aligned}$$

Now take $w_h = r_h^t u - \tilde{r}_h^t u$ and use (5.13) and (5.14) to deduce that

$$\begin{aligned} \alpha\|r_h^t u - \tilde{r}_h^t u\|_{1,2,\Omega^t}^2 &\leq \left| \int_{\Omega^t} v_h (u - \tilde{r}_h^t u)'(r_h^t u - \tilde{r}_h^t u) \right| \\ &\leq v_{max}|u - \tilde{r}_h^t u|_{1,2,R_h^t} \|r_h^t u - \tilde{r}_h^t u\|_{0,2,R_h^t} \\ &\leq v_{max} h^{1/2}|u - \tilde{r}_h^t u|_{1,\infty,\Omega^t}\, h\|r_h^t u - \tilde{r}_h^t u\|_{1,2,\Omega^t}. \end{aligned}$$

The conclusion then follows from (5.17). □

Lemma 5.5.1 has several important consequences. First,

$$|r_h^t u - \tilde{r}_h^t u|_{1,\infty,\Omega^t} \leq Ch^r |u|_{r,\infty,\Omega^t} \tag{5.18}$$

due to the inverse estimate (5.16). Second, the estimate

$$\|r_h^t u - \tilde{r}_h^t u\|_{0,\infty,\Omega^t} \leq Ch^{r+1/2}|u|_{r,\infty,\Omega^t} \tag{5.19}$$

holds by virtue of the Sobolev embedding $H^1(\Omega^t) \subset L^\infty(\Omega^t)$. Combining (5.18), (5.19), and (5.17) gives

$$\|r_h^t u - u\|_{0,\infty,\Omega^t} + h|r_h^t u - u|_{1,\infty,\Omega^t} \leq Ch^r \|u\|_{r,\infty,\Omega^t} \tag{5.20}$$

upon using the triangle inequality. In addition, we obtain the following superconvergent estimate for the average of $(r_h^t u - u)'$ over any element $K = (x_{i-1}(t), x_i(t))$ of the mesh.

Lemma 5.5.2. *There exists C independent of h and t such that*

$$\left| \int_K (r_h^t u - u)' \, dx \right| \leq Ch^{r+1} \|u\|_{r,\infty,\Omega^t}.$$

for every $h > 0$, every $t \in (0, T]$, every $u \in W^{r,\infty}(\Omega^t) \cap \mathcal{V}^t$, and every element $K = (x_{i-1}(t), x_i(t))$.

Proof. Let $y_h \in \mathcal{V}_h^t$ denote the solution to

$$a^t(y_h, w_h) = a^t(u, w_h) \quad \forall w_h \in \mathcal{V}_h^t.$$

The results of [134] imply that

$$|\tilde{r}_h^t u - y_h|_{1,\infty,\Omega^t} \leq Ch^r \|u\|_{r,\infty,\Omega^t}.$$

Combining this estimate with (5.18) gives

$$|r_h^t u - y_h|_{1,\infty,\Omega^t} \leq Ch^r \|u\|_{r,\infty,\Omega^t}.$$

Now write

$$\int_K (r_h^t u - u)' \, dx = \int_K (r_h^t u - y_h)' \, dx + \int_K (y_h - u)' \, dx$$

and observe that the second term vanishes due to the fact that $y_h(x_i(t)) = u(x_i(t))$ at the nodes $x_i(t)$ [45]. Conclude using

$$\begin{aligned} \left| \int_K (r_h^t u - u)' \, dx \right| &\leq h|r_h^t u - y_h|_{1,\infty,\Omega^t} \\ &\leq Ch^{r+1} \|u\|_{r,\infty,\Omega^t}. \end{aligned}$$

□

5.5.3 Application of the Abstract Error Estimate

We now estimate the three terms appearing on the right-hand side of (5.12), as well as $\|\rho(t_+^n) - \rho(t^n)\|_{0,2,\Omega^{t^n}}$, and $\|\rho(0_+)\|_{0,2,\Omega^0}$.

We begin with an estimate for the first term appearing on the right-hand side of (5.12), whose proof is similar to that in Chapter 3, Section 3.6.3.

Lemma 5.5.3. *There exists C independent of h and t such that for every $h > 0$ and every $t \in (0, T]$,*

$$e^{\kappa t} \inf_{w_h \in \mathcal{V}_h^t} \|D_t(e^{-\kappa t}u) - w_h\|_{1,2,\Omega^t} \leq Ch^{r-3/2} \left(\|u\|_{r+1,\infty,\Omega^t} + h^{1/2}|\dot{u}|_{r,2,\Omega^t} + \kappa h^{1/2}|u|_{r,2,\Omega^t} \right)$$

Proof. Expand

$$\begin{aligned} D_t(e^{-\kappa t}u) &= \partial_t(e^{-\kappa t}u) + v_h(e^{-\kappa t}u)' \\ &= e^{-\kappa t}\dot{u} - \kappa e^{-\kappa t}u + e^{-\kappa t}v_h u'. \end{aligned}$$

Thus, by (5.15),

$$\begin{aligned} e^{\kappa t} \inf_{w_h \in \mathcal{V}_h^t} \|D_t(e^{-\kappa t}u) - w_h\|_{1,2,\Omega^t} &\leq Ch^{r-1}|\dot{u} - \kappa u + v_h u'|_{r,2,\Omega^t,h} \\ &\leq Ch^{r-1}\left(|\dot{u}|_{r,2,\Omega^t,h} + \kappa|u|_{r,2,\Omega^t,h} + |v_h u'|_{r,2,\Omega^t,h}\right) \\ &= Ch^{r-1}\left(|\dot{u}|_{r,2,\Omega^t} + \kappa|u|_{r,2,\Omega^t} + |v_h \cdot u'|_{r,2,\Omega^t,h}\right). \end{aligned} \tag{5.21}$$

Next, use the fact that, with a constant C depending only on r, it holds that

$$\begin{aligned} |v_h u'|_{r,2,\Omega^t,h} &\leq C\|v_h\|_{r,2,\Omega^t,h}\|u\|_{r+1,\infty,\Omega^t,h} \\ &= C\|v_h\|_{1,2,\Omega^t,h}\|u\|_{r+1,\infty,\Omega^t}. \end{aligned} \tag{5.22}$$

Finally, combine (5.21), (5.22), and (5.5.3.ii) to obtain the desired bound. □

Next, we bound the second and third terms appearing on the right-hand side of (5.12).

Lemma 5.5.4. *There exists C independent of h and t such that for every $h > 0$ and every $t \in (0, T]$, the inequality*

$$|\Lambda_h^t(\rho, w)| \leq Ce^{-\kappa t}h^{r-3/2}\|u\|_{r,\infty,\Omega^t}\|w\|_{1,2,\Omega^t} \tag{5.23}$$

holds for every $w \in \mathcal{V}^t$, and the inequality

$$|\Lambda_h^t(\rho, w)| \leq Ce^{-\kappa t}h^{r-1/2}\|u\|_{r,\infty,\Omega^t}\|w\|_{2,2,\Omega^t} \tag{5.24}$$

holds for every $w \in H^2(\Omega^t) \cap \mathcal{V}^t$.

Proof. Write

$$\Lambda_h^t(\rho, w) = \int_0^{s(t)} A_h \rho' w' \, dx + \int_0^{s(t)} B_h \rho' w \, dx + \int_0^{s(t)} C_h \rho w \, dx \tag{5.25}$$

with

$$\begin{aligned} A_h &= -v_h', \\ B_h &= -\dot{v}_h - v_h v_h', \\ C_h &= \kappa v_h', \end{aligned}$$

and observe that

$$\|A_h\|_{0,\infty,\Omega^t} \le |v_h|_{1,\infty,\Omega^t} \le Ch^{-1}, \tag{5.26}$$

$$\|B_h\|_{0,\infty,\Omega^t} \le \|\dot{v}_h\|_{0,\infty,\Omega^t} + v_{max}|v_h|_{1,\infty,\Omega^t} \le Ch^{-1}, \tag{5.27}$$

$$\|C_h\|_{0,\infty,\Omega^t} \le \kappa|v_h|_{1,\infty,\Omega^t} \le Ch^{-1}. \tag{5.28}$$

Thus, since $R_h^t := \mathrm{supp}(v_h(\cdot, t))$ has measure $\le h$ for every t, it follows from (5.13) that

$$\|A_h\|_{0,2,\Omega^t} + \|B_h\|_{0,2,\Omega^t} + \|C_h\|_{0,2,\Omega^t} \le Ch^{-1/2}. \tag{5.29}$$

Now consider the first term appearing on the right-hand side of (5.25). By (5.29) and (5.20),

$$\begin{aligned} \left| \int_0^{s(t)} A_h \rho' w' \, dx \right| &\le \|A_h\|_{0,2,R_h^t} |\rho|_{1,\infty,R_h^t} |w|_{1,2,R_h^t} \\ &\le Ch^{-1/2} \cdot e^{-\kappa t} h^{r-1} \|u\|_{r,\infty,\Omega^t} \cdot |w|_{1,2,\Omega^t} \\ &= Ce^{-\kappa t} h^{r-3/2} \|u\|_{r,\infty,\Omega^t} |w|_{1,2,\Omega^t}. \end{aligned} \tag{5.30}$$

Similarly, using also (5.14),

$$\begin{aligned} \left| \int_0^{s(t)} B_h \rho' w \, dx \right| &\le \|B_h\|_{0,2,R_h^t} |\rho|_{1,\infty,R_h^t} \|w\|_{0,2,R_h^t} \\ &\le Ch^{-1/2} \cdot e^{-\kappa t} h^{r-1} \|u\|_{r,\infty,\Omega^t} \cdot h|w|_{1,2,\Omega^t} \\ &= Ce^{-\kappa t} h^{r-1/2} \|u\|_{r,\infty,\Omega^t} |w|_{1,2,\Omega^t}, \end{aligned} \tag{5.31}$$

and

$$\begin{aligned}\left|\int_0^{s(t)} C_h \rho w \, dx\right| &\le \|C_h\|_{0,2,R_h^t} |\rho|_{0,\infty,R_h^t} \|w\|_{0,2,R_h^t} \\ &\le Ch^{-1/2} \cdot e^{-\kappa t} h^r \|u\|_{r,\infty,\Omega^t} \cdot h|w|_{1,2,\Omega^t} \\ &= Ce^{-\kappa t} h^{r+1/2} \|u\|_{r,\infty,\Omega^t} |w|_{1,2,\Omega^t}. \end{aligned} \tag{5.32}$$

In the event that $w \in H^2(\Omega^t) \cap \mathcal{V}^t$, the estimate (5.30) for the first term may be sharpened as follows. Let w_h denote the elementwise affine nodal interpolant of w. Since A_h and w_h' are constant on each element, and since A_h vanishes outside R_h^t, we have

$$\begin{aligned}\int_0^{s(t)} A_h \rho' w' \, dx &= \int_0^{s(t)} A_h \rho' w_h' \, dx + \int_0^{s(t)} A_h \rho' (w - w_h)' \, dx \\ &= (A_h w_h')|_{R_h^t} \int_{R_h^t} \rho' \, dx + \int_0^{s(t)} A_h \rho' (w - w_h)' \, dx \\ &=: T_1 + T_2 \end{aligned}$$

The second term is easily bounded using (5.29), (5.20), and standard estimates for linear interpolation, giving

$$\begin{aligned}|T_2| &\le \|A_h\|_{0,2,\Omega^t} |\rho|_{1,\infty,\Omega^t} |w - w_h|_{1,2,\Omega^t} \\ &\le Ch^{-1/2} \cdot e^{-\kappa t} h^{r-1} \|u\|_{r,\infty,\Omega^t} \cdot h|w|_{2,2,\Omega^t} \\ &= Ce^{-\kappa t} h^{r-1/2} \|u\|_{r,\infty,\Omega^t} |w|_{2,2,\Omega^t}. \end{aligned}$$

The term T_1 is bounded using (5.26), Lemma 5.5.2, the stability of linear interpolation in $W^{1,\infty}$, and the Sobolev embedding $H^2(\Omega^t) \subset W^{1,\infty}(\Omega^t)$. Namely,

$$\begin{aligned}|T_1| &\le \|A_h\|_{0,\infty,\Omega^t} |w_h|_{1,\infty,\Omega^t} \left|\int_{R_h^t} \rho' \, dx\right| \\ &\le Ch^{-1} \cdot |w|_{1,\infty,\Omega^t} \cdot e^{-\kappa t} h^{r+1} \|u\|_{r,\infty,\Omega^t} \\ &\le Ce^{-\kappa t} h^r \|w\|_{2,2,\Omega^t} \|u\|_{r,\infty,\Omega^t}. \end{aligned}$$

□

We now turn to the estimation of $\|\rho(t_+^n) - \rho(t^n)\|_{0,2,\Omega^{t^n}}$. For this purpose, we invoke Theorem 4.2.4 from Chapter 4, which provides estimates for the difference

$$\begin{aligned} r_h^{t_+^n} u - r_h^{t^n} u &= (r_h^{t_+^n} u - u) - (r_h^{t^n} u - u) \\ &= e^{\kappa t^n} \left(\rho(t_+^n) - \rho(t^n)\right) \end{aligned}$$

when the finite elements spaces $\mathcal{V}_h^{t_+^n}$ and $\mathcal{V}_h^{t^n}$ are nearby (in the sense of 4.2.2.iii) and the bilinear forms $a_h^{t_+^n}$ and $a_h^{t_n}$ are nearby (in the sense of 4.5). In the setting considered in this chapter, (4.2.2.iii) holds with $\gamma = 1$. Furthermore, (4.5) holds with $\delta = 2$, $\mu = \nu = 1$, and $\eta = q = \infty$. Indeed, by (5.5.3.ii), (5.13), and (5.14),

$$\begin{aligned} |a_h^{t_+^n}(y,w) - a_h^{t^n}(y,w)| &= \int_{R_h^{t^n}} (v_h(\cdot,t^n) - v_h(\cdot,t_+^n)) y' w \, dx \\ &\leq 2\|v_h\|_{0,\infty} |y|_{1,2,R_h^{t^n}} \|w\|_{0,2,R_h^{t^n}} \\ &\leq Ch^{1/2} |y|_{1,\infty,R_h^{t^n}} \cdot h^{1/2} \|w\|_{0,\infty,R_h^{t^n}} \\ &\leq Ch^{1/2} |y|_{1,\infty,\Omega^{t^n}} \cdot h^{1/2} \cdot h|w|_{1,\infty,\Omega^{t^n}} \end{aligned}$$

for any $y, w \in W^{1,\infty}(\Omega^t) \cap \mathcal{V}^t$. It follows from Theorem 4.2.4 that

$$e^{\kappa t^n} \|\rho(t_+^n) - \rho(t^n)\|_{0,2,\Omega^{t^n}} \leq Ch^{r+1/2} |u|_{r,\infty,\Omega^{t^n}}. \tag{5.33}$$

Summing over n and noting that $N \sim h^{-1}$ by (5.5), we obtain

$$\sum_{n=1}^{N} e^{\kappa t^n} \|\rho(t_+^n) - \rho(t^n)\|_{0,2,\Omega^{t^n}} \leq Ch^{r-1/2} \sup_{0\leq t\leq T} |u|_{r,\infty,\Omega^t}. \tag{5.34}$$

We conclude with the estimation of $\|\rho(0_+)\|_{0,2,\Omega^0}$. By the (temporally uniform) coercivity and continuity of a_h^t, it follows from classical arguments (namely, via Céa's Lemma [45, Lemma 2.28], the Aubin-Nitsche Lemma [45, Lemma 2.31], and (5.15)) that there exists $C > 0$ independent of h such that

$$\|\rho(0_+)\|_{0,2,\Omega^0} \leq Ch^r |u|_{r,2,\Omega^0} \tag{5.35}$$

for every $h > 0$.

Inserting the estimates of Lemma 5.5.3, (5.23), (5.24), (5.34), and (5.35) into the abstract estimates (5.11) and (5.12) proves Theorem 5.4.1.

5.6 Concluding Remarks

We have proven an a priori error estimate for the numerical solution of a model moving-boundary problem with a universal mesh in one dimension. For polynomial finite elements, the estimate is suboptimal by half an order in the L^2-norm, reflecting the frequency and extent of remeshing as well as the regularity of the mesh velocity induced by the use of a universal mesh. The proof that we presented, though restricted to the one-dimensional setting, is adaptable to the two-dimensional setting with minor modifications, but the analogues of Proposition 5.3.1 and (5.5.3.ii) are more difficult to verify. The difficulties are exacerbated by the need for curved elements along the boundary in two dimensions. In addition, a logarithmic factor $\log h^{-1}$ enters into the error estimate via (5.33) when using piecewise linear finite elements in two dimensions.

Chapter 6

Numerical Examples

6.1 Introduction

This chapter presents examples that illustrate the application of universal meshes to the simulation of free- and moving-boundary problems. We focus on two applications: (1) two-dimensional incompressible, low Reynolds number flow around moving obstacles with prescribed evolution, and (2) free-surface flow with surface tension.

To simplify the presentation and to emphasize the main contributions of the present work, we restrict our attention to problems for which the flow has a low Reynolds number and the boundary is smooth (C^2-regular). Needless to say, higher Reynolds number flows pose additional challenges (the need for high resolution in boundary layers and for stabilization of convective terms in the spatial discretization) that warrant enhancements to the present strategy to ensure its viability. Likewise, the design of universal meshes for domains with lower regularity, such as domains with corners, remains an area of active research.

Organization. This chapter is organized as follows. In Section 6.2, we recall the governing equations for incompressible, viscous flow around a moving obstacle with prescribed evolution, and we recast the equations in weak form. In Section 6.3, we present a discretization of the aforementioned equations using a universal mesh in conjunction with Taylor-Hood finite elements [129]. This presentation generalizes that of Chapter 2, which focuses on a parabolic model problem. To integrate in time, we propose the use of implicit Runge-Kutta schemes as well as a fractional step scheme. In Section 6.4, we apply the proposed methods to simulate flow around various obstacles with prescribed evolution: a rotating ellipse, an oscillating disk, a rotating stirrer, and a pair of pitching airfoils. We study numerically the convergence orders of the methods in the context of the rotating ellipse, where an analytical solution is readily manufactured. In Section 6.5, we extend the method to simulate free surface flow with surface tension. We perform a comparison between the proposed method and

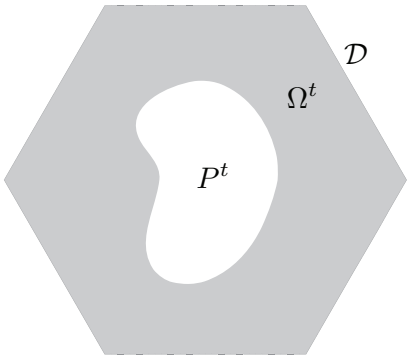

Figure 6.1: Fluid domain $\Omega^t = \mathcal{D} \setminus P^t$.

an ALE scheme in Section 6.6, and we close with some concluding remarks in Section 6.7.

6.2 Problem

We begin by studying incompressible, viscous fluid flow around a moving obstacle immersed in a domain $\mathcal{D} \subset \mathbb{R}^2$. We denote by $P^t \subset \mathcal{D}$ the domain occupied by the obstacle at time t and by $\Omega^t = \mathcal{D} \setminus P^t$ the domain occupied by the fluid. Taking the fluid density to be everywhere unity, the governing equations for the velocity u and pressure p read

$$\frac{\partial u}{\partial t} + u \cdot \nabla_x u - \nu \Delta_x u = -\nabla_x p \qquad \text{in } \mathcal{D} \setminus P^t \tag{6.1}$$

$$\nabla_x \cdot u = 0 \qquad \text{in } \mathcal{D} \setminus P^t, \tag{6.2}$$

where $\nu > 0$ is the kinematic viscosity of the fluid. On the interface between the obstacle and the fluid, the no-slip condition holds:

$$u(x,t) = v_P(x,t), \quad x \in \partial P^t \tag{6.3}$$

where $v_P(x,t)$ is the prescribed velocity of the obstacle at $x \in \partial P^t$. On the remainder of the fluid boundary $\partial\mathcal{D}$, and depending on the example under consideration, we impose either the natural boundary conditions

$$pn - \nu \left(\nabla_x u + (\nabla_x u)^T \right) n = 0 \qquad \text{on } \partial\mathcal{D} \tag{6.4}$$

or the no-slip condition

$$u = 0 \qquad \text{on } \partial\mathcal{D}, \tag{6.5}$$

and in this last case the pressure field is defined up to a constant.

Weak Formulation. For later use, it is convenient to record a weak formulation of (6.1-6.2). Let us introduce two collections of function spaces, one for each choice of boundary conditions discussed above. When the boundary conditions are given by (6.3-6.4), we denote

$$\begin{aligned}\mathring{\mathcal{V}}^t &= \{u \in H^1(\Omega^t)^2 \mid u = 0 \text{ on } \partial P^t\}\\ \mathcal{V}^t &= \{u \in H^1(\Omega^t)^2 \mid u = v_P(\cdot,t) \text{ on } \partial P^t\}\\ \mathcal{Q}^t &= L^2(\Omega^t).\end{aligned}$$

When the boundary conditions are given by (6.3) and (6.5), we denote

$$\begin{aligned}\mathring{\mathcal{V}}^t &= H_0^1(\Omega^t)^2\\ \mathcal{V}^t &= \{u \in H^1(\Omega^t)^2 \mid u = v_P(\cdot,t) \text{ on } \partial P^t,\ u = 0 \text{ on } \partial\mathcal{D}\}\\ \mathcal{Q}^t &= L^2(\Omega^t)/\mathbb{R}.\end{aligned}$$

In either of these two settings, a weak formulation of (6.1-6.2) reads: Find $u(\cdot,t) \in \mathcal{V}^t$ and $p(\cdot,t) \in \mathcal{Q}^t$ such that

$$m^t(\dot{u},w) + a^t(u,w) + c^t(w,p) = 0 \quad \forall w \in \mathring{\mathcal{V}}^t \tag{6.6}$$

$$c^t(u,q) = 0 \quad \forall q \in \mathcal{Q}^t \tag{6.7}$$

for every $t \in (0,T]$, where the meanings of $\mathring{\mathcal{V}}^t$, $\mathcal{V}^t$, and $\mathcal{Q}^t$ depend upon the boundary conditions under consideration, and

$$m^t(u,w) = \int_{\Omega^t} u \cdot w \, dx \tag{6.8}$$

$$a^t(u,w) = \nu \int_{\Omega^t} \left(\nabla_x u + (\nabla_x u)^T\right) : \nabla_x w \, dx + \int_{\Omega^t} (u \cdot \nabla_x u) \cdot w \, dx \tag{6.9}$$

$$c^t(u,p) = -\int_{\Omega^t} (\nabla \cdot u) p \, dx. \tag{6.10}$$

The well-posedness of this system in the case of a fixed domain without advection is proven in [45].

6.3 Method

In this section, we present a discretization of (6.1-6.2) that is based upon the use of a universal mesh. Our approach follows that of Chapter 2, where a framework for constructing numerical methods for moving-boundary problems using universal meshes is introduced in the context of a parabolic model problem.

As in Chapter 2, the discretization proceeds in several steps: (1) partitioning the temporal axis

into short time intervals $\bigcup_{n=1}^{N}(t^{n-1},t^n] = (0,T]$; (2) constructing a conforming mesh $\mathcal{S}_h(t)$ for Ω^t, $t \in (t^{n-1},t^n]$, over each short time interval by adapting the universal mesh; (3) performing a Galerkin projection of the governing equations onto a finite element space associated with $\mathcal{S}_h(t)$ over each short time interval; and (4) choosing a time integrator to numerically integrate the resulting system of ODE's over $(t^{n-1},t^n]$ for each n. In the last step, the initial condition for numerical integration over $(t^{n-1},t^n]$ will come from projecting the discrete solution at time $t = t^{n-1}$ onto the finite element space associated with the triangulation $\mathcal{S}_h(t_+^{n-1})$, which generally differs from $\mathcal{S}_h(t^{n-1})$.

A distinctive feature of our discretization is, of course, the manner in which the conforming triangulation $\mathcal{S}_h(t)$ of Ω^t is constructed. As in Chapter 2, our method constructs $\mathcal{S}_h(t)$ by immersing Ω^t in a universal mesh $\mathcal{T}_h$, identifying a subtriangulation of $\mathcal{T}_h$ that approximates the immersed domain, and adjusting a few elements so that it conforms exactly to Ω^t (see Fig. 6.2). We recall the construction of $\mathcal{S}_h(t)$ using a universal mesh in the following subsection and refer the reader back to Chapter 2 for greater detail.

The conditions under which a given background triangulation $\mathcal{T}_h$ can be so adjusted to conform to a family of domains Ω^t, $t \in [0,T]$, were laid forth in [116, 118] and expanded in Chapter 2. Briefly, the procedure is guaranteed to succeed if:

(6.3.i) Ω^t is C^2-regular for every t.

(6.3.ii) $\mathcal{T}_h$ is sufficiently refined in a neighborhood of $\partial\Omega^t$ for every t.

(6.3.iii) All triangles in $\mathcal{T}_h$ have angles bounded above by a constant $\vartheta < \pi/2$.

(6.3.iv) The intervals $(t^{n-1},t^n]$ satisfy $\max\limits_{1\le n\le N}(t^n - t^{n-1}) \le Ch$ with a sufficiently small constant C.

6.3.1 Universal Mesh

Let $\mathcal{T}_h$ be a triangulation of $\mathcal{D}$ satisfying conditions (6.3.i-6.3.iv), with h denoting the maximum diameter of an element $K \in \mathcal{T}_h$. For $i = 0,1,2,3$, let $\mathcal{T}_{h,i}^t$ denote the collection of triangles $K \in \mathcal{T}_h$ for which exactly i vertices of K do not lie in the interior of Ω^t.

Fix a partition $0 = t^0 < t^1 < \cdots < t^N = T$ of the temporal axis. Our approach for constructing a conforming mesh $\mathcal{S}_h(t)$ for Ω^t, $t \in (t^{n-1},t^n]$, consists of identifying a subtriangulation $\mathcal{S}_h^n$ of the background triangulation $\mathcal{T}_h$ and defining a time-dependent bijection

$$\Phi^t : \mathcal{S}_h^n \to \Omega^t, \quad t \in (t^{n-1},t^n].$$

Here and in the sequel, we abuse notation by writing $\mathcal{S}_h^n$ to denote both the triangulation (the list of vertices and their connectivities) as well as the region in $\mathbb{R}^2$ that it occupies. Our choice of $\mathcal{S}_h^n$ is

$$\mathcal{S}_h^n = \mathcal{T}_{h,0}^{t^{n-1}} \cup \mathcal{T}_{h,1}^{t^{n-1}} \cup \mathcal{T}_{h,2}^{t^{n-1}}, \tag{6.11}$$

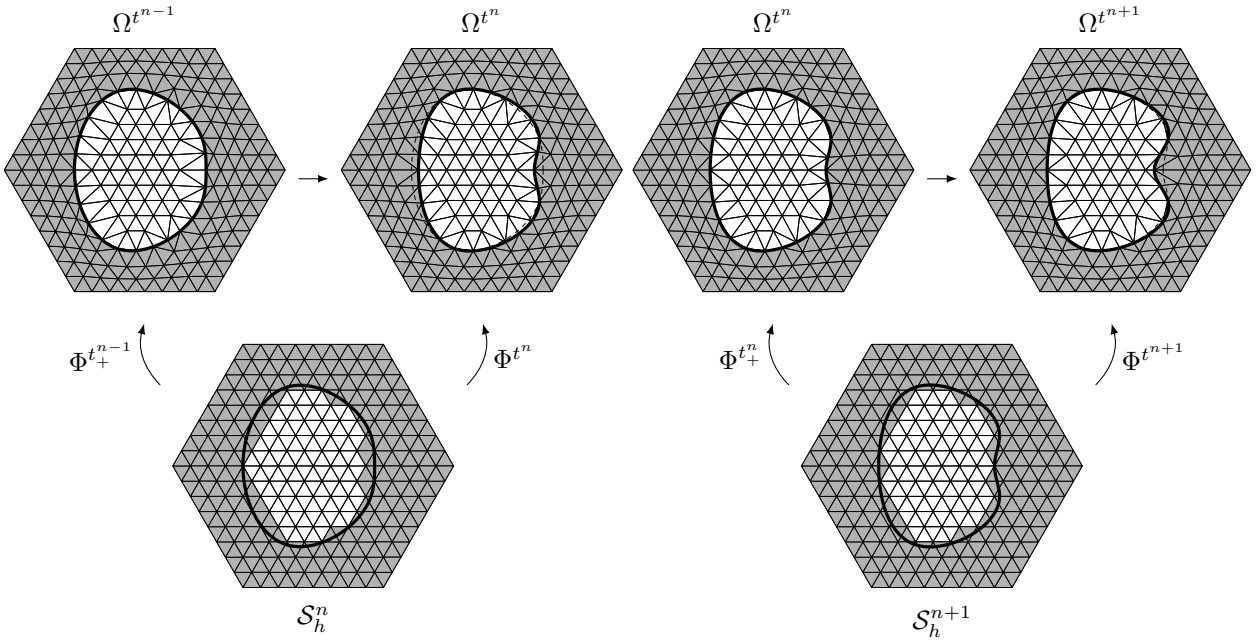

Figure 6.2: Illustration of the manner in which a universal mesh provides a conforming triangulation of an immersed domain Ω^t for all times t. Over a short time interval $(t^{n-1}, t^n]$, an approximating subtriangulation $\mathcal{S}_h^n$ is identified and adapted to the immersed domain using a map $\Phi^t : \mathcal{S}_h^n \to \Omega^t$, $t \in (t^{n-1}, t^n]$. Over the next short time interval $(t^n, t^{n+1}]$, a new subtriangulation $\mathcal{S}_h^{n+1}$ is identified and adapted to the immersed domain using a map $\Phi^t : \mathcal{S}_h^{n+1} \to \Omega^t$, $t \in (t^n, t^{n+1}]$. For visual clarity, the boundary of $\Omega^{t^{n-1}}$ has been juxtaposed in dashed lines onto the conforming mesh $\Phi^{t^n}(\mathcal{S}_h^n)$ for Ω^{t^n}. Likewise, the boundary of Ω^{t^n} has been juxtaposed in dashed lines onto the conforming mesh $\Phi^{t^{n+1}}(\mathcal{S}_h^{n+1})$ for $\Omega^{t^{n+1}}$

which is simply the set of triangles in the background triangulation with at least one vertex lying inside $\Omega^{t^{n-1}}$. Our choice of the map $\Phi^t : \mathcal{S}_h^n \to \Omega^t$ is that detailed in Chapter 2, Section 2.5.

For each $t \in (t^{n-1}, t^n]$, the map Φ^t delivers a conforming mesh of Ω^t having the same connectivity as $\mathcal{S}_h^n$ but consisting of triangles $\Phi^t(K)$, $K \in \mathcal{S}_h^n$. We label this curvilinear mesh $\Phi^t(\mathcal{S}_h^n)$ and set

$$\mathcal{S}_h(t) = \Phi^t(\mathcal{S}_h^n), \quad t \in (t^{n-1}, t^n].$$

The remainder of this section is devoted to a discretization of (6.1-6.2) using finite element spaces over the evolving subtriangulation $\mathcal{S}_h(t)$. As is customary for readers familiar with ALE schemes, the resulting discretization (cf. (6.21)) over each short time interval $(t^{n-1}, t^n]$ will resemble

a discretization of

$$\frac{Du}{Dt} + (u - v) \cdot \nabla_x u - \nu \Delta_x u = -\nabla_x p \qquad \text{in } \mathcal{D} \setminus P^t \tag{6.12}$$

$$\nabla_x \cdot u = 0 \qquad \text{in } \mathcal{D} \setminus P^t, \tag{6.13}$$

where

$$\frac{Du}{Dt} = \frac{\partial u}{\partial t} + v \cdot \nabla_x u$$

denotes the *material time derivative* of u along the path of a material particle that moves with the mesh $\mathcal{S}_h(t)$, whose velocity we denote by

$$v(\Phi^t(X), t) = \dot{\Phi}^t(X) = \left.\frac{\partial}{\partial t}\right|_X \Phi^t(X). \tag{6.14}$$

Since the subtriangulation $\mathcal{S}_h(t)$ changes abruptly at each t^n, $n = 1, 2, \ldots, N$, a projection will be used to transfer information between finite element spaces at such instants; cf. Section 6.3.3.

6.3.2 Galerkin Formulation over Short Time Intervals

We now describe a spatial discretization of (6.1-6.2) that is obtained by performing a Galerkin projection of the weak equations (6.6-6.7) onto finite element subspaces $\mathring{\mathcal{V}}_h^t \subset \mathring{\mathcal{V}}^t$, $\mathcal{V}_h^t \subset \mathcal{V}^t$, and $\mathcal{Q}_h^t \subset \mathcal{Q}^t$ over a short time interval $(t^{n-1}, t^n]$. We focus on the case in which the boundary conditions are given by (6.3-6.4). The case in which the boundary conditions are given by (6.3) and (6.5) is handled similarly.

Here, we consider the use of Taylor-Hood $\mathcal{P}^k$-$\mathcal{P}^{k-1}$ finite elements with an integer $k \geq 2$ [129]. Such elements approximate the velocity field u and the pressure field p with continuous functions that are elementwise polynomials of degree at most k and $k-1$, respectively, on $\mathcal{S}_h(t)$. These finite element spaces are easy to construct with the aid of the map $\Phi^t : \mathcal{S}_h^n \to \Omega^t$ introduced in Section 6.3.1. Namely,

$$\begin{aligned}
\mathring{\mathcal{V}}_h^t &= \left\{ u_h \in C^0(\overline{\Omega^t})^2 \;\middle|\; u_h \circ \Phi^t\big|_K \in \mathcal{P}^k(K)^2 \,\forall K \in \mathcal{S}_h^n,\ u_h = 0 \text{ on } \partial P^t \right\} \\
\mathcal{V}_h^t &= \left\{ u_h \in C^0(\overline{\Omega^t})^2 \middle| \, u_h \circ \Phi^t\big|_K \in \mathcal{P}^k(K)^2 \,\forall K \in \mathcal{S}_h^n,\ u_h = i_h^t v_P(\cdot, t) \text{ on } \partial P^t \right\} \\
\mathcal{Q}_h^t &= \left\{ p_h \in C^0(\overline{\Omega^t}) \;\middle|\; p_h \circ \Phi^t\big|_K \in \mathcal{P}^{k-1}(K) \,\forall K \in \mathcal{S}_h^n \right\}.
\end{aligned}$$

Here, $i_h^t v_P(\cdot, t)$ denotes the nodal interpolant of $v_P(\cdot, t)$ onto the space of continuous functions on ∂P^t that are edgewise polynomials of degree k, i.e. $i_h^t v_P(\Phi^t(\cdot), t) \in \mathcal{P}^k(e)$ for every edge $e \subset \partial \mathcal{S}_h^n$.

The Galerkin projection of (6.6-6.7) over $(t^{n-1}, t^n]$ then reads: Find $u_h(\cdot, t) \in \mathcal{V}_h^t$ and $p_h(\cdot, t) \in$

$\mathcal{Q}_h^t$ such that

$$m^t(\dot{u}_h, w_h) + a^t(u_h, w_h) + c^t(w_h, p_h) = 0 \quad \forall w_h \in \mathring{\mathcal{V}}_h^t \tag{6.15}$$

$$c^t(u_h, q_h) = 0 \quad \forall q_h \in \mathcal{Q}_h^t \tag{6.16}$$

for every $t \in (t^{n-1}, t^n]$.

The system (6.15-6.16) is equivalent to a system of differential-algebraic equations (DAEs). To deduce this, it is convenient to construct bases for $\mathring{\mathcal{V}}_h^t$, $\mathcal{V}_h^t$, and $\mathcal{Q}_h^t$ by composing (a subset of) shape functions on the background mesh $\mathcal{T}_h$ with the map $(\Phi^t)^{-1}$. Let

$$\widetilde{\mathcal{V}}_h = \left\{ U_h \in C^0(\overline{\mathcal{D}})^2 \middle|\, U_h|_K \in \mathcal{P}^k(K)^2 \, \forall K \in \mathcal{T}_h \right\}$$
$$\widetilde{\mathcal{Q}}_h = \left\{ P_h \in C^0(\overline{\mathcal{D}}) \middle|\, P_h|_K \in \mathcal{P}^{k-1}(K) \, \forall K \in \mathcal{T}_h \right\}.$$

In what follows, we will derive from (6.15-6.16) a system of DAEs of dimension $\mathcal{N}_u + \mathcal{N}_p$, where $\mathcal{N}_u = \dim(\widetilde{\mathcal{V}}_h)$ and $\mathcal{N}_p = \dim(\widetilde{\mathcal{Q}}_h)$.

Let $\{\widetilde{N}_a\}_{a=1}^{\mathcal{N}_u}$ and $\{\widetilde{M}_k\}_{k=1}^{\mathcal{N}_p}$ be the standard Lagrange bases for $\widetilde{\mathcal{V}}_h$ and $\widetilde{\mathcal{Q}}_h$, respectively, indexed by global degree of freedom numbers. Let $\{X_a\}_{a=1}^{\mathcal{N}_u}$ and $\{Y_k\}_{k=1}^{\mathcal{N}_p}$ denote the locations of the corresponding degrees of freedom in $\mathcal{T}_h$. Additionally, let

$$\mathring{\mathcal{I}}_u^n = \{1 \le a \le \mathcal{N}_u \mid \mathrm{supp}(\widetilde{N}_a) \cap \mathrm{int}(\mathcal{S}_h^n) \neq \emptyset,\ \widetilde{N}_a = 0 \text{ on } \partial\mathcal{S}_h^n \setminus \partial\mathcal{D}\}$$
$$\mathcal{I}_u^n = \{1 \le a \le \mathcal{N}_u \mid \mathrm{supp}(\widetilde{N}_a) \cap \mathrm{int}(\mathcal{S}_h^n) \neq \emptyset\}$$
$$\mathcal{I}_p^n = \{1 \le k \le \mathcal{N}_p \mid \mathrm{supp}(\widetilde{M}_k) \cap \mathrm{int}(\mathcal{S}_h^n) \neq \emptyset\}.$$

where $\mathrm{supp}(f)$ denotes the support of a function f and $\mathrm{int}(S)$ denotes the interior of a set S. Bases for the spaces $\mathring{\mathcal{V}}_h^t$, $\mathcal{V}_h^t$, and $\mathcal{Q}_h^t$ are easily constructed with the aid of the functions $n_a^t : \Omega^t \to \mathbb{R}^2$ and $m_k^t : \Omega^t \to \mathbb{R}$ given by

$$n_a^t(\Phi^t(X)) = \widetilde{N}_a(X), \quad a \in \mathcal{I}_u^n \tag{6.17}$$

and

$$m_k^t(\Phi^t(X)) = \widetilde{M}_k(X), \quad k \in \mathcal{I}_p^n. \tag{6.18}$$

Namely,

$$\mathring{\mathcal{V}}_h^t = \mathrm{span}\left\{ n_a^t \mid a \in \mathring{\mathcal{I}}_u^n \right\}$$
$$\mathcal{V}_h^t = \mathring{\mathcal{V}}_h^t + \sum_{a \in \mathcal{I}_u^n \setminus \mathring{\mathcal{I}}_u^n} v_P(\Phi^t(X_a), t) n_a^t$$
$$\mathcal{Q}_h^t = \mathrm{span}\left\{ m_k^t \mid k \in \mathcal{I}_p^n \right\}.$$

If we adopt the convention that $n_a^t = 0$ in Ω^t for $a \notin \mathcal{I}_u^n$ and $m_k^t = 0$ in Ω^t for $k \notin \mathcal{I}_p^n$, we may

expand

$$u_h(x,t) = \sum_{a=1}^{\mathcal{N}_u} \mathbf{u}_a(t) n_a^t(x) \tag{6.19}$$

and

$$p_h(x,t) = \sum_{k=1}^{\mathcal{N}_p} \mathbf{p}_k(t) m_k^t(x) \tag{6.20}$$

as linear combinations of the shape functions n_a^t and m_a^t, bearing in mind that

$$u_h(\cdot,t) \in \mathcal{V}_h^t \implies \mathbf{u}_a(t) = v_P(\Phi^t(X_a),t) \; \forall a \in \mathcal{I}_u^n \setminus \mathring{\mathcal{I}}_u^n.$$

In the expansions above, we adopt the convention that $\mathbf{u}_a(t) = 0$ for $a \notin \mathcal{I}_u^n$ and $\mathbf{p}_k(t) = 0$ for $k \notin \mathcal{I}_p^n$. Observe that by (6.17),

$$\begin{aligned}
\dot{u}_h(x,t) &= \sum_{a=1}^{\mathcal{N}_u} \dot{\mathbf{u}}_a(t) n_a^t(x) + \sum_{a=1}^{\mathcal{N}_u} \mathbf{u}_a(t) \frac{\partial n_a^t}{\partial t}(x) \\
&= \sum_{a=1}^{\mathcal{N}_u} \dot{\mathbf{u}}_a(t) n_a^t(x) + \sum_{a=1}^{\mathcal{N}_u} \mathbf{u}_a(t) (-v(x,t) \cdot \nabla_x n_a^t(x)) \\
&= \sum_{a=1}^{\mathcal{N}_u} \dot{\mathbf{u}}_a(t) n_a^t(x) - v(x,t) \cdot \nabla_x u_h(x,t)
\end{aligned}$$

where v is given by (6.14).

It follows that (6.15-6.16) is equivalent to the system of DAEs

$$\mathbf{M}(t) \begin{pmatrix} \dot{\mathbf{u}}(t) \\ 0 \end{pmatrix} + \mathbf{K}(t) \begin{pmatrix} \mathbf{u}(t) \\ \mathbf{p}(t) \end{pmatrix} + \begin{pmatrix} \mathbf{b}(\mathbf{u}(t),t) \\ 0 \end{pmatrix} = \begin{pmatrix} \mathbf{f}(t) \\ 0 \end{pmatrix} \tag{6.21}$$

where

$$\mathbf{M}(t) = \begin{pmatrix} \mathbf{M}_u(t) & 0 \\ 0 & 0 \end{pmatrix}$$

$$\mathbf{K}(t) = \begin{pmatrix} \mathbf{K}_u(t) & \mathring{\mathbf{C}}(t)^T \\ \mathbf{C}(t) & \mathbf{Z} \end{pmatrix}$$

and the entries of $\mathbf{M}_u(t), \mathbf{K}_u(t) \in \mathbb{R}^{\mathcal{N}_u \times \mathcal{N}_u}$, $\mathbf{C}(t), \mathring{\mathbf{C}}(t) \in \mathbb{R}^{\mathcal{N}_p \times \mathcal{N}_u}$, $\mathbf{Z} \in \mathbb{R}^{\mathcal{N}_p \times \mathcal{N}_p}$, and $\mathbf{b}(\mathbf{u}(t),t), \mathbf{f}(t) \in$

$\mathbb{R}^{\mathcal{N}_u}$ are given by

$$\mathbf{M}_{u,ab}(t) = \begin{cases} m^t(n_b^t, n_a^t) & \text{if } a \in \mathring{\mathcal{I}}_u^n, b \in \mathcal{I}_u^n \\ 0 & \text{otherwise} \end{cases}$$

$$\mathbf{K}_{u,ab}(t) = \begin{cases} a_\nu^t(n_b^t, n_a^t) & \text{if } a \in \mathring{\mathcal{I}}_u^n, b \in \mathcal{I}_u^n \\ \delta_{ab} & \text{otherwise} \end{cases}$$

$$\mathbf{C}_{kb}(t) = \begin{cases} c^t(n_b^t, m_k^t) & \text{if } k \in \mathcal{I}_p^n, b \in \mathcal{I}_u^n \\ 0 & \text{otherwise} \end{cases}$$

$$\mathring{\mathbf{C}}_{kb}(t) = \begin{cases} c^t(n_b^t, m_k^t) & \text{if } k \in \mathcal{I}_p^n, b \in \mathring{\mathcal{I}}_u^n \\ 0 & \text{otherwise} \end{cases}$$

$$\mathbf{Z}_{kl} = \begin{cases} 0 & \text{if } k \in \mathcal{I}_p^n \\ \delta_{kl} & \text{otherwise} \end{cases}$$

$$\mathbf{b}_a(\mathbf{u}(t), t) = \begin{cases} b^t(u_h - v, u_h, n_a^t) & \text{if } a \in \mathring{\mathcal{I}}_u^n \\ 0 & \text{otherwise} \end{cases}$$

$$\mathbf{f}_a(t) = \begin{cases} v_P(\Phi^t(X_a), t) & \text{if } a \in \mathcal{I}_u^n \setminus \mathring{\mathcal{I}}_u^n \\ 0 & \text{otherwise.} \end{cases}$$

Here, δ_{ab} denotes the Kronecker delta, and

$$a_\nu^t(u, w) = \nu \int_{\Omega^t} \left(\nabla_x u + (\nabla_x u)^T\right) : \nabla_x w \, dx$$
$$b^t(u_1, u_2, w) = \int_{\Omega^t} (u_1 \cdot \nabla_x u_2) \, w \, dx.$$

In hindsight, it is now evident that (6.21) is a discretization of the equations (6.12-6.13) that were alluded to earlier.

Remark. In the preceding paragraphs, we opted to construct a system of DAEs of dimension $\mathcal{N}_u + \mathcal{N}_p$ over each short time interval $(t^{n-1}, t^n]$, even though a portion of those DAEs correspond to degrees of freedom in the background mesh that do not belong to $\mathcal{S}_h^n$. This was accomplished by incorporating the set of trivial DAEs $\mathbf{u}_a(t) = 0$ for $a \notin \mathcal{I}_u^n$ and $\mathbf{p}_k(t) = 0$ for $k \notin \mathcal{I}_p^n$ into the system via the prescriptions $\mathbf{K}_{u,ab}(t) = \delta_{ab}$ for $a \notin \mathcal{I}_u^n$ and $\mathbf{Z}_{kl}(t) = \delta_{kl}$ for $k \notin \mathcal{I}_p^n$, respectively. The boundary conditions $\mathbf{u}_a(t) = v_P(\Phi^t(X_a), t)$ for $a \in \mathcal{I}_u^n \setminus \mathring{\mathcal{I}}_u^n$ were incorporated similarly via the prescriptions of $\mathbf{K}_u(t)$ and $\mathbf{f}(t)$.

We did this to highlight an important feature of the universal mesh: it permits the use of the same

data structures (e.g., the matrices $\mathbf{M}(t)$ and $\mathbf{K}(t)$) over the complete duration of the simulation, not merely over the intervals during which the mesh evolves continuously. The sparsity patterns of these data structures are invariant since the connectivity of the background mesh never changes.

Having said that, it is worth noting that one could, in principle, choose to replace the background mesh with a new one satisfying (6.3.i-6.3.iv) at any temporal node t^n. Such a strategy may be useful if, for example, a local refinement or coarsening is desired at a particular stage of the simulation. Needless to say, the sizes and sparsity patterns of the data structures would generally change in this scenario. However, the theory presented in Chapter 3 suggests that the order of accuracy of the method is maintained as long as such replacements of the background mesh occur a number of times that remains bounded under refinement.

6.3.3 Initial Condition on each Short Time Interval

In order to complete the prescription of $(\mathbf{u}(t), \mathbf{p}(t))$ over a short time interval $(t^{n-1}, t^n]$, the system of DAEs (6.21) must be supplemented with an initial condition $\mathbf{u}(t_+^{n-1})$. Note that an initial condition for the pressure $\mathbf{p}$ is unnecessary.

Since the spaces $\mathcal{V}_h^{t^{n-1}}$ and $\mathcal{V}_h^{t_+^{n-1}}$ generally need not coincide, a projection is needed in order transfer information between finite element spaces. To this end, we set

$$u_h(\cdot, t_+^{n-1}) = i_h^{t_+^{n-1}} u_h(\cdot, t^{n-1}), \tag{6.22}$$

where i_h^t is the nodal interpolant onto $\mathcal{V}_h^t$ [45, Chapter 1]. The corresponding vector $\mathbf{u}(t_+^{n-1})$ then consists of the coefficients $\mathbf{u}_a(t_+^{n-1})$ in the expansion (6.19).

We remark that more generally, one may consider the use of other surjective, linear projectors onto $\mathcal{V}_h^t$, such as the the orthogonal projector onto $\mathcal{V}_h^t$ with respect to the L^2- or H^1-inner products. The theory presented in Chapter 3 supports the use of the L^2-projection, though the use of interpolation has always proven satisfactory in our numerical examples.

6.3.4 Temporal Discretization

The setup we have described thus far offers the freedom to employ a time integrator of one's choosing to numerically integrate (6.21), a system of DAEs of index 2, from $t = t^{n-1}$ to $t = t^n$. Below we present two examples of integration schemes: a Singly Diagonally Implicit Runge-Kutta (SDIRK) scheme [32, 70], and a fractional step scheme [31, 34, 130]. In accordance with common guidelines for numerically solving DAEs, the SDIRK schemes we consider are stiffly accurate (and hence L-stable) methods [27, 70]. The same schemes are considered by, for instance, [112, 113], in their studies of high-order methods for the Navier-Stokes equations on fixed domains.

For the forthcoming discussion, we remind the reader that the temporal nodes t^n demarcate changes in the reference triangulation $\mathcal{S}_h^n$; hence, the time step Δt adopted during integration

from t^{n-1} to t^n must be less than or equal to $t^n - t^{n-1}$ for every n. In practice, we often take $\Delta t = t^n - t^{n-1}$, though this is by no means a necessity. Recall also that, in accordance with (6.3.iv), the time intervals $(t^n - t^{n-1})$ scale with the mesh spacing h.

Singly Diagonally Implicit Runge-Kutta. Consider the use of a stiffly accurate s-stage Singly Diagonally Implicit Runge-Kutta (SDIRK) scheme of order $\leq s$ with a time step $\Delta t \leq (t^n - t^{n-1})$. At a given time $\tau_0 \in [t^{n-1}, t^n]$, such an integrator advances the current numerical solution $(\mathbf{u}_0, \mathbf{p}_0) \approx (\mathbf{u}(\tau_{0+}), \mathbf{p}(\tau_{0+}))$ to time $t = \tau_0 + \Delta t$ by solving a sequence of s systems of equations, as detailed below. The coefficients $\gamma > 0$ and $\beta_{ij} \in \mathbb{R}$, $i = 1, 2, \ldots, s$, $j = 0, 1, \ldots, i-1$, for various SDIRK methods are tabulated in Appendix 2.A, Tables 2.3-2.6.

Algorithm 6.3.1 SDIRK scheme for integration from $t = \tau_0 \in [t^{n-1}, t^n]$ to $t = \tau_0 + \Delta t \in [t^{n-1}, t^n]$.

Require: Initial condition $(\mathbf{u}_0, \mathbf{p}_0) \approx (\mathbf{u}(\tau_{0+}), \mathbf{p}(\tau_{0+}))$.

1: **for** $i = 1, 2, \ldots, s$ **do**

2: Set

$$\tau_i = \sum_{j=0}^{i-1} \beta_{ij} \tau_j + \gamma \Delta t$$

and

$$\mathbf{u}_* = \sum_{j=0}^{i-1} \beta_{ij} \mathbf{u}_j.$$

3: Solve

$$(\mathbf{M}(\tau_i) + \gamma \Delta t \mathbf{K}(\tau_i)) \begin{pmatrix} \mathbf{u}_i \\ \mathbf{p}_i \end{pmatrix} + \gamma \Delta t \begin{pmatrix} \mathbf{b}(\mathbf{u}_i, \tau_i) \\ 0 \end{pmatrix} = \mathbf{M}(\tau_i) \begin{pmatrix} \mathbf{u}_* \\ 0 \end{pmatrix} + \gamma \Delta t \begin{pmatrix} \mathbf{f}(\tau_i) \\ 0 \end{pmatrix}$$

for $\begin{pmatrix} \mathbf{u}_i \\ \mathbf{p}_i \end{pmatrix}$.

4: **end for**

5: **return** $(\mathbf{u}_s, \mathbf{p}_s) \approx (\mathbf{u}(\tau_0 + \Delta t), \mathbf{p}(\tau_0 + \Delta t))$.

As mentioned in Chapter 2, implementing an SDIRK method amounts to computing s "backward-Euler" steps, with the initial condition at the i^{th} stage given by a linear combination of the solutions at the previous stages. Also, notice that the deformed mesh $\mathcal{S}_h(t)$ is constructed at each one of the s stages of the integration step, namely, for $t \in \{\tau_1, \ldots, \tau_s\}$.

Fractional Step Scheme. Our second example of a time integrator is a fractional step scheme with a time step $\Delta t \leq (t^n - t^{n-1})$. The scheme we propose is an adaptation of classical fractional step schemes [31, 34, 130] to the setting in which the fluid domain evolves with time.

At a given time $\tau_0 \in [t^{n-1}, t^n]$, the fractional step scheme that we propose advances the current

numerical solution $\mathbf{u}_0 \approx \mathbf{u}(\tau_{0+})$ to time $t = \tau_0 + \Delta t$ using a sequence of three steps. First, a preliminary approximation $\mathbf{u}_* \approx \mathbf{u}(\tau_0 + \Delta t)$ that need not satisfy the incompressibility constraint is computed. Next, $\mathbf{u}_*$ is projected onto the space of divergence-free vector fields by solving a Neumann problem for an auxiliary variable $\boldsymbol{\phi}$, leading to a divergence-free quantity $\mathbf{u}_1 \approx \mathbf{u}(\tau_0+\Delta t)$ that serves as the time-Δt advancement of $\mathbf{u}_0$. Finally, an approximation $\mathbf{p}_{1/2}$ to the pressure at $t = \tau_0 + \Delta t/2$ is computed.

To present the scheme in detail, we denote by $\mathbf{M}_p(t)$ and $\mathbf{K}_p(t)$ the $\mathcal{N}_p \times \mathcal{N}_p$ matrices with entries

$$\mathbf{M}_{p,kl}(t) = \begin{cases} \displaystyle\int_{\Omega^t} m_k^t m_l^t \, dx & \text{if } k \in \mathcal{I}_p^n, l \in \mathcal{I}_p^n \\ 0 & \text{otherwise} \end{cases}$$

$$\mathbf{K}_{p,kl}(t) = \begin{cases} \displaystyle\int_{\Omega^t} \nabla_x m_k^t \cdot \nabla_x m_l^t \, dx & \text{if } k \in \mathcal{I}_p^n, l \in \mathcal{I}_p^n \\ \delta_{kl} & \text{otherwise.} \end{cases}$$

We denote $\tau_{1/2} = \tau_0 + \Delta t/2$, and we use $\bar{\mathbf{p}}_{1/2}$ to denote a preliminary approximation to $\mathbf{p}(\tau_{1/2})$, which will be specified shortly. The details of the algorithm follow.

Algorithm 6.3.2 Fractional step scheme for integration from $t = \tau_0 \in [t^{n-1}, t^n]$ to $t = \tau_0 + \Delta t \in [t^{n-1}, t^n]$.

Require: Initial condition $\mathbf{u}_0 \approx \mathbf{u}(\tau_{0+})$, and preliminary approximation $\bar{\mathbf{p}}_{1/2} \approx \mathbf{p}(\tau_{1/2})$.

1: Solve

$$\mathbf{M}_u(\tau_{1/2}) \left(\frac{\mathbf{u}_* - \mathbf{u}_0}{\Delta t} \right) + \mathbf{K}_u(\tau_{1/2}) \left(\frac{\mathbf{u}_0 + \mathbf{u}_*}{2} \right) + \mathring{\mathbf{C}}(\tau_{1/2})^T \bar{\mathbf{p}}_{1/2} + \mathbf{b} \left(\frac{\mathbf{u}_0 + \mathbf{u}_*}{2}, \tau_{1/2} \right) = \frac{\mathbf{f}(\tau_0) + \mathbf{f}(\tau_0 + \Delta t)}{2}$$

for $\mathbf{u}_*$.

2: With $\boldsymbol{\ell} = \Delta t^{-1} \mathbf{C}(\tau_{1/2}) \mathbf{u}_*$, solve

$$\mathbf{K}_p(\tau_{1/2}) \boldsymbol{\phi} = \boldsymbol{\ell}$$

for $\boldsymbol{\phi}$.

3: Set

$$\mathbf{u}_1 = \mathbf{u}_* - \Delta t \mathbf{M}_u(\tau_{1/2})^{-1} \mathring{\mathbf{C}}(\tau_{1/2})^T \boldsymbol{\phi}$$

$$\mathbf{p}_{1/2} = \bar{\mathbf{p}}_{1/2} + \boldsymbol{\phi} + \frac{\nu \Delta t}{2} \mathbf{M}_p(\tau_{1/2})^{-1} \boldsymbol{\ell}.$$

4: Return $(\mathbf{u}_1, \mathbf{p}_{1/2}) \approx (\mathbf{u}(\tau_0 + \Delta t), \mathbf{p}(\tau_0 + \Delta t/2))$.

The precise choices that we made in the update formulas (the boundary conditions imposed on $\mathbf{u}_*$, the boundary conditions imposed on $\boldsymbol{\phi}$, and the update to the pressure) correspond to those made by the projection method "PmII" described in [31]. In particular, we prescribe the boundary values of $\mathbf{u}_*$ with the known values of the velocity field at $\tau_0 + \Delta t$, we impose homogeneous Neumann boundary conditions on $\boldsymbol{\phi}$, and we use a pressure update that is known to deliver second-order accuracy in time for both the velocity and pressure variables in the case of a fixed domain.

To understand the origin of the preceding scheme, it is instructive to consider its spatially continuous, temporally discrete counterpart on a fixed domain ($\Omega^t = \Omega^0 = \mathcal{D} \setminus P^0 \ \forall t$). In this setting, Algorithm 6.3.2 reduces to the following scheme, where we denote by $u_0, u_*, u_1, \phi, p_{1/2}$, and $\bar{p}_{1/2}$ the spatially continuous counterparts of $\mathbf{u}_0, \mathbf{u}_*, \mathbf{u}_1, \boldsymbol{\phi}, \mathbf{p}_{1/2}$, and $\bar{\mathbf{p}}_{1/2}$, respectively:

1. Solve

$$\frac{u_* - u_0}{\Delta t} - \frac{\nu}{2}(\Delta_x u_0 + \Delta_x u_*) + \nabla_x \bar{p}_{1/2} + \frac{u_0 + u_*}{2} \cdot \nabla_x \frac{u_0 + u_*}{2} = 0 \quad \text{in} \quad \Omega^0 \tag{6.23}$$

$$u_* = 0 \quad \text{on} \quad \partial\mathcal{D} \tag{6.24}$$

$$u_* = v_P(\cdot, \tau_0 + \Delta t) \quad \text{on } \partial P^0 \tag{6.25}$$

   for u_*.

2. Solve

$$\begin{aligned} \Delta t \Delta_x \phi &= \nabla_x \cdot u_* \quad \text{in } \Omega^0 \\ \frac{\partial \phi}{\partial n} &= 0 \qquad \text{on } \partial\Omega^0 \end{aligned}$$

   for ϕ.

3. Set

$$u_1 = u_* - \Delta t \nabla_x \phi \tag{6.26}$$

$$p_{1/2} = \bar{p}_{1/2} + \phi - \frac{\nu \Delta t}{2} \Delta_x \phi. \tag{6.27}$$

As mentioned earlier, the scheme above is precisely the second-order method "PmII" of [31]. We have numerical evidence (cf. Section 6.4.1) and heuristic reasoning to suggest that our extension of the method to moving domains is likewise second-order accurate in time, though a justification of this assertion warrants further analysis.

Note that in step 2 of the algorithm, the linear system to be solved for $\boldsymbol{\phi}$ is singular, as it corresponds to a Neumann problem whose solution is determined up to the addition of a constant. This is because for boundary conditions (6.3) and (6.5), the pressure is defined up to a constant. Defining $\boldsymbol{\phi}$ unambiguously requires, for example, imposing the value of one entry of the vector $\boldsymbol{\phi}$

arbitrarily. If a boundary condition of the form (6.4) were to be adopted on part of $\partial\mathcal{D}$, then ϕ would need to satisfy homogeneous Dirichlet boundary conditions therein.

Finally, we describe our choice of $\bar{\mathbf{p}}_{1/2}$, which is set to be equal to the last computed value $\mathbf{p}_{-1/2}$, interpolated onto the appropriate finite element space if necessary. More precisely, we set $\bar{\mathbf{p}}_{1/2} = \mathbf{p}_{-1/2}$ if $\tau_0 \neq t^{n-1}$ and $\bar{\mathbf{p}}_{1/2} = 0$ if $\tau_0 = 0$; otherwise, we set $\bar{\mathbf{p}}_{1/2}$ equal to the vector of coefficients in the expansion

$$\sum_{k=1}^{\mathcal{N}_p} \bar{\mathbf{p}}_{1/2,k} m_k^{t_+^{n-1}} = i_h^{t_+^{n-1}} \left(\sum_{k=1}^{\mathcal{N}_p} \mathbf{p}_{-1/2,k} m_k^{t^{n-1}} \right),$$

where, abusing notation, i_h^t denotes the nodal interpolant onto $\mathcal{Q}_h^t$. Note that choosing $\bar{\mathbf{p}}_{1/2} = 0$ for $\tau_0 = 0$ reduces the accuracy of the very first time step to first order (cf. [31]), however, it is easy see that (by analogy with multi-step methods for ODEs [70]) this does not reduce the order of the scheme's global truncation error.

6.3.5 Algorithm Summary

A summary of the proposed algorithm for integration over $[0, T]$ using a universal mesh $\mathcal{T}_h$ and a temporal partition $0 = t^0 < t^1 < \cdots < t^N = T$ is as follows.

Algorithm 6.3.3 Integration over $[0, T]$ using a universal mesh $\mathcal{T}_h$ and a temporal partition $0 = t^0 < t^1 < \cdots < t^N = T$.

Require: Initial condition $\mathbf{u}(0)$.

1: **for** $n = 1, 2, \ldots, N$ **do**
2: Identify the subtriangulation $\mathcal{S}_h^n$ of $\mathcal{T}_h$ consisting of triangles with at least one vertex lying inside $\Omega^{t^{n-1}}$.
3: Adapt $\mathcal{S}_h^n$ to $\Omega^{t^{n-1}}$ by computing $\mathcal{S}_h(t_+^{n-1}) := \Phi^{t_+^{n-1}}(\mathcal{S}_h^n)$, where $\Phi^t : \mathcal{S}_h^n \to \Omega^t$ is the universal mesh map (2.24).
4: Project $\mathbf{u}(t^{n-1})$ onto the finite element space $\mathcal{V}_h^{t_+^{n-1}}$ associated with $\mathcal{S}_h(t_+^{n-1})$, through (6.22), giving $\mathbf{u}(t_+^{n-1})$.
5: Numerically integrate (6.21) from $t = t_+^{n-1}$ to $t = t^n$ using a time integrator of one's choosing with time step $\Delta t \leq (t^n - t^{n-1})$, giving $(\mathbf{u}(t^n), \mathbf{p}(t^n))$.
6: **end for**
7: **return** $(\mathbf{u}(T), \mathbf{p}(T))$

Remarks.

1. In the last step of the algorithm, the numerical integration may require the evaluation of $\mathcal{S}_h(t) = \Phi^t(\mathcal{S}_h^n)$ at intermediate times $t \in (t^{n-1}, t^n]$ in order to assemble the quantities $\mathbf{M}(t)$, $\mathbf{K}(t)$, $\mathbf{b}(\mathbf{u}(t), t)$, and $\mathbf{f}(t)$ at intermediate stages of integration.

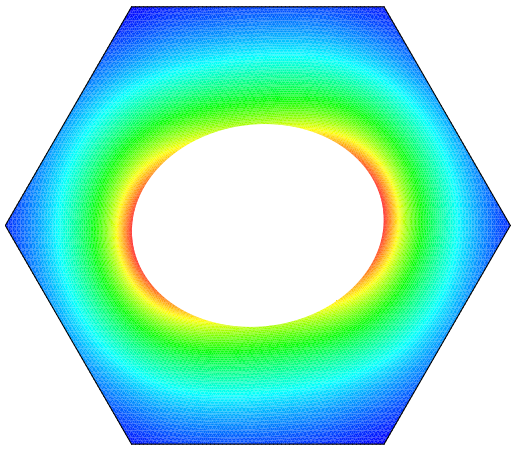

Figure 6.3: Velocity magnitude contours for the manufactured solution (6.28-6.30) at time $t = 0.05$.

2. When the fractional step scheme (6.3.2) is adopted for numerical integration, the output of step (4) in such a scheme is $(\mathbf{u}(t^n), \mathbf{p}(t^n - \Delta t/2))$.

6.4 Numerical Simulations of Flow Past Moving Obstacles

In this section, we apply the proposed methods to simulate flow around various obstacles with prescribed evolution. We consider five examples of obstacles: a rotating ellipse, an oscillating disk, a swimming organism, a rotating stirrer, and a pair of pitching airfoils. We consider the rotating ellipse in order to study numerically the convergence of the methods. The remaining examples serve to illustrate the features of the methodology.

6.4.1 Rotating Ellipse

To study numerically the convergence of the methods, we considered the case in which obstacle P^t is an ellipse with semi-major axis $a = 1.0$ and semi-minor axis $b = 0.8$, rotating at a fixed angular velocity $\omega = 2.5$, as depicted in Fig. 6.3. Using [87] for inspiration, we manufactured a solution by adding a forcing term to the right-hand side of (6.1) so that the exact solution is given by

$$u_1(x_1, x_2, t) = -\frac{a^2 + b^2}{\sqrt{a^4 - b^4}} \omega e^{-\xi} (b \cos \omega t \sin \eta + a \sin \omega t \cos \eta) \tag{6.28}$$

$$u_2(x_1, x_2, t) = -\frac{a^2 + b^2}{\sqrt{a^4 - b^4}} \omega e^{-\xi} (b \sin \omega t \sin \eta - a \cos \omega t \cos \eta) \tag{6.29}$$

$$p(x_1, x_2, t) = \sin(x_1) \sin(x_2), \tag{6.30}$$

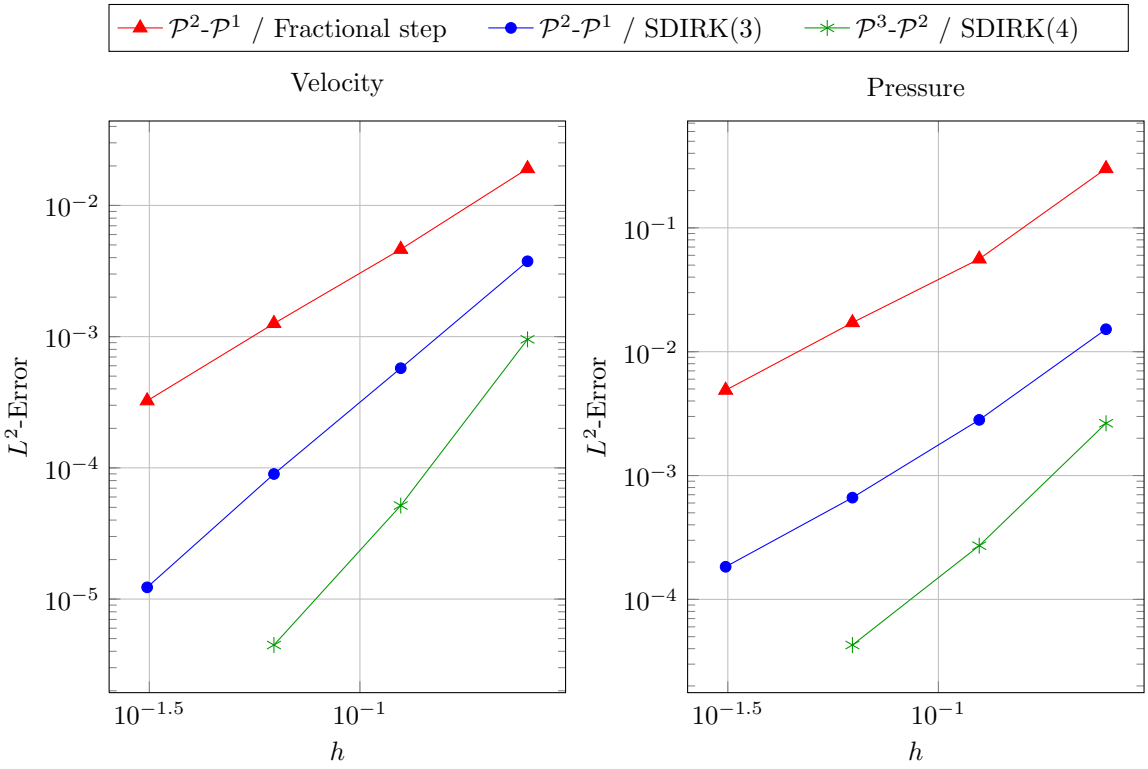

Velocity h_0/h	$\mathcal{P}^2$-$\mathcal{P}^1$ / Fractional step Error	Order	$\mathcal{P}^2$-$\mathcal{P}^1$ / SDIRK(3) Error	Order	$\mathcal{P}^3$-$\mathcal{P}^2$ / SDIRK(4) Error	Order
1	1.91e-02	-	3.75e-03	-	9.53e-04	-
2	4.63e-03	2.04	5.75e-04	2.71	5.16e-05	4.21
4	1.26e-03	1.88	8.98e-05	2.68	4.47e-06	3.53
8	3.24e-04	1.96	1.23e-05	2.87	-	-
Expected Order		1.5		2.5		3.5

Pressure h_0/h	$\mathcal{P}^2$-$\mathcal{P}^1$ / Fractional step Error	Order	$\mathcal{P}^2$-$\mathcal{P}^1$ / SDIRK(3) Error	Order	$\mathcal{P}^3$-$\mathcal{P}^2$ / SDIRK(4) Error	Order
1	3.01e-01	-	1.52e-02	-	2.64e-03	-
2	5.61e-02	2.42	2.81e-03	2.43	2.71e-04	3.28
4	1.72e-02	1.71	6.63e-04	2.09	4.28e-05	2.66
8	4.89e-03	1.81	1.83e-04	1.85	-	-
Expected Order		1.5		1.5		2.5

Figure 6.4: Convergence rates in the $L^2(\Omega^T)$-norm for the solution to incompressible, viscous flow around a rotating ellipse using three combinations of finite elements and time integrators with $\Delta t \propto h$: (1) Taylor-Hood $\mathcal{P}^2$-$\mathcal{P}^1$ elements together with the fractional step scheme (6.3.2), (2) Taylor-Hood $\mathcal{P}^2$-$\mathcal{P}^1$ elements together with a third-order implicit Runge-Kutta scheme, and (3) Taylor-Hood $\mathcal{P}^3$-$\mathcal{P}^2$ elements together with a fourth-order implicit Runge-Kutta scheme. Also shown in the tables are expected orders of convergence inferred from the theory presented in Chapters 3-5.

with $\xi \geq 0$ and $\eta \in [0, 2\pi)$ related to the cartesian coordinates x_1 and x_2 via

$$x_1 \cos \omega t + x_2 \sin \omega t = \frac{\sqrt{a^4 - b^4}}{a} \cosh \xi \cos \eta$$
$$-x_1 \sin \omega t + x_2 \cos \omega t = \frac{\sqrt{a^4 - b^4}}{b} \sinh \xi \sin \eta.$$

The velocity field so manufactured has the property that it is everywhere divergence-free and satisfies the no-slip condition (6.3) on ∂P^t. On the remainder of the fluid boundary, we prescribed the known values of the velocity field. We took $\nu = 1.0$ so that the Reynolds number of the flow was $Re = u_2(a, 0, 0)a/\nu = 2.5$.

We studied the L^2-error in u and p at time $T = 0.05$ on a sequence of uniform refinements of an equilateral triangle mesh with a lowest resolution mesh spacing of $h_0 = 0.25$, using a time step $\Delta t = Th/h_0$ and a temporal subdivision $t^n = n\Delta t$, $n = 0, 1, 2, \ldots, T/\Delta t$. We considered three combinations of finite elements and time integrators: Taylor-Hood $\mathcal{P}^2$-$\mathcal{P}^1$ elements together with the fractional step scheme (6.3.2),[1] Taylor-Hood $\mathcal{P}^2$-$\mathcal{P}^1$ elements together with an SDIRK scheme of order 3 (cf. Table 2.5), and Taylor-Hood $\mathcal{P}^3$-$\mathcal{P}^2$ elements together with an SDIRK scheme of order 4 (cf. Table 2.6). The resulting spatial discretizations for $h_0/h = 1, 2, 4$, and 8, respectively, had 1,851, 7,155, 28,131, and 111,555 degrees of freedom (for $\mathcal{P}^2$-$\mathcal{P}^1$ elements) and 4,419, 17,283, 68,355, and 271,875 degrees of freedom (for $\mathcal{P}^3$-$\mathcal{P}^2$ elements). For each of the combinations of finite elements and time integrators considered, we observed convergence rates that are at worst suboptimal by half an order. These results are consistent with the predictions of Chapter 5, which derive a priori error estimates that are suboptimal by half an order in the L^2-norm for schemes that adopt a universal mesh in conjunction with piecewise polynomial finite element spaces to solve a parabolic model problem.

6.4.2 Oscillating Disk

As a second example, we considered the case in which the obstacle P^t is a disk of radius $R = 1/2$ whose center oscillates vertically with amplitude A and frequency ω about a point $(x_0, y_0) = (-3, 0)$:

$$P^t = \{(x, y) \mid (x - x_0)^2 + (y - y_0 + A\cos(\omega t))^2 < R^2\}.$$

[1] In the case of the fractional step scheme, the error in p was measured at $t = T - \Delta t/2$ rather than at $t = T$.

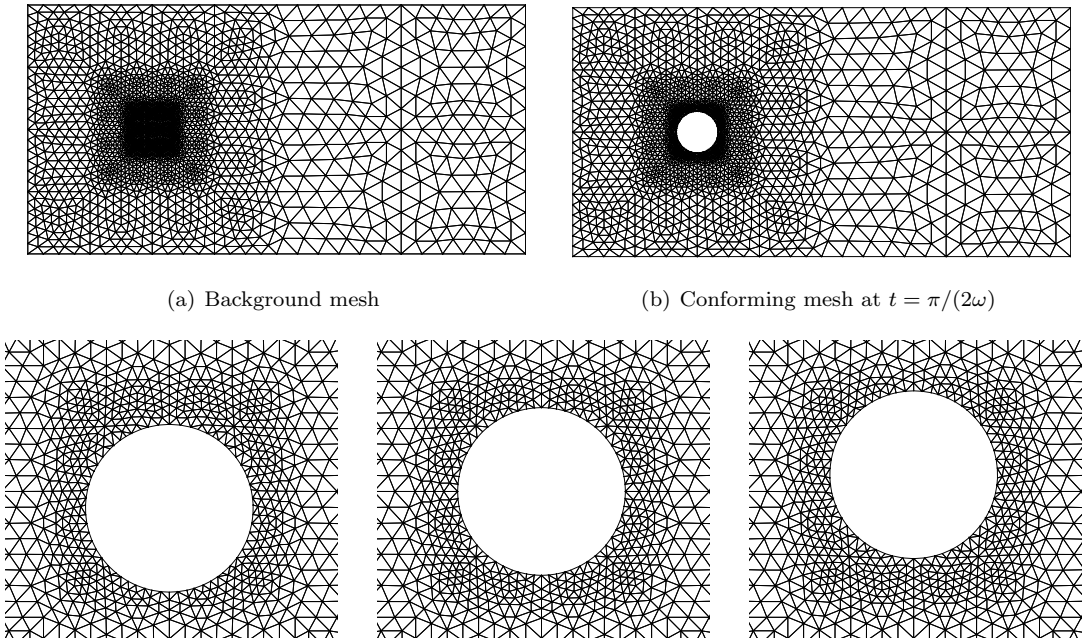

(a) Background mesh

(b) Conforming mesh at $t = \pi/(2\omega)$

(c) Close-up of conforming mesh at $t = 0$

(d) Close-up of conforming mesh at $t = \pi/(2\omega)$

(e) Close-up of conforming mesh at $t = \pi/\omega$

Figure 6.5: Universal mesh for a disk with unit diameter oscillating with amplitude $A = 0.1$ and frequency ω.

We immersed the oscillating disk in a domain $\mathcal{D} = [-6, 6] \times [-3, 3]$ and prescribed boundary conditions

$$\begin{aligned} u &= \left(u_\infty(1 - e^{-t/2}), 0\right) && \text{on } [-6,6] \times \{-3\} \cup [-6,6] \times \{3\} \cup \{-6\} \times [-3,3] \\ pn - \nu(\nabla_x u + \nabla_x^T u)n &= 0 && \text{on } \{6\} \times [-3,3]. \\ u &= (0, \omega A \sin(\omega t)) && \text{on } \partial P^t, \end{aligned}$$

where $u_\infty = 1/2$.

Fig. 6.5 shows the universal mesh that we adopted for this simulation, as well as snapshots of the resulting conforming mesh for $\Omega^t = \mathcal{D} \setminus P^t$ at a few representative instants in time when $A = 0.1$. The background mesh was constructed by inserting stencils of acute triangles into an adaptively refined quadtree; see [20] for details.

We first considered the cases in which $A = 0.1$ and $\omega = 0.8\omega_0$, ω_0, and $1.2\omega_0$, where ω_0 is the natural vortex shedding frequency for flow past a fixed disk of radius R, assuming a Strouhal number $St = (\omega_0/2\pi)(2R)/u_\infty = 0.195$. We took $\nu = 1/370$ so that $Re = (2R)u_\infty/\nu = 185$. We solved the problem using Taylor-Hood $\mathcal{P}^2$-$\mathcal{P}^1$ elements (leading to 18,701 degrees of freedom) together with

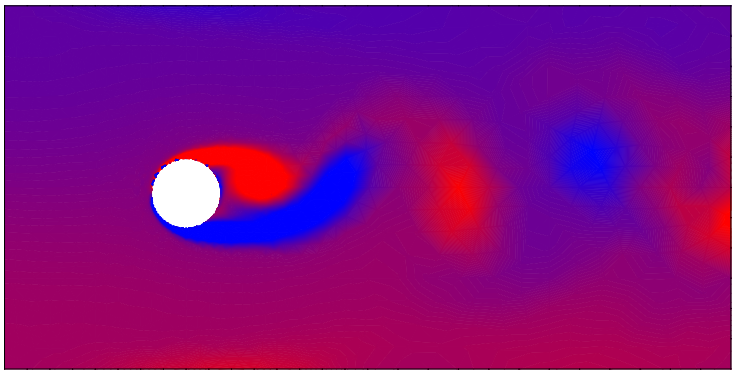

(a) $\omega/\omega_0 = 0.8$

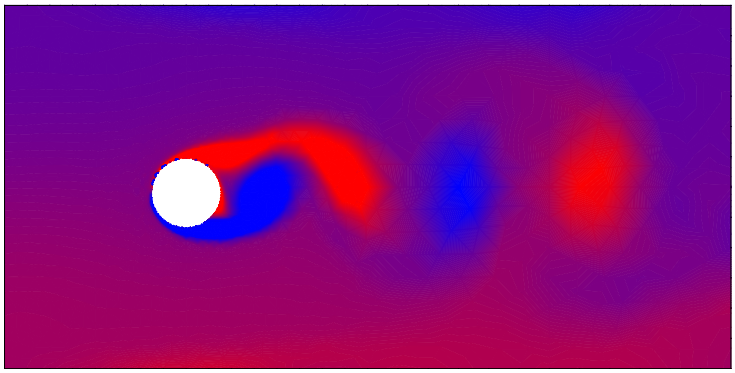

(b) $\omega/\omega_0 = 1$

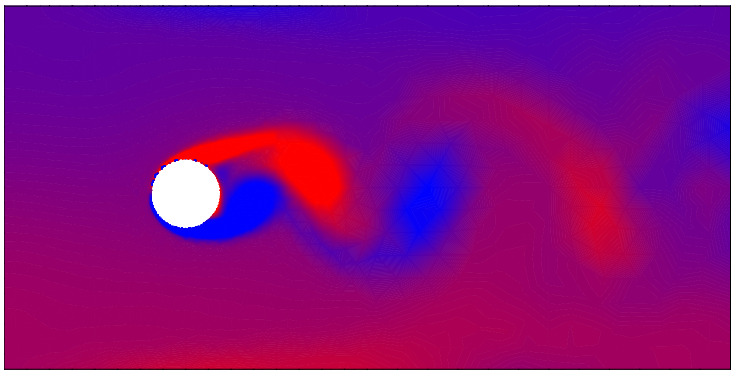

(c) $\omega/\omega_0 = 1.2$

Figure 6.6: Vorticity contours during flow past a disk with unit diameter oscillating with amplitude $A = 0.1$ and frequency (a) $\omega = 0.8\omega_0$, (b) $\omega = \omega_0$, and (c) $\omega = 1.2\omega_0$. The snapshot shown in each case corresponds to the largest time $t < 80$ for which the disk's vertical displacement is $-A$. A characteristic shift in the vortex shedding pattern's phase relative to the disk's oscillation occurs as ω passes through ω_0.

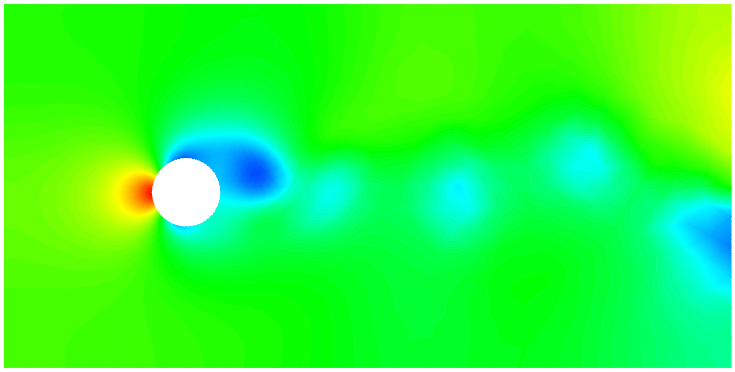

(a) $\omega/\omega_0 = 0.8$

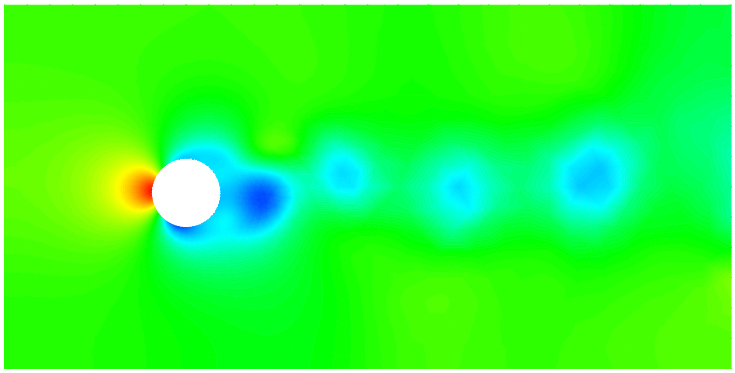

(b) $\omega/\omega_0 = 1$

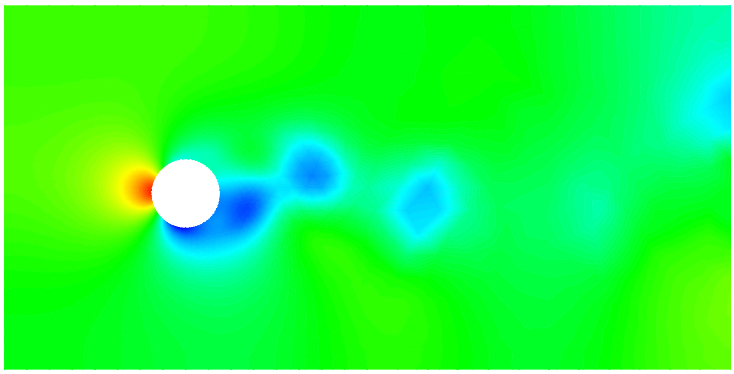

(c) $\omega/\omega_0 = 1.2$

Figure 6.7: Pressure contours during flow past a disk with unit diameter oscillating with amplitude $A = 0.1$ and frequency (a) $\omega = 0.8\omega_0$, (b) $\omega = \omega_0$, and (c) $\omega = 1.2\omega_0$. These snapshots correspond to the same instants in time as in Fig. 6.6.

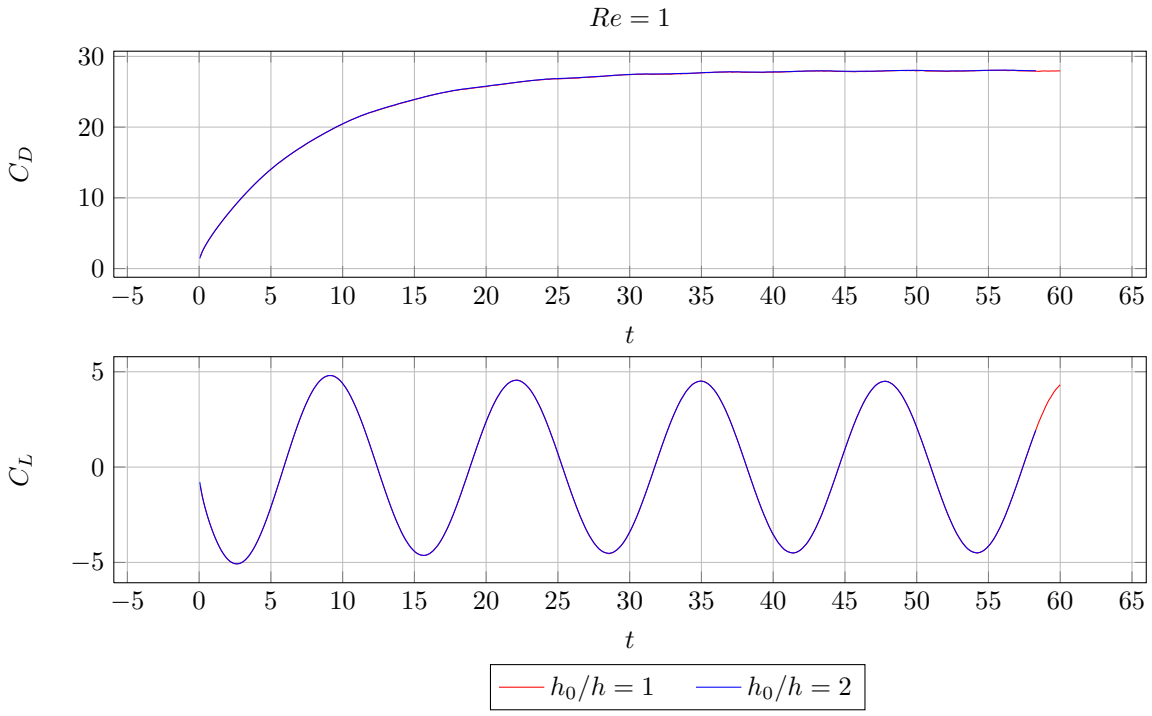

Figure 6.8: Drag and lift coefficients during flow past an oscillating disk at $Re = 1$. The results of two simulations are plotted, one corresponding to the mesh in Fig. 6.5 and one corresponding to a refinement thereof.

the fractional step scheme (6.3.2), using $\Delta t = 0.2$ and $t^n = n\Delta t$. Figs. 6.6-6.7 show contours of the vorticity $\nabla_x \times u$ and the pressure p in each of the three cases at the largest time $t < 80$ for which the disk's vertical displacement is $-A$. We observed a characteristic shift in the vortex shedding pattern's phase relative to the disk's oscillation as ω passed through ω_0, which is consistent with past numerical and experimental studies of flow past an oscillating disk [69, 110].

Next, we fixed $\omega = 0.8\omega_0$ and $A = 0.2$ and studied the temporal evolution of the drag coefficient C_D and the lift coefficient C_L for the cases in which $\nu = 1/2$ (so that $Re = 1$) and $\nu = 1/370$ (so that $Re = 185$). Figs. 6.8-6.9 show the drag and lift coefficients obtained using meshes obtained from uniform refinements of the mesh depicted in Fig. 6.5, whose maximum element diameter is $h_0 := 0.58$. We used Taylor-Hood $\mathcal{P}^2$-$\mathcal{P}^1$ elements together with a 3^{rd}-order SDIRK scheme (cf. Table 2.5), taking $\Delta t = 0.1h/h_0$ and $t^n = n\Delta t$. The resulting spatial discretizations had 18,701 and 74,335 degrees of freedom for $h_0/h = 1, 2$, respectively. The drag and lift coefficients were computed by direct integration over the boundary of the cylinder.

For $Re = 185$ (Fig. 6.9), the simulation on the coarsest mesh exhibits spurious oscillations of the drag and lift coefficients, but these are significantly reduced upon refinement. We suspect that the oscillations are attributable to the interpolation of the solution onto a new finite element space

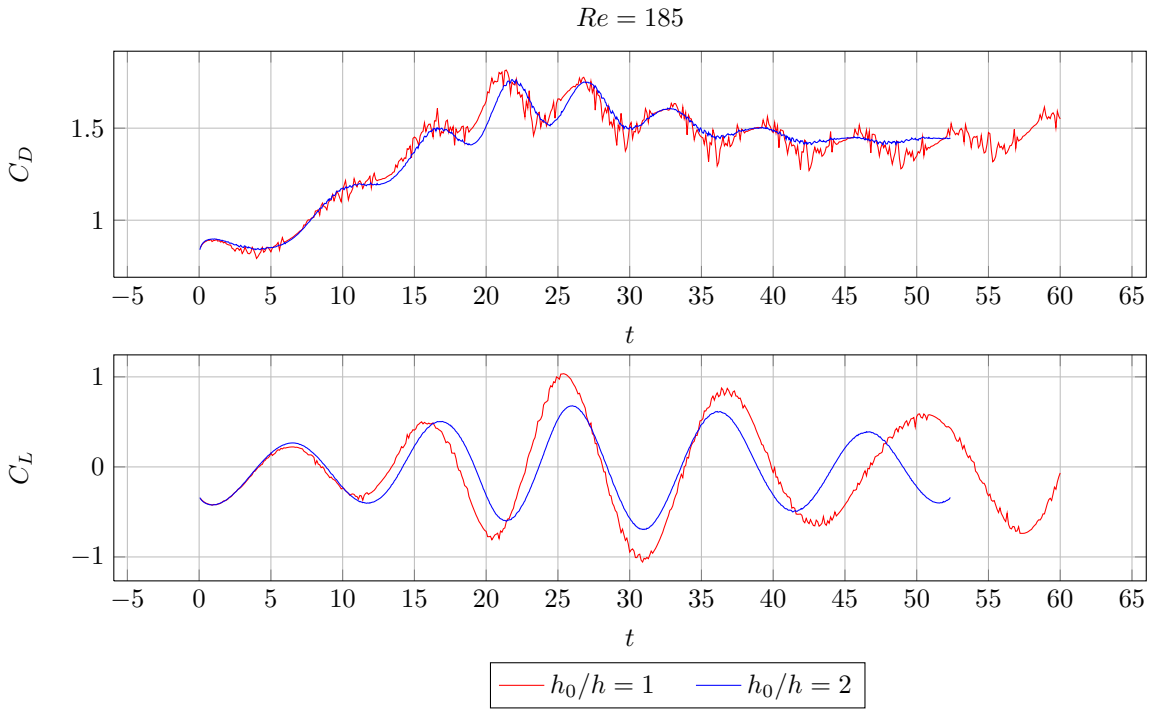

Figure 6.9: Drag and lift coefficients during flow past an oscillating disk at $Re = 185$. The results of two simulations are plotted, one corresponding to the mesh in Fig. 6.5 and one corresponding to a refinement thereof.

at each time t^n (cf. Section 6.3.3), since identical numerical experiments with a fixed disk rendered drag and lift coefficient time series that were free of artificial oscillations. Diffusion seems to also play a role in mitigating the artificial oscillations, as evidenced by their absence in Fig. 6.8, where $Re = 1$. Based upon these observations, it may be worthwhile to explore the possibility of designing more sophisticated strategies for transferring information between finite element spaces, such as projecting the velocity onto the space of divergence-free vector fields after interpolating, in order to obtain more satisfactory results on coarse meshes at high Reynolds numbers.

Fig. 6.10 shows the convergence of the computed drag and lift coefficients under the aforementioned mesh refinement. To measure the errors in the time series, we computed a rectangle-rule approximation $\mathcal{E}$ to the integrated error

$$\left(\int_0^1 (C_D(t) - \bar{C}_D(t))^2 \, dt \right)^{1/2}$$

between the computed solution $C_D(t)$ and a reference solution $\bar{C}_D(t)$ obtained from a fine mesh with $h = 0.145$, and likewise for the lift coefficient. The errors in all cases converged to zero at rates approximately of the order $h^{1.5}$.

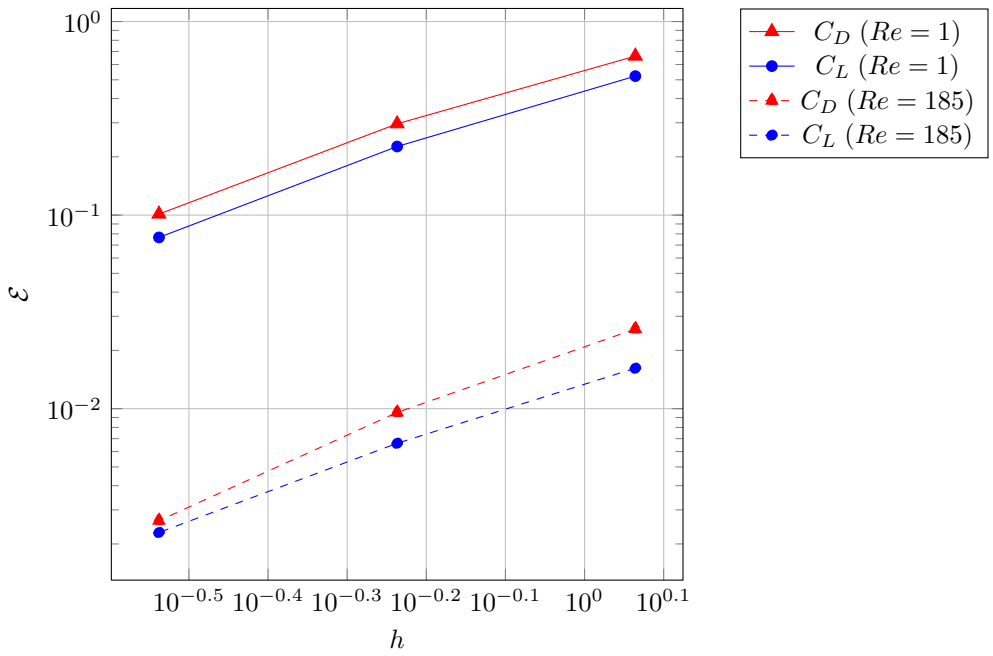

Figure 6.10: Convergence of the drag and lift coefficient time series under mesh refinement. The reported error $\mathcal{E}$ is the square root of (a rectangle-rule approximation of) the integrated squared error $(C_i(t) - \bar{C}_i(t))^2$, $i = L, D$, over the interval $[0, 1]$, relative to a reference solution $\bar{C}_i(t)$ obtained from a fine mesh with $h = 0.145$.

6.4.3 Swimming Organism

Our third example is inspired by the case in which the obstacle P^t is a swimming organism undergoing prescribed shape changes. The organism we consider is a Euglenoid, a unicellular organism whose motility strategy is studied in [7]. We obtained a time-dependent closed cubic spline from the aforementioned study's authors to define the boundary of the swimmer relative to its center of mass. Purely for simplicity, we considered this spline as the boundary of a *planar* organism, instead of the actual organism, which would require the use of axi-symmetry.

We immersed the swimmer in a hexagonal domain $\mathcal{D}$ of diameter 4 and solved for the motion of the surrounding fluid, holding the swimmer's center of mass fixed, imposing the no-slip condition (6.3) on ∂P^t, and imposing Neumann boundary conditions (6.4) on $\partial\mathcal{D}$. The motion of the swimmer was periodic with period $T = 1$ and the velocity of its boundary due to shape changes varied in magnitude from 0 to ≈ 2 in dimensionless units. We took $\nu = 1$ and the approximate length of the swimmer is 2, so that $Re \approx 4$.

We solved the problem using Taylor-Hood $\mathcal{P}^2$-$\mathcal{P}^1$ elements on a uniform background mesh of equilateral triangles ($h = 0.0625$, 18,701 degrees of freedom) using an SDIRK scheme of order 1 (equivalently, backward Euler; cf. Table 2.3) with $\Delta t = 0.0125$ and $t^n = n\Delta t$. Snapshots of the

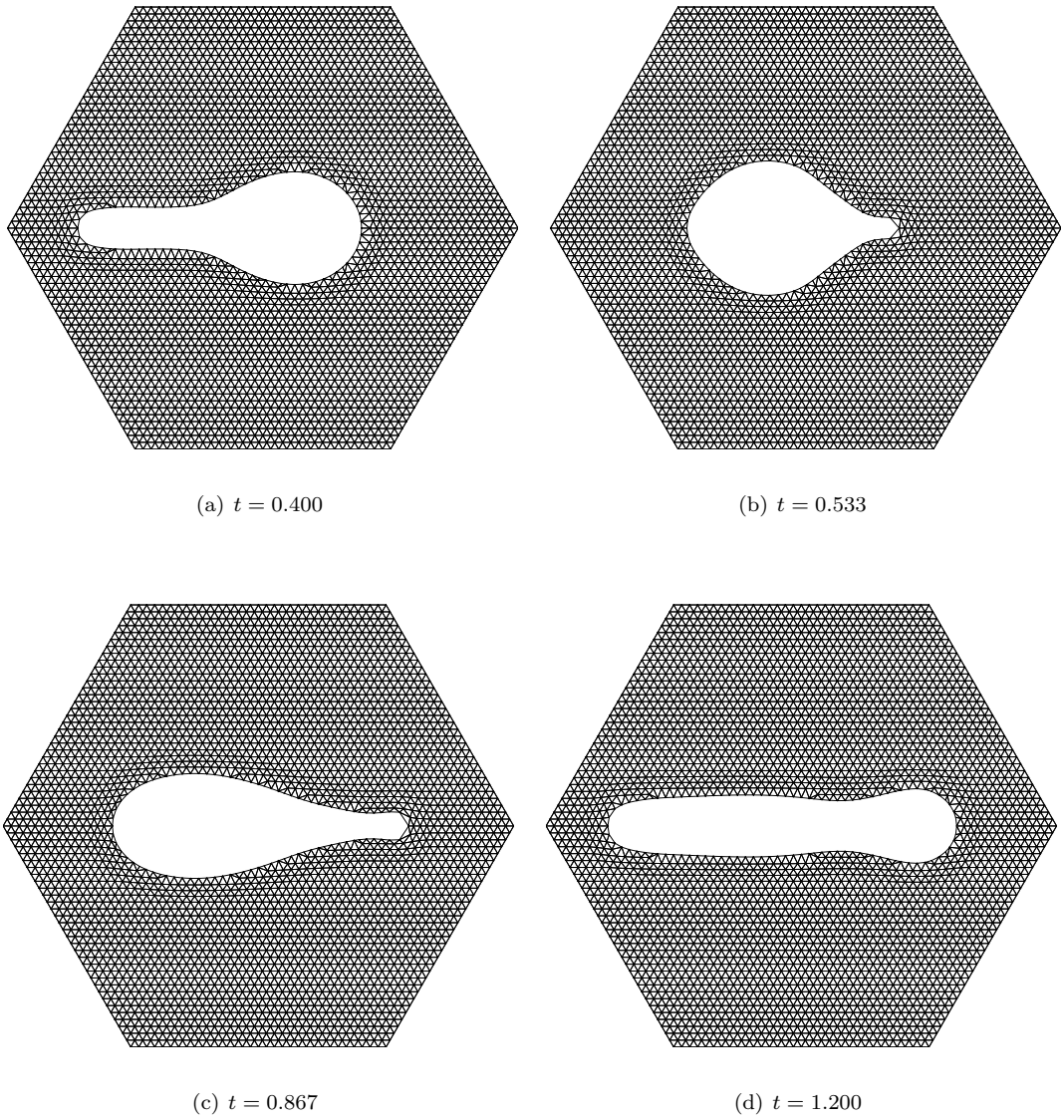

(a) $t = 0.400$ (b) $t = 0.533$

(c) $t = 0.867$ (d) $t = 1.200$

Figure 6.11: Universal mesh for a swimming organism.

conforming mesh and velocity magnitude contours during the simulation are displayed in Figs. 6.11 and 6.12, respectively.

The example illustrates the ability of a universal mesh and the integration algorithm to handle non-rigid domain deformations. Note that for this particular background mesh, the rightmost tip of the swimmer is inadequately refined at some instants in time, as in Fig. 6.11(b). To address this, it is possible to construct an adaptively refined background mesh, analogous to that in Fig. 6.5. We

decided not to do it here, so that the motion of the mesh and its adaption to the evolving geometry can be seen clearly over the uniform grid.

6.4.4 Stirring a Viscous Fluid

Our next example considers the case in which the obstacle boundary is a closed cubic spline in the shape of a propeller-like stirrer that rotates at a prescribed angular velocity

$$\omega(t) = \omega_0(1 - e^{-t/\tau}) \tag{6.31}$$

with $\omega_0 = 5.0$ and $\tau = 0.01$. The stirrer blades were of length ≈ 1.4 and average width ≈ 0.3. We took $\nu = 0.2$ in our simulations, so that the Reynold's number of the flow (treating the stirrer diameter as the characteristic length scale) was approximately 100. To approximate the velocity and pressure, we adopted Taylor-Hood $\mathcal{P}^2$-$\mathcal{P}^1$ elements. To integrate in time, we used an SDIRK scheme of order 3. We immersed the stirrer in hexagonal domain $\mathcal{D}$ of diameter 4 and imposed Neumann boundary condtions (6.4) on $\partial\mathcal{D}$. We adopted a uniform background mesh of equilateral triangles ($h = 0.0625$, 18,701 degrees of freedom).

Figs. 6.13 and 6.14 display snapshots of the mesh and velocity magnitude contours, respectively, at various times during the simulation. The robust nature of the methods introduced here is patent in this example, as traditional deforming-mesh methods could easily encounter difficulties with mesh entanglement upon rotation of the stirrer.

We also solved the problem using a universal mesh of a rectangular domain $\mathcal{D}$ with adaptive refinement in a neighborhood of the propeller, again using Taylor-Hood finite elements. This time, we imposed uniform flow $u = (2, 0)$ on the left, top, and bottom walls of the rectangle, and Neumann boundary conditions on the right wall. We took $\omega_0 = 1$ and $\nu = 0.01$, and we magnified the stirrer so that its blades were of length ≈ 1.7 and average width ≈ 0.4, giving $Re = 580$. Figure 6.15 shows contours of the vorticity at two instants in time.

6.4.5 Pitching Airfoils

As a final example, we consider in Fig. 6.16 the solution of incompressible, viscous flow past a pair of NACA0015 airfoils that change their pitch sinusoidally in time. We solved the problem at $Re = 1000$ using a universal mesh together with Taylor-Hood finite elements. For simplicity, the tips of the airfoils were blunted so that the algorithm described in Chapter 2, Section 2.5 (which applies to smooth geometries) could be applied in its most basic form. Figure 6.16 shows contours of the vorticity at two instants in time corresponding to the maximum and minimum pitch (17° and -17°, respectively) of the airfoils.

6.5 Free-Surface Flow with Surface Tension

In this section, we extend the method detailed in Section 6.3 to simulate free-surface flow with surface tension. We again denote by $\Omega^t \subset \mathbb{R}^2$ the domain occupied by the fluid at time t, and we assume that the free surface constitutes the entire boundary $\partial\Omega^t$. The governing equations for the velocity u and pressure p read

$$\frac{\partial u}{\partial t} + u \cdot \nabla_x u - \nu \Delta_x u = -\nabla_x p + f \quad \text{in } \Omega^t, \tag{6.32}$$

$$\nabla_x \cdot u = 0 \quad \text{in } \Omega^t, \tag{6.33}$$

where $\nu > 0$ is the kinematic viscosity of the fluid and f is a body force. We model surface tension on the free surface $\partial\Omega^t$ via the boundary condition

$$-pn + \nu \left(\nabla_x u + (\nabla_x u)^T\right) n = \gamma \kappa n \quad \text{on } \partial\Omega^t, \tag{6.34}$$

where $\gamma > 0$ is a constant and κ denotes the curvature of the boundary. The motion of the free surface is governed by the kinematic constraint

$$v_n = u \cdot n, \quad \text{on } \partial\Omega^t, \tag{6.35}$$

where v_n denotes the normal component of the velocity of the free surface.

Weak formulation. Denote

$$\mathcal{V}^t = H^1(\Omega^t)^2,$$
$$\mathcal{Y}^t = L^2(\Omega^t).$$

A weak formulation of the problem reads: Find $u(\cdot,t) \in \mathcal{V}^t$, $p(\cdot,t) \in \mathcal{Y}^t$, and $\Omega^t \subset \mathbb{R}^2$ such that (6.35) holds and

$$m^t(\dot{u}, w) + a^t(u, w) + c^t(w, p) = m^t(f, w) + (\gamma\kappa n, w)_{\partial\Omega^t} \quad \forall w \in \mathcal{V}^t, \tag{6.36}$$

$$c^t(u, y) = 0 \quad \forall y \in \mathcal{Y}^t \tag{6.37}$$

for every $t \in (0, T)$, where m^t, a^t, and c^t are defined in (6.8-6.10), and

$$(g, w)_{\partial\Omega^t} = \int_{\partial\Omega^t} g \cdot w \, dx.$$

Spatial discretization. We now present a spatial discretization of the problem that uses a universal mesh to discretize the moving fluid domain.

For the sake of generality, we leave the discretization of the free surface $\partial\Omega^t$ unspecified for the moment, supposing only that the numerical approximation to $\partial\Omega^t$ belongs to a finite-dimensional configuration manifold Q which is a subset of the space of simple, closed, C^2-regular curves. We denote by $\mathbf{q}(t)$ the generalized coordinates describing the configuration of the approximate free surface at time t, and we denote the dimension of Q by M. We use $\Omega(\mathbf{q}(t)) \subset \mathbb{R}^2$ to denote the numerical approximation of the moving fluid domain corresponding to the coordinate vector $\mathbf{q}(t)$.

An instructive example to keep in mind is the case in which Q is the space of closed cubic splines that interpolate a set of $M/2$ distinct points (x_1, y_1), (x_2, y_2), $(x_{M/2}, y_{M/2})$. In this setting, a suitable choice of generalized coordinates is

$$\mathbf{q}(t) = (x_1(t), y_1(t), x_2(t), y_2(t), \ldots, x_{M/2}(t), y_{M/2}(t)),$$

and $\Omega(\mathbf{q}(t))$ is the region in $\mathbb{R}^2$ enclosed by the spline passing through $\{(x_i(t), y_i(t)\}_{i=1}^{M/2}$.

To discretize the fluid velocity and pressure, we again consider the use of Taylor-Hood $\mathcal{P}^k$-$\mathcal{P}^{k-1}$ finite elements with an integer $k \geq 2$ [129]. Namely,

$$\mathcal{V}_h^t = \left\{ u_h \in C^0(\overline{\Omega(\mathbf{q}(t))})^2 \,\middle|\, u_h \circ \Phi^t\big|_K \in \mathcal{P}^k(K)^2 \,\forall K \in \mathcal{S}_h^n \right\},$$
$$\mathcal{Y}_h^t = \left\{ p_h \in C^0(\overline{\Omega(\mathbf{q}(t))}) \,\middle|\, p_h \circ \Phi^t\big|_K \in \mathcal{P}^{k-1}(K) \,\forall K \in \mathcal{S}_h^n \right\}.$$

with $\mathcal{S}_h^n$ given by (6.11) and with $\Phi^t : \mathcal{S}_h^n \to \Omega^t$ the universal mesh map.

Enforcement of the kinematic constraint (6.35) poses a challenge in this framework, since the discretization of the free surface bears little relation to the spatial discretization adopted in the interior of the fluid domain. This implies that the trace of the discrete fluid velocity u_h belongs, in general, to a function space which is different from that to which the velocity of the discrete free surface belongs. The latter space is $T_{\mathbf{q}(t)}Q$, the tangent space of Q at $\mathbf{q}(t)$; in the case of closed cubic splines, $T_{\mathbf{q}(t)}Q$ may be identified with the space spanned by infinitesimal deformations of the spline induced by infinitesimal motions of its control points.

In order to enforce (6.35) at the discrete level, we assume that a linear mapping

$$G : \mathcal{V}_h^t \to T_{\mathbf{q}(t)}Q$$

is adopted to approximate the evaluation of the trace of the fluid velocity u_h on the free surface. This mapping might, for instance, evaluate u_h at the control points of a spline, or perform an L^2-projection of the trace of u_h onto $T_{\mathbf{q}(t)}Q$.

The spatially discrete problem then reads: Find $u_h(\cdot, t) \in \mathcal{V}_h^t$, $p_h(\cdot, t) \in \mathcal{Y}_h^t$, and $\mathbf{q}(t) \in Q$ such

that

$$m^t(\dot{u}_h, w_h) + a^t(u_h, w_h) + c^t(w_h, p_h) = m^t(f, w_h) + (\gamma\kappa n, w_h)_{\partial\Omega(\mathbf{q}(t))} \quad \forall w_h \in \mathcal{V}_h^t, \tag{6.38}$$

$$c^t(u_h, y_h) = 0 \quad \forall y_h \in \mathcal{Y}_h^t, \tag{6.39}$$

$$\dot{\mathbf{q}}(t) = G(u_h(\cdot, t)) \tag{6.40}$$

for every $t \in (0, T)$.

Using the same notation as in Section 6.3.1, but now with

$$\mathring{\mathcal{I}}_u^n = \mathcal{I}_u^n = \{1 \le a \le \mathcal{N}_u \mid \mathrm{supp}(\widetilde{N}_a) \cap \mathrm{int}(\mathcal{S}_h^n) \neq \emptyset\},$$

the system (6.38-6.40) is equivalent to a system of differential algebraic equations of the form

$$\mathbf{M}(\mathbf{q}(t)) \begin{pmatrix} \dot{\mathbf{u}}(t) \\ 0 \end{pmatrix} + \mathbf{K}(\mathbf{q}(t)) \begin{pmatrix} \mathbf{u}(t) \\ \mathbf{p}(t) \end{pmatrix} + \begin{pmatrix} \mathbf{b}(\mathbf{u}(t), \mathbf{q}(t), \dot{\mathbf{q}}(t)) \\ 0 \end{pmatrix} = \begin{pmatrix} \mathbf{f}(\mathbf{q}(t)) \\ 0 \end{pmatrix}, \tag{6.41}$$

$$\tag{6.42}$$

$$\dot{\mathbf{q}}(t) = \mathbf{G}(\mathbf{q}(t))\mathbf{u}(t). \tag{6.43}$$

where

$$\mathbf{f}_a(\mathbf{q}(t)) = \begin{cases} m^t(f, n_a^t) + (\gamma\kappa n, n_a^t)_{\partial\Omega(\mathbf{q}(t))} & \text{if } a \in \mathcal{I}_u^n, \\ 0 & \text{otherwise,} \end{cases}$$

and $\mathbf{M}(\mathbf{q}(t))$, $\mathbf{K}(\mathbf{q}(t))$, and $\mathbf{b}(\mathbf{u}(t), \mathbf{q}(t), \dot{\mathbf{q}}(t))$ are as in Section 6.3.1. Note that we have now written $\mathbf{M}(\mathbf{q}(t))$, $\mathbf{K}(\mathbf{q}(t))$, and $\mathbf{b}(\mathbf{u}(t), \mathbf{q}(t), \dot{\mathbf{q}}(t))$ rather than $\mathbf{M}(t)$, $\mathbf{K}(t)$, and $\mathbf{b}(\mathbf{u}(t), t)$, respectively, in order to emphasize that the temporal variation of these quantities is via their dependence on the domain $\Omega(\mathbf{q}(t))$.

6.5.1 Droplet Impacting a Solid Surface

We now apply the method to simulate a droplet impacting a solid surface. We modeled the solid surface via a potential barrier

$$V(x) = V_0/x_2$$

with $V_0 > 0$, and we applied a body force

$$f = -\nabla_x V + g\mathbf{e}_2,$$

where $\mathbf{e}_2$ is the unit vector in the x_2-direction and $g > 0$ is the acceleration due to gravity. We took $V_0 = 5$, $g = 15$, $\nu = 0.1$, $\gamma = 1.5$, and the initial radius of the droplet equal to 0.6. Contours of the velocity magnitude are shown in Fig. 6.17. The solution was computed on a background mesh of equilateral triangles with $h = 0.0625$, using a time step $\Delta t = 0.005$. The observed maximum velocity of the fluid was near 4, so that the flow had Reynolds number $Re = 24$ and Weber number $We = 6.4$. We approximated the free surface using a closed cubic spline with $M/2 = 30$ control points, and we imposed the kinematic constraint (6.35) via collocation at the control points. The simulation showcases the ease with which the method handles large deformations while maintaining a sharp representation of the free surface.

6.6 Comparison between Universal Meshes and ALE Schemes

We conclude this chapter by presenting a comparison between the method proposed here and an ALE scheme. To perform the comparison, we consider the problem studied in Section 6.4.1: incompressible flow around a rotating ellipse with prescribed angular velocity $\omega = 2.5$. We took the semi-major and semi-minor axes of the ellipse equal to $a = 1.0$ and $b = 0.6$, respectively, and we set $\nu = 1$ so that $Re = 2.5$. We added a forcing term to the right-hand side of (6.1) and imposed Neumann boundary conditions on the outer boundary of the fluid domain so that the exact solution is given by (6.28-6.30).

We computed the solution using two methods: (1) the method introduced in this chapter involving universal meshes, and (2) an ALE scheme with an elasticity-based mesh motion. In both cases, Taylor-Hood $\mathcal{P}^2$-$\mathcal{P}^1$ finite elements were used in conjunction with a 3^{rd}-order implicit Runge Kutta time integrator. In the case of the ALE scheme, we generated a mesh motion by numerically solving a Galerkin finite element discretization of the equations of linear elasticity,

$$
\begin{aligned}
&-\mu\Delta_X U - (\mu+\lambda)\nabla_X(\nabla_X \cdot U) = 0 \quad \text{in } \Omega^0,\\
&U(X,t) = \left(X_1(\cos(\omega t)-1) - X_2\sin(\omega t), X_1\sin(\omega t) + X_2(\cos(\omega t)-1)\right), \quad X \in \partial\Omega^0,
\end{aligned}
$$

for the displacements $U(X,t)$ of the nodes at time t, using piecewise linear finite elements over a mesh of Ω^0. We took $\lambda = \mu = 1$.

To compare the two methods, we computed the L^2-error in the velocity u and pressure p at times $t \leq 0.2$ for meshes of various resolutions, and plotted the errors as a function of the number of degrees of freedom n_{dof} involved in the computations. For the simulations that used universal meshes, $n_{dof} = 3n_V + 2n_E$, where n_V and n_E denote the number of vertices and edges in the background mesh, respectively (2 velocity degrees of freedom per vertex, 2 velocity degrees of freedom per edge, and 1 pressure degree of freedom per vertex). For the ALE simulations, $n_{dof} = 5n_V + 2n_E$ (an extra 2 displacement degrees of freedom per vertex).

Figure 6.6 plots the errors versus number of degrees of freedom, at various times $t \leq 0.2$. At early times t, the two approaches commit comparable errors for comparable cost. As time progresses, the errors incurred by both methods grow, but deterioration of the quality of the mesh generated by the ALE scheme leads in this case to a more rapid increase in the error relative to universal meshes.

6.7 Concluding Remarks

We have presented a framework for computing incompressible, viscous flow within moving fluid domains using a universal mesh. By immersing the domain in a background mesh and adjusting a few elements in a neighborhood of the boundary, the strategy provides a conforming triangulation of the fluid domain at all times over which a spatial discretization of the fluid velocity and pressure fields of any desired order may be constructed using standard finite elements. The resulting semidiscrete equations may be integrated in time using standard time integrators for ODEs. We illustrated the framework using Taylor-Hood finite elements together with Runge-Kutta time integrators and a fractional step scheme. Numerical convergence tests confirmed the theory presented in Chapter 5, which predicts orders of convergence that are suboptimal by half an order in the L^2-norm for a model parabolic problem. We demonstrated the method's versatility on numerical examples that involve flow past an oscillating disk, a swimming organism, a rotating stirrer, and a pair of airfoils. We then extended the method to handle free-surface flows with surface tension, and we applied it to simulate the impact of a droplet on a solid surface.

All examples in the chapter involved flows with low-to-moderate Reynolds number. This enabled us to obtain accurate solutions with relatively coarse and isotropic meshes. For larger Reynolds numbers, we expect to have to modify the spatial discretization by including a stabilization of the advection term. More importantly, meshes will have to be anisotropic and refined around the boundary of the moving obstacle in order to capture the boundary layer.

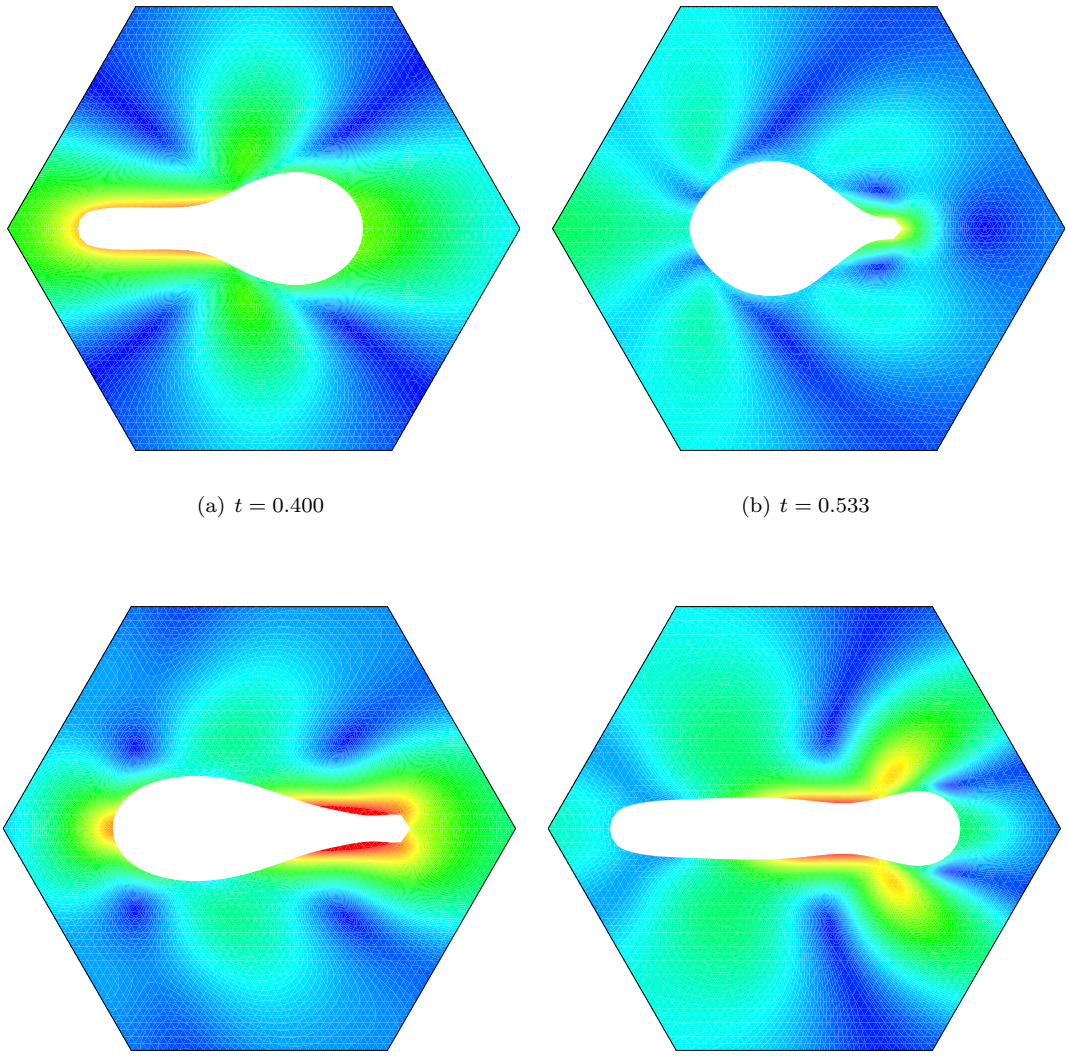

(a) $t = 0.400$

(b) $t = 0.533$

(c) $t = 0.867$

(d) $t = 1.200$

Figure 6.12: Velocity magnitude contours during a simulation of flow around a swimming organism with prescribed shape changes.

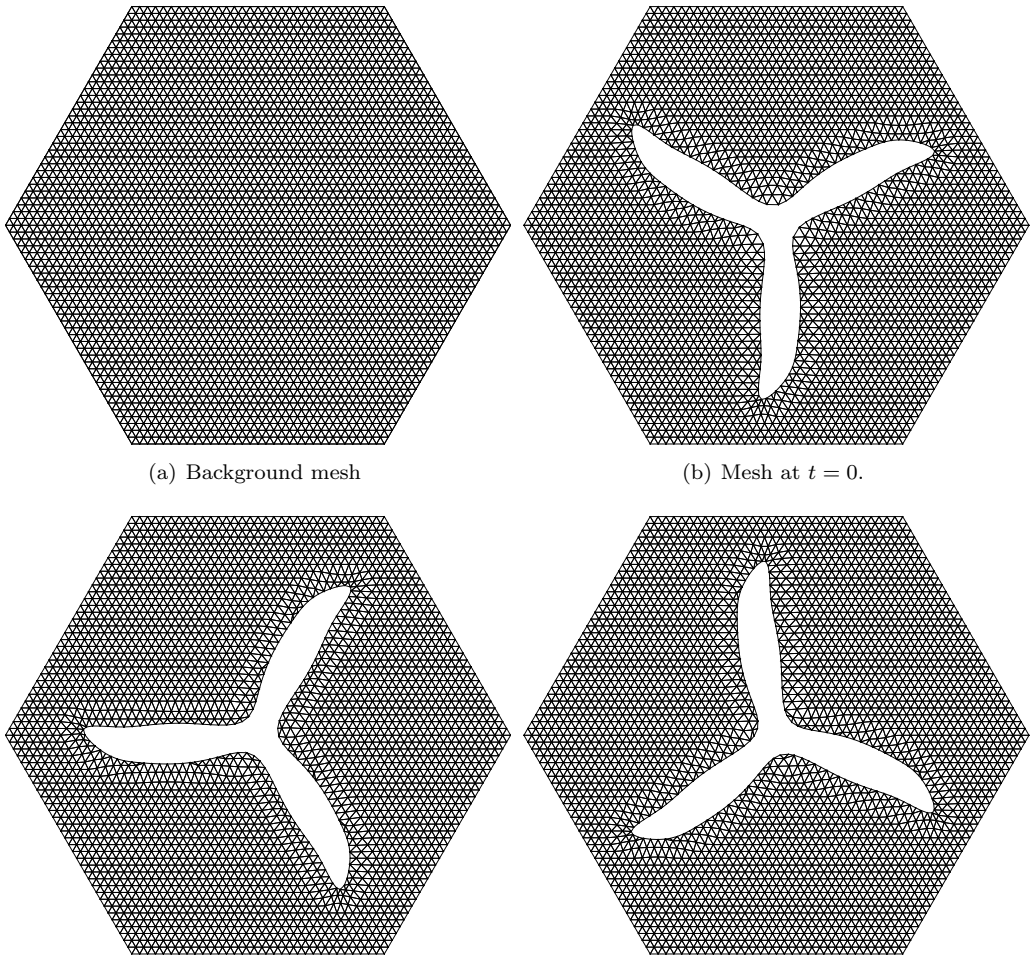

(a) Background mesh

(b) Mesh at $t = 0$.

(c) Mesh at $t = 0.125$.

(d) Mesh at $t = 0.25$.

Figure 6.13: Universal mesh for a rotating stirrer.

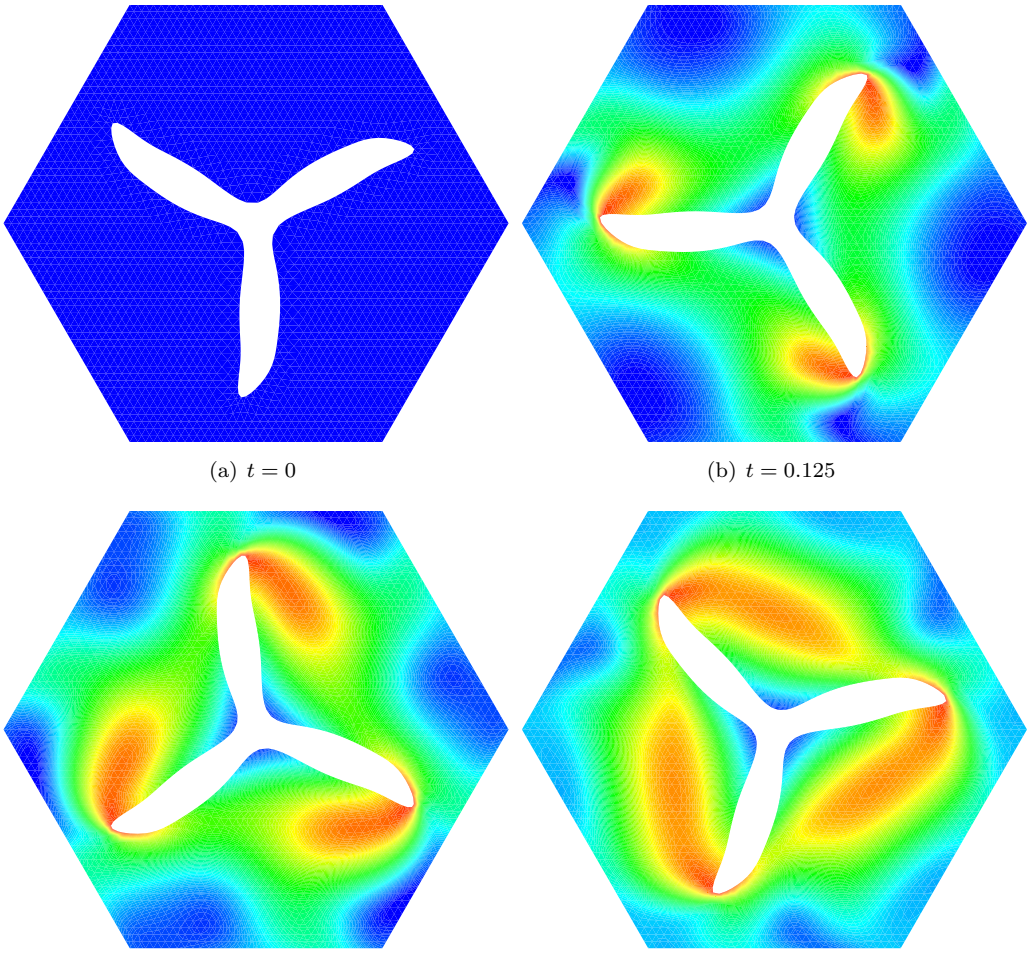

(a) $t = 0$ (b) $t = 0.125$

(c) $t = 0.25$ (d) $t = 0.375$

Figure 6.14: Velocity magnitude contours during a simulation of stirring of a viscous fluid.

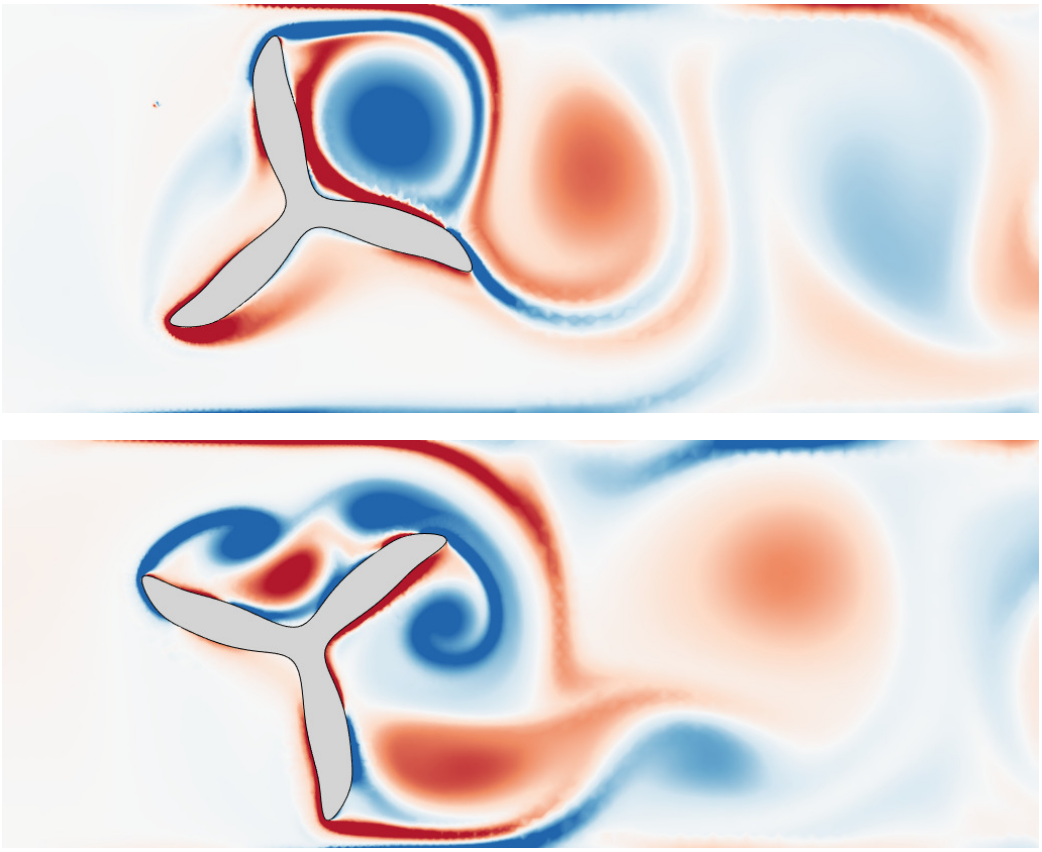

Figure 6.15: Vorticity contours during a simulation of flow past a rotating stirrer. The simulation consists of incompressible viscous flow, computed using a universal mesh together with Taylor-Hood finite elements.

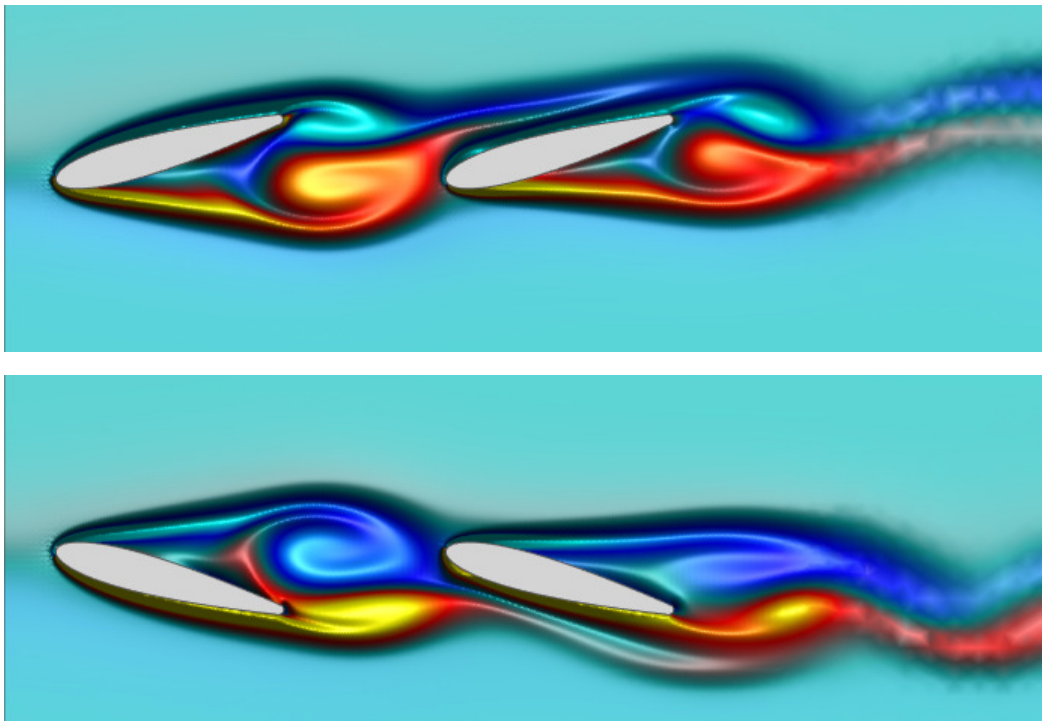

Figure 6.16: Vorticity contours during a simulation of flow past pitching airfoils. The simulation consists of incompressible viscous flow, computed using a universal mesh together with Taylor-Hood finite elements.

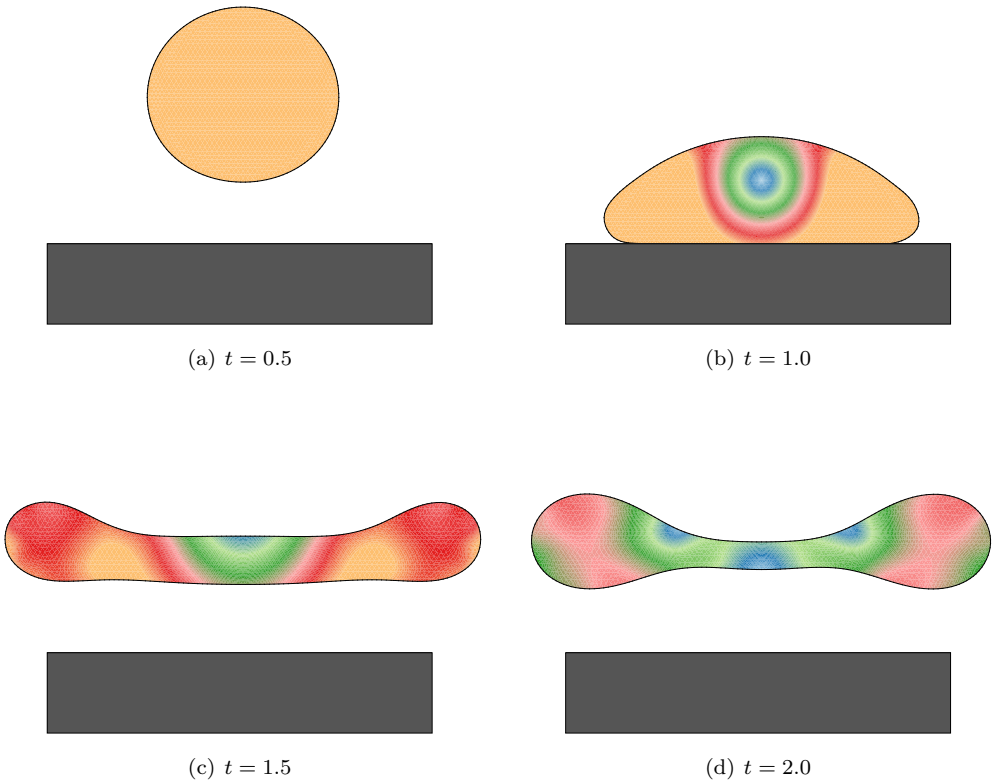

(a) $t = 0.5$ (b) $t = 1.0$

(c) $t = 1.5$ (d) $t = 2.0$

Figure 6.17: Velocity magnitude contours during a simulation of a droplet impacting a solid surface (modeled as a potential barrier).

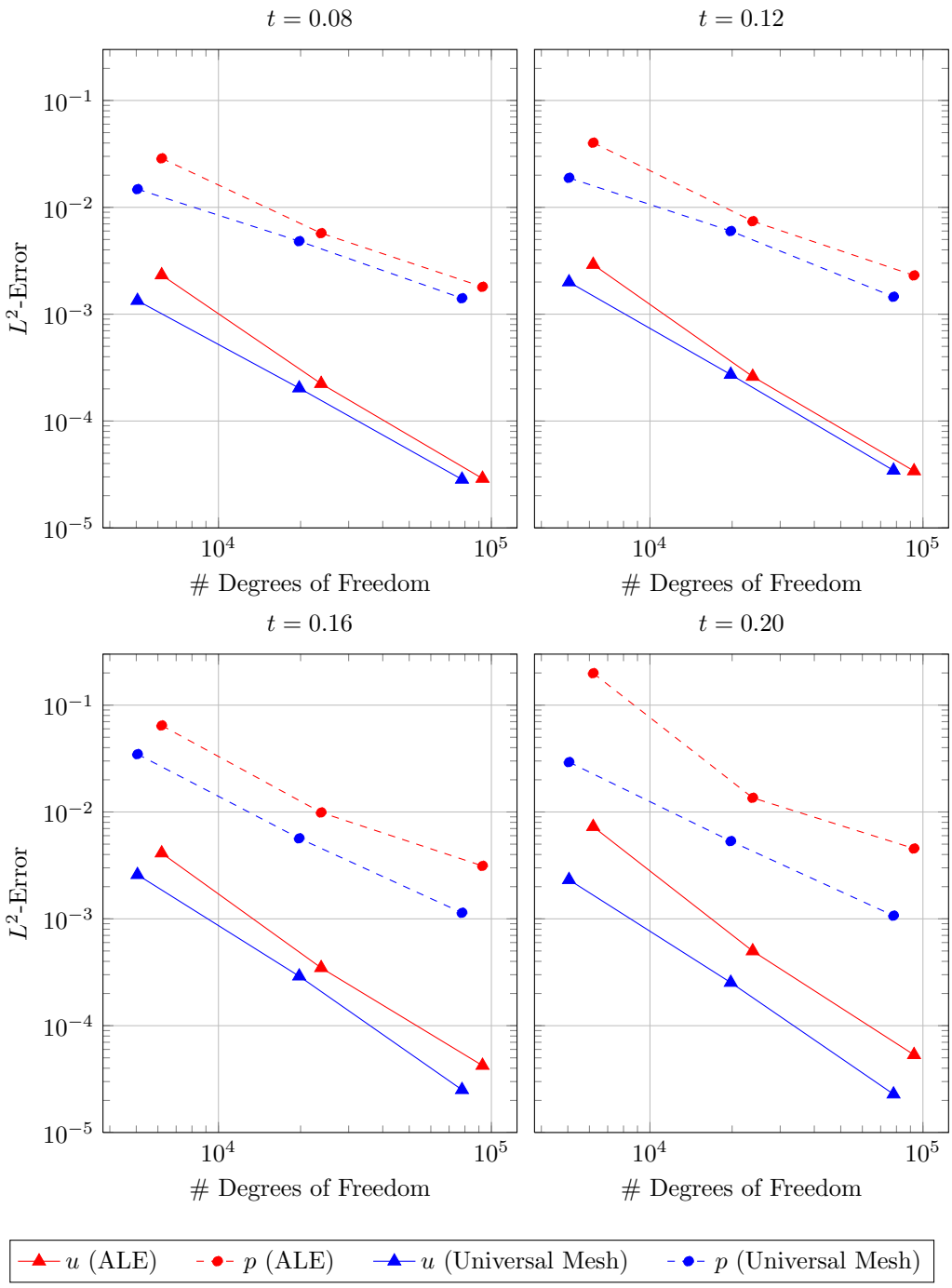

Figure 6.18: L^2-error in velocity u and pressure p versus number of degrees of freedom, at various times t during a simulation of fluid flow around a rotating ellipse. Two methods are compared: an ALE scheme with an elasticity-based mesh motion, and a universal mesh. In both cases, Taylor-Hood finite elements are used in conjunction with a 3^{rd}-order implicit Runge Kutta time integrator. At early times t, the two approaches commit comparable errors for comparable cost. As time progresses, the errors incurred by both methods grow, but deterioration of the quality of the mesh generated by the ALE scheme leads in this case to a more rapid increase in the error relative to universal meshes.

Bibliography

[1] M. R. Albert and K. O'Neill. "Moving boundary-moving mesh analysis of phase change using finite elements with transfinite mappings". In: *International Journal for Numerical Methods in Engineering* 23 (1986), pp. 591–607.

[2] A. S. Almgren, J. B. Bell, P. Colella, and T. Marthaler. "A Cartesian grid projection method for the incompressible Euler equations in complex geometries". In: *SIAM Journal on Scientific Computing* 18.5 (1997), pp. 1289–1309.

[3] H. Amann. *Ordinary differential equations: An introduction to nonlinear analysis*. Vol. 13. Walter de Gruyter, 1990.

[4] D. Anderson, G. B. McFadden, and A. Wheeler. "Diffuse-interface methods in fluid mechanics". In: *Annual review of fluid mechanics* 30.1 (1998), pp. 139–165.

[5] A. B. Andreev. "Supercloseness between the elliptic projection and the approximate eigenfunction and its application to a postprocessing of finite element eigenvalue problems". In: *Numerical Analysis and Its Applications*. Springer, 2005, pp. 100–107.

[6] T. Apostol. *Mathematical Analysis*. Reading, Massachusetts: Addison-Wesley, 1981.

[7] M. Arroyo, L. Heltai, D. Millán, and A. DeSimone. "Reverse engineering the euglenoid movement". In: *Proceedings of the National Academy of Sciences* 109.44 (2012), pp. 17874–17879.

[8] H. Askes, E. Kuhl, and P. Steinmann. "An ALE formulation based on spatial and material settings of continuum mechanics. Part 2: Classification and applications". In: *Computer Methods in Applied Mechanics and Engineering* 193.39 (2004), pp. 4223–4245.

[9] R. F. Ausas, F. S. Sousa, and G. C. Buscaglia. "An improved finite element space for discontinuous pressures". In: *Computer Methods in Applied Mechanics and Engineering* 199.17 (2010), pp. 1019–1031.

[10] F. Aymone and J. Luis. "Mesh motion techniques for the ALE formulation in 3D large deformation problems". In: *International journal for numerical methods in engineering* 59.14 (2004), pp. 1879–1908.

[11] I. Babuška and A. Miller. "The post-processing approach in the finite element method, Part 1: Calculation of displacements, stresses and other higher derivatives of the displacements". In: *International Journal for numerical methods in engineering* 20.6 (1984), pp. 1085–1109.

[12] I. Babuška, T. Strouboulis, C. S. Upadhyay, and S. K. Gangaraj. "Computer-based proof of the existence of superconvergence points in the finite element method; superconvergence of the derivatives in finite element solutions of Laplace's, Poisson's, and the elasticity equations". In: *Numerical Methods for Partial Differential Equations* 12.3 (1996), pp. 347–392.

[13] J. Baiges and R. Codina. "The fixed-mesh ALE approach applied to solid mechanics and fluid–structure interaction problems". In: *International journal for numerical methods in engineering* 81.12 (2010), pp. 1529–1557.

[14] J. Baiges, R. Codina, and H. Coppola-Owen. "The fixed-mesh ALE approach for the numerical simulation of floating solids". In: *International Journal for Numerical Methods in Fluids* 67.8 (2011), pp. 1004–1023.

[15] R. E. Bank and J. Xu. "Asymptotically exact a posteriori error estimators, Part I: Grids with superconvergence". In: *SIAM Journal on Numerical Analysis* 41.6 (2003), pp. 2294–2312.

[16] P. Z. Bar-Yoseph, S. Mereu, S. Chippada, and V. J. Kalro. "Automatic monitoring of element shape quality in 2-D and 3-D computational mesh dynamics". In: *Computational Mechanics* 27.5 (2001), pp. 378–395.

[17] J. Barlow. "Optimal stress locations in finite element models". In: *International Journal for Numerical Methods in Engineering* 10.2 (1976), pp. 243–251.

[18] S. A. Bayyuk, K. Powell, and B Van Leer. "A simulation technique for 2-D unsteady inviscid flows around arbitrarily moving and deforming bodies of arbitrary geometry". In: *Ann Arbor* 1001 (1993), pp. 48109–2140.

[19] G. Beckett, J. A. Mackenzie, and M. L. Robertson. "A moving mesh finite element method for the solution of two-dimensional Stefan problems". In: *Journal of Computational Physics* 168 (2001), pp. 500–518.

[20] M. Bern, D. Eppstein, and J. Gilbert. "Provably good mesh generation". In: *Journal of Computer and System Sciences* 48.3 (1994), pp. 384–409.

[21] D. Boffi and L. Gastaldi. "Stability and geometric conservation laws for ALE formulations". In: *Computer methods in applied mechanics and engineering* 193.42 (2004), pp. 4717–4739.

[22] A. Bonito, I. Kyza, and R. H. Nochetto. "Time-discrete higher order ALE formulations: A priori error analysis". In: *Numerische Mathematik* 125.2 (2013), pp. 225–257.

[23] A. Bonito, I. Kyza, and R. H. Nochetto. "Time-discrete higher order ALE formulations: Stability". In: *SIAM Journal on Numerical Analysis* 51.1 (2013), pp. 577–604.

[24] R. Bonnerot and P. Jamet. "A second order finite element method for the one-dimensional Stefan problem". In: *International Journal for Numerical Methods in Engineering* 8 (1974), pp. 811–820.

[25] R. Bonnerot and P. Jamet. "A third order accurate discontinuous finite element method for the one-dimensional Stefan problem". In: *Journal of Computational Physics* 32 (1979), pp. 145–167.

[26] J. Brandts and M. Křížek. "Gradient superconvergence on uniform simplicial partitions of polytopes". In: *IMA Journal of Numerical Analysis* 23.3 (2003), pp. 489–505.

[27] K. E. Brenan, S. L. Campbell, and L. R. Petzold. *Numerical solution of initial-value problems in differential-algebraic equations*. Vol. 14. SIAM, 1996.

[28] S. C. Brenner and L. R. Scott. *The Mathematical Theory of Finite Element Methods*. New York: Springer, 1994.

[29] H. Brezis. *Functional analysis, Sobolev spaces and partial differential equations*. New York: Springer, 2011.

[30] H. Brezis. *Operateurs Maximaux Monotones Et Semi-Groupes De Contractions Dans Les Espaces De Hilbert*. Amsterdam: North Holland, 1973.

[31] D. L. Brown, R. Cortez, and M. L. Minion. "Accurate projection methods for the incompressible Navier–Stokes equations". In: *Journal of Computational Physics* 168.2 (2001), pp. 464–499.

[32] K. Burrage, J. C. Butcher, and F. H. Chipman. "An implementation of singly-implicit Runge-Kutta methods". In: *BIT Numerical Mathematics* 20.3 (1980), pp. 326–340.

[33] M. M. Chiaramonte, E. S. Gawlik, H. Kabaria, and A. J. Lew. "Universal Meshes for the Simulation of Brittle Fracture and Moving Boundary Problems". In: *IUTAM Symposium on Innovative Numerical Approaches for Materials and Structures in Multi-Field and Multi-Scale Problems*. Lecture Notes in Applied and Computational Mechanics. Berlin: Springer, 2015.

[34] A. J. Chorin. "Numerical solution of the Navier-Stokes equations". In: *Mathematics of computation* 22.104 (1968), pp. 745–762.

[35] P. Ciarlet. *The finite element method for elliptic problems*. Vol. 4. North-Holland Publishing Company, 1978.

[36] B. Cockburn, M. Luskin, C. W. Shu, and E. Süli. "Enhanced accuracy by post-processing for finite element methods for hyperbolic equations". In: *Mathematics of Computation* 72.242 (2003), pp. 577–606.

[37] J.-F. Cori, S. Etienne, D. Pelletier, and A. Garon. "Implicit Runge-Kutta time integrators for fluid-structure interactions". In: *48th AIAA Aerospace Sciences Meeting and Exhibit, Orlando, FL*. 2010, pp. 4–7.

[38] R. Cortez and M. Minion. "The blob projection method for immersed boundary problems". In: *Journal of Computational Physics* 161.2 (2000), pp. 428–453.

[39] M. Crouzeix and V. Thomee. "Stability in L^p and $W^{1,p}$ of the L^2-projection onto Finite Element Function Spaces". In: *Mathematics of Computation* 48.178 (1987), pp. 531–532.

[40] D. DeZeeuw and K. G. Powell. "An adaptively refined Cartesian mesh solver for the Euler equations". In: *Journal of Computational Physics* 104.1 (1993), pp. 56–68.

[41] J. Dolbow and I. Harari. "An efficient finite element method for embedded interface problems". In: *International journal for numerical methods in engineering* 78.2 (2009), pp. 229–252.

[42] J. Donea, S. Giuliani, and J. P. Halleux. "An arbitrary Lagrangian-Eulerian finite element method for transient dynamic fluid-structure interactions". In: *Computer Methods in Applied Mechanics and Engineering* 33.1 (1982), pp. 689–723.

[43] T. Dupont. "Mesh modification for evolution equations". In: *Mathematics of Computation* 39 (1982), pp. 85–107.

[44] C. M. Elliott and C. Venkataraman. "Error analysis for an ALE evolving surface finite element method". In: *arXiv preprint arXiv:1403.1402* (2014).

[45] A. Ern and J. L. Guermond. *Theory and Practice of Finite Elements*. New York: Springer, 2004.

[46] L. C. Evans. *Partial Differential Equations*. Graduate studies in mathematics. American Mathematical Society, 2010.

[47] E. A. Fadlun, R Verzicco, P. Orlandi, and J. Mohd-Yusof. "Combined immersed-boundary finite-difference methods for three-dimensional complex flow simulations". In: *Journal of Computational Physics* 161.1 (2000), pp. 35–60.

[48] C. Farhat and P. Geuzaine. "Design and analysis of robust ALE time-integrators for the solution of unsteady flow problems on moving grids". In: *Computer Methods in Applied Mechanics and Engineering* 193.39 (2004), pp. 4073–4095.

[49] C. Farhat, P. Geuzaine, and C. Grandmont. "The discrete geometric conservation law and the nonlinear stability of ALE schemes for the solution of flow problems on moving grids". In: *Journal of Computational Physics* 174.2 (2001), pp. 669–694.

[50] C. Farhat, K. G. van der Zee, and P. Geuzaine. "Provably second-order time-accurate loosely-coupled solution algorithms for transient nonlinear computational aeroelasticity". In: *Computer methods in applied mechanics and engineering* 195.17 (2006), pp. 1973–2001.

[51] C. Farhat, A. Rallu, K. Wang, and T. Belytschko. "Robust and provably second-order explicit–explicit and implicit–explicit staggered time-integrators for highly non-linear compressible fluid–structure interaction problems". In: *International Journal for Numerical Methods in Engineering* 84.1 (2010), pp. 73–107.

[52] C. Farhat, C. Degand, B. Koobus, and M. Lesoinne. "Torsional springs for two-dimensional dynamic unstructured fluid meshes". In: *Computer methods in applied mechanics and engineering* 163.1 (1998), pp. 231–245.

[53] J. J. Feng, C. Liu, J. Shen, and P. Yue. "An energetic variational formulation with phase field methods for interfacial dynamics of complex fluids: Advantages and challenges". In: *Modeling of soft matter*. Springer, 2005, pp. 1–26.

[54] E. Ferrer and R. H. Willden. "A high order Discontinuous Galerkin–Fourier incompressible 3D Navier–Stokes solver with rotating sliding meshes". In: *Journal of Computational Physics* 231.21 (2012), pp. 7037–7056.

[55] L. Formaggia and F. Nobile. "A stability analysis for the arbitrary Lagrangian Eulerian formulation with finite elements". In: *East West Journal of Numerical Mathematics* 7 (1999), pp. 105–132.

[56] L. Formaggia and F. Nobile. "Stability analysis of second-order time accurate schemes for ALE–FEM". In: *Computer methods in applied mechanics and engineering* 193.39 (2004), pp. 4097–4116.

[57] L. Gastaldi. "A priori error estimates for the arbitrary Lagrangian Eulerian formulation with finite elements". In: *Journal of Numerical Mathematics* 9.2 (2001), pp. 123–156.

[58] E. S. Gawlik, H. Kabaria, and A. J. Lew. "High-order methods for low Reynolds number flows around moving obstacles based on universal meshes". In: *International Journal for Numerical Methods in Engineering (to appear)* (2015).

[59] E. S. Gawlik and A. J. Lew. "High-order finite element methods for moving boundary problems with prescribed boundary evolution". In: *Computer Methods in Applied Mechanics and Engineering* 278 (2014), pp. 314 –346.

[60] E. S. Gawlik and A. J. Lew. "Supercloseness of orthogonal projections onto nearby finite element spaces". In: *Mathematical Modelling and Numerical Analysis* 49 (2014), pp. 559–576.

[61] E. S. Gawlik and A. J. Lew. "Unified analysis of finite element methods for problems with moving boundaries". In: *(Submitted)* (2014).

[62] A. Gerstenberger and W. A. Wall. "An extended finite element method/Lagrange multiplier based approach for fluid–structure interaction". In: *Computer Methods in Applied Mechanics and Engineering* 197.19 (2008), pp. 1699–1714.

[63] P. Geuzaine, C. Grandmont, and C. Farhat. "Design and analysis of ALE schemes with provable second-order time-accuracy for inviscid and viscous flow simulations". In: *Journal of Computational Physics* 191.1 (2003), pp. 206–227.

[64] F. Gibou and R. Fedkiw. "A fourth order accurate discretization for the Laplace and heat equations on arbitrary domains, with applications to the Stefan problem". In: *Journal of Computational Physics* 202 (2005), pp. 577–601.

[65] G. Goodsell. "Pointwise superconvergence of the gradient for the linear tetrahedral element". In: *Numerical Methods for Partial Differential Equations* 10.5 (1994), pp. 651–666.

[66] G. Goodsell and J. R. Whiteman. "A unified treatment of superconvergent recovered gradient functions for piecewise linear finite element approximations". In: *International Journal for Numerical Methods in Engineering* 27.3 (1989), pp. 469–481.

[67] B. E. Griffith and C. S. Peskin. "On the order of accuracy of the immersed boundary method: higher order convergence rates for sufficiently smooth problems". In: *Journal of Computational Physics* 208.1 (2005), pp. 75–105.

[68] H. Guillard and C. Farhat. "On the significance of the geometric conservation law for flow computations on moving meshes". In: *Computer Methods in Applied Mechanics and Engineering* 190.11 (2000), pp. 1467–1482.

[69] E Guilmineau and P Queutey. "A numerical simulation of vortex shedding from an oscillating circular cylinder". In: *Journal of Fluids and Structures* 16.6 (2002), pp. 773–794.

[70] E. Hairer and G. Wanner. *Solving Ordinary Differential Equations II: Stiff and DIfferential-Algebraic Problems*. Berlin: Springer, 2002.

[71] A. Hansbo and P. Hansbo. "A finite element method for the simulation of strong and weak discontinuities in solid mechanics". In: *Computer methods in applied mechanics and engineering* 193.33 (2004), pp. 3523–3540.

[72] A. Hay, K. Yu, S Etienne, A. Garon, and D Pelletier. "High-order temporal accuracy for 3D finite-element ALE flow simulations". In: *Computers & Fluids* 100 (2014), pp. 204–217.

[73] B. T. Helenbrook. "Mesh deformation using the biharmonic operator". In: *International journal for numerical methods in engineering* 56.7 (2003), pp. 1007–1021.

[74] C. W. Hirt, A. A. Amsden, and J. L. Cook. "An arbitrary Lagrangian-Eulerian computing method for all flow speeds". In: *Journal of Computational Physics* 14.3 (1974), pp. 227–253.

[75] X. Hu, B. Khoo, N. Adams, and F. Huang. "A conservative interface method for compressible flows". In: *Journal of Computational Physics* 219.2 (2006), pp. 553–578.

[76] Y. Huang and J. Xu. "Superconvergence of quadratic finite elements on mildly structured grids". In: *Mathematics of Computation* 77.263 (2008), pp. 1253–1268.

[77] T. J. R. Hughes, W. K. Liu, and T. K. Zimmermann. "Lagrangian-Eulerian finite element formulation for incompressible viscous flows". In: *Computer methods in applied mechanics and engineering* 29.3 (1981), pp. 329–349.

[78] J.-P. P. J. Donea A. Huerta and A. Rodriguez-Ferran. "Encyclopedia of Computational Mechanics". In: *Encyclopedia of Computational Mechanics*. Ed. by E. Stein, R. de Borst, and T. J. R. Hughes. New York: John Wiley and Sons, Ltd., 2004. Chap. 14: Arbitrary Lagrangian-Eulerian Methods.

[79] P. Jamet. "Galerkin-type approximations which are discontinuous in time for parabolic equations in a variable domain". In: *SIAM Journal on Numerical Analysis* 15 (1978), pp. 912–928.

[80] A. A. Johnson and T. E. Tezduyar. "Mesh update strategies in parallel finite element computations of flow problems with moving boundaries and interfaces". In: *Computer methods in applied mechanics and engineering* 119.1 (1994), pp. 73–94.

[81] Y.-S. Kang, D. Sohn, J. H. Kim, H.-G. Kim, and S. Im. "A sliding mesh technique for the finite element simulation of fluid–solid interaction problems by using variable-node elements". In: *Computers & Structures* 130 (2014), pp. 91–104.

[82] A. R. Khoei, M. Anahid, and K. Shahim. "An extended arbitrary Lagrangian–Eulerian finite element method for large deformation of solid mechanics". In: *Finite Elements in Analysis and Design* 44.6 (2008), pp. 401–416.

[83] D. Kim and H. Choi. "Immersed boundary method for flow around an arbitrarily moving body". In: *Journal of Computational Physics* 212.2 (2006), pp. 662–680.

[84] P. Knupp, L. G. Margolin, and M. Shashkov. "Reference Jacobian optimization-based rezone strategies for arbitrary Lagrangian Eulerian methods". In: *Journal of Computational Physics* 176.1 (2002), pp. 93–128.

[85] M. Křížek and P. Neittaanmäki. "On superconvergence techniques". In: *Acta Applicandae Mathematica* 9.3 (1987), pp. 175–198.

[86] M. Křížek and P. Neittaanmäki. "Superconvergence phenomenon in the finite element method arising from averaging gradients". In: *Numerische Mathematik* 45.1 (1984), pp. 105–116.

[87] H. Lamb. *Hydrodynamics*. Cambridge university press, 1993.

[88] J. Lee, J. Kim, H. Choi, and K.-S. Yang. "Sources of spurious force oscillations from an immersed boundary method for moving-body problems". In: *Journal of computational physics* 230.7 (2011), pp. 2677–2695.

[89] P. Lesaint and R. Touzani. "Approximation of the heat equation in a variable domain with application to the Stefan problem". In: *SIAM Journal on Numerical Analysis* 26 (1989), pp. 366–379.

[90] R. J. Leveque and Z. Li. "The immersed interface method for elliptic equations with discontinuous coefficients and singular sources". In: *SIAM Journal on Numerical Analysis* 31.4 (1994), pp. 1019–1044.

[91] A. J. Lew and G. C. Buscaglia. "A discontinuous-Galerkin-based immersed boundary method". In: *International Journal for Numerical Methods in Engineering* 76.4 (2008), pp. 427–454.

[92] B. Li. "Lagrange interpolation and finite element superconvergence". In: *Numerical Methods for Partial Differential Equations* 20.1 (2004), pp. 33–59.

[93] Z. Li and M.-C. Lai. "The immersed interface method for the Navier–Stokes equations with singular forces". In: *Journal of Computational Physics* 171.2 (2001), pp. 822–842.

[94] G. M. Lieberman. *Second Order Parabolic Differential Equations*. Singapore: World Scientific, 1996.

[95] M. N. Linnick and H. F. Fasel. "A high-order immersed interface method for simulating unsteady incompressible flows on irregular domains". In: *Journal of Computational Physics* 204.1 (2005), pp. 157–192.

[96] J. Liu, G. Hu, and Q. Zhu. "Superconvergence of tetrahedral quadratic finite elements for a variable coefficient elliptic equation". In: *Numerical Methods for Partial Differential Equations* 29 (3 2012), pp. 1043–1055.

[97] W. K. Liu, H. Chang, C. J. Chen, and T. Belytschko. "Arbitrary Lagrangian-Eulerian Petrov-Galerkin finite elements for nonlinear continua". In: *Computer Methods in Applied Mechanics and Engineering* 68.3 (1988), pp. 259–310.

[98] R. Löhner and C. Yang. "Improved ALE mesh velocities for moving bodies". In: *Communications in numerical methods in engineering* 12.10 (1996), pp. 599–608.

[99] I Lomtev, R. Kirby, and G. Karniadakis. "A discontinuous Galerkin ALE method for compressible viscous flows in moving domains". In: *Journal of Computational Physics* 155.1 (1999), pp. 128–159.

[100] D. R. Lynch. "Unified Approach to Simulation on Deforming Elements with Application to Phase Change Problems". In: *Journal of Computational Physics* 47 (1982), pp. 387–411.

[101] J. A. Mackenzie and W. R. Mekwi. "An unconditionally stable second-order accurate ALE–FEM scheme for two-dimensional convection–diffusion problems". In: *IMA Journal of Numerical Analysis* 32.3 (2012), pp. 888–905.

[102] S Marella, S Krishnan, H Liu, and H. Udaykumar. "Sharp interface Cartesian grid method I: an easily implemented technique for 3D moving boundary computations". In: *Journal of Computational Physics* 210.1 (2005), pp. 1–31.

[103] J. Marsden, T. Ratiu, and R. Abraham. *Manifolds, tensor analysis, and applications (Third edition)*. New York: Springer-Verlag, 2007.

[104] A. Masud. "Effects of mesh motion on the stability and convergence of ALE based formulations for moving boundary flows". In: *Computational Mechanics* 38.4-5 (2006), pp. 430–439.

[105] D. J. Mavriplis and C. R. Nastase. "On the geometric conservation law for high-order discontinuous Galerkin discretizations on dynamically deforming meshes". In: *Journal of Computational Physics* 230.11 (2011), pp. 4285–4300.

[106] M. Meinke, L. Schneiders, C. Günther, and W. Schröder. "A cut-cell method for sharp moving boundaries in Cartesian grids". In: *Computers & Fluids* 85 (2013), pp. 135–142.

[107] C. A. A. Minoli and D. A. Kopriva. "Discontinuous Galerkin spectral element approximations on moving meshes". In: *Journal of Computational Physics* 230.5 (2011), pp. 1876–1902.

[108] F. Montefusculo, F. Sousa, and G. Buscaglia. "High-order ALE schemes with applications in capillary flows". In: *(Submitted)* (2014).

[109] L. A. Oganesyan and L. A. Rukhovets. "Study of the rate of convergence of variational difference schemes for second-order elliptic equations in a two-dimensional field with a smooth boundary". In: *USSR Computational Mathematics and Mathematical Physics* 9.5 (1969), pp. 158–183.

[110] A Ongoren and D Rockwell. "Flow structure from an oscillating cylinder Part 1. Mechanisms of phase shift and recovery in the near wake". In: *Journal of Fluid Mechanics* 191 (1988), pp. 197–223.

[111] R. B. Pember, J. B. Bell, P. Colella, W. Y. Curtchfield, and M. L. Welcome. "An adaptive Cartesian grid method for unsteady compressible flow in irregular regions". In: *Journal of computational Physics* 120.2 (1995), pp. 278–304.

[112] P. O. Persson. "High-Order LES Simulations using Implicit-Explicit Runge-Kutta Schemes". In: *Proc. of the 49th AIAA Aerospace Sciences Meeting and Exhibit.* AIAA-2011-684. 2011.

[113] P. O. Persson. "High-Order Navier-Stokes Simulations using a Sparse Line-Based Discontinuous Galerkin Method". In: *Proc. of the 50th AIAA Aerospace Sciences Meeting and Exhibit.* AIAA-2012-456. 2012.

[114] C. S. Peskin. "The immersed boundary method". In: *Acta Numerica* 11.0 (2002), pp. 479–517.

[115] R. Rangarajan and A. J. Lew. "Parameterization of planar curves immersed in triangulations with application to finite elements". In: *International Journal for Numerical Methods in Engineering* 88.6 (2011), pp. 556–585.

[116] R. Rangarajan and A. J. Lew. "Universal Meshes: A method for triangulating planar curved domains immersed in nonconforming triangulations". In: *International Journal for Numerical Methods in Engineering* 98.4 (2014), pp. 236–264.

[117] R. Rangarajan, A. Lew, and G. C. Buscaglia. "A discontinuous-Galerkin-based immersed boundary method with non-homogeneous boundary conditions and its application to elasticity". In: *Computer Methods in Applied Mechanics and Engineering* 198.17 (2009), pp. 1513–1534.

[118] R. Rangarajan and A. J. Lew. "Analysis of a method to parameterize planar curves immersed in triangulations". In: *SIAM Journal on Numerical Analysis* 51.3 (2013), pp. 1392–1420.

[119] S. Rhebergen and B. Cockburn. "A space–time hybridizable discontinuous Galerkin method for incompressible flows on deforming domains". In: *Journal of Computational Physics* 231.11 (2012), pp. 4185–4204.

[120] S. Rhebergen and B. Cockburn. "Space-Time Hybridizable Discontinuous Galerkin Method for the Advection–Diffusion Equation on Moving and Deforming Meshes". In: *The Courant–Friedrichs–Lewy (CFL) Condition*. Springer, 2013, pp. 45–63.

[121] J. F. Rodrigues. *Obstacle Problems in Mathematical Physics*. Amsterdam: Elsevier, 1987.

[122] A. H. Schatz, I. H. Sloan, and L. B. Wahlbin. "Superconvergence in finite element methods and meshes that are locally symmetric with respect to a point". In: *SIAM Journal on Numerical Analysis* 33.2 (1996), pp. 505–521.

[123] L. Schneiders, D. Hartmann, M. Meinke, and W. Schröder. "An accurate moving boundary formulation in cut-cell methods". In: *Journal of Computational Physics* 235 (2013), pp. 786–809.

[124] J. H. Seo and R. Mittal. "A sharp-interface immersed boundary method with improved mass conservation and reduced spurious pressure oscillations". In: *Journal of computational physics* 230.19 (2011), pp. 7347–7363.

[125] J. A. Sethian. *Level set methods and fast marching methods : evolving interfaces in computational geometry, fluid mechanics, computer vision, and materials science*. Cambridge: Cambridge University Press, 1999.

[126] M. Souli, A. Ouahsine, and L. Lewin. "ALE formulation for fluid–structure interaction problems". In: *Computer methods in applied mechanics and engineering* 190.5 (2000), pp. 659–675.

[127] J. M. Sullivan and D. R. Lynch. "Finite element simulation of planar instabilities during solidification of an undercooled melt". In: *Journal of Computational Physics* 69 (1987), pp. 81–111.

[128] N. Takashi. "ALE finite element computations of fluid-structure interaction problems". In: *Computer methods in applied mechanics and engineering* 112.1 (1994), pp. 291–308.

[129] C. Taylor and P. Hood. "A numerical solution of the Navier-Stokes equations using the finite element technique". In: *Computers & Fluids* 1.1 (1973), pp. 73–100.

[130] R. Temam. "Une méthode d'approximation de la solution des équations de Navier-Stokes". In: *Bulletin de la Société Mathématique de France* 96 (1968), pp. 115–152.

[131] T. E. Tezduyar et al. "Modelling of fluid–structure interactions with the space–time finite elements: Arterial fluid mechanics". In: *International Journal for Numerical Methods in Fluids* 54.6-8 (2007), pp. 901–922.

[132] V. Thomee. *Galerkin Finite Element Methods for Parabolic Problems*. Berlin: Springer, 1991.

[133] H. S. Udaykumar, R. Mittal, P. Rampunggoon, and A. Khanna. "A sharp interface Cartesian grid method for simulating flows with complex moving boundaries". In: *Journal of Computational Physics* 174.1 (2001), pp. 345–380.

[134] L. B Wahlbin. *Superconvergence in Galerkin finite element methods*. Berlin: Springer, 1995.

[135] J. Wang and M. S. Gadala. "Formulation and survey of ALE method in nonlinear solid mechanics". In: *Finite Elements in Analysis and Design* 24.4 (1997), pp. 253–269.

[136] L. Wang and P.-O. Persson. "A Discontinuous Galerkin Method for the Navier-Stokes Equations on Deforming Domains using Unstructured Moving Space-Time Meshes". In: (2013).

[137] M. F. Wheeler. "An optimal L^∞ error estimate for Galerkin approximations to solutions of two-point boundary value problems". In: *SIAM Journal on Numerical Analysis* 10.5 (1973), pp. 914–917.

[138] S. Xu and Z. Wang. "An immersed interface method for simulating the interaction of a fluid with moving boundaries". In: *Journal of Computational Physics* 216 (2006), pp. 454–493.

[139] X. Yang, X. Zhang, Z. Li, and G.-W. He. "A smoothing technique for discrete delta functions with application to immersed boundary method in moving boundary simulations". In: *Journal of Computational Physics* 228.20 (2009), pp. 7821–7836.

[140] Z. Yang and D. J. Mavriplis. "Unstructured dynamic meshes with higher-order time integration schemes for the unsteady Navier-Stokes equations". In: *AIAA paper* 1222.2005 (2005), p. 1.

[141] W. Ying, C. S. Henriquez, and D. J Rose. "Composite backward differentiation formula: an extension of the TR-BDF2 scheme". In: *Submitted to Applied Numerical Mathematics* (2009).

[142] N. Zabaras and Y. Ruan. "Moving and deforming finite-element simulation of two-dimensional Stefan problems". In: *Communications in Applied Numerical Methods* 6 (1990), pp. 495–506.

[143] X. Zeng and C. Farhat. "A systematic approach for constructing higher-order immersed boundary and ghost fluid methods for fluid–structure interaction problems". In: *Journal of Computational Physics* 231.7 (2012), pp. 2892–2923.

[144] P. Zhao and J. C. Heinrich. "Front-tracking finite element method for dendritic solidification". In: *Journal of Computational Physics* 173 (2001), pp. 765–796.

[145] W. P. Ziemer. *Weakly Differentiable Functions: Sobolev Spaces and Functions of Bounded Variation*. New York: Springer, 1989.

[146] O. C. Zienkiewicz and J. Z. Zhu. "The superconvergent patch recovery and a posteriori error estimates. Part 1: The recovery technique". In: *International Journal for Numerical Methods in Engineering* 33.7 (1992), pp. 1331–1364.

[147] A. Zilian and A Legay. "The enriched space–time finite element method (EST) for simultaneous solution of fluid–structure interaction". In: *International Journal for Numerical Methods in Engineering* 75.3 (2008), pp. 305–334.